Friction Conditioning in Metal Forming Using Engineered Surface Micro-Geometries (ESMGs)

Baharozan Mohid

Glasgow, February 2011

Friction Conditioning in Metal Forming Using Engineered Surface Micro-Geometries (ESMGs)

Baharozan Mohid

This thesis is submitted to the Department of
Design, Manufacture and Engineering Management
University of Strathclyde
For the degree of Doctor of Philosophy

Glasgow, February 2011

‘This thesis is the result of the author’s original research. It has been composed by the author and has not been previously submitted for examination which has led to the award of a degree’

Signed :
Date : 10th February 2011

TABLE OF CONTENTS

Chapter 5 Experimental Evaluation of Performance of Piezoelectric Actuators under Long-term Cyclic Operations ……………………………………….….. 157

Chapter 6 Discussion ……………………………….................. 203

LIST OF FIGURES

LIST OF TABLES

ACKNOWLEDGEMENTS

First of all, I would like to express my sincere gratitude to my supervisors, Dr. Andrzej Rosochowski and Prof. Raj Balendra. Their invaluable guidance, advice and suggestions have contributed to the successful completion of this work.

Many thanks to my colleagues at the Metal Forming Research Group for their enlightening ideas and constructive comments to improve this research, especially for Dr Kris Chodnikiewicz and Dr Malgorzata Rosochowska.

I am very grateful to Majlis Amanah Rakyat (the Government of Malaysia) and Universiti Kuala Lumpur (UniKL MFI) for providing financial support throughout the duration of the study.

On a more personal note, I am hugely indebted to my wife Madzenah Abu Kassim, who is always patient, understanding and encouraging. I also wish to thank to my daughters and boy, Nabilah, Laila, Cika and Acim, who have been through a lot with us all the time. My family was my source of inspiration.

Finally, I would like to thank my parents, for their love, help and encouragement.

Baharozan MOHID
Glasgow, February 2011

DEDICATION

Notte
Nabilah
Laila
Cika
Acim

And Arwah Wak Mokit & Wak Tonah

ABSTRACT

Friction is a dominant parameter in most metal deformation processes. The interfacial friction between the die and the work-material has a significant effect on material flow; the greater the friction, the greater the forging force, with the consequent effect of reduced tool life. Similarly, in forward extrusion, the interfacial friction between the work-material and the chamber contributes significantly to the extrusion force. The present research addresses the use of the surface micro-geometries (ESMGs) to reduce the interfacial friction in the forging and forward extrusion technology. The approach adopted is to incorporate ESMGs on either the tool surface or the work-material surface with using bespoke texturing system that operates at 50 Hz to render surfaces with impressions of consistent geometry. The tool can be used to render different prescriptions (geometry, density, pattern and orientation) of ESMGs from depth of 0.5 to 50μm on surfaces with undulations of up to 50μm consistently. 3D FE models are presented for establishing the ideal prescription of ESMGs to be used in the experimental evaluations. The results of the FE model were validated by observing the collapse of ESMGs during material deformation. Other experimental evaluations define the influence of different prescriptions of ESMGs in upsetting and forward extrusion. The upsetting results show that ESMGs textured on the tool surface increases friction. However, ESMGs on the work-material surface reduce interfacial friction in comparison to smooth work-materials. In forward extrusion, billets with ESMGs need lower extrusion forces in comparison to billets with smooth surfaces. It may be concluded that ESMGs on work-material surfaces improve the bulk-deformations processes, by reducing friction. The performance of the piezoelectric actuator, which is used to actuate the indention tool during the ESMGs texturing process, has been evaluated under the working frequency of up to 200Hz. The evaluation results show that the actuator is able to provide excellent performance with no degradation of blocking force, free stroke and capacitance for up to 10^9 numbers of cycles of long-term operation. Therefore, it can be concluded that the tested piezoelectric actuator enables achieving consistent ESMG characteristics such as depth and diameter for up to 2 years texturing operation.

Chapter 1

Introduction

1.0 Introduction

The aim of this chapter is to define and determine the research motivation, its aim and objectives. In doing so, this chapter provides the relevant background and rationale for the research undertaken. The research aim, research objectives and thesis structure are explained in this chapter.

1.1 Research Motivation

Friction in metal forming processes has a large influence on material flow, die filling, necessary load and energy, local stresses on tool surface and dimensional accuracy of products [1-3]. In addition, it causes tool surface wear [4]and consequently results in reduced tool life [5]. Thus, reducing friction is of great significance to improve tool life, productivity and product quality [5-7].

Many methods of reducing friction might be used in metal forming process. In some metal forming processes, tools made from low adhesion material such as ceramics, silicon nitride and silicon carbide are used [8]. However, the processes of fabricating such tools are rather complex and expensive. In addition, the application of a liquid lubricant to achieve better tribological performance is still required. Another method that has been studied by numerous researchers and practitioners [9-23] is the application of ultrasonic vibrations on either tool or workpiece. However, this method has not been found appropriate for hot forming operations [21] and has not been widely used due to economic reasons.

For reasons of economics, lubrication is the most widely used technique for reducing friction. However, metal forming processes have been found to be associated with phenomena of high pressure, severe deformation and surface area expansion. These phenomena result in changes in interfacial conditions and lead lubricant film breakdown [24]. Consequently, direct contact at a sliding interface (between die and workpiece) could occur in the area of lubricant breakdown, which finally results in formation of wear particles due to low tribological performance. Continuous supply of lubricant to the sliding interface area to solve this problem could result in many problems for the environment due to a waste of lubricant materials.

In the last decade, the application of specially designed surface texture to reduce friction in metal forming process has received considerable attention from academicians and practitioners [25-29]. It is important to note that common terminology has not been established yet, so the terms “structured”, “textured”, or “engineered” surface are in use [30]. In some other publications, such surface is also called “patterned surface” [31] or surface with “idealized geometry” [32]. The concept used is that during the workpiece deformation, lubricant trapped on the textured surface produces hydrostatic pressure effect that results in the reduction of friction coefficient [25, 27, 28, 33-35]. As the deformation increases, the lubricant is expelled on to the surfaces which are in contact, and consequently creates thin film of lubricant that also causes the reduction of friction coefficient. Furthermore, the micro-pockets on the textured surface act as traps for particles resulting from the abrasive tool wear [36] and consequently eliminate elements causing further tool wear.

Studies reported that incorporation of surface texture on either functional surfaces of forging tools [37, 38] or surfaces of work materials [25, 26, 39, 40] would improve lubrication and consequently increase both the tool-life and the extent of plastic deformation achievable. However, evidence as to how the surface texture parameters such as pattern, density and geometry [29] influence friction is still missing. There is still not enough research work on the possibility of using textured surfaces in metal forming. The studies concerning the application of surface texture in friction reduction are mainly carried out for a sliding contact condition that does not involve plastic deformation. Therefore, the results of these studies might not be relevant to metal forming processes, in which high contact pressure prevails and large plastic deformation takes place. This suggests that there is a need for research into the influence of these parameters under different tribological conditions.

Another important aspect that needs to be considered is the technique of producing surface texture. In mass production applications, producing textured surfaces requires a high-speed, high precession and an economical technique. However, the existing technological processes do not comply with these requirements. Several methods of producing textured surfaces have been introduced such as: (1) lithographic processes (chemical or electrochemical), (2) energy beam processes (laser beam, electron beam, focused ion beam or electric discharge) and (3) mechanical processes (grinding, abrasive jet machining or indentation). These different processes have been used to produce different geometry of textured surfaces such as uniformly distributed shallow grooves [41-43], pyramidal recesses [35], circular ESMGs [29, 35, 37, 41] or square recesses [42]. Applications as well as advantages and disadvantages of these processes are presented in **Table 1.1.**

A prototype of surface texturing system based on indentation technique has been developed at the University Strathclyde [44] (see Chapter 2, section 2.3.6). The system is capable of producing textured surfaces with a depth of indentations of 0.5 - 50μm at a rate of up to 50 indentations per second. The diamond indenter that is used to perform indentation is driven by a piezoelectric actuator, i.e. multi-layer stack ceramic actuator (MSCA). Therefore, the consistency of indentations throughout a long term texturing operation depends on the MSCA displacement consistency. However, as stated in [45-48], the ability of the actuator to deliver displacement and force may be degraded significantly due to many factors (see Chapter 3, section 3.1.1). This may lead to changes in indentation characteristics such as depth and diameter. Therefore, a long-term experimental evaluation of the actuator is required and, if necessary, a technique of performance decay compensation for mass production operation is proposed.

Following the above points, the research aim and objectives for this study have been developed and will be discussed in the following section.

Table 1.1: Surface texturing techniques used over the last decade

No.	Technological process	Applications, advantages and disadvantages
1	Lithographic processes including chemical or electrochemical processes	Produce specially designed surface patterns on flat surfaces - require masks and are multi-stage [30, 49]; produce pock-marked surfaces with random sizes and pattern of pits [40, 41, 50, 51]
2	Energy beam processes using:	
	- laser beam	Produces geometric array of micro valleys and peaks on flat strip or cylindrical surface of polymers, glass, ceramics and metals [30, 36, 38, 52-71]
	- electron beam	An alternative to laser beam with the main advantage that the minimum attainable spot size is significantly smaller [30, 72]
	- focused ion beam	Produces excellent details; slow removal rate of the order of a few $\mu m^3/s$ [30]
	- electric discharge	Produces pock-marked surface with random sizes and pattern of pits [50, 73]
3	Mechanical processes using:	
	- grinding	Produces grooves with random distribution [40]
	- abrasive jet machining	Produces random distribution of valleys on 3D surfaces of metals [73] and ceramics [74]
	- indentation	Produces arrays of micro-ESMGs with specific patterns and geometries on metal, glass and ceramic surfaces [27, 44]
4	Replication using embossing, moulding or casting	Produces microstructures on the surfaces of metals, ceramics and plastics with low cost, but there are problems with thermal cycling of moulds and mould filling [41, 42, 75]

1.2 Research Aim and Objectives

Taking into account the previous discussion, the aim of this research is to evaluate the potential for reducing friction in metal forming using Engineered Surface Micro-Geometries (ESMGs). For the purpose of this research, the term, Engineered Surface Micro-Geometries (ESMGs) is used to replace the term of "textured surface", for which depth, density and geometry are evaluated in this study. There are six objectives underpinning the research aim:

a. To develop 3D FE model for simulating deformation of various shapes of ESMGs on ring specimen surface during metal forming processes.
b. To determine appropriate geometrical shape of ESMG for the purpose of trapping and transporting lubricant during metal forming process using the developed FE model.
c. To experimentally evaluate the performance of ESMGs in friction reduction in metal forming process and propose optimum ESMGs' characteristics for friction reduction.
d. To evaluate the performance of the Multi-layer Stack Ceramic Actuator (MSCA) under long-term cyclic operation condition and, if necessary, compensate the performance degradation.
e. To propose a methodology for the application of ESMGs in metal forming processes.

The flow diagram of the research process is illustrated in **Figure 1.1**. The first research element is the development of 3D FE model to simulate the deformation behaviour of ESMGs during metal forming. The results of this simulation will be used to determine the ESMGs' geometry that may be appropriate for the purpose of trapping and transporting lubricant. The second research element is the experimental evaluation of friction reduction potential in metal forming using ESMGs. In this evaluation, ring test and forward extrusion test are used to quantify the influence of ESMGs on friction. The third research element is the evaluation of the existing ESMGs texturing equipment. It involves design and development of a piezoelectric actuator tester and driver (called power pulse generator), which is then followed by experimental evaluation of the performance of MSCA under long-term cyclic operations and, if necessary, development of a decay compensation procedure.

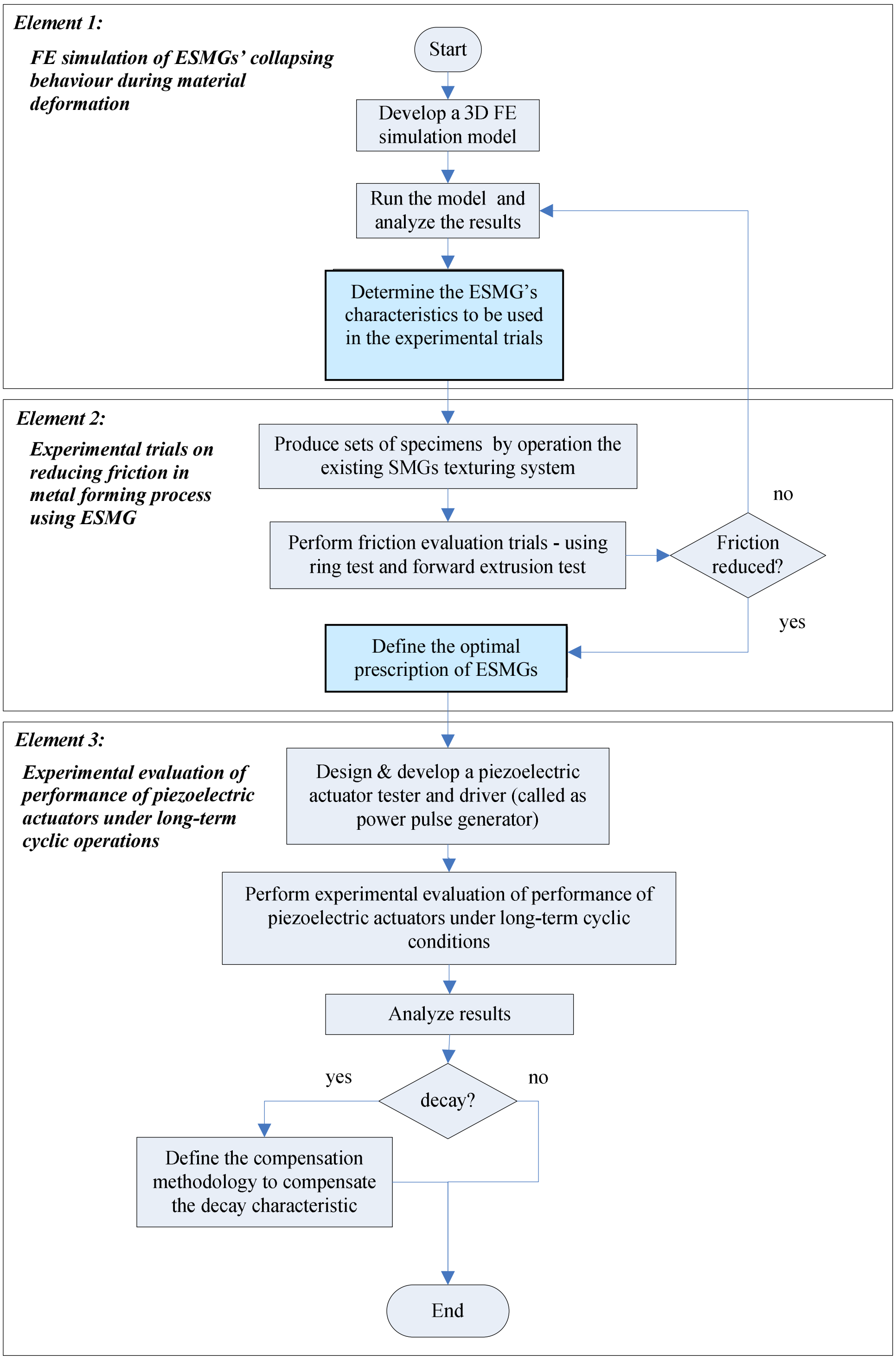

Figure 1.1: Flow diagram of the research

1.3 Organisation of the Thesis

This thesis is composed of seven chapters that are organised as follows:

Chapter 1 presents the motivation, aim, objectives and structure of the research.

Chapter 2 focuses on friction and its influence on metal forming processes. It reviews methods of evaluating and controlling friction in metal forming. Also, this chapter reviews current concepts of using ESMGs for reducing friction in metal forming processes. In addition, the techniques of producing ESMGs, including their advantages and disadvantages, are discussed. Finally, the design concept of the state-of-the-art indentation machine is also described.

Chapter 3 presents the FE simulation model used to analyse the change in geometry and dimensions of ESMGs during deformation. The research was conducted with a view to achieving two main objectives: (a) to develop a 3D FE model to simulate the deformation of ESMGs with various geometries and dimensions and (2) to determine the optimum geometry and dimensions of the ESMGs to be used in the experimental evaluation of the performance of ESMGs in friction reduction. The chapter begins with an introduction to FE simulation concepts, it then focuses on the FE model development and the procedures for analysing results and finally it discusses the results obtained.

In Chapter 4, the experimental trials of friction reduction in metal forming using ESMGs are presented. It begins with description of the apparatus, materials and procedures for both testing methods i.e. ring test and forward extrusion test. In the next section, the results of evaluation trials, with a view to defining the key characteristics of ESMGs that influence the reduction of interfacial friction, are discussed. Lastly, recommendations as to the most preferred ESMG characteristics are presented.

Chapter 5 presents the long-term performance of the piezoelectric actuator that is used to actuate the movement of the indentation tool. This chapter describes the experimental setup, defines the method and summarises the results of the experimental study of the said actuator.

Chapter 6 summarises the findings described in Chapters 3 to 5 to determine the optimum characteristics of ESMGs that might be appropriate for reducing interfacial friction in metal forming processes and proposes the method of the application of ESMGs in metal forming.

Finally, Chapter 7 summarises the conclusions from the study, highlighting main contributions and formulates recommendations for future research.

Chapter 2

Literature Review

2.0 Introduction

As noted in Chapter 1, this research is focused on studying the possibility of controlling friction during metal forming processes by using Engineered Surface Micro-Geometries (ESMGs). The aim of this chapter is to provide an overview of the concepts and theories that are used as a basis for this study. First, in section 2.1, the discussion starts by introducing the concept of friction and its influence on metal forming processes. Section 2.2 reviews methods of reducing friction in metal forming, where the concepts of using ESMGs to reduce friction are discussed. The existing techniques of texturing ESMGs, including their advantages and disadvantages, are discussed in section 2.3. A brief introduction to piezoelectric actuators, their degradation phenomena and methods of evaluating and monitoring degradation are explained in section 2.4. In section 2.5, the measurement concepts, the advantages and disadvantages of several friction measurement techniques in the application to metal forming processes are explained. Finally, the chapter closes with section 2.6, which provides a brief summary of the important points of this chapter.

2.1 Friction and its Influence on Metal Forming

Friction has been found to be an important parameter in most metal forming operations. Friction is the resistance to movement encountered when one surface or object slides over another [76]. In metal working processes, friction arises when a workpiece slides against the die. The occurrence of friction in the metal forming processes can be described by the illustration shown in **Figure 2.1** [76].

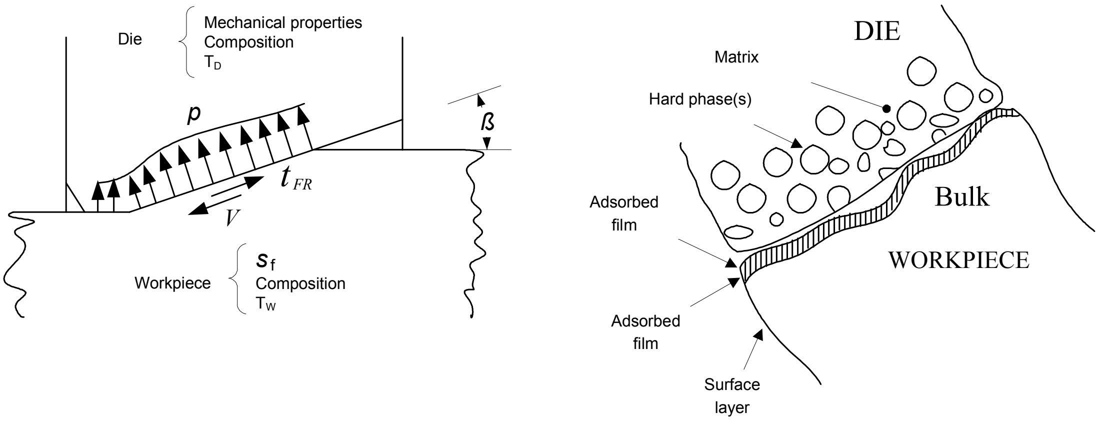

(a) (b)

Figure 2.1: Friction at die/workpiece interface during metal forming processes; (a) on the macro scale and (b) on the micro scale (*taken from [76]*)

As shown in **Figure 2.1 (a)**, friction in metal forming is influenced by several parameters such as die temperature, T_D, workpiece temperature, T_W, die and workpiece material properties, normal pressure, p, and workpiece velocity, V. In cold metal forming processes, the values of T_D and T_W are normally close to room temperature, although the work of deformation and friction are transformed into heat, which may rise temperature to hundreds of degrees Celsius. As deformation of the workpiece proceeds, friction opposes the relative motion between the workpiece and the die, which can be described using average friction shear stress, τ_{FR}.

The microscopic representation of both the die and the workpiece is shown in **Figure 2.1 (b)**. The magnitude of the minute peaks, asperities and valleys plays an important role in creating friction. Other factors that are also important are the interfacial conditions, which may involve a lubricant and/or an oxide layer. The two widely accepted mathematical representations of friction are coefficient of friction, μ, and the frictional shear factor, m. The coefficient of friction, μ, is the ratio of frictional force to normal force, or frictional stress to normal stress (die pressure), and can be written as:

$$\mu = \frac{F_{FR}}{F_n} = \frac{\tau_{FR}}{\sigma} \quad \ldots\ldots\ldots\ldots\ldots\ldots\ldots\ldots\ldots\ldots\ldots\ldots\ldots\ldots(1)$$

where F_{FR} is friction force, F_n is normal force, τ_{FR} is frictional shear stress, and σ is normal stress.

Under high pressures of bulk metal forming processes, the use of the Coulomb's coefficient friction leads to unrealistically high shear stress. Therefore, frictional shear factor m has been introduced to relate the frictional shear stress and the shear flow stress, which is defined as:

$$m = \frac{\tau_{FR}}{k} \quad \ldots\ldots\ldots\ldots\ldots\ldots\ldots\ldots\ldots\ldots\ldots\ldots\ldots\ldots\ldots\ldots(2)$$

where, m is frictional shear factor, τ_{FR} is frictional shear stress, and k is yield shear stress.

Friction has been found to be an important factor in most metal forming operations. For example, in forging and extrusion processes, the interfacial friction between die and workpiece has a significant effect on the material flow, stresses and formation of surface defects as well as the process load [1-3]. In addition, interfacial friction between die and workpiece causes die wear [4], which results in reduced die life [5]. Consequently, this may results in unexpected breakdowns, the need for re-adjustment of the machine, and low product quality due to die damage. The main reason for die wear is the contact stress between the asperities present on the die and the workpiece surfaces, which results in removal of asperities due to the mechanism of abrasion [6]. The severity of this phenomenon depends on several factors such as hardness of the surface, working temperature and lubrication [77].

In hot forging, die damage is normally due to the complex processes that relate to thermo-mechanical fatigue (cracking origin), friction (wear origin) and ambience (oxidation origin) [6]. In addition, oxide debris present in the contact region due to abrasion of the surface asperities changes the lubricant characteristics. Interfacial friction between workpiece and chamber contributes significantly to the forward extrusion force, where the greater the friction the greater the extrusion force.

The magnitude of the peak extrusion load, which occurs during the die filling phase, also increases as a function of billet/die interface friction [78]. High levels of friction at the billet/die interface leads to the increase of die deformation during loading, which in turn results in the increase of form-errors in the extruded component; it also leads to die defects [79]. In addition, high friction at the billet/die interface leads to temperature rise at the die land zone. This phenomenon could results in changes of material flow pattern in the die [80].

In conclusion, interfacial friction between workpiece and die in most metal forming processes is undesirable and needs to be controlled. Therefore, reducing friction at the workpiece/die interface is of great significance [5-8] for improving die life, productivity and quality. Many methods of reducing friction in metal forming processes have been studied and used by numerous researchers and practitioners. These will be explained in the following section.

2.2 Methods of Reducing Friction in Metal Forming Operations

In metal forming, interfacial friction conditions may be controlled [81] either by: (a) using lubricant, (b) using dies made from low adhesion materials such as carbides and ceramics and (c) applying ultrasonic vibration to create a gap between the surfaces of workpiece and die. However, in many cases, combinations of these are used.

For reasons of economics, lubrication is the most widely used technique for combating friction. Lubrication materials which are normally used in metal forming processes are: (1) oils, (2) emulsions, (3) synthetic and semi-synthetic solutions, (4) soaps, greases, and waxes, (5) lubrication additives such as sulphur, chlorine, and phosphorus and (6) solid lubricants such as graphite, molybdenum disulphide (MoS_2), soft metallic and polymeric films such as lead, indium, cadmium, tin, silver, and polymers (PTFE) and glass (at elevated temperature only). Some lubrication materials are used not only for friction reduction, but also act as a thermal barrier between hot workpieces and relatively cool dies. Also, lubrication materials enable the workpiece temperature to decrease slowly and thereby enhance the flow of the workpiece into the die cavity.

Metal forming processes have been found to be associated with high pressure, severe deformation and surface area expansion. These phenomena result in changes in interfacial conditions due to lubricant film breakdown [24]. Consequently, direct contact at a sliding interface (between die and workpiece) could occur in the area where the breakdown of lubricant has occurred and finally result in formation of wear particles due to low tribological performance. These wear particles cause the friction coefficient to raise significantly [82]. In some metal forming processes, this problem can be overcome by a continuous supply of lubricant to the contact surfaces, such as in some wire drawing operations. However, this could result in a waste of lubricating materials and also create many problems for the environment.

In some metal forming processes, dies made from low adhesion ceramics such as silicon nitride and silicon carbide may help in reducing friction [8], especially when applied with a mineral oil [8, 83]. However, the processes of fabrication of these dies are rather complex and have a high cost. Ceramic dies are also brittle when subjected to tension.

Many researchers have studied the effect of ultrasonic vibrations in various metal forming processes over the last 50 years [9-23]. Blaha [9] and Langenecker [10] were the first to conduct an experimental study into the effect of ultrasonic vibration in metal forming and they found significant reductions in the flow stress. Several review papers have been published on this subject, and ultrasonic vibrations have generally been found to be able to reduce the forming load and interfacial friction in certain metal forming processes. However, as reported by Hung et al. [21], in hot extrapolated compression tests and hot ring compression tests, increasing temperature by ultrasonic vibration may reduce flow stress but increase interfacial friction.

As has been noted, various methods of reducing friction have been introduced, but these methods may be inappropriate in some applications and cases. Therefore, combination of methods has always been used, with a view to enhancing and improving tribological performance for specific industrial applications.

Recently, the application of specially designed surface texture to reduce friction in metal forming process has come into light and received considerable attention from academicians and practitioners. The details of concepts and the examples of application of Engineered Surface Micro-Geometries (ESMGs) in metal forming processes are explained in the following section.

2.2.1 Reducing Friction by Using ESMGs

In the past few years, many research works have been carried out to evaluate the possibility of applying ESMGs to reduce friction in many fields such as metal forming, automotive engineering, Micro-Electro-Mechanical Systems (MEMS) and medical. For all these applications, ESMGs could operate under lubricated interfacial condition, where the functions of ESMGs are to trap and to transport lubricant onto the surfaces that are in contact. The trapped lubricant in the ESMG's cavity enables the formation of hydrostatic and hydrodynamic lubrication pressure effects that result in lubricant to flow into the contact zone and form thin lubricant film. The formation of this thin lubricant film improves lubrication performance and as a result reduces the friction coefficient [25, 27, 28, 33-35, 55, 60, 84, 85]. Furthermore, ESMGs also act as traps for abrasive tool wear particles [37].

In metal forming operations, the phenomenon of the trapped lubricant escaping from ESMGs during workpiece deformation was described by Mizuno [86] and later by Kudo et al. [84], Bech et al. [35], Azushima et al. [25, 27, 34], Bay et al. [28] and Rasp and Wichern [32]. The well known concepts that explain this phenomenon are called Micro Plasto Hydrodynamic Lubrication (MPHDL) and Micro Plasto HydroStatic Lubrication (MPHSL). **Figure 2.2 (a)** show the forward escape of lubricant by Micro Plasto HydroStatic Lubrication (MPHSL) occurs when $q_o > p$ and **Figure (b)** show the back-ward escape of lubricant by Micro Plasto HydroDynamic Lubrication (MPHDL) occurs when $q_o + q > p$. It is important to note that q_o is the hydrostatic pressure, q is the hydrodynamic pressure at the rear edge of the lubricant pocket and p is the die pressure.

Kudo et al.[84], Azushima et al. [25, 27, 34]and Bech et al. [35] have performed a series of experimental studies by directly filming the interfacial condition of a strip drawn using a transparent die. In these studies, the pyramidal shape of ESMGs, with a side angle of approximately 10° and a side length of 1mm, were textured on metal strips. The textured strips were drawn through a transparent wedge shaped die. From the studies, they found that during the deformation, the occurrence of MPHSL was caused by the trapped lubricant pressure in the ESMGs that exceeded the die/workpiece interface pressure on the surrounding of the plateau, and the occurrence of MPHDL was caused by the drag of viscous lubricant due to the relative speed between strips and dies surface.

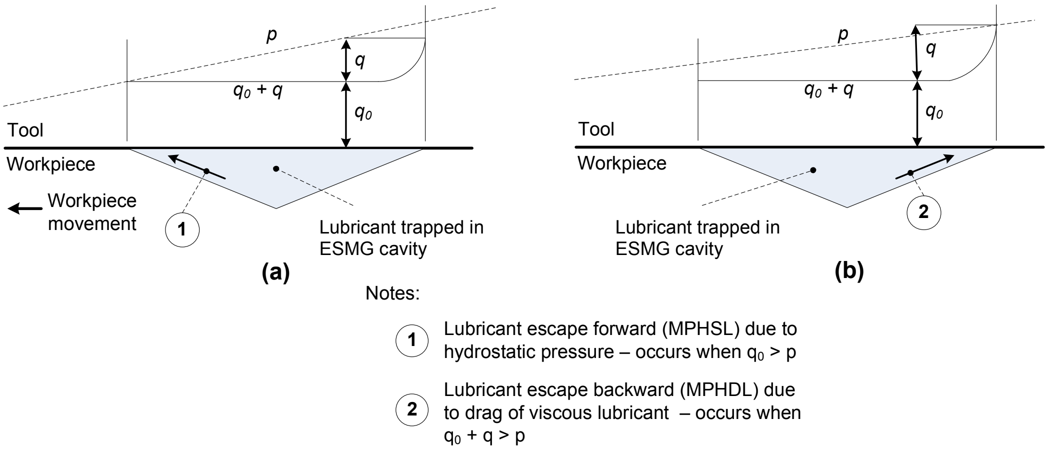

Figure 2.2: Schematics of explaining the escape of trapped lubricant in strip drawing; (a) forward escape by Micro Plasto HydroStatic Lubrication (MPHSL), when $q_o > p$, (b) back-ward escape by Micro Plasto HydroDynamic Lubrication (MPHDL), when $q_o + q > p$

According to Azushima et al. [25, 27, 34] and confirmed by Bech et al. [35], the MPHSL and MPHDL formation mechanisms occur even at low speed of workpiece material flow and are influenced by several factors:

a) Lubricant viscosity: The usage of lubricant with low viscosity results in pure MPHSL, but high viscosity lubricant results in pure MPHDL.
b) Relative speed of material flow sliding against tool: By increasing the relative speed and velocity of a workpiece, which slides against tool, the formation of the MPHDL film increases.
c) Material properties of workpiece: Increasing the strain hardening exponent increases the formation of MPHDL as well as decreases the MPHSL film.
d) Deformation degree of workpiece: Deformation degree of workpiece influences the quantity of lubricant escapes from ESMGs, but not for the formation of either MPHDL or MPHSL.
e) ESMG parameters such as shape and dimension: ESMG parameters have been found to play an important role in the ESMGs deformation trend. It has been confirmed by Shimizu et al. [39], that the larger radius of curvature and the smaller slope of the ESMGs increase the tendency of MPHDL. In spite of that, the larger radius and the bigger slope increase the tendency of MPHSL film formation. The deformation trend of ESMGs during the strip drawing has been analysed by Rasp and Wichern [32] using FE method. They have confirmed that ESMGs with a low diameter-to-depth ratio are much difficult to deform than ESMGs with a large diameter-to-depth ratio.

f) Friction at the tool/workpiece interface: The friction at tool/non-textured workpiece interface increases the pressure on the textured surface that results in higher tendency of MPSHL.

In the last few decades, the application of ESMGs to reduce friction in metal forming processes has received considerable attention from academics and practitioners. For this reason, many methods of ESMGs texturing systems have been designed and developed, where each system has its own texturing capability, advantages and disadvantages (see section 2.3). The performance in reducing friction and the deformation trends of various characteristics of ESMGs produced by the developed texturing system were evaluated in different metal forming processes. During the evaluation process, ESMGs were textured either on workpiece or tool surface.

The merit of ESMGs produced by shot blasting and electrical discharge in friction reduction during rolling operations was experimentally evaluated by Jonasson, M. et al. [73]. In the trials, ESMGs with random distribution and size of valleys were textured on the roll surface. The results of the study indicated that ESMGs textured using electrical discharge provided lower friction as compared to the non-textured and shot blasted ESMGs.

The trial of using ESMGs in deep drawing process was performed by Pantelis, D.I. et al. [53]. In the trial, laser-textured ESMGs with the depth of 250 μm, a diameter of 1200 μm and a spacing of 1200 μm were textured on a BS300 grey cast iron blank holder surface using the pulsed-CO_2 laser treatment system. The friction of the textured blank holder was evaluated under dry interfacial conditions with the normal force of 320N and the speed of up to 300rpm using pin-on-disk configuration friction test system. As reported, the friction coefficient was decreased by 15% and the wear resistance was increased by 25%.

The application of ESMGs in cold forging operations was evaluated by Geiger, M. et al. [37]. In the evaluations, laser-textured ESMGs with a diameter of approximately 100μm, various depths (less than 10μm) and sharp edges removed by lapping, were textured on hard coated cold forging tools. The textured surface was lubricated with lubricant (with the viscosity of 100mm^2/s) at 40°C. It was noticed from the results that the ESMGs textured on the forging tool reduced friction and increased the tool life. However, according to the FEA performed by H. Saiki and Marumo, Y. [87], ESMGs textured on forging tools increased the friction coefficient. This was due to the plastically deformed material, which flowed into the ESMGs cavities and consequently resulted in the increase of the flow resistance. Another attempt of using ESMGs in forging was made by Wagner, K et al. [38] with the believe that ESMGs could reduce friction and increase tool life. In summary, these initial trials have produced controversial and doubtful results that need further research.

The merit of laser-textured ESMGs produced on the sheet metal cutting tool has been evaluated by Voevodin, A. A. and Zabinski [67]. ESMGs with a diameter of between 10 - 20μm and a depth of between 3 – 5μm textured on surface of Inconel 718 substrates coated with 8 μm TiCN hard coating were evaluated using a ball-on-disk tribometer test. The evaluations were performed under the testing conditions of 0.8GPa contact pressure. The contact surfaces were lubricated with MoS_2. The results indicated that the ESMGs helped to keep fresh lubricant availability during cyclic punching and cutting operations. In addition, it was also reported that the optimum ESMGs area density was about 10%, which corresponded to 50μm separation of 10μm sized ESMGs. Laser-textured ESMGs with a diameters of 35μm and 50μm, a depth of 10μm and 30μm and area density of 8 and 30%, lubricated with different types of oil were evaluated by Andersson, P. et al. [68]. The results of the trials have confirmed that laser-textured ESMGs reduce friction and increase wear resistance. It was also discovered that high viscosity lubricant is suitable for ESMG with low area density and a large depth in comparison with the diameter, but low viscosity lubricant is suitable for the lubrication of surface with high area density of ESMGs at low sliding velocities.

In summary, the incorporation of ESMGs on the workpiece surface and possibly on the functional surfaces of metal forming tools has been found to be beneficial in reducing friction, increasing tool-life and extending plastic deformation achievable. Even though a lot of research has been performed by many research groups, the efforts were mostly focused on the application of laser-created ESMGs and sliding contact without involving plastic deformation. Thus, the optimum prescription (depth, diameter, area density and orientation) of ESMGs, especially in specific metal forming application such as cold forward extrusion and cold forging, has yet to be explored. The performance of the recommended ESMGs and the interfacial conditions are still ambiguous, controversial and doubtful.

2.3 Techniques of Creating ESMGs

ESMGs with different characteristics might be produced by processes such as: (1) lithographic processes (chemical, ion beam and electrochemical), (2) energy beam processes (laser beam, electron beam, focused ion beam and electric discharge) and (3) mechanical processes such as grinding, shot blasting, abrasive jet machining and indentation.

2.3.1 Electric arc and electrochemical process

Electric arc and electrochemical processes might be used to produce a random distribution of ESMGs on any shape of metal surface. An example of texture produced using an electrochemical process is shown in **Figure 2.3**.

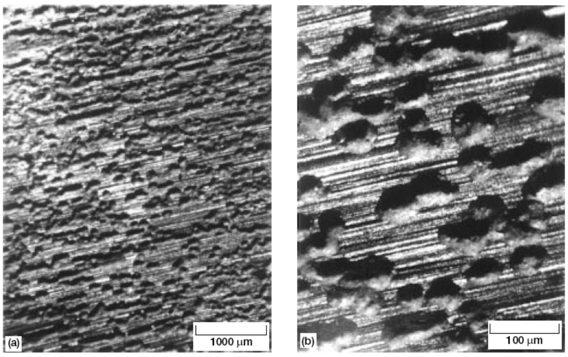

(a) **(b)**

Figure 2.3: (a) Example of surface texture produced using an electrochemical process and (b) magnification surface (a) *(taken from NASA technical Memorandum 107508 [88])*

2.3.2 Laser surface texturing

The most widespread technique for creating ESMGs is based on using high-power laser energy, which is known as laser surface texturing. The LaserMatte^{TM} roll-texturing system introduced by Cold Metal Products, Inc., Youngstown, OH in 1996 is an example of a surface texturing system that was developed based on high-power lasers [89]. Many researchers have used different types of laser energy such as pulsed-CO_2 lasers [53], NY:YAG lasers [55, 59, 62] and excimer lasers [37, 38, 54, 74], but it seems that excimer lasers are most commonly used. By using an excimer laser, ESMGs can be created on many engineering material surfaces such as metals, glass, ceramics and polymers. A schematic diagram of how an excimer laser is used to produce ESMGs is shown in **Figure 2.4**. In order to incorporate ESMGs on metal surfaces using laser energy, short high-pulse energy bursts of only a few nanoseconds are applied to the surface leading to melting, evaporation and plasma formation of the irradiated material [37]. This therefore results in a wavy texture, with pile-up, burr and debris at the margins of every ESMG that needs cleaning and lapping [37]. An example of surface texture produced using lasers is shown in **Figure 2.5**. This method allows achieving high precision of the texture depth, however, the low ablation rate of 0.02 µm/s for steel surface is not conducive with the economic requirements of the mass-production process [37].

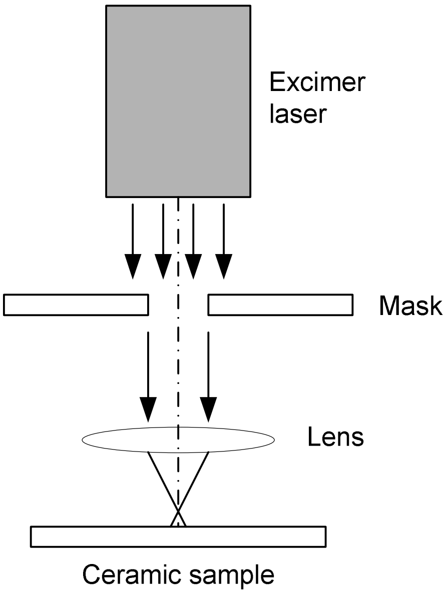

Figure 2.4: Schematic diagram of the ESMG production process using an excimer laser in conjunction with a mask *(taken from [74])*

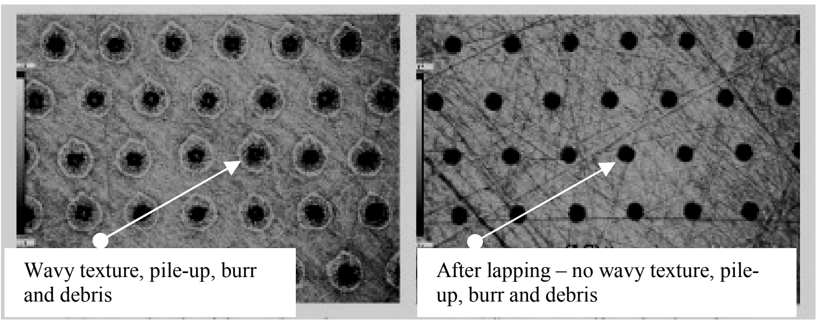

(a) (b)

Figure 2.5: ESMGs produced using lasers; (a) without lapping and (b) with lapping *(taken from [58])*

2.3.3 Grinding

Grinding is the easiest method of producing surface textures on metal surfaces, but it is limited to the production of grooves with different surface roughness. The common method of producing different surface roughness using grinding is by using different types of grinding wheels [24]. As shown in **Figure 2.6**, texturing surface using grinding process is simple and easy, but it only produces groove with a random pattern and dimension.

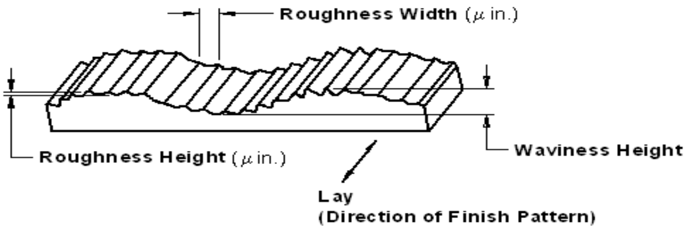

Figure 2.6: Surface structure produced using grinding process *(taken from [168])*

2.3.4 Shot blasting

As reported in [73], another surface texturing method suitable for metal surfaces is shot blasting. The main application of steel shot blasting is for cleaning, stripping and improving properties of a metal surface. However it can also be used for incorporating ESMGs on metal surfaces. The characteristics of steel shot blasted ESMGs are determined by the size of the steel shot. Larger sized steel shot will produce a rougher surface, and use of smaller steel shot will result in a smoother surface. Due to the nature of the process, shot blasting process produce dimples with a random dimension and pattern.

2.3.5 Abrasive jet machining

Abrasive jet machining is similar to the blasting process and it has been found effective in removing hard and brittle material such as ceramics, glass [90], and silicon nitride [91].

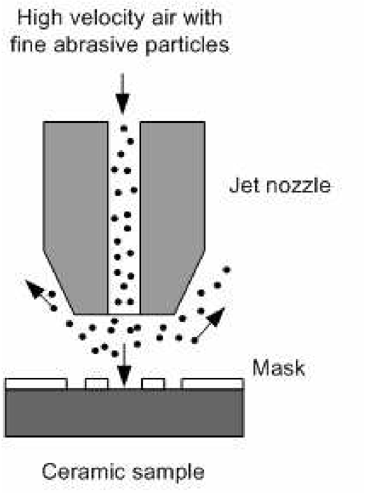

Figure 2.7: Illustration of the concept of abrasive jet machining (*taken from [74]*)

The shape of the ESMGs produced using this process is semi-spherical [74]. **Figure 2.7** is a schematic diagram of the process. To date, the application of this process for producing ESMGs on metal surfaces is rare.

2.3.6 Indentation

A prototype of ESMG texturing system based on indentation technique has been developed at the University of Strathclyde [44]. **Figure 2.8** shows the schematic diagram of the system. An indentation tool made of diamond is actuated by a piezoelectric actuator, which is of a Multi-layer Stack Ceramic Actuator (MSCA) type. MSCA is able to deliver the maximum working force of 4.3 kN. Based on several trials, the developed system has been found capable of creating ESMGs with a depth of 0.5 - 50μm, at a speed of up to 50Hz (50 ESMGs per second) on undulating surfaces.

As shown in **Figure 2.8**, the indentation tool is attached to the Z-axis slide of a 3-axis NC machine. Controlling units, i.e. power pulse generator and intermediate switching unit, were designed to drive the indentation tool. The diamond indenter determines the geometry of the ESMGs. The NC machine may be programmed to texture any prescription of pattern, depth and density of ESMGs. The speed of the indenter tool may be adjusted by controlling the frequency of the control signal from the power pulse generator.

To obtain uniform dimensions of ESMGs throughout a long term texturing operation, the actuator displacement must be consistent. Unfortunately, according to many reports such as in [45-48], the ability of the actuator to deliver displacement and force may degrade significantly due to many factors; this may result in change of ESMG characteristics such as depth and diameter. The following section explains the phenomenon of performance degradation of piezoelectric actuators.

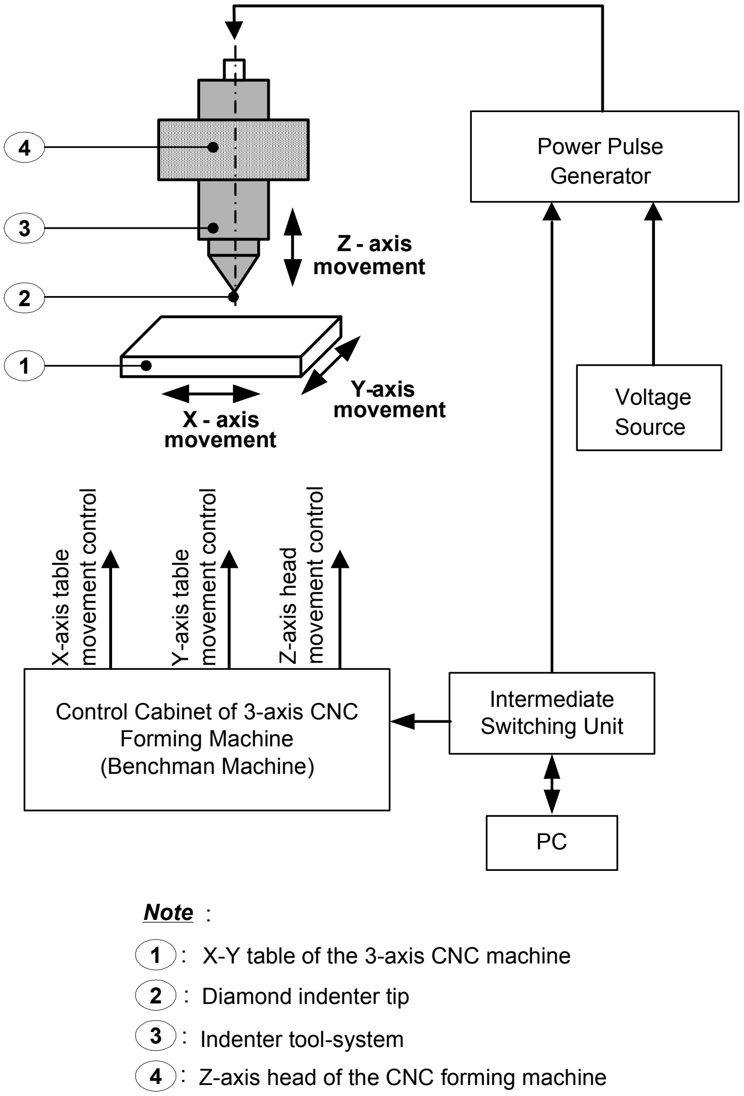

Figure 2.8: Schematic diagram of the indentation texturing system

2.4 Degradation Phenomena in Piezoelectric Actuators

One aspect that should be considered in connection with the application of piezoelectric actuators is degradation of their performance. Performance degradation of piezoelectric actuators is referred to as ageing, fatigue, change of properties or deterioration, which is represented as a function of time. It is the application of either mechanical or electrical loading that is the main cause of ferroelectric and mechanical fatigue occurring in the PZT material, which degrades the actuator's performance.

Many research projects were carried out to define the causes and effects of ferroelectric fatigue in piezoelectric actuators. Sakai and Kawamoto [92, 93] have illustrated the mechanism of ferroelectric fatigue as shown in **Figure 2.9**. Ferroelectric fatigue is related to domain switching (90° switching) and micro-cracking, which are directly influenced by the electrical and mechanical loading conditions and operating temperature. Domain switching changes could decrease the value of the electromechanical coupling factor, K_p, that finally causes the displacement decrease effect. Chaplya et al. [94] have described the causes and effects of ferroelectric fatigue as being multiple and interdependent, as illustrated in **Figure 2.10**.

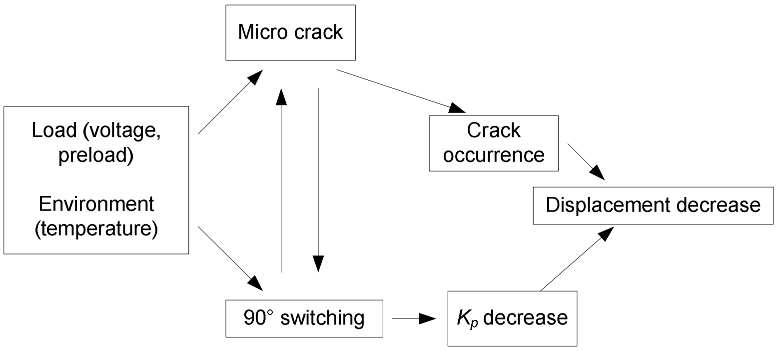

Figure 2.9: Ferroelectric fatigue associated with domain switching and micro-cracking mechanisms, suggested by Sakai and Kawamoto [92, 93]

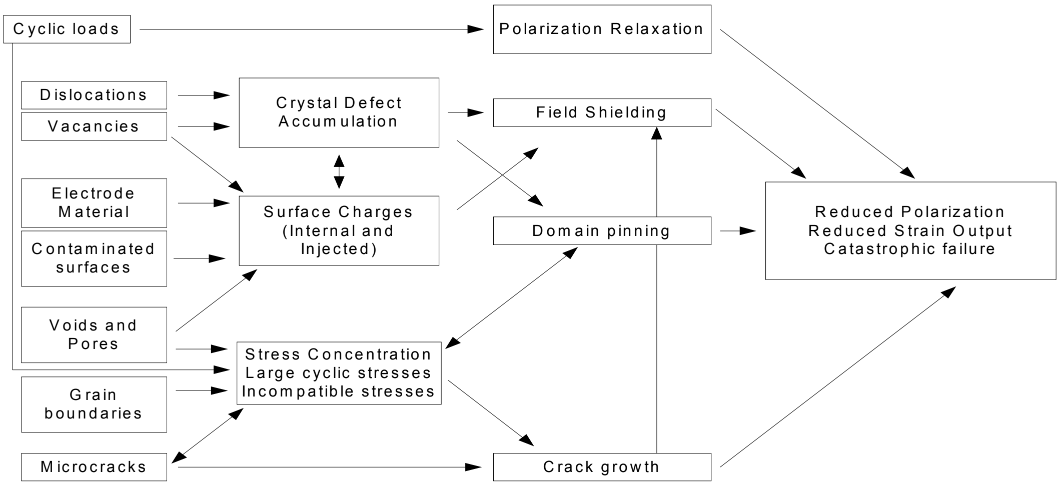

Figure 2.10: Diagram of possible ferroelectric fatigue mechanisms, proposed by Chaplya et al. [94]

Repetitive high driving voltage (more than the coercive field, E_c) and high mechanical load applied to the piezoelectric actuator cause generation of heat, which results in micro-cracking, stress relaxation and domain pinning [95, 96], and consequently shortens the actuator's lifetime [92-94, 97-99]. However, Wang et al. [45] have reported that PZT ceramics operating under electrical fields below the coercive field value do not degrade mechanically. A linear relationship between the logarithmic lifetime representation and operational temperature of a piezoelectric actuator operating under DC voltage has been reported by several authors [92, 97, 100]. Vibration which occurs after applying a sharp-rise step/pulse voltage to the actuator causes a large tensile force and thus creates micro cracks in the material [101].

In conclusion, the factors causing the phenomenon of piezoelectric degradation are: (1) unsuitable driving techniques [92, 93, 101], (2) high electric field (more than the coercive field, E_c) [45, 93] and high input power, which results in self heat generation [93, 94, 99], (3) high operational environment temperature [45, 97, 100] and (4) repetitive mechanical loading [94]. It is rather difficult to understand changes in the ferroelectric properties of a multilayer actuator because it has a complex structure including PZT ceramic layers, glue, and electrodes. Therefore, several researchers have designed different methods of evaluating and monitoring the degradation of performance of piezoelectric actuators, which are explained in section 2.4.1 and section 2.4.2.

2.4.1 Methods of Evaluating Degradation

The main function of a piezoelectric multilayer actuator is to produce a consistent displacement magnitude throughout its lifetime. Therefore, it is really important to evaluate displacement degradation [93, 95, 97, 100, 102]. Several techniques can be used to measure displacement degradation. The first one is by direct measurement using a high-resolution gap sensor [93, 102], and the second one is by using a laser-vibration-system as proposed in [93]. These methods are rather simple and straightforward. Displacement degradation could also be measured by using an indirect measurement method. Under an applied DC voltage, the displacement of the actuator decreases as the leakage current through the actuator is increased, therefore the displacement degradation could be indirectly measured by measuring the leakage current using the circuit shown in **Figure 2.11 (a)** [97]. Under an AC (unipolar) voltage supply, the displacement degradation could be measured from the electric charge stored in the actuator by using the switching circuit shown in **Figure 2.10 (b)** [100]. An increase of the actuator's capacitance value, which can be measured using a standard capacitance meter [94, 99], indicates that its performance has degraded [103].

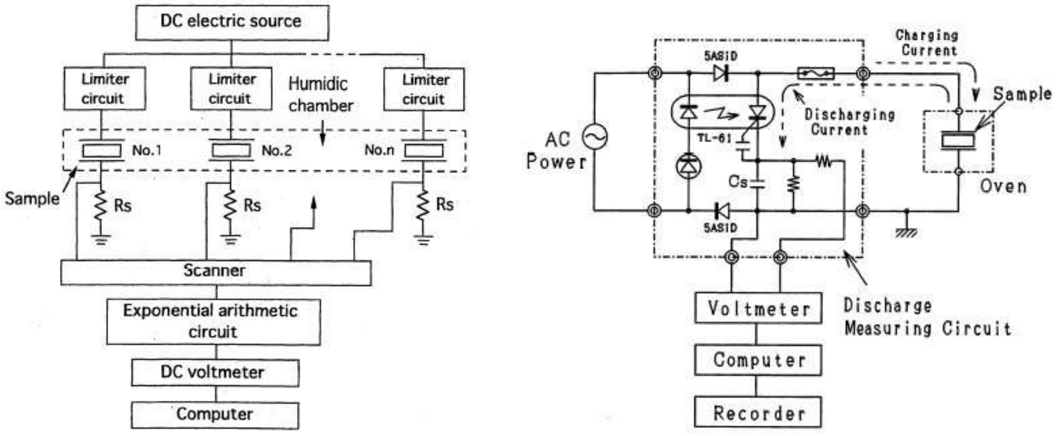

(a) (b)

Figure 2.11: Circuit used for displacement measurement; (a) measurement of leakage current [97] and (b) measurement of charge stored in the actuator [100]

Piezoelectric properties such as relative dielectric constant, $\varepsilon_{33}^{T}/\varepsilon_0$ electromechanical coupling factor K_p, mechanical quality factor Q_m, coercive field E_c, and piezoelectric coefficient d_{33} [104], can be analyzed to understand the degradation phenomena of the ceramic material of a multilayer actuator. The relative dielectric constant $\varepsilon_{33}^{T}/\varepsilon_0$, electromechanical coupling factor, K_p, and mechanical quality factor, Q_m, are normally measured by using an impedance analyzer [92, 93, 102]. The coercive field E_c can be calculated from the *D-E* hysteresis loop, which is obtained from a Sawyer-Tower circuit [45, 95, 96, 105].

Non-electrical method used to evaluate degradation is scanning electron microscopy (SEM) [95] to examine cracks/fractures that are often observed to be parallel to the internal electrodes [106].

2.4.2 Degradation Monitoring Systems

The lifetime and degradation tendency of a multilayer piezoelectric actuator depends on many factors such as material properties, construction, manufacturing process and driving technique. Therefore, it is beneficial to apply lifetime and degradation monitoring to the actuator system.

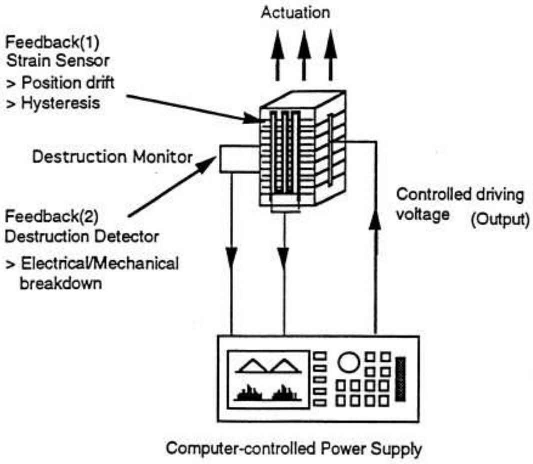

Figure 2.12: Intelligent actuator system suggested by Uchino [101]

Figure 2.12 shows an intelligent actuator system introduced by Uchino [101]. The system consists of two feedback systems: the first feedback system is a strain sensor for detecting displacement and the second one is an acoustic emission (AE) sensor for detecting actuator breakdown, which can stop the actuator system safely.

Cain et al. [107] introduced three different methods or systems of real time monitoring. The first method was by using an acoustic emission (AE) system to show the internal physical processes occurring in the multilayer materials when driven at high electrical fields. The second method used an optical imaging system for detecting micro cracks within the multilayer actuator. And lastly, they proposed a technique that used a thermal imaging system to display changes of temperature in the multilayer material during operation, but unfortunately this system did not work well due to some limitations of the camera system that was used.

2.5 Techniques of Measuring Friction

As discussed in Section 2.2, interfacial conditions in metal forming processes have been found to be influenced by many parameters such as strain hardening, viscoplasticity, microstructural evolution, surface temperature, elastic deformations of the dies, and, in the ultimate case, tool/die damage. This leads to difficulty in quantifying actual friction conditions during deformation of work materials.

In order to calculate the pressures, forces and energy requirements in metal forming processes, the magnitude of friction τ_{FR} needs to be determined either in terms of μ

or *m*. The magnitude of friction can be determined either by matching numerical and experimentally results or direct measurement carried out on small-scale laboratory versions of actual metalworking processes.

For the past several decades, due to economic factors and the tendency to seek to obtain essential additional information such as lubricant breakdown, pickup formation and die wear, different types of physical simulation of actual metalworking processes have been widely used to evaluate frictional conditions in metal forming processes [108-116]. The most typical experimental methods are:

(a) Using tribometer systems,
(b) Performing ring compression tests (ring test), and
(c) Extruding various samples

2.5.1 Tribometer test system

The tribometer has become a versatile piece of standard laboratory apparatus that is suitable for measuring the combination of friction and wear properties of metals and lubricants. The tribometer can be realized with different test rigs such as block-on-ring, ring-on-disk, pin-on-disk and four-ball-wear.

A pin-on-disk version of tribometer appears to provide valuable results for determining the friction coefficient, μ, in sliding contact. The measurement of friction coefficient can be performed under different test conditions such as sliding speed, temperature and contact pressure normal to the contact surface. The references

[54, 58, 108, 117-126] provide examples of several applications of the tribometer with different test rigs over several decades. For example, the pin-on-disk test used by Kovalchenko [58] and the block-on-ring test used by Geiger et al. [54, 127] to evaluate the influence of ESMGs on ceramic surfaces are shown in **Figure 2.13** and **Figure 2.14** respectively.

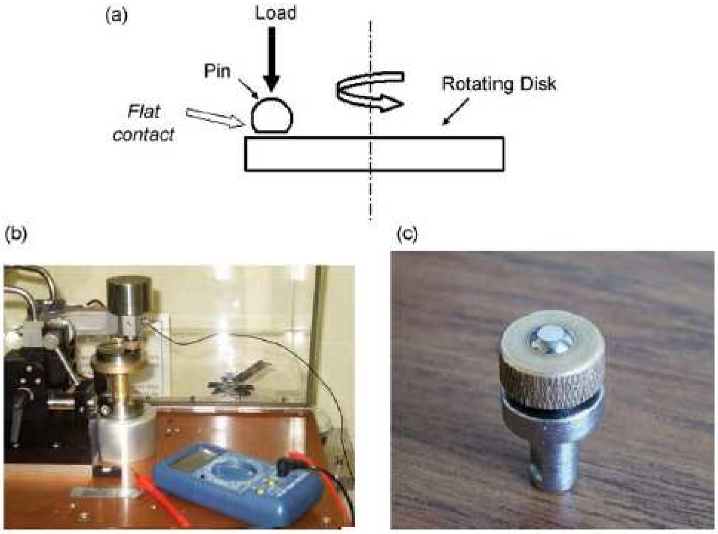

Figure 2.13: Pin-on-disk; (a) schematic diagram of contact configuration, (b) photo of the test rig and (c) photo of the ball specimen with flat contact area *(taken from [58])*

In the pin-on-disk test, the known axial load (see **Figure 2.13 (a)**) is applied along the axis of the pin and the frictional force is measured by restraining the pin motion with a force transducer. The measurement of frictional force is converted into the coefficient of friction, μ, whereas wear is measured by microscopic examination of the pin and disk.

As shown in **Figure 2.14**, the ceramic block is loaded against the ceramic ring, which is turning around its rotating axis. The coefficient of friction, μ, is determined continuously by measuring the tangential force F_R acting on the block and dividing it by the applied normal load, F_N.

The tribometer system is suitable for measuring friction under a sliding condition. It is not suitable for measuring friction during severe deformation of workpieces due to the absence of macroscopic plastic deformation [116]. Therefore, the bulk-plastic-deformation test is much more appropriate.

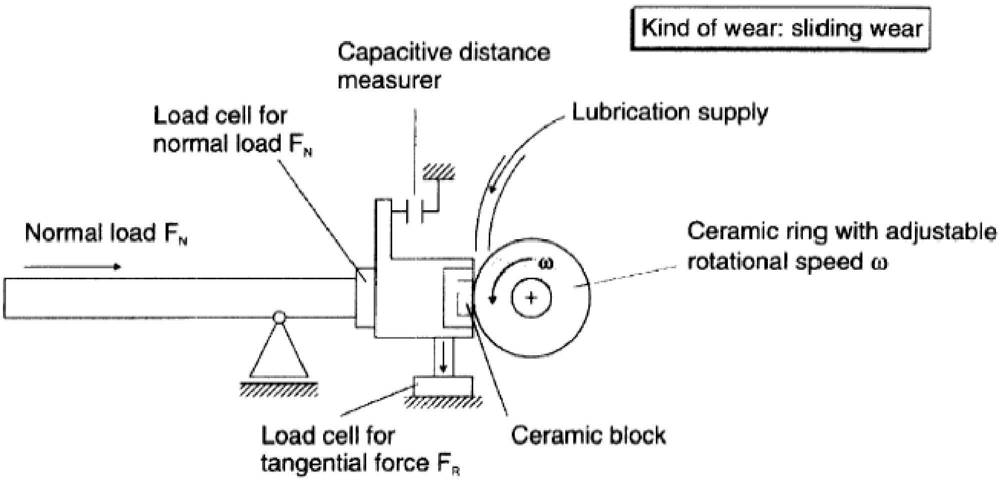

Figure 2.14: Schematic diagram of the functions of the block-on-ring tribometer

(taken from [54])

2.5.2 Ring test

Nowadays, the ring test has become a standard test and is widely used for evaluating friction. The concept of ring test was introduced by Kunogi [128] and Male and Cockcroft [129]. A ring test provides an average value of the coefficient of friction, μ, over the specimen surface. As a result, the test is not sufficient for investigating phenomena of friction in detail, but it is an excellent method for evaluating overall interfacial friction conditions over the specimen surface. The experimental procedure of the ring test is simple and straightforward; it has been widely recognized as one of the best techniques for determining friction conditions between the workpiece and the die during the deformation process [130-134]. Therefore, ring testing has often been used for determining friction conditions during the bulk deformation of material, especially in forging processes [135-137].

The most widely used ring specimen dimension ratio is 6:3:2 (outer diameter: inner diameter: height). During the test, the ring specimen is compressed plastically between two flat platens. As a result, the specimen material deforms either inwards or outwards as shown in **Figure 2.15 (a)**. For high interfacial friction, the internal diameter reduces, while for lower interfacial friction, the material flows outwards, resulting in a higher inner diameter. The value of the coefficient of friction, μ, is determined by superimposing the data of the inner diameter and height changes on the calibration curve as shown in **Figure 2.15 (b)**. For many years, researchers workers have used the experimental friction calibration curves established by Male and Cockcroft [129].

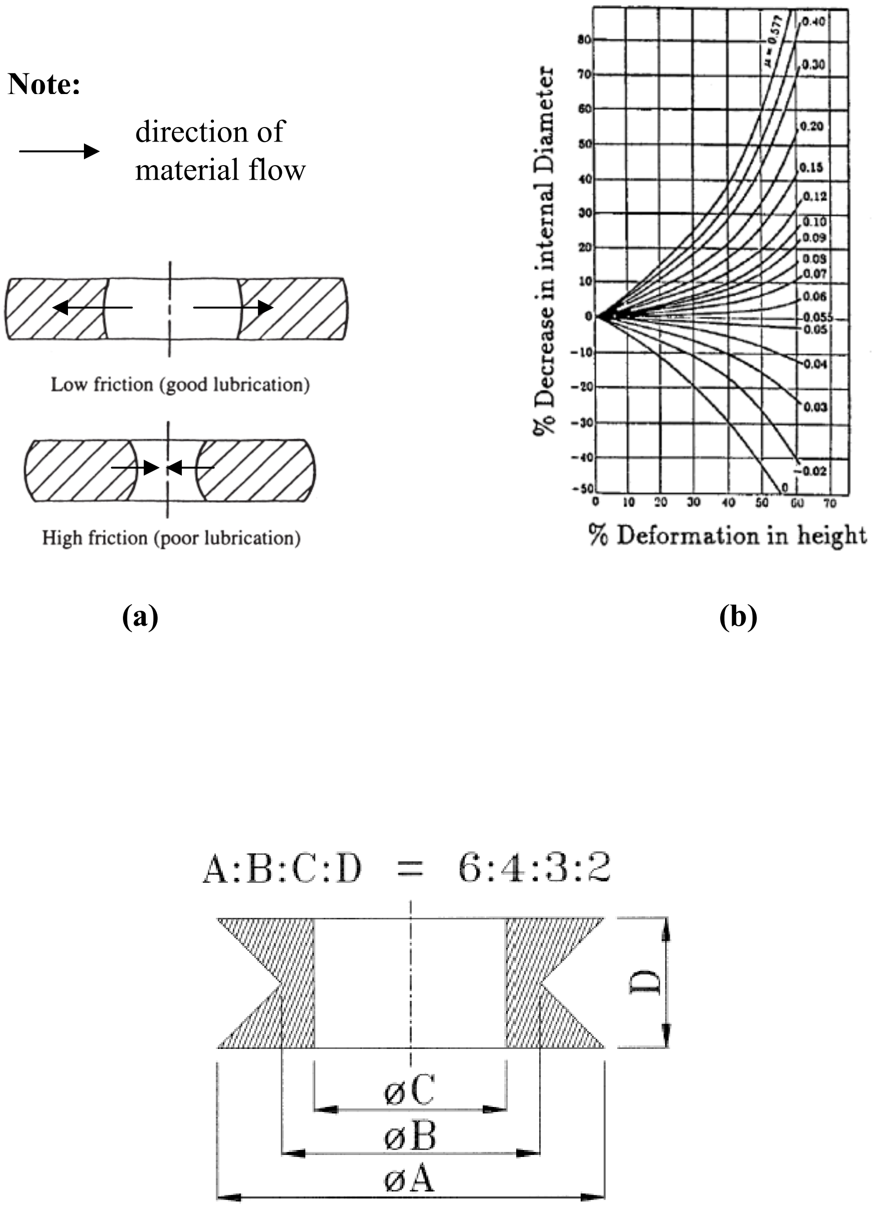

(a) (b)

(c)

Figure 2.15: Ring test; (a) condition of the ring after compression [133, 138], (b) friction calibration curves [133, 138] and (c) alternative ring geometry proposed by Petersen et al. [139]

When evaluating friction by using the above mentioned ring test geometry (6:3:2), the interface stresses will always be greater than the flow stress of the material. Therefore, quantification of friction is impeded for a process where the interface stress occurs at a level below that of the flow stress of the material. For this reason, Petersen et al. [139] have proposed an alternative ring test geometry which allows for evaluation of friction under low pressure conditions. The ring test geometry proposed by them is shown in **Figure 2.15 (c)**. The effects of different parameters on the friction evaluation results, such as bulging, strain hardening, specimen geometry, strain rate, lubrication and temperature have been explained theoretically and experimentally in the literature.

According to Andersson et al. [137], the heat-transfer coefficient has an effect on the ring test, however, it can be considered small compared with the inaccuracies arising from the calibration curves. The FEM-based comparison between the calibration curves of flow softening material and those generated for non-softening material has been performed by Dutton et al. [134], who found that the differences are quite small and almost negligible.

Sofuoglu et al. [133, 138] have investigated the effects of material properties, strain-rate sensitivity and barrelling on friction calibration curves. In their study, physical modelling using two different types of Plasticine material and FE modelling of the ring compression test were performed to obtain the friction calibration curves. The results of their investigation proved that the behaviour of the calibration curves is in reality affected by: material properties, test conditions, strain rate and barrelling of the ring specimen. As a result, they have strongly emphasized that the use of generalized friction calibration curves, as proposed by Male and Cockcroft, regardless of material type and test conditions must be avoided. Robinson et al. [140] confirmed that, in the ring test, individual calibration curves for each material are needed to accurately predict the friction coefficients for specific deformation behaviours. These curves might be obtained from either physical or FE modelling simulation.

As discussed previously, the friction values were obtained by plotting dimensional changes, i.e. the changes in internal diameter of the ring against the reduction in height ratio. Therefore, the measurement of the internal diameter and the height of the deformed ring are crucial. In the literature, several different techniques are considered, which have been used by researchers to measure the changes of the ring dimensions. Bhattacharyya and Moltschaniwskyj [135] used a Nikon profile projector to measure the dimensions of the ring specimens. Wang and Lenard [141] and Li et al. [142] have determined the inner diameter of the specimens by measuring it in two directions, at a right angle, at both ends of the specimen and in the middle. Robinson et al. (2004) [140] took an average value of the inner diameter from three measurements at three arbitrary angles across the centre of the ring.

According to a recent paper by Hartley et al. [143], the inner diameter of a ring specimen can be measured by placing a ball-bearing of known diameter on to the specimen as shown in **Figure 2.16**, so that the inner diameter, ID, can be calculated as:

$$ID = 2\sqrt{\frac{D^2}{4} - \left(OH - h - \frac{D}{2}\right)^2} \quad \ldots\ldots\ldots\ldots\ldots\ldots\ldots\ldots\ldots\ldots\ldots\ldots (3)$$

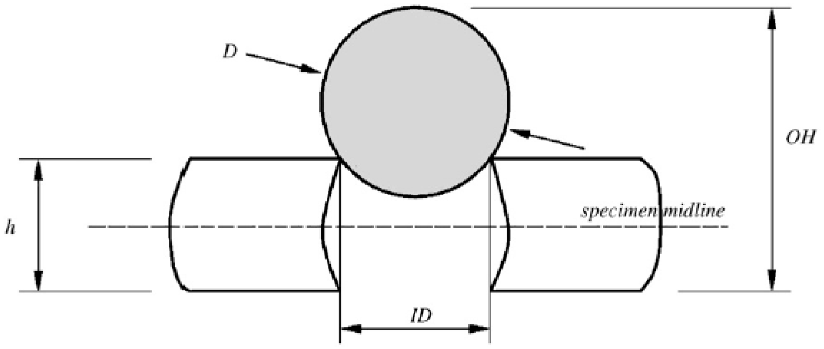

Figure 2.16: Diagram illustrating the inner ring diameter (ID) measurement technique used by Hartley et al. [143]

According to Hartley et al., the dimensions stated in **Figure 2.16** were measured by using a micrometer with an accuracy of ±0.01, so that the calculated ID resulted in an error of 0.6%, which was considered sufficient for the purpose of quality control during the manufacture, preparation of the specimens and after compression.

In simple terms, the step-by-step procedure for evaluating interfacial friction by using a ring test is as follows:

1. Obtain different friction calibration curves for different ring materials using FE computer software.
2. Perform the ring compression test.
3. Superimpose the ring compression test results on the calibration curves to estimate magnitude of the coefficient of friction, μ.

2.5.3 Extrusion test

In the ring test, die geometry and material flow are simple, the surface expansion is small and the forming pressure is low [144, 145]. Therefore, ring test is not able to simulate severe conditions, which occur in most metal forming operations. Forging operations have been found to be associated with severe tribological conditions due to high interfacial pressure and substantial surface enlargement [146]. Therefore, in severe tribological conditions, friction evaluation based on extrusion processes is more suitable. Consequently many techniques of friction evaluation using extrusion processes have been introduced, which are explained in the following sections.

2.5.3.1 Open-Die Backward Extrusion Test

Sofuoglu and Gedikli [147] have used open-die backward extrusion (ODBET) in quantitative evaluation of the coefficient of friction, μ, in large deformation processes. Using the FE model, a cylindrical specimen was compressed between the top and bottom platens. **Figure 2.17 (a)** shows the FE model of the ODBET used to obtain friction calibration curves. The top platen had a hole in its centre for the material to flow through it. The height of the material that flowed in the centre hole is called extruded height. The friction calibration curves were obtained by relating the percentage of the deformation in height terms to the percentage increase in the extruded height of the specimen. Even though the test procedures are simple and easy, their validity and reliability are not yet clearly defined. Therefore, this method is still not widely used by other researchers and industry.

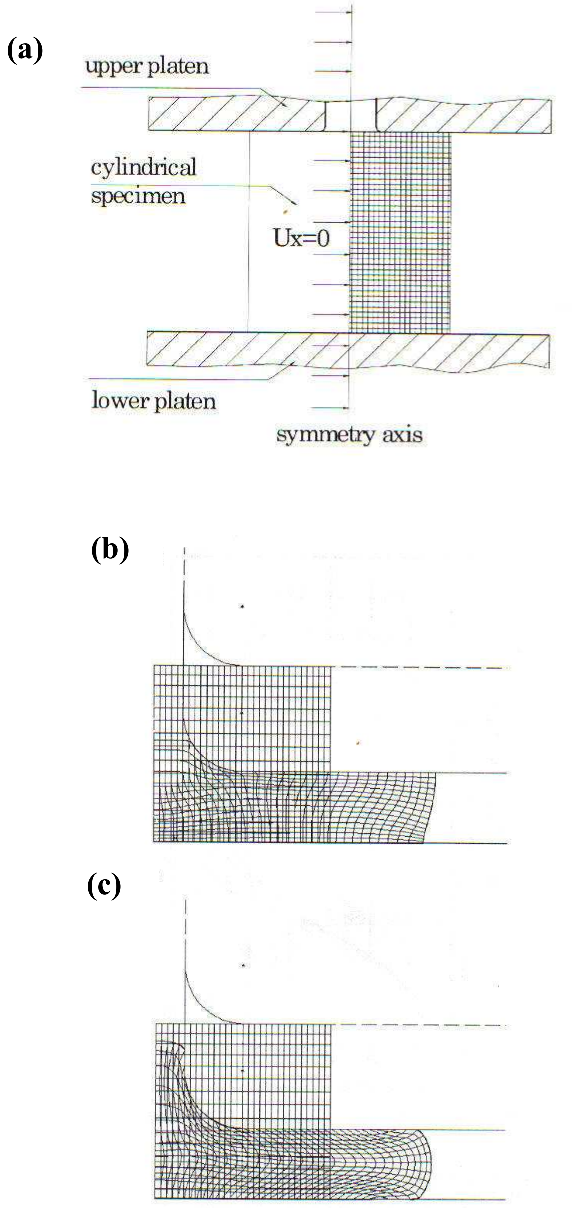

Figure 2.17: FE model of the ODBET; (a) original shape of the specimen, (b) comparison between original shape and deformed shape with μ = 0.0 and (c) comparison between original shape and deformed shape with μ = 0.4 *(taken from [147])*

2.5.3.2 Backward Cup Extrusion Test

By using backward cup extrusion test (BCET), the extrusion force, F_u, and the counter punch force, F_c, are measured by two separate load cells. **Figure 2.18** shows the conceptual diagram of the BCET. The friction coefficient, μ, at the billet/container interface during the cupping operation is described in [149], i.e.: $F_o = F_c - F_u = A\ \sigma\ \mu$; where F_o is the force acting on the billet's outer cylindrical surface area of the billet, F_u is the punch extrusion force, F_c is the force acting on the counter punch and A is the billet's outer cylindrical surface area that is in contact with the inner surface of the container.

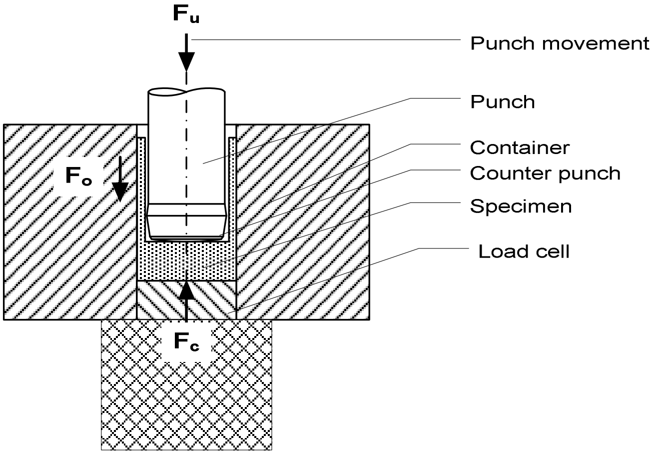

Figure 2.18: Conceptual diagram of the BCET

2.5.3.3 Double Backward Extrusion Test

In the double backward extrusion test (DBET), the measurement of the extruded cup's height, which represents the material flow behaviour, and the punch stroke, is used for quantification of the friction factor, m, by superimposing the data on the calibration curves that are obtained from FEM analysis [150]. According to Forcellese et al. [151], the double cup extrusion test is strongly influenced by the friction factor, and the loads required to form the workpiece are lower than those needed for single forward and backward extrusions. However, Ghobrial et al. [152], Tan et al. [153] and Schrader et al. [154] reported that punch travel, strain hardening (material properties), reduction in area and lubrication, are factors that affect the material flow of the workpiece and directly affect the results of the test. **Figure 2.19** shows the conceptual diagram of DBET.

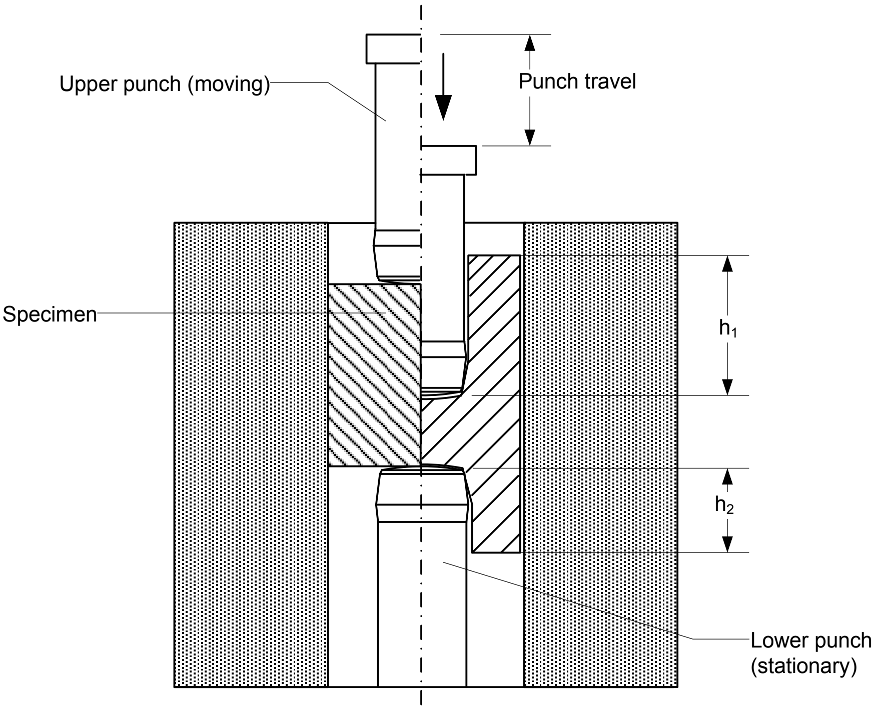

Figure 2.19: Conceptual diagram of DBET

2.5.3.4 Combined Forward Rod Backward Can Extrusion Test

Nakamura et al. [146, 155] proposed another friction testing method that uses a combined forward rod backward can extrusion test (CFRBCET). The design of the punch, the container and the die used in this test is shown in **Figure 2.20.** This method enables estimation of the friction factor, m, and friction coefficient, μ, along the chamber and the conical die surface, by using a theoretical calibration curves diagram. The calibration curves represent the relationship between the punch travel, the extruded rod length, and the value of m or μ. The advantages of this test are: (1) friction can be determined without considering the forming force and the flow stress, (2) friction of the punch nose in the backward can extrusion can be disregarded, and (3) the influence of the hardening of the workpiece is insignificant.

2.5.3.5 Combined Forward Conical Can-Backward Straight Can Extrusion Test

As well as the above, Nakamura et al. [127] introduced another method of estimating friction using a combined forward conical can backward straight can extrusion test (CFCCBSCET) as shown in **Figure 2.21**. Using this method, the interfacial friction along the conical punch surface could be estimated by superimposing the measurement data of the can's height and the punch travel on to the calibration curves diagram that is generated theoretically.

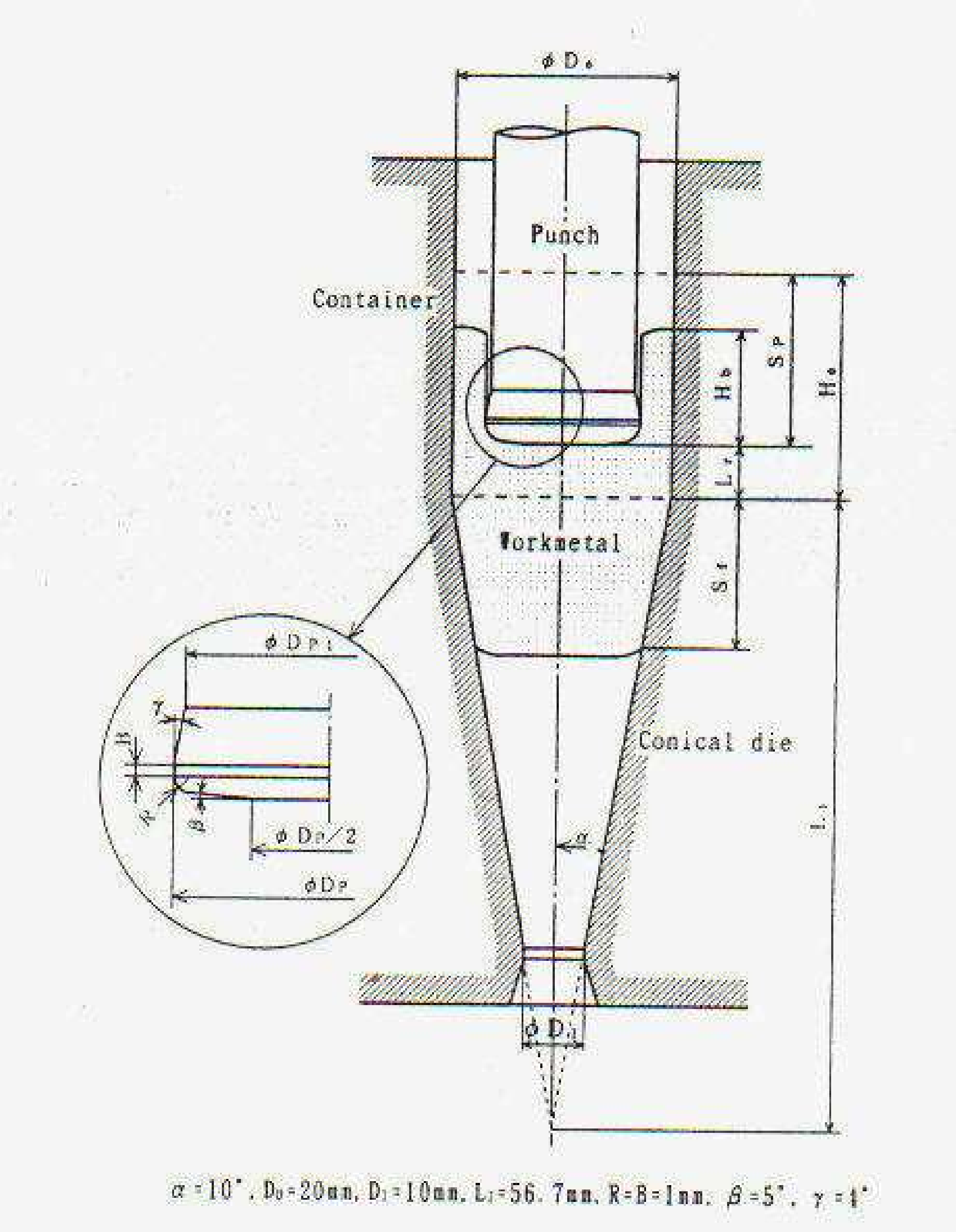

Figure 2.20: The design of the punch, container and die used in CFRBCET *(taken from [146, 155])*

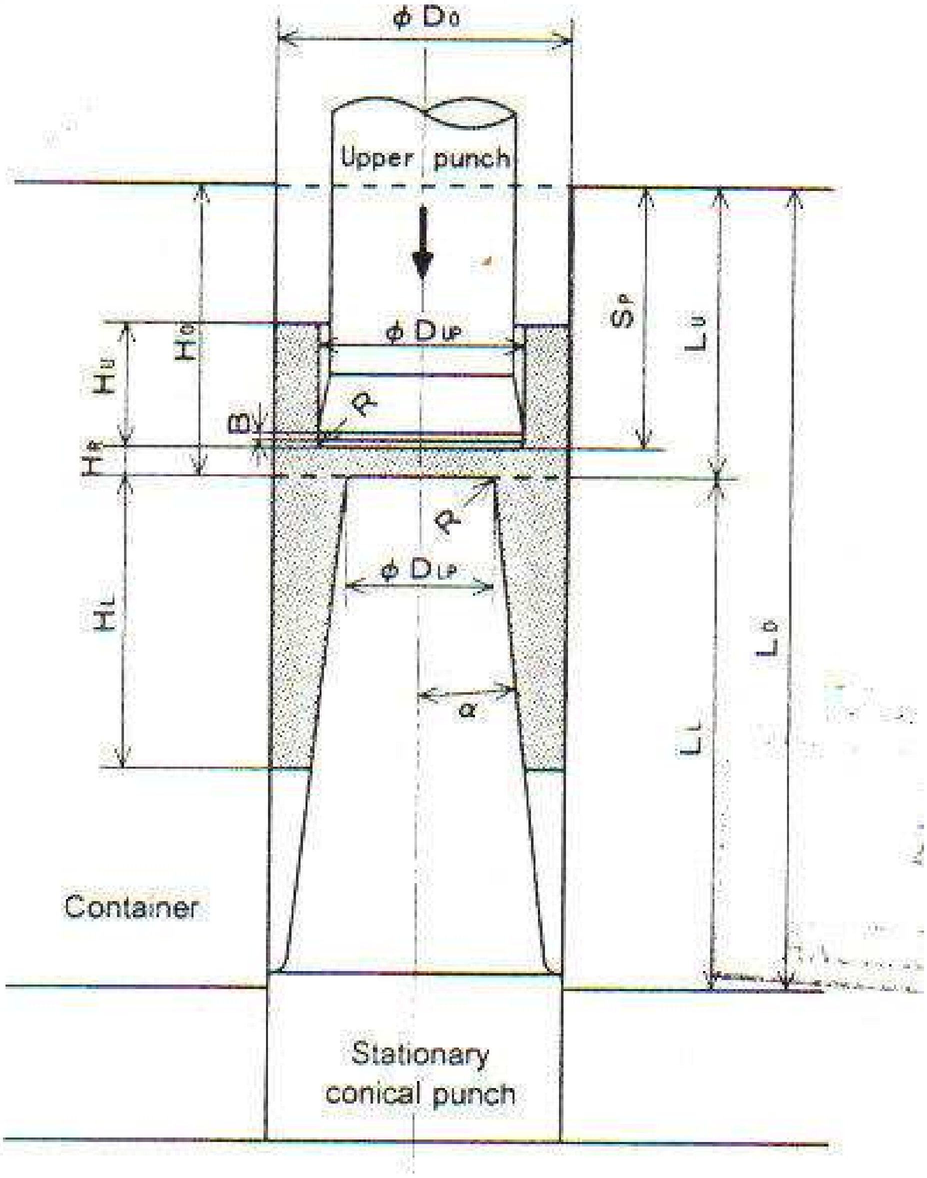

Figure 2.21: The design of punches and container used in CFCCBSCET *(taken from [127])*

2.5.3.6 Forward Extrusion Test

The friction coefficient/factor may also be measured by using forward extrusion test. Among the friction tests that are based on extrusion process, forward extrusion test is most widely used because the design of the testing tools is simple and manufacture easy. **Figure 2.22** shows the schematic diagram of the forward extrusion process. The magnification of the extruded billet, the chamber and the die is shown in **Figure 2.22 (f)**. **Figure 2.23** shows the force-displacement signature of the forward extrusion process.

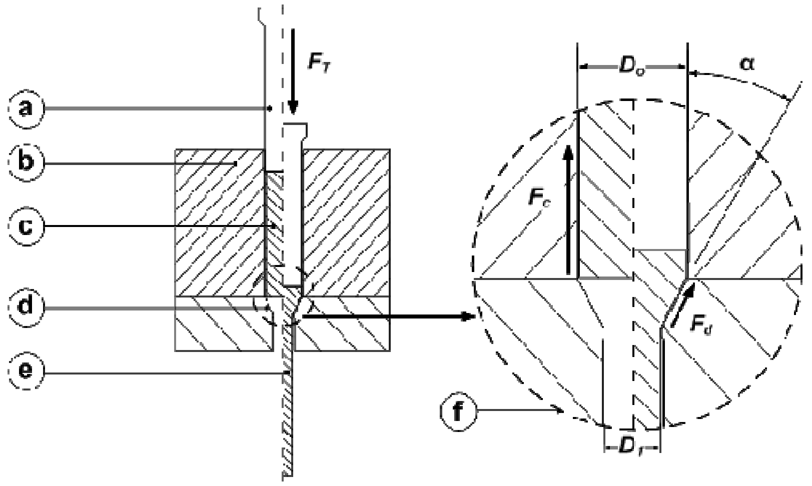

Note:

a : punch
b : chamber
c : billet
d : die with conical shape
e : extruded billet
f : magnification of the die, billet and chamber showing the chamber diameter D_o, diameter of the extruded billet D_1, die opening angle α, friction force at billet and chamber interface F_C, and friction force at billet and die interface F_d.

Figure 2.22: Schematic representation of forward extrusion process

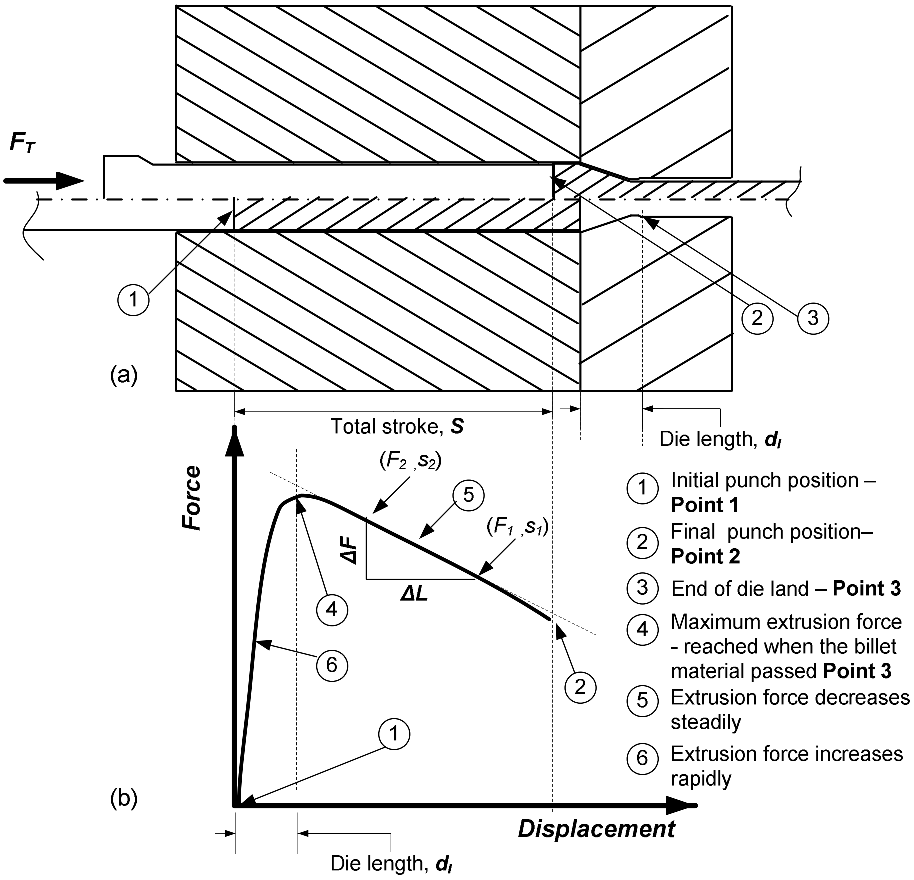

Figure 2.23: Relationship between extrusion force and punch stroke (displacement); (a) Schematic representation of the punch stroke and material flow in the chamber and die and (b) Typical extrusion force-displacement curve that corresponds to the punch stroke in (a)

During the extrusion process, in order to push the billet through the chamber and deform it in the die, the total extrusion force, F_T, required is determined [144, 156, 157] as:

$$F_T = F_C + F_d + F_{dd} \quad \ldots\ldots\ldots\ldots\ldots\ldots\ldots\ldots\ldots\ldots \quad (4)$$

where F_C is the friction force at the billet/chamber interface, F_d the friction force at the billet/die interface, and F_{dd} is the deformation force in the die.

As shown in **Figure 2.23,** the displacement of the punch starts at point 1 and finishes at point 2. Between these points, the extrusion force increases rapidly as the billet material starts to fill the conical die cavity, and the force achieves the maximum value (at point 4**)** when the billet material has fully filled the conical die cavity and passed into the die land (at point 3). At this point, both F_d and F_{dd} achieve their maximum values and remain constant afterwards. After point 3, the extrusion process reaches the steady state condition, where actually the extrusion process begins.

Under the steady state condition, the friction force at the billet/chamber interface, F_C is determined as [144]:

$$F_C = \tau \pi D_o L \quad \ldots\ldots\ldots\ldots\ldots\ldots \quad (5)$$

where τ is the frictional shear stress between billet and chamber, D_o is the chamber diameter, and L is the billet length in the chamber.

The frictional shear stress τ is determined as:

$$\tau = m \frac{\sqrt{3}}{3} \bar{\sigma} \quad \ldots\ldots\ldots\ldots\ldots\ldots \quad (6)$$

where m is the friction factor, and $\bar{\sigma}$ is the normal flow stress.

By substituting equation (6) into equation (5), the friction force at the billet/chamber interface, F_C, can be written as:

$$F_C = m\frac{\sqrt{3}}{3}\bar{\sigma}\pi D_0 L \ldots\ldots\ldots\ldots\ldots\ldots \tag{7}$$

As is clearly shown in equation (7), the friction factor, m, and the billet length in the chamber, L, both have an effect on the value of F_C.

By substituting equation (7) into equation (4), F_T can be written as:

$$F_T = m\frac{\sqrt{3}}{3}\bar{\sigma}\pi D_0 L + F_d + F_{dd} \ldots\ldots\ldots\ldots\ldots \tag{8}$$

During the steady state condition, as the punch displacement increases, the value of L decreases that results in a decrease of contact area between the chamber and the billet surface. Therefore, the result is a gradual decrease of extrusion force F_T as shown in **Figure 2.23 (b)**. As the length of the billet in the chamber changes by ΔL, equation (8) can be written as:

$$\Delta F_t = m\frac{\sqrt{3}}{3}\bar{\sigma}\pi d_0 \Delta L + \Delta F_d + \Delta F_{dd} \ldots\ldots\ldots\ldots \tag{9}$$

Because the values of F_d and F_{dd} are constant during extrusion, the values of ΔF_d and ΔF_{dd} are thus all equal to zero, and as a result equation (9) can be written as:

$$\Delta F_t = m\frac{\sqrt{3}}{3}\bar{\sigma}\pi D_0 \Delta L \ldots\ldots\ldots\ldots\ldots\ldots \tag{10}$$

Thus the friction factor, m can be determined as:

$$m = \frac{\Delta F_t}{\Delta L}\left(\frac{1}{\frac{\sqrt{3}}{3}(\pi \bar{\sigma} D_o)}\right) \quad \ldots\ldots\ldots\ldots\ldots\ldots\ldots\ldots\ldots\ldots\ldots\ldots \quad (11)$$

where, as shown in **Figure 2.23 (b)**, $\frac{\Delta F_t}{\Delta L}$ is the slope of the force-displacement curve during the steady state; $\Delta F_t = F_2 - F_1$, and $\Delta L = S_2 - S_1$

In the case of extrusion of the same material, using the same billet, the values of $\bar{\sigma}$, and D_0 are the same. Therefore, any difference in force-displacement slope at the steady state is only due a different magnitude of friction factor, m [78, 149, 158-160].

2.6 Summary

Friction is the resistance of movement encountered when one surface or object slides over another. It has been found to be an important parameter in most metal forming operations. Interfacial friction between die and workpiece causes die surface wear, which results in a negative effect on die life. Consequently, friction may result in unexpected production breakdowns, the need for re-adjustment of the machine and low product quality due to die damage. Therefore, controlling interfacial friction is essential in order to optimize die life, improve productivity and improve product quality. The most widely used technique for controlling friction is by using a lubricant. However, forging and extrusion always involve high pressure and surface expansion, which may result in lubricant film breakdown. Thus, direct contact between die and workpiece could occur in the area of the breakdown of lubricant films.

Some researchers have defined the technique for maintaining lubricant between the contact surfaces by using Engineered Surface Micro-Geometries (ESMGs). ESMGs act as lubricant pockets, entrapping microscopic quantities of lubricant and expelling the lubricant on to the surfaces of the die and the workpiece. However, research that focuses on the application of ESMGs in forward extrusion and cold forging has yet to be conducted. Laser ablation is a popular method of creating ESMGs even though it does not currently match industrial productivity requirements.

Several methods of evaluating interfacial friction have been introduced, for example: (1) using a tribometer, (2) ring test and (3) various extrusion processes. The ring test is the simplest and most widely used approach. For the forward extrusion process, the relationship between interfacial friction and total extrusion force has been clearly defined in the literature. Therefore, friction can be evaluated using the forward extrusion process by evaluating the changes of the total extrusion force, F_t.

Chapter 3

FE Simulation of ESMG Collapsing Phenomenon during Material Deformation

Glossary

FEM = Finite Element Method

FE = Finite Element

A_{ESMG} = 2D ESMG profile area

φ = ESMGs' initial opening angle

d_o = ESMGs' initial depth

D_o = ESMGs' initial diameter

3.0 Introduction

This chapter presents two FE simulation models of ring compression test, i.e: 1) 2D FE model and 2) 3D FE model. The 2D model was used to obtain the friction calibration curves. It is important to note that the friction calibration curves obtained from this model were used in section 4.4.1 in Chapter 4.

The 3D FE model was used to analyse the geometry and dimensions of ESMGs during deformation. The 3D FE model was developed with a view to achieving two main objectives: (a) to simulate the deformation of various geometries and dimensions of ESMGs on steel surfaces and (b) to determine the optimum geometry and dimensions of the ESMGs to be used in the experimental evaluation of the performance of ESMGs in friction reduction. The ESMG characteristics that are analyzed in this chapter are the geometrical shape and depth of the ESMGs during deformation of the workpiece material.

3.1 Importance of the Study

The changes of the ESMGs' (pockets') characteristics such as shape and dimensions during the deformation of the workpiece determine the lubricant volume that is squeezed out from the pockets on to the contact surface [34]. The deformation of the pockets is, however, influenced by the deformation of the workpiece. On the other hand the amount of lubricant that is redistributed to the contact surfaces somehow influences the workpiece's deformation behaviours. Thus the deformation behaviours of the workpiece and the ESMGs, which act as lubricant pockets, are interrelated as shown in **Figure 3.1**. Therefore, the deformation behaviour of the ESMGs during the deformation process of the workpiece is an important aspect that needs to be studied and understood.

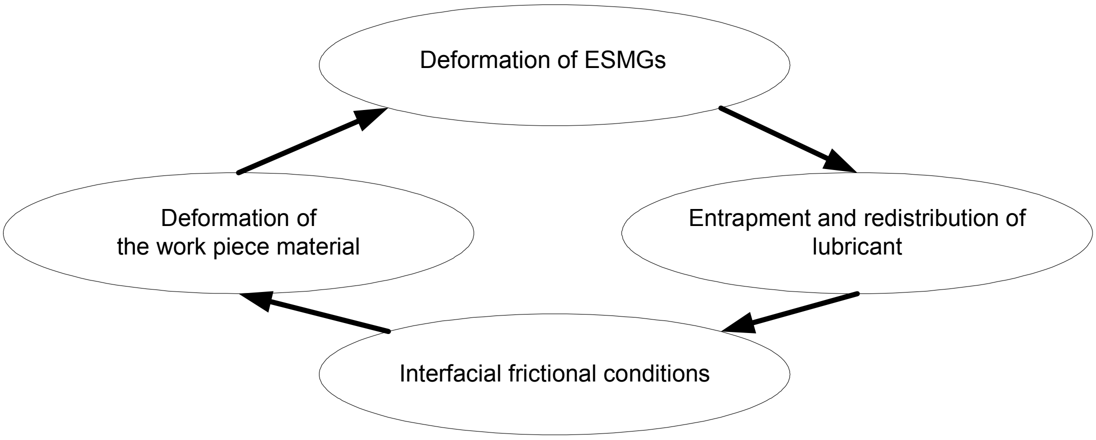

Figure 3.1: Interrelation between deformation of workpiece, deformation of ESMGs, entrapment/redistribution of lubricant and interfacial conditions during metal forming processes

A few attempts have been made to understand deformation of ESMGs during metal forming processes. For example, a direct observation technique, which employed a CCD-camera focused through a transparent tool, has been used by Bay and Azushima [25, 27, 28, 35]. Using this technique, the deformation behaviour of

ESMGs and the flow of lubricant were directly observed and recorded using the CCD camera. However, performing such experiments is expensive and time-consuming.

Another attempt to describe the deformation behaviours of the ESMGs was made by Rasp and Wichern [32]. They simulated the deformation of ESMGs during the rolling process using a 2D FE model. However, the 2D model did not allow them to perform further examination in terms of viewing and analysing the entire ESMG geometrical change during the deformation process.

The published results do not give sufficient information regarding the influence of different ESMG geometries and dimensions on different workpiece surfaces, with different material properties, in terms of behaviour of ESMGs during the deformation process. Thus, the optimum characteristics of ESMGs (such as geometry, pattern, dimensions, location and area density) have yet to be clearly defined.

Therefore, in this chapter, a series of FE simulations is presented to analyse the deformation behaviours of ESMGs with different geometries and dimensions. The research was conducted with a view to achieving two main objectives: (a) to develop a 3D FE model to simulate the deformation of ESMGs with various geometries and dimensions and (b) to determine the optimum geometry and dimensions of the ESMGs for use in cold forging processes.

3.2 Development of the FE Model and Analysis Procedures

3.2.1 Development of the FE Model

The finite-element method (FEM) was originally introduced to solve complex problems in the fields of civil engineering and aeronautics. Although the FEM has been known since the 1950s, it has only been widely used for the last two decades. Lately, FEM has become an important technique in a wide variety of complex engineering analyses such as metal forming, heat transfer, acoustics and thermodynamics. It has proven to be an important and useful tool for analysing bulk deformation processes, particularly defining conditions of die filling, friction and stress and strain distribution [161, 162].

3.2.1.1 Sub-modelling

The ABAQUS/Standard and ABAQUS/Explicit FEM software packages provide the sub-modelling technique that is used to study a local part of the model with a refined mesh, based on interpolation of the solution from the global model. The most important reason for using the sub-modelling technique is to obtain an accurate and detailed solution regarding the local region.

To discuss further the sub-modelling technique, it is beneficial to understand the terminology used in this technique. The definitions and the relations between a global-model, sub-model, sub-model boundaries, global-model node and driven node are illustrated in **Figure 3.2**. As shown in **Figure 3.2 (a)**, global-model refers to the model in which the solution is interpolated on to the relevant parts of the sub-model boundary. The global-model may itself be a sub-model of a larger global-model, as shown in **Figure 3.2 (b)**. In other words, the solutions of the larger sub-model may themselves be used in the smaller sub-model by interpolating them on to the relevant parts of the smaller sub-model boundary. The driven nodes are the nodes on the sub-model boundaries whose values are defined by interpolating the solution from the global-model.

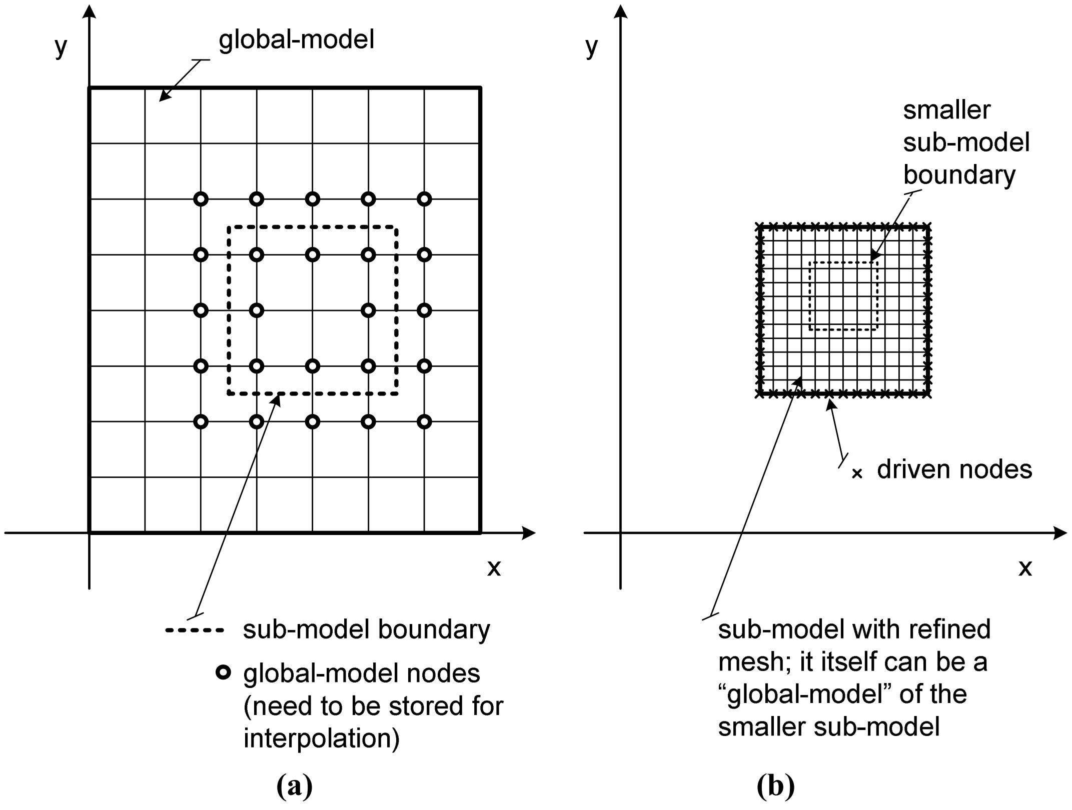

Figure 3.2: Illustration of the sub-model terminology

3.2.1.2 2D FE Model

Because, in reality, the shape of the calibration curves is affected by material properties, test conditions, strain rate and barrelling of the ring specimen, the use of generalized friction calibration curves regardless of material type and test conditions must be avoided [133, 138]. Therefore, the objective of this part is to establish the friction calibration curves of the ring specimens that were used in the ring-test experiment.

The FE model was developed using the ABAQUS/Standard simulation software code with consideration of the actual dimensions and material properties of the ring specimens used in the ring test experiment. As to the nature of the shape of the ring specimens, a quarter of the cross section of the ring specimen was used to develop the 2D FE model, as illustrated in **Figure 3.3**.

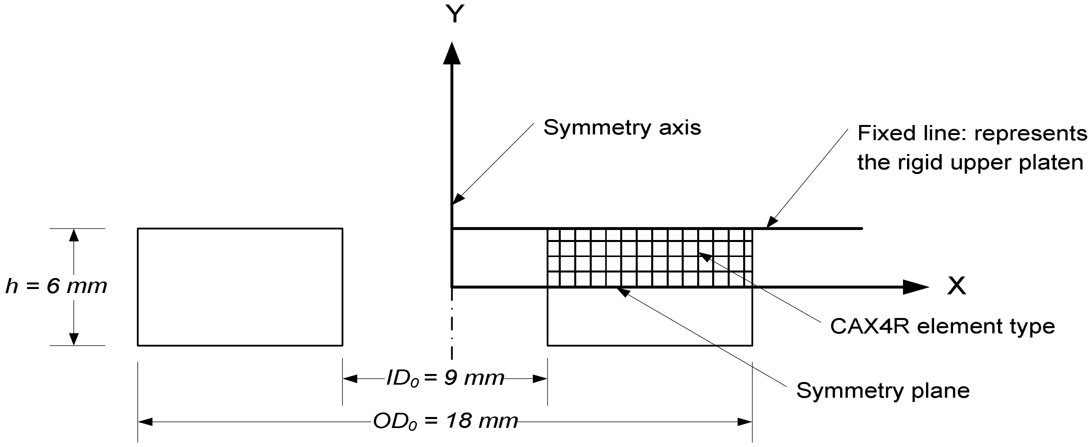

Figure 3.3: A quarter of the cross section of the ring specimen used to develop the 2D FE model

The CAX4R element type is used to mesh the ring model and a fixed line is used to represent the top platen. The *CONTACT PAIR option is used for the interaction properties, and various friction coefficients are changed in every series of simulations using the *SURFACE DEFINITION option. The post-yield stress/strain data of the steel CK15 used in the FE model is stated in **Table E.3** of Appendix E.

3.2.1.3 3D FE Model

In this study, FE analysis was used to evaluate changes in the dimensions of the ESMGs with the deformation of the ring specimens. A 3D model was analysed using the commercial FE software, ABAQUS/Standard version 6.4.1.

As the dimensions of the ESMGs were very small in comparison with the dimensions of the ring specimens, a special procedure involving sub-modelling (as discussed earlier in this chapter) was required to obtain an accurate solution. A diagram illustrating the procedure of FE modelling is shown in **Figure 3.4**. First, a global model without ESMGs was analysed. Due to the symmetry of the ring specimen (see **Figure 3.4 (a)**) only 1/8 of the ring was analysed (**Figure 3.4 (b)** and **Figure 3.4 (c)**). The coefficient of friction between the dies and the specimen was set to 0.05.

Next, a simulation was run during which the solution obtained for the global model was interpolated on to the sub-model, which was a small part of the global model containing a single ESMG and meshed using very fine elements (**Figure 3.4 (d)**). Sub-models for the ESMGs located close to the outer and inner ring diameter and in the middle of the ring were created. These locations are marked in **Figure 3.4 (d)** as

A, C and B, respectively. The dimensions of the sub-models were approximately 0.5 x 0.5 x 0.5 mm. These were meshed using C3D4 elements with the edge length not exceeding 5 μm in the ESMG region. The specimen material properties used in the simulations were obtained from the cylindrical compression test, as proposed by Rastegaev. A detailed explanation of the test is given in Appendix E.

In order to verify the validity of the FE simulation results, the ESMGs' profiles that were obtained from the simulations were compared with the experimental results. The profiles, the diameter and depth of the ESMGs were measured using the non-contact optical profiler, Veeco WYKO Surface Profiler.

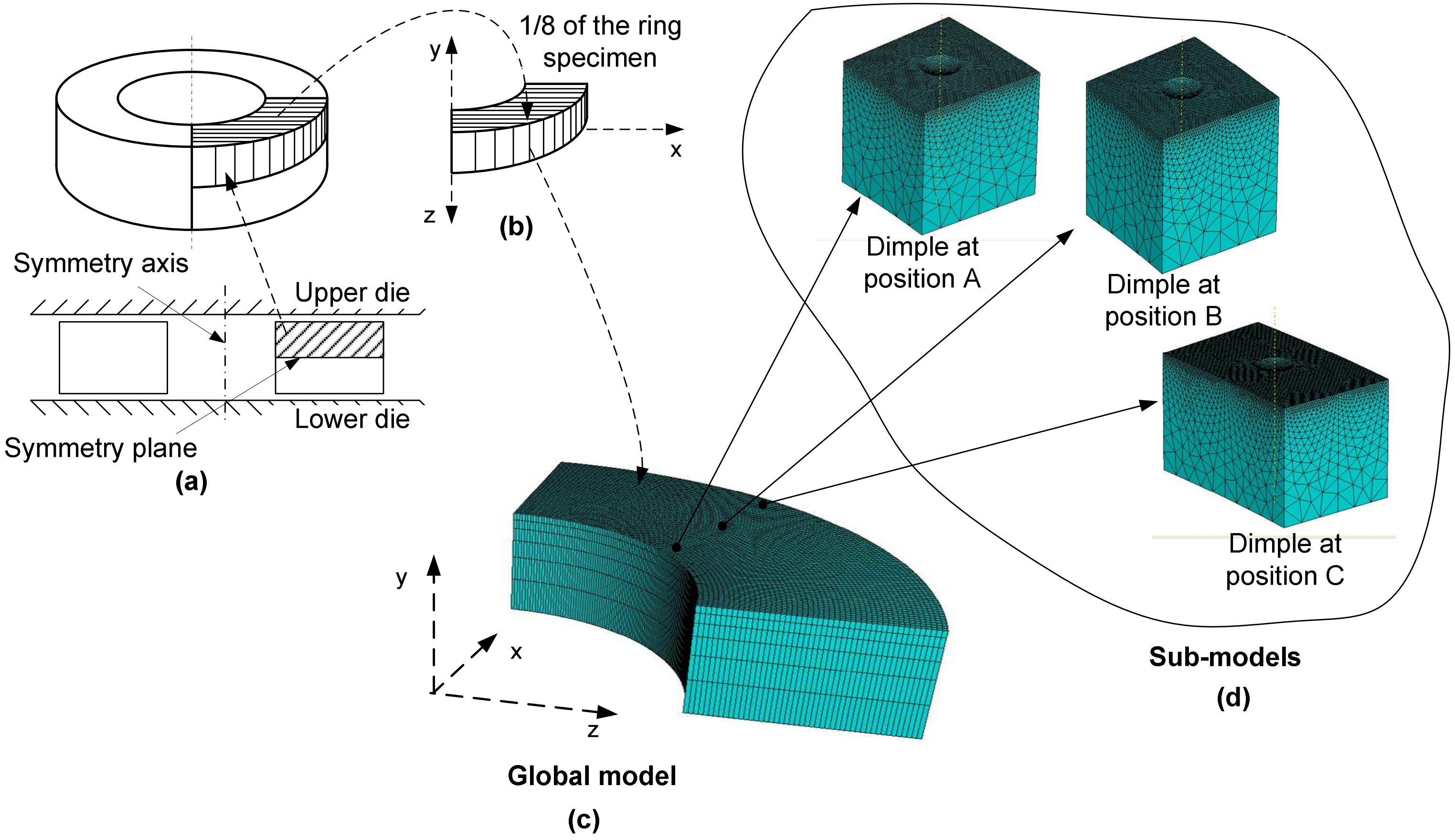

Figure 3.4: Diagram illustrating the procedure of FE modelling of the ring compression test; (a) ring and its symmetry, (b) global model, (c) meshed global model and (d) three sub-models with the refined mesh

3.2.2 Analysis Procedures

To obtain a clear understanding of the ESMG dimensional changes during the deformation process, conical, spherical, and cylindrical ESMGs, as shown in **Table 3.1**, were simulated at three different positions of the ring specimen (positions A, B and C as shown in **Figure 3.4**).

Table 3.1: Various geometries and dimensions of ESMGs analyzed in the study

No.	Initial Geometry	Dimensions		
		Diameter D_o [μm]	Depth d_o [μm]	Opening angle φ
1	Conical 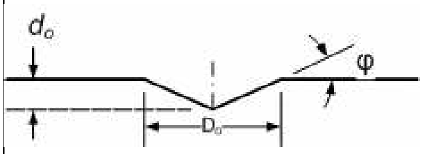	152	5	4°
		152	15	11°
		152	30	21°
		152	45	31°
2	Cylindrical 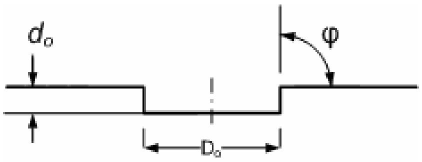	152	5	90°
		152	15	90°
		152	30	90°
		152	45	90
3	Spherical 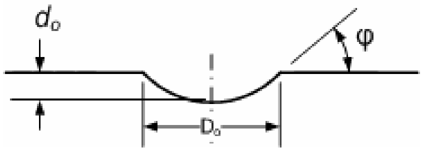	152	5	4
		152	15	20°
		152	30	35°
		152	45	50°

The results of the simulations were analysed both qualitatively and quantitatively. To analyse the ESMG dimensional changes qualitatively, 3D images and 2D surface profiles of the deformed ESMGs for various ring height reductions were observed and compared. For the quantitative method, the reduction of the 2D ESMG profile area, A_{ESMG}, (refer to **Figure 3.5**) was used to represent the dimensional changes in the function of the ring height reduction. In addition, the reduction of A_{ESMG} was also used to represent the amount of lubricant that was squeezed out from the ESMG cavity during the deformation process.

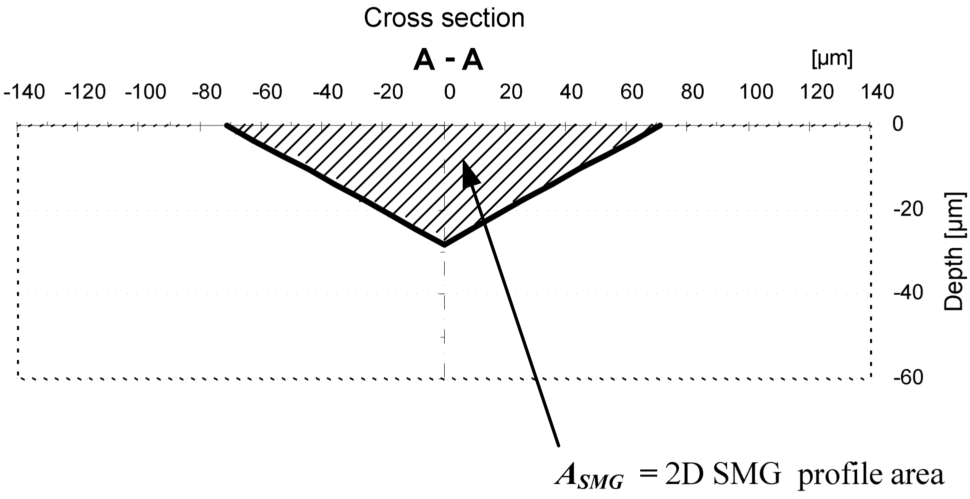

Figure 3.5: 2D ESMG profile area, A_{ESMG}, of the conical ESMG, the reduction of A_{ESMG} represents the amount of the trapped lubricant squeezed out from the ESMG during the deformation process

3.3 Results and Discussions

3.3.1 Validation of the simulation results

A comparison of the FE simulation and experimental results for a spherical ESMG with a depth of 13µm and a diameter of 152µm that was located in the middle of the ring is shown in **Figure 3.6** to **Figure 3.9**. These figures show 3D images and the profiles of the ESMGs for 0%, 4%, 12% and 25% deformation of the ring specimen. The experimental and computed results show good agreement. A reduction in the ring height that was larger than 25% would be required to reduce the volume of a 13µm deep ESMG to zero.

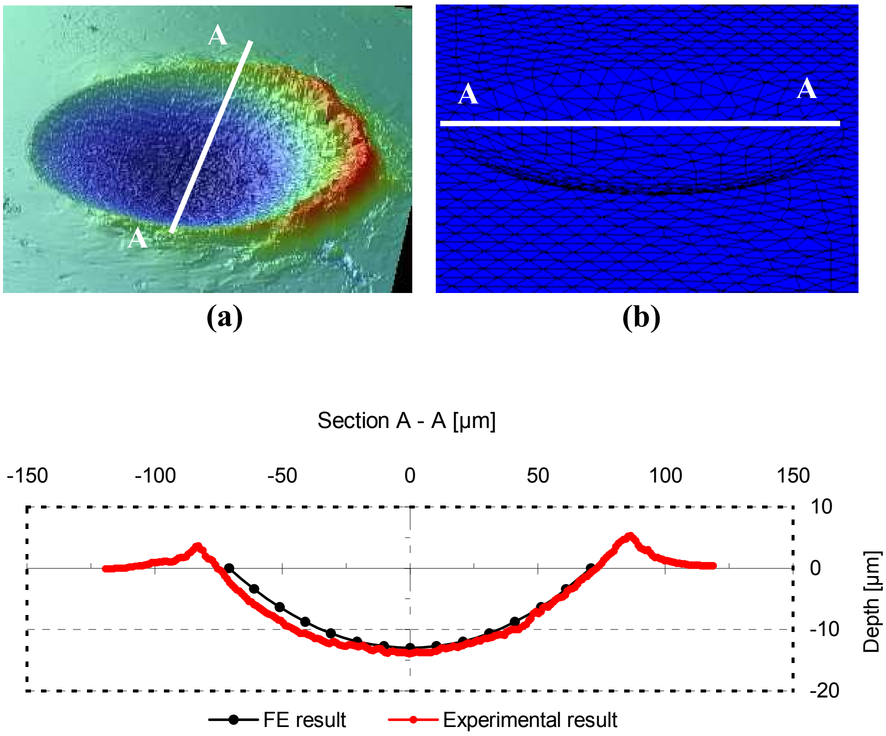

(a)

(b)

(c)

Figure 3.6: ESMGs before compression; (a) experimental ESMG, (b) FE model of ESMG and (c) profiles of both ESMG

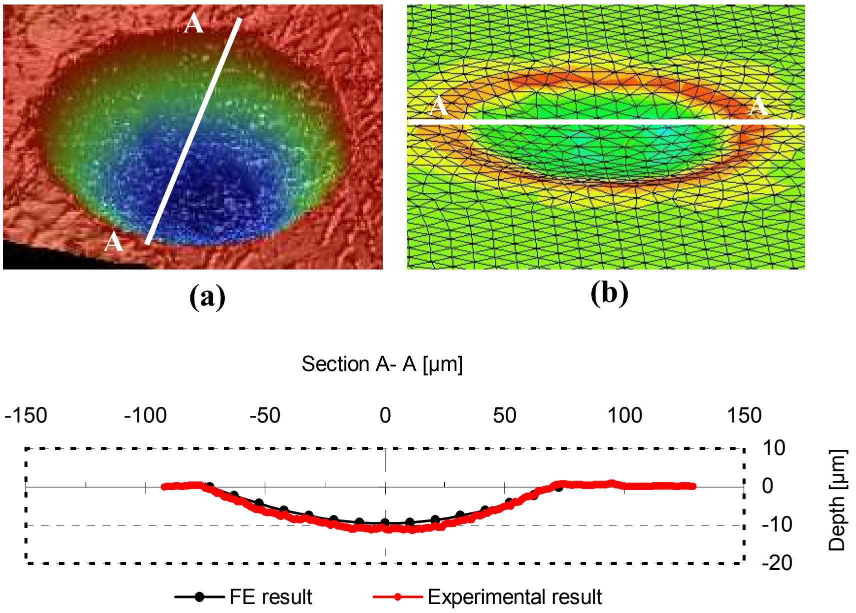

(a) (b)

(c)

Figure 3.7: ESMGs after 4% deformation of the ring; (a) experimental ESMG, (b) computed ESMG and (c) profiles of both ESMGs

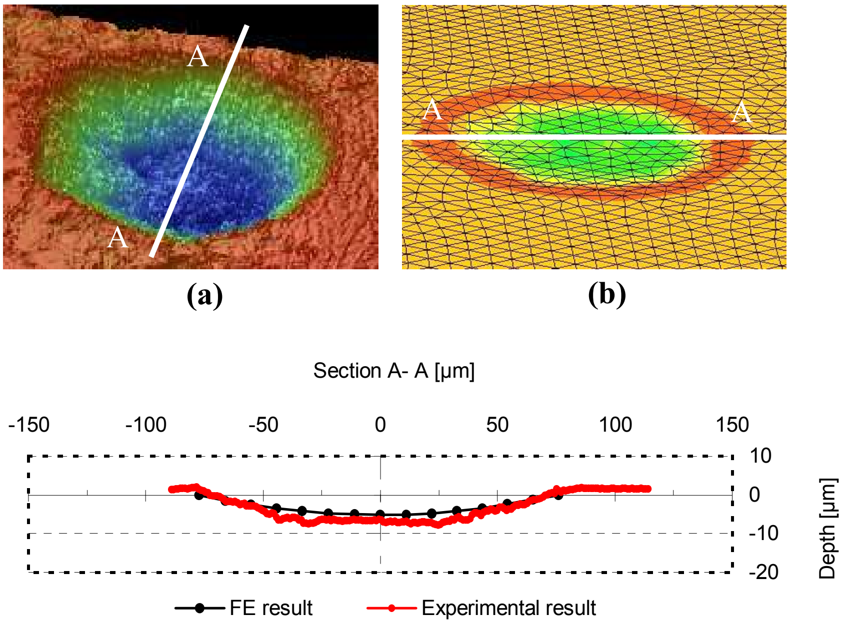

(a) (b)

(c)

Figure 3.8: ESMGs after 12% deformation of the ring; (a) experimental ESMG, (b) computed ESMG and (c) profiles of both ESMGs.

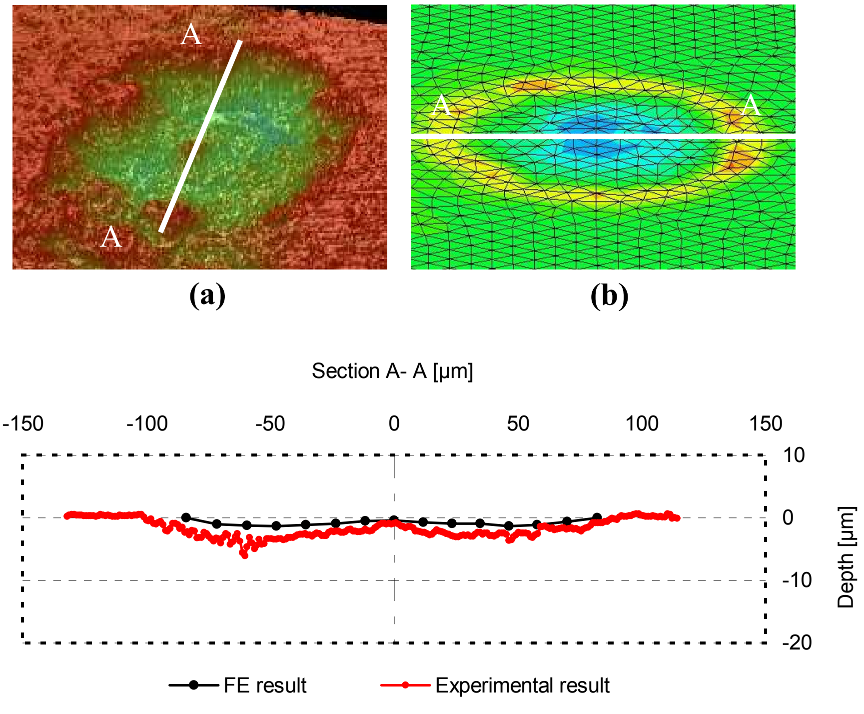

(a) (b)

(c)

Figure 3.9: ESMGs after 25% deformation of the ring; (a) experimental ESMG, (b) computed ESMG and (c) profiles of both ESMGs.

3.3.2 Dimensional changes and optimal ESMG geometry

The simulation results that demonstrate the 3D dimensional change of the conical, cylindrical and spherical ESMGs with initial depths of 45μm, 30μm 15μm and 5μm, at various height reductions of the ring specimen, are shown in **Figures 3.10 (a)** to **Figure 3.21 (a)** and, the 2D profiles along the cross section (A-A) are shown in **Figures 3.10 (b)** to **Figure 3.21 (b)**. The reductions of A_{ESMG} of the conical, cylindrical and spherical ESMGs for various ring specimen height reductions are shown in **Figures 3.22** to **Figure 3.24**.

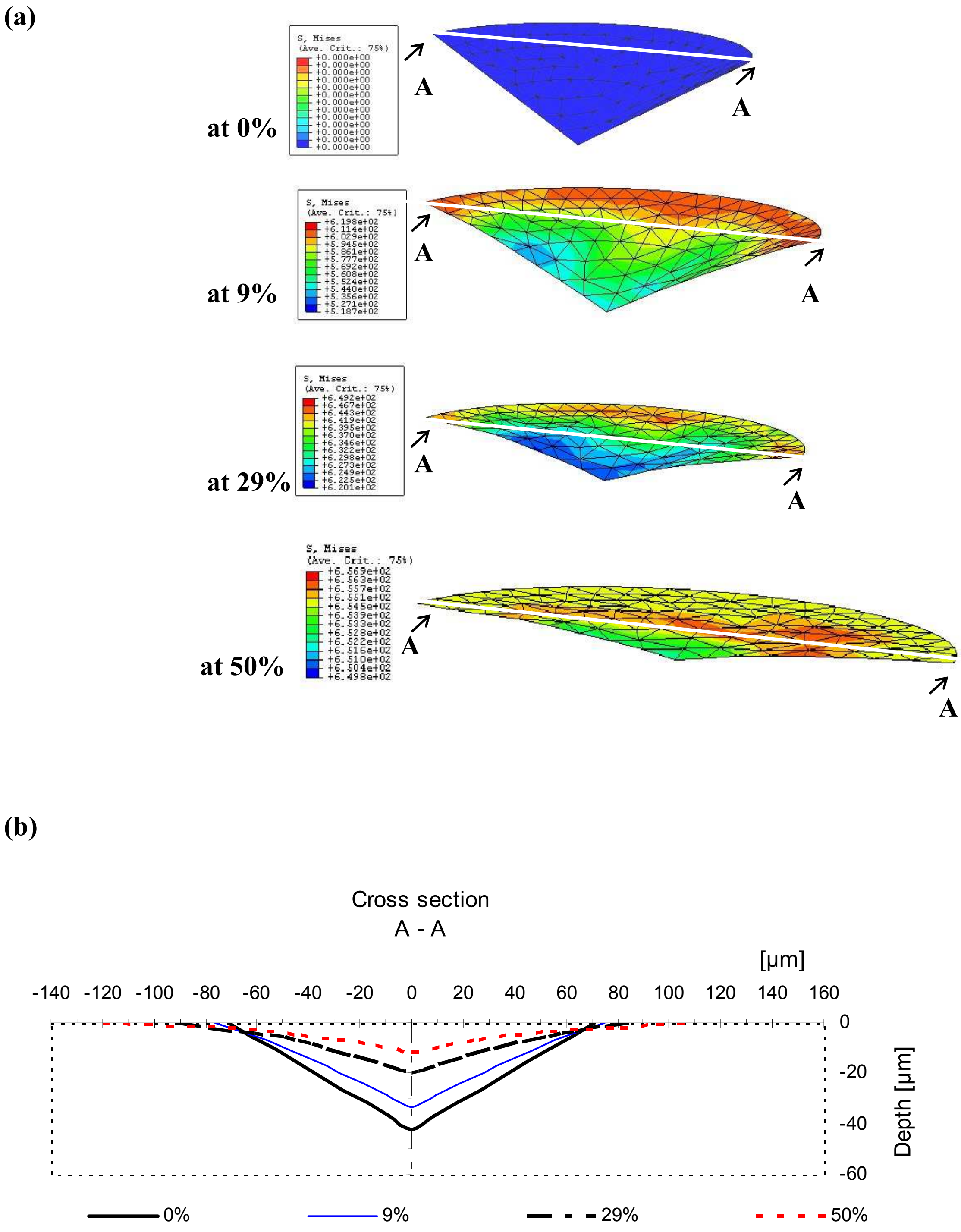

Figure 3.10: (a) The computed 3D images and (b) profiles of cross section A-A of a conical ESMG with an initial depth of 45µm at various ring height reductions (0%, 9%, 20% and 50%)

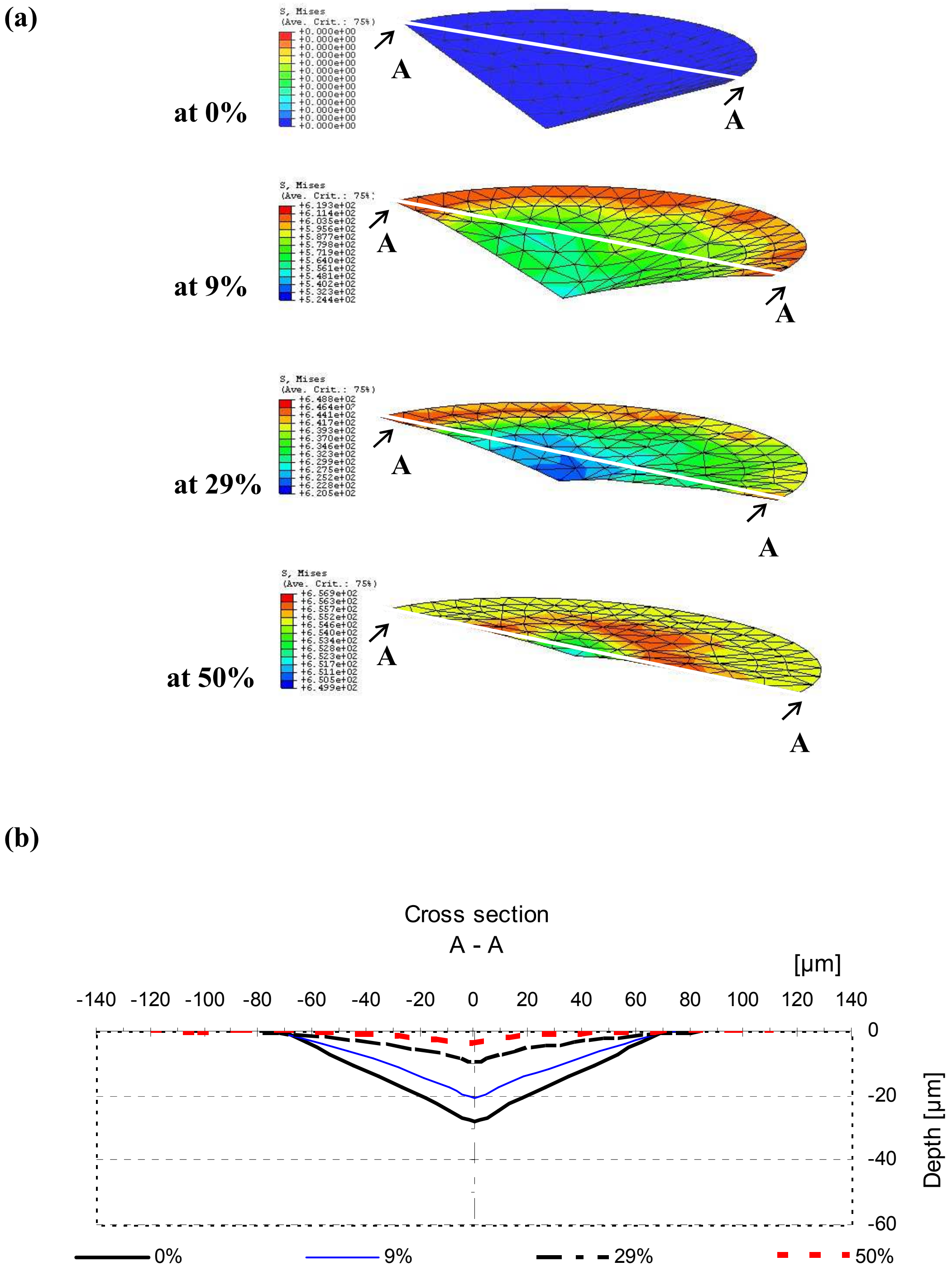

Figure 3.11: (a) The computed 3D images and (b) profiles of cross section A-A of a conical ESMG with an initial depth of 30μm at various ring height reductions (0%, 9%, 20% and 50%)

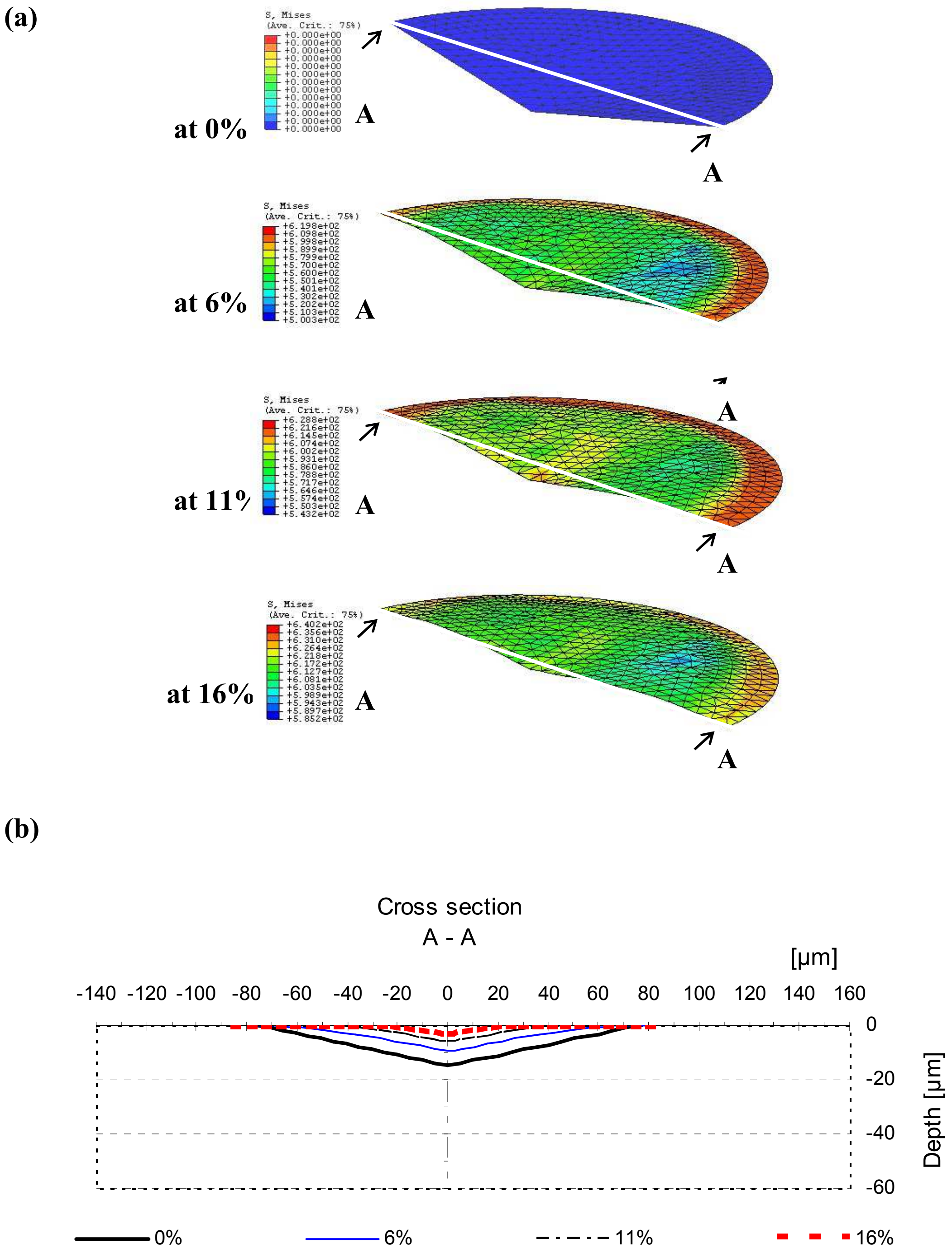

Figure 3.12: (a) The computed 3D images and (b) profiles of cross section A-A of a conical ESMG with an initial depth of 15μm at various ring height reductions (0%, 6%, 11% and 16%)

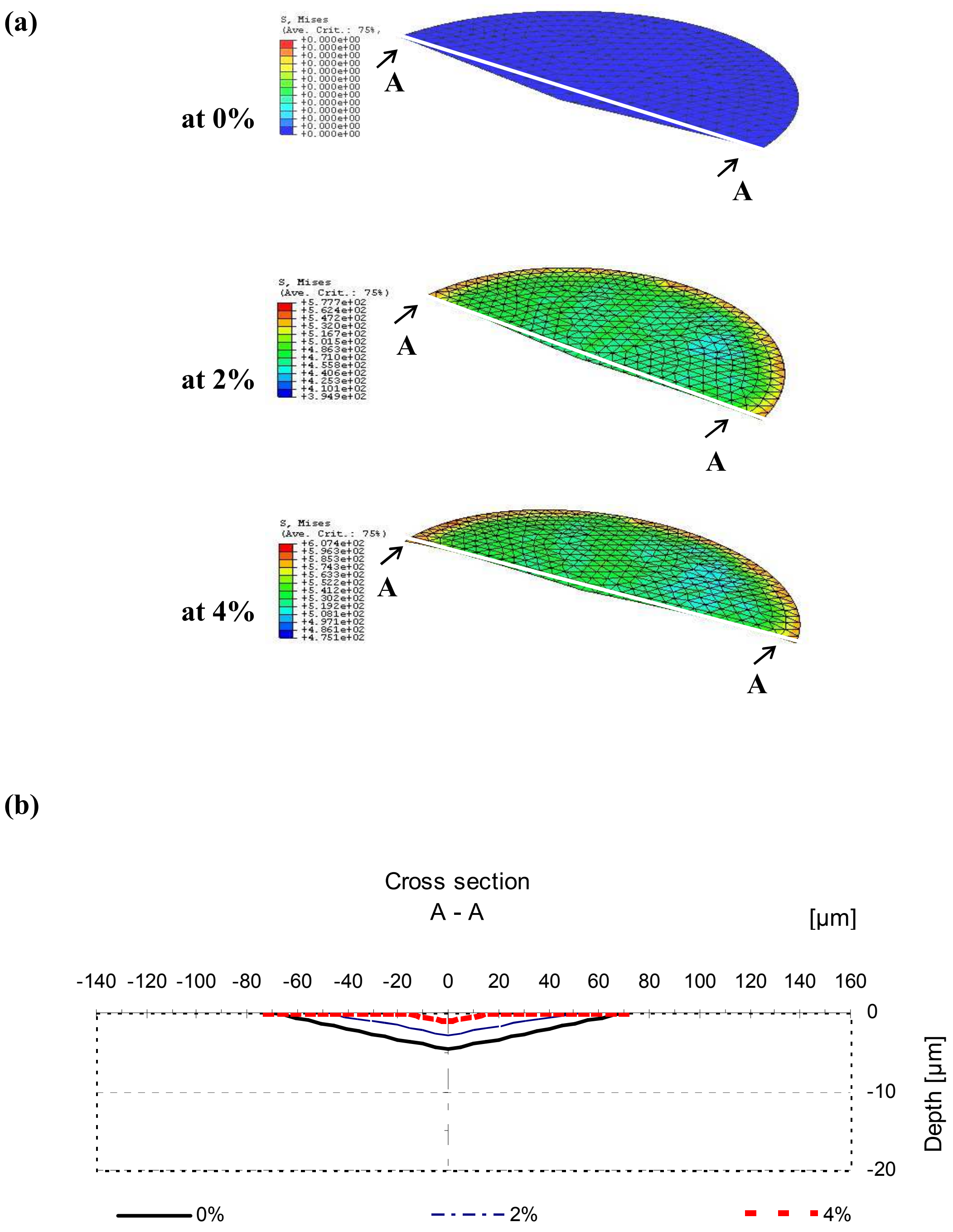

Figure 3.13: (a) The computed 3D image and (b) profiles of cross section A-A of a conical ESMG with an initial depth of 5μm at various ring height reductions (0%, 2% and 4%)

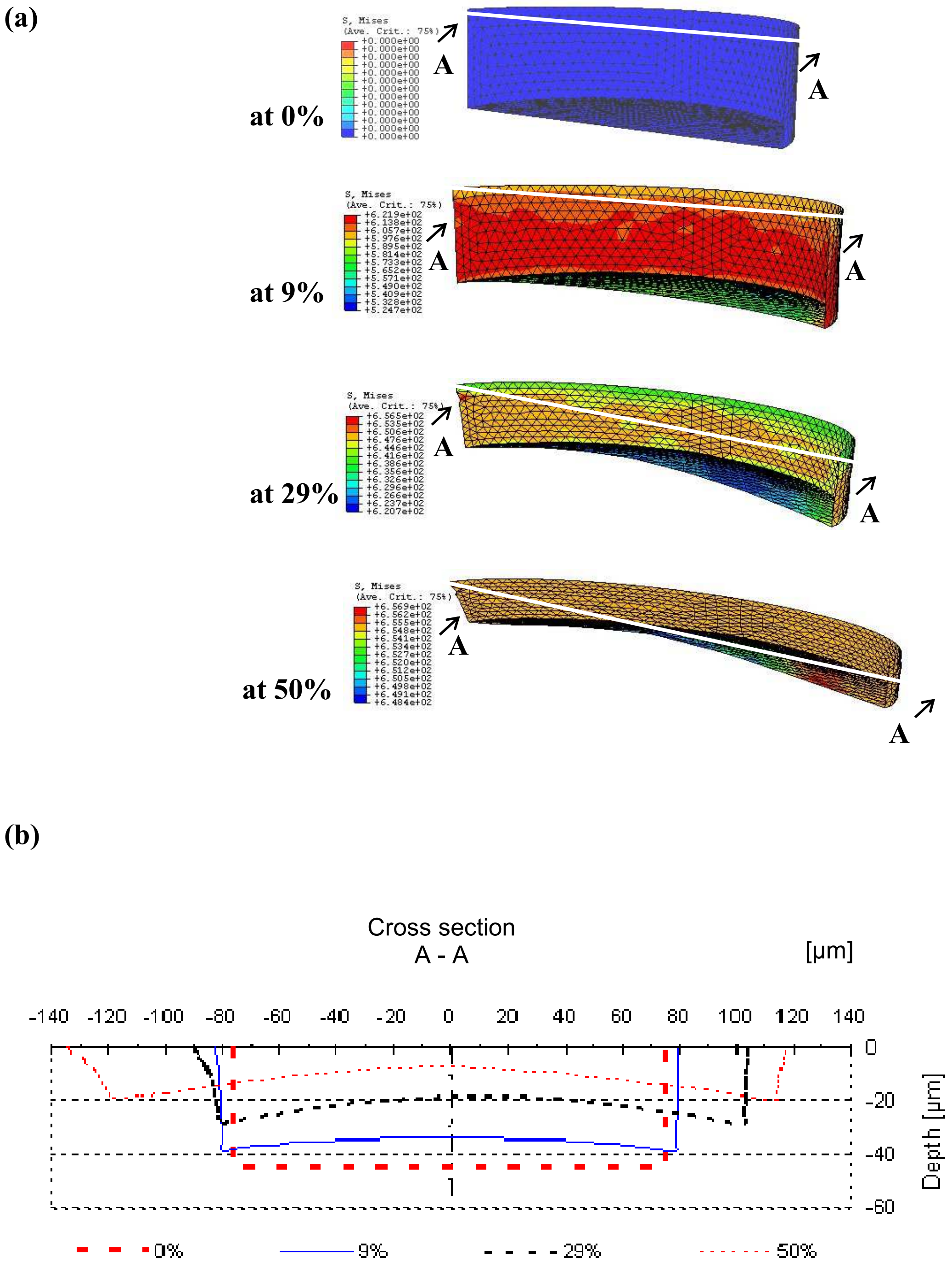

Figure 3.14: (a) The computed 3D image and (b) profiles of cross section A-A of a cylindrical ESMG with an initial depth of 45μm at various ring height reductions (0%, 9%, 29% and 50%)

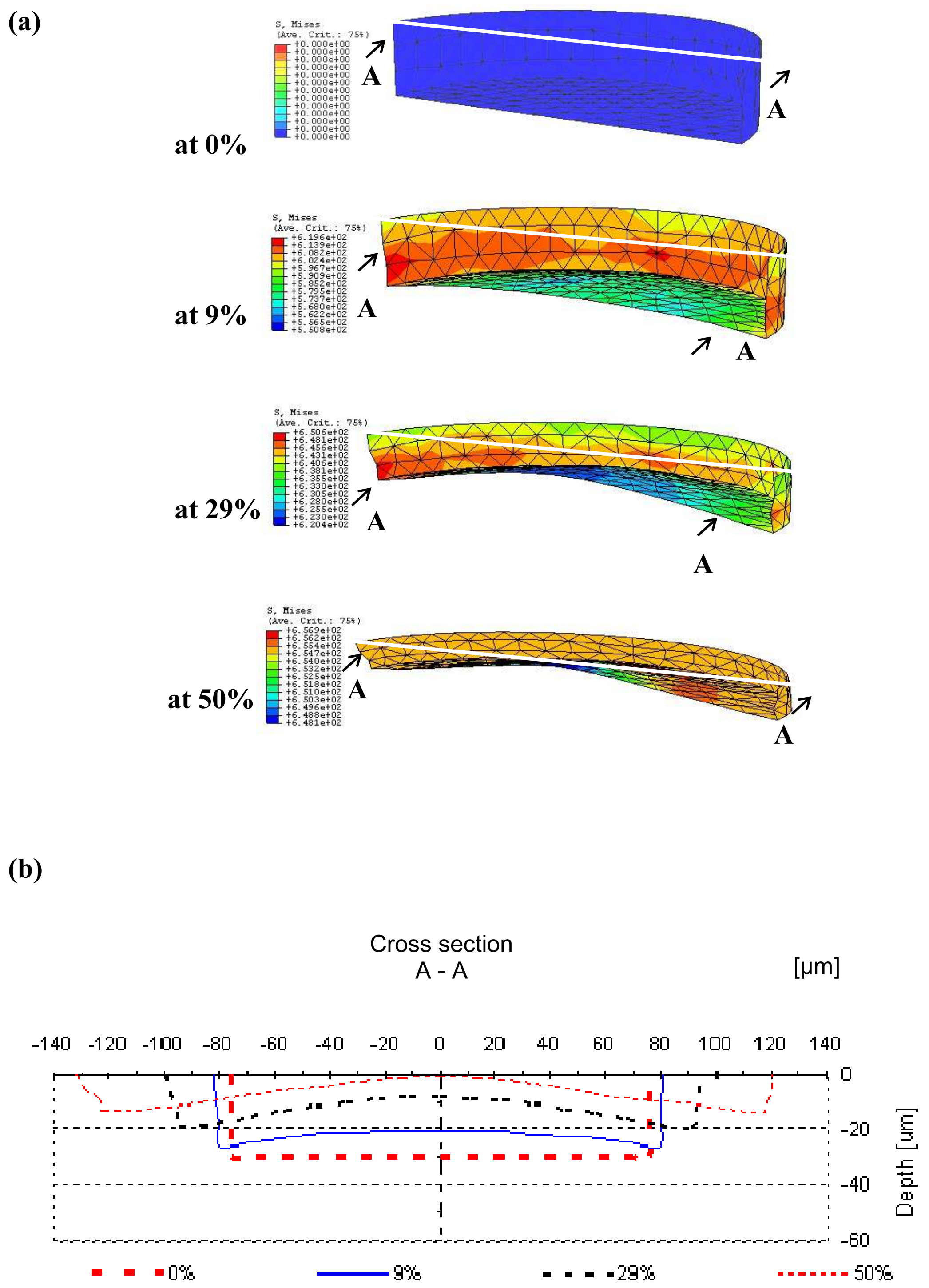

Figure 3.15: (a) The computed 3D image and (a) profiles of cross section A-A of a cylindrical ESMG with an initial depth of 30µm at various ring height reductions (0%, 9%, 29% and 50%)

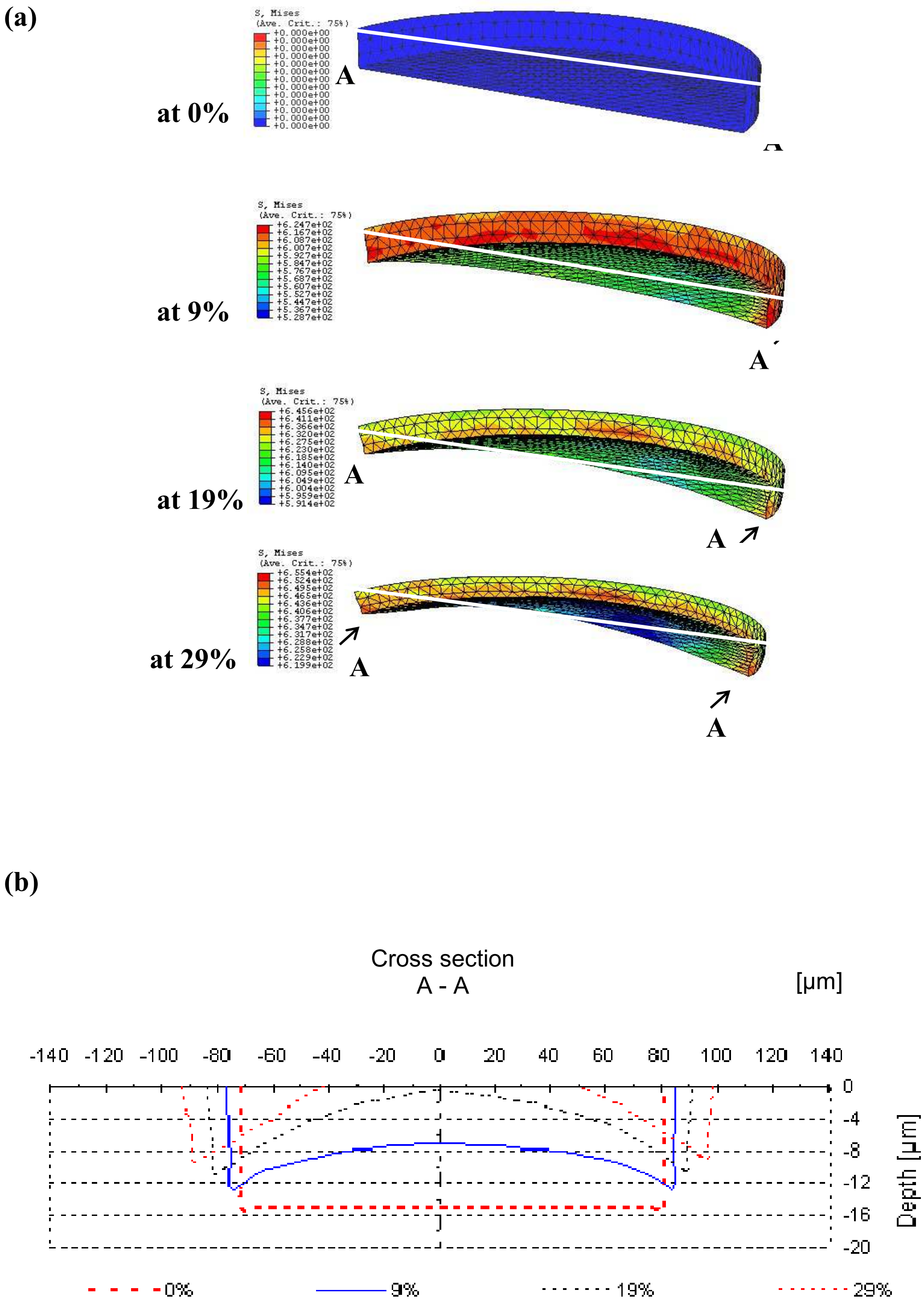

Figure 3.16: (a) The computed 3D image and (a) profiles of cross section A-A of a cylindrical ESMG with an initial depth of 15µm at various ring height reductions (0%, 9% 19% and 29%)

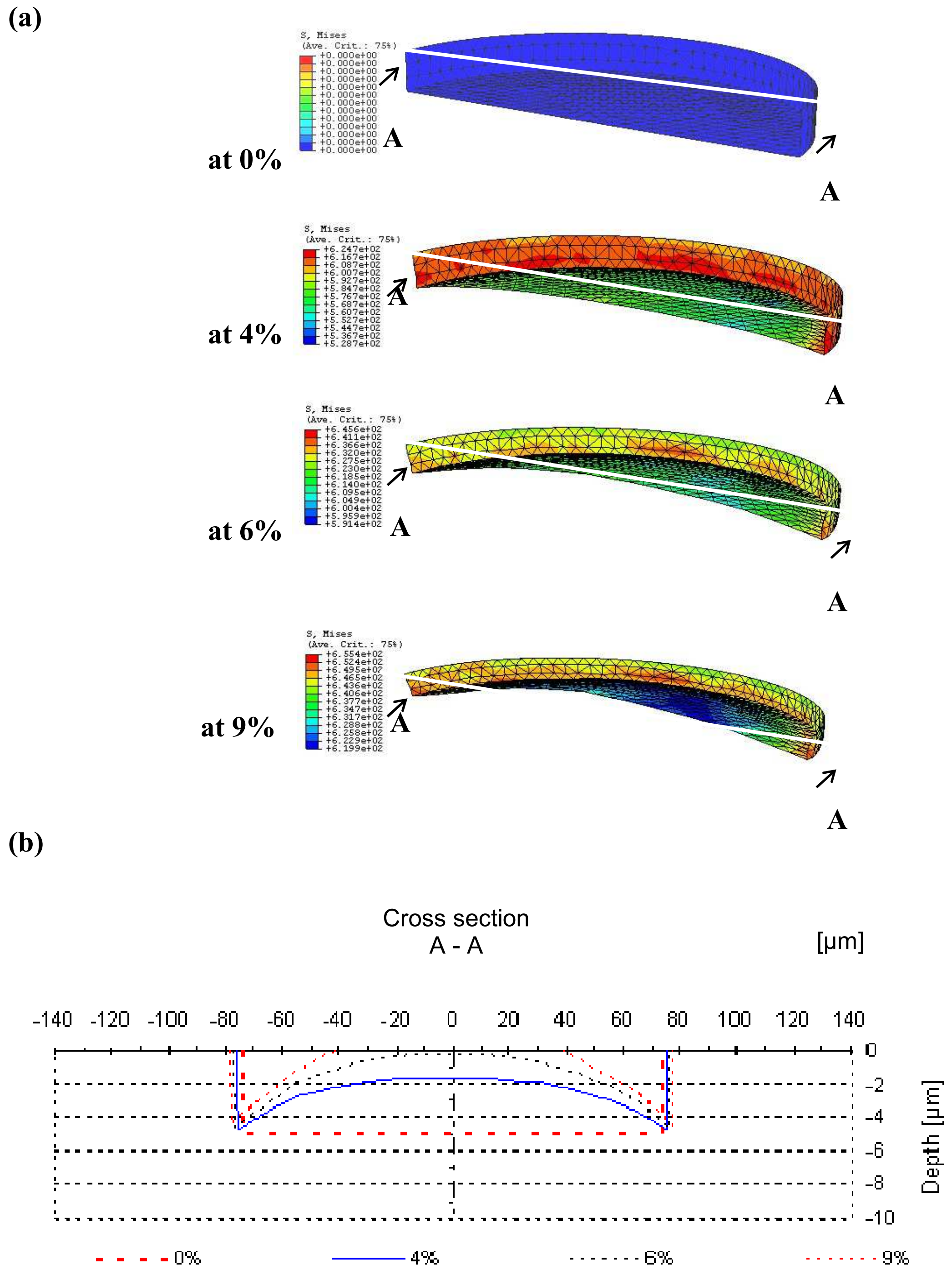

Figure 3.17: (a) The computed 3D image and (b) profiles of cross section A-A of a cylindrical ESMG with an initial depth of 5μm at various ring height reductions (0%, 4% 6% and 9%)

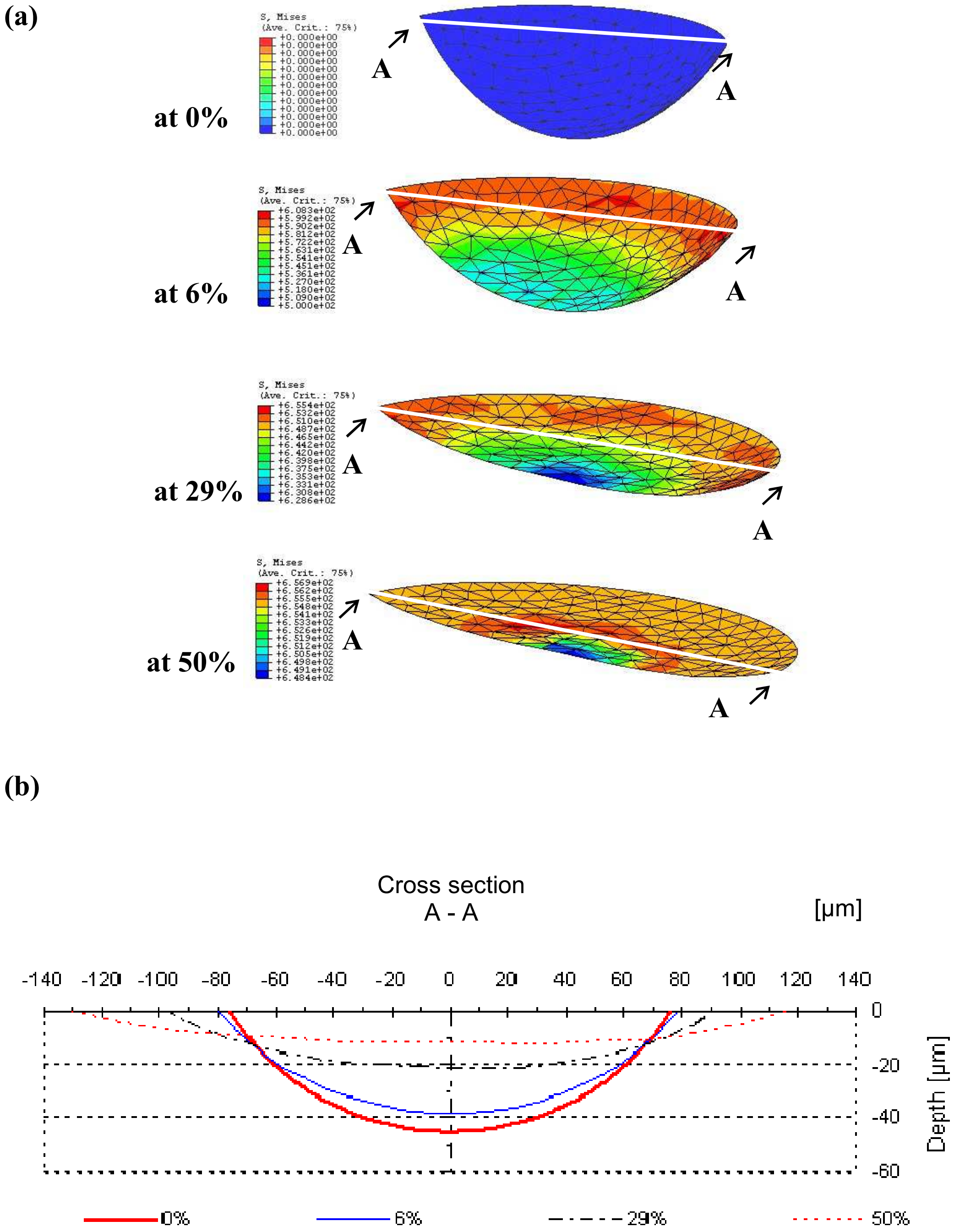

Figure 3.18: (a) The computed 3D image and (b) profiles of cross section A-A of a spherical ESMG with an initial depth of 45µm at various ring height reductions (0%, 6%, 29% and 50%)

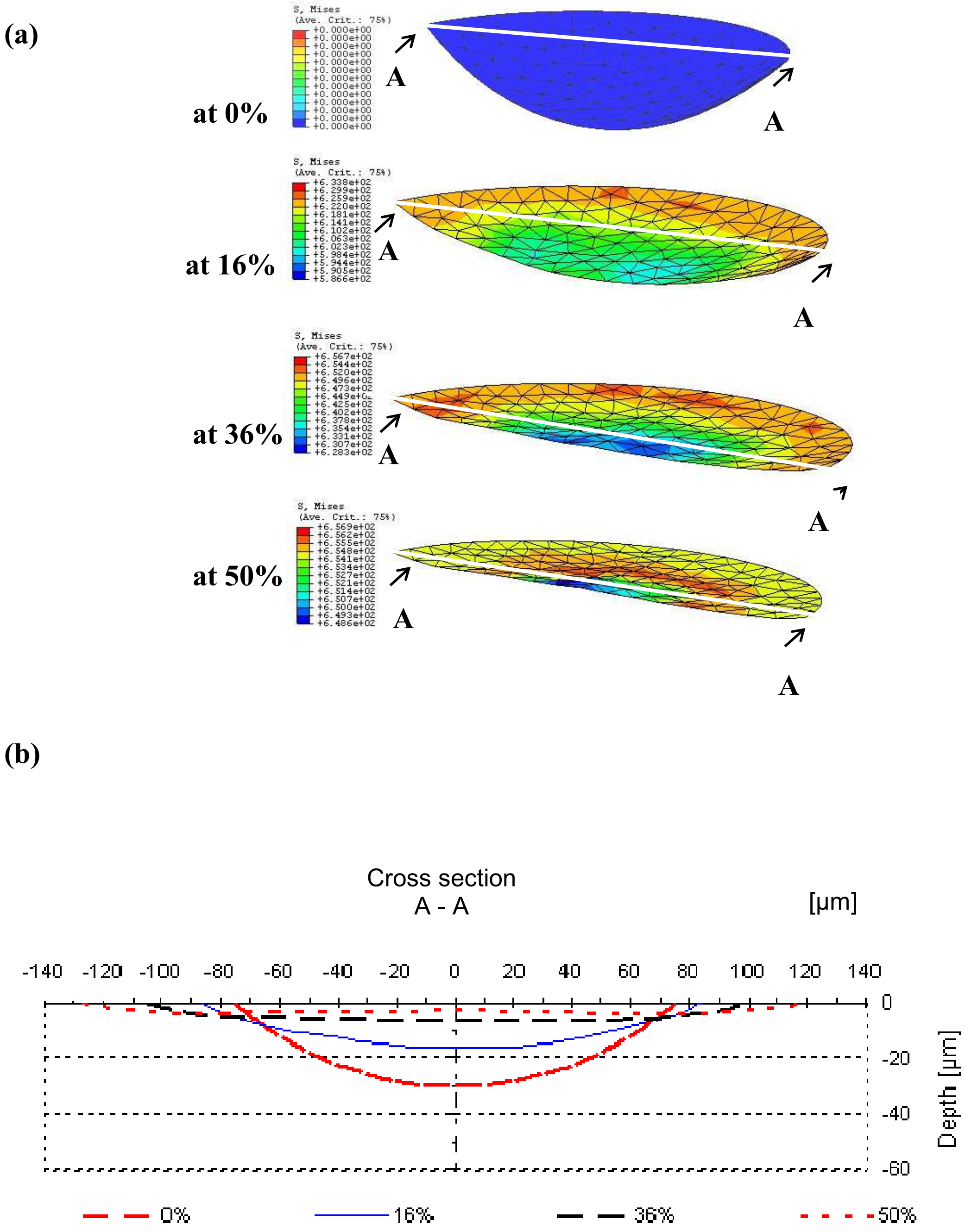

Figure 3.19: (a) The computed 3D image and (b) profiles of cross section A-A of a spherical ESMG with an initial depth of 30μm at various ring height reductions (0%, 16%, 36% and 50%)

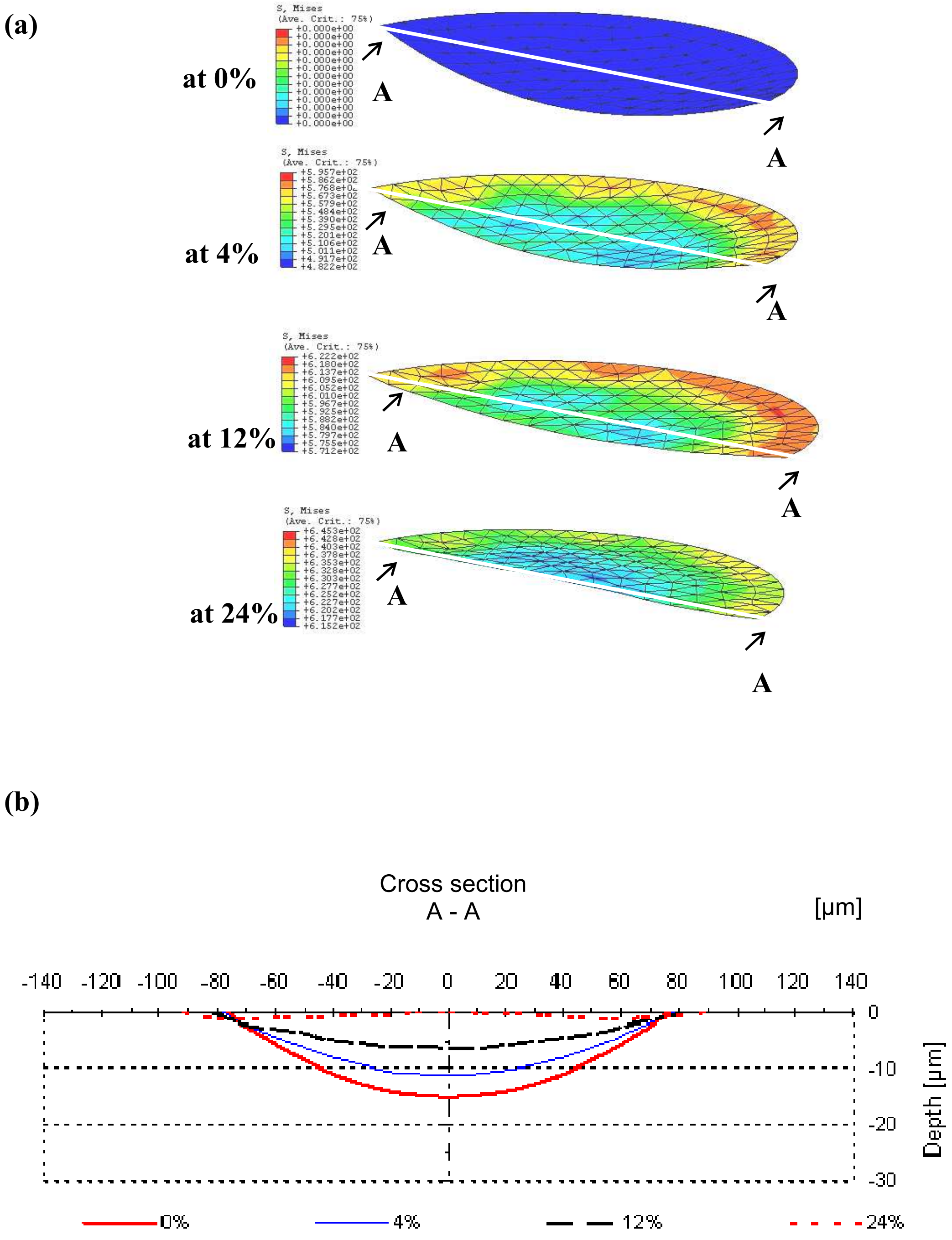

Figure 3.20: (a) The computed 3D image and (b) profiles of cross section A-A of a spherical ESMG with an initial depth of 15μm at various ring height reductions (0%, 4%, 12% and 24%)

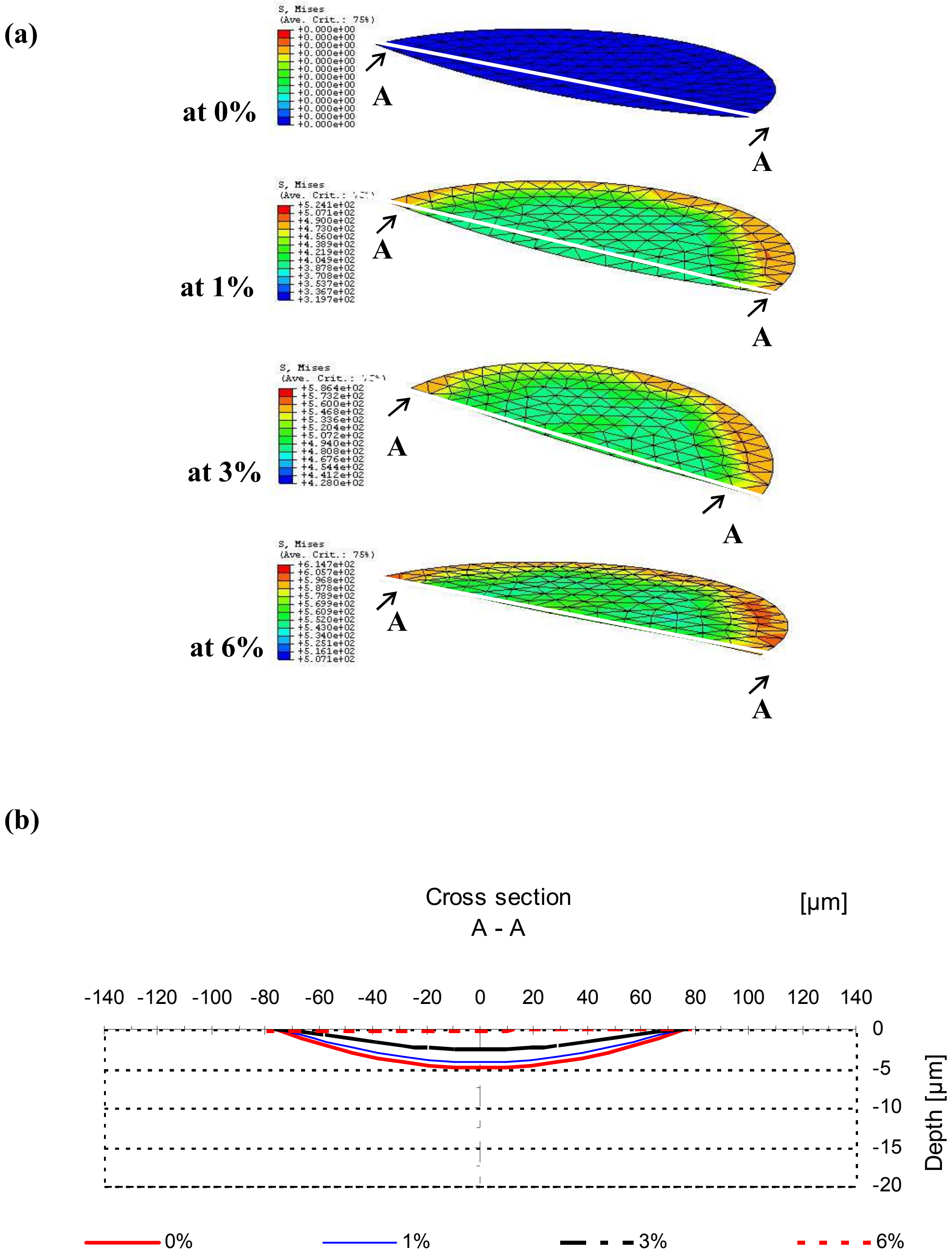

Figure 3.21: (a) The computed 3D image and (b) profiles of cross section A-A of a spherical ESMG with an initial depth of 5µm at various ring height reductions (0%, 1%, 3% and 6%)

As shown in **Figures 3.10 (b)** to **Figure 3.13 (b)**, throughout the deformation of the ring specimen, the whole ESMGs' conical surface is pushed up and expanded. The surface closer to the edge of the conical ESMG is found to be the first surface that touches the upper die and is followed by the surface closer to the centre.

Figures 3.14 (a) to **Figure 3.17 (a)** show the 3D images of the deformation of a cylindrical ESMG with different depths at various ring height reduction and their 2D profiles are shown in **Figures 3.14 (b)** to **Figure 3.17 (b).** These figures show that, during the deformation process, the diameter of the ESMG increases as the ring height reduction increases. Meanwhile, the base surface closer to the centre is pushed upward much more than the surface closer to the sidewall, which results in the depth around the centre being much smaller when compared with the surface near to the edge. As the ring height reduction increases, the inner base surface around the centre of the ESMG is found to be the first part that touches the upper die. Therefore, as shown in **Figure 3.15 (b)**, **Figure 3.16 (b)** and **Figure 3.17 (b)**, at the end of the process, the cylindrical ESMG turns into a toroidal shape.

The initial cavity volume of the cylindrical ESMG is much higher as compared with the conical and spherical ESMG. Due to this reason, the spherical ESMG is capable to trap and squeeze much higher volume during the deformation. However, it has been observed that the sidewall acts as a rigid surface that is resistant to collapse. In addition, because of the difficulty of making the sidewall collapse, the cylindrical ESMG gives the slowest rate of A_{ESMG} reduction when compared with the conical and spherical ESMG (see **Figure 3.22** to **Figure 3.25**), which may result in surface defect.

As shown in **Figures 3.18** to **Figure 3.21**, starting from the beginning of the reduction of the ring height, the whole inner surface of the spherical ESMG starts to deform, and simultaneously the ESMG diameter also increases. This deformation condition results in a decrease of the opening angle, φ.

When comparing the A_{ESMG} reduction curves between the conical, cylindrical and spherical ESMGs, it is seen that the conical ESMG is the most likely to collapse. As shown in **Figure 3.22**, for the conical ESMG with an initial depth of 45μm, a 50% reduction of ring height results in a reduction of 70% of A_{ESMG} but this is only 55% for the cylindrical ESMG and 50% for the spherical ESMG. Meanwhile, for the conical ESMG with an initial depth of 30μm (see **Figure 3.23**), a 50% reduction of ring height results in an A_{ESMG} reduction of 90%, but for the spherical and cylindrical ESMGs, the result is only 75% and 60% respectively.

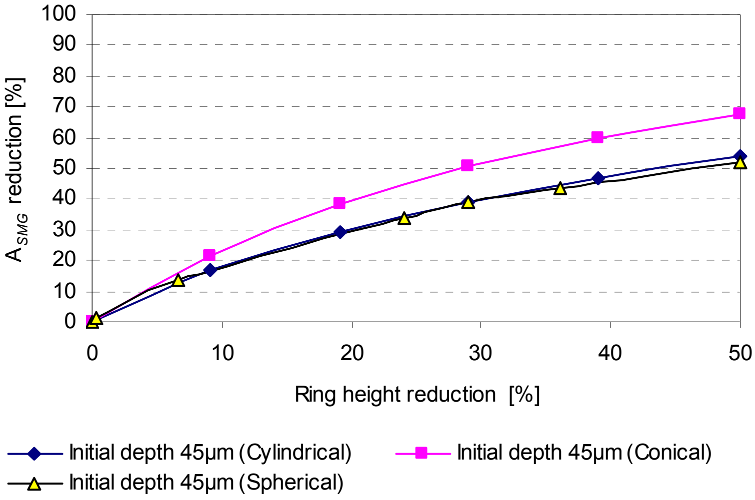

Figure 3.22: A_{ESMG} reduction versus height reduction of the ring specimen for the ESMG with an initial depth of 45μm

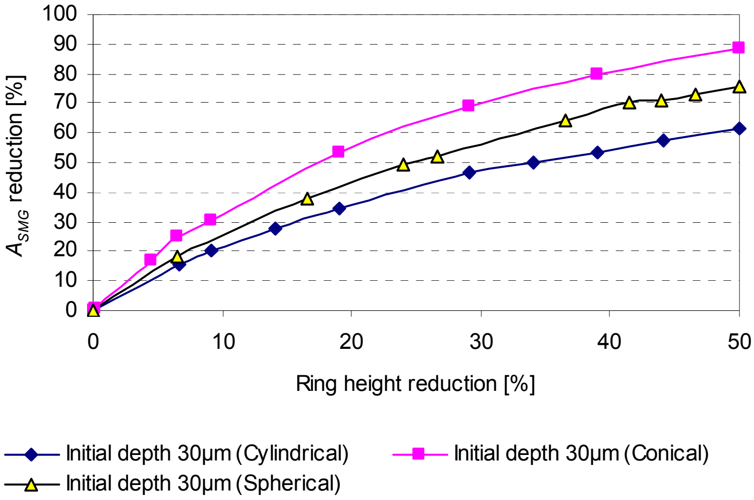

Figure 3.23: A_{ESMG} reduction versus height reduction of the ring specimen for the ESMG with an initial depth of 30µm

As shown in **Figure 3.24**, at the ring height reduction of 22%, the A_{ESMG} of the conical ESMG with an initial depth of 15µm is reduced by up to 98%, which indicates that the ESMG has almost totally collapsed; whereas, at the some ring reduction, the spherical ESMG has collapsed by 85% and the cylindrical ESMG only by 70%. The shallower conical, cylindrical and spherical ESMGs (5µm in depth) have collapsed almost totally at lower ring height reduction rates (less than 10%), which is clearly shown in **Figure 3.25**.

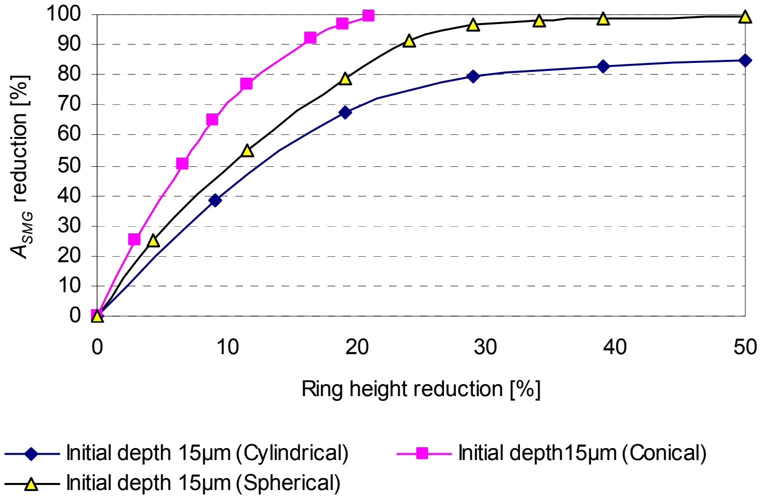

Figure 3.24: A_{ESMG} reduction versus height reduction of the ring specimen for the ESMG with an initial depth of 15µm

The optimal geometry and dimensions of an ESMG are determined based on the concept that the ESMG should be able to provide the maximum amount of lubricant throughout the process of the deformation of the workpiece and leaving minimal surface defects at the end of the process [32]. Therefore, the A_{ESMG} reduction rate, the deformation behaviour of the ESMG surface, and the deformation rate of the workpiece are important factors that need to be considered in determining the optimal ESMG parameters. For deformation of up to 50%, the 5µm depth for conical and spherical ESMGs (opening angle, $\varphi = 4°$) has been found to be unable to store and redistribute enough lubricant, as they will collapse almost totally at the beginning of the deformation (see **Figure 3.25**).

As shown in **Figure 3.24**, the conical ESMG with a depth of 15µm and opening angle of 11° was found to collapse totally after just 22% deformation; nevertheless, the cylindrical ESMG collapsed only by 85% at 50% deformation, which may be leaving a surface defect. But, **Figure 3.24** also shows that the spherical ESMG with the same depth collapsed by 98% at 50% deformation, while leaving minimal surface defects. Therefore, it can be concluded that spherical ESMGs with the depth of approximately 15μm and opening angle of 20° (see **Table 3.1**) are able to provide the maximum amount of lubricant throughout the deformation process (up to 50% ring height reduction) and, at the end of the process, leave minimal surface defects.

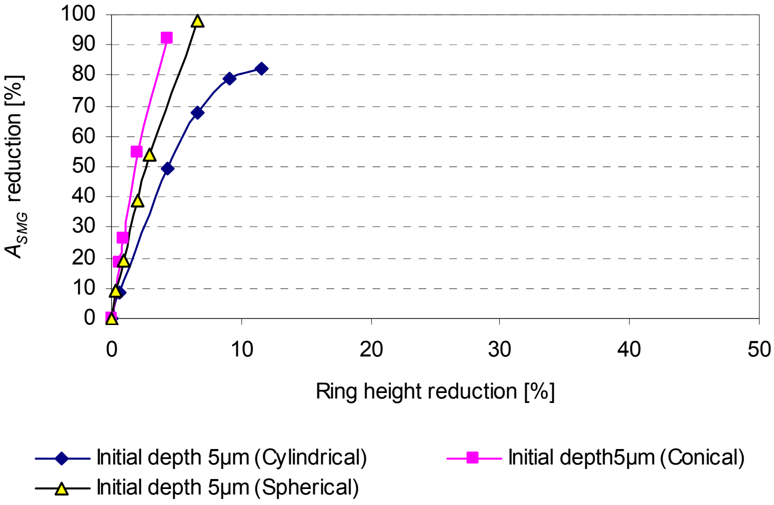

Figure 3.25: A_{ESMG} reduction versus height reduction of the ring specimen for the ESMG with an initial depth of 5μm

3.3.3 ESMG deformation behaviour at different positions

Table 3.2 to **Table 3.5** show the changes in the shape of the spherical ESMGs, with four different initial depths, collapsed by the reduction in the ring height, for three different locations, i.e. close to the inner edge of the ring (position A), in the middle of the ring (position B) and at the outer ring edge (position C). These tables show: (a) the top view and (b) the 2D profiles at cross section A-A for position A, position B and position C.

As shown in these tables**,** the depth of each spherical ESMG decreases with the increase in the reduction of the ring height and, it has been observed that ESMGs closer to the inner edge are deformed into more of an oval shape compared to the ESMGs that are closer to the outer edge. It is understood that the ring surface expansion at a position close to the inner edge is less equal axial (radial strain larger than circumferential strain) than the surface expansion close to the outer edge. In additional, as seen in **Table 3.2 (b)** and **Table 3.3 (b)**, ESMGs closer to the outer ring edge give the greatest reduction in depth. This means that ESMGs near to the outer edge, experience higher contact pressure, which causes their earlier to collapse compared to the ESMGs near to the inner edge.

The same effect can be seen in **Figure 3.26** and **Figure 3.27**, where the ESMG near to the outer edge (position C) gives a higher A_{ESMG} reduction rate than the ESMG near to the middle (position B) and the inner edge (position A). Therefore, during the deformation of the ring specimen, it can be assumed that the amount of lubricant that is squeezed out from the ESMG close to the outer edge is higher than on the surface close to the inner edge. However, for shallow ESMGs, as those illustrated in **Figure 3.28** and **Figure 3.29**, this effect is negligible.

Table 3.2: Shape of ESMG with initial depth of 45μm at 3 different positions (A, B and C) resulting from two levels of ring height reduction; (a) top view and (c) ESMGs profiles at cross section A-A

<table>
<tr><th>At 29% of ring height reduction</th><th>At 50% of ring height reduction</th></tr>
<tr><td colspan="2">(a) Top View</td></tr>
<tr><td colspan="2"><i>at position A</i></td></tr>
<tr><td>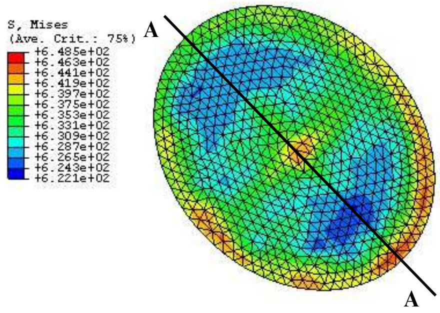 </td><td>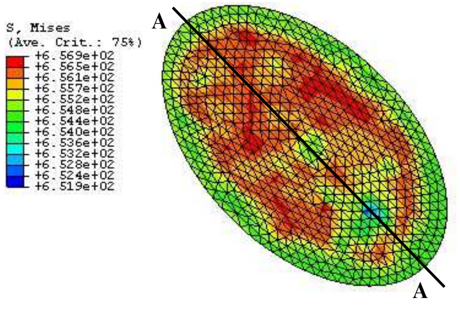 </td></tr>
<tr><td colspan="2"><i>at position B</i></td></tr>
<tr><td>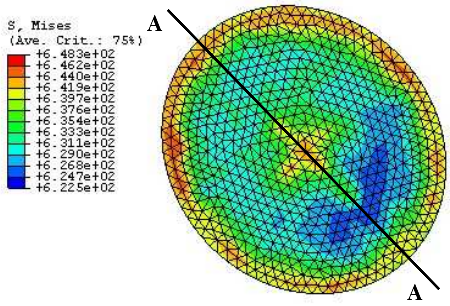 </td><td>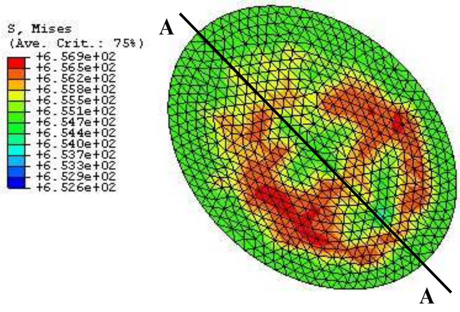 </td></tr>
<tr><td colspan="2"><i>at position C</i></td></tr>
<tr><td>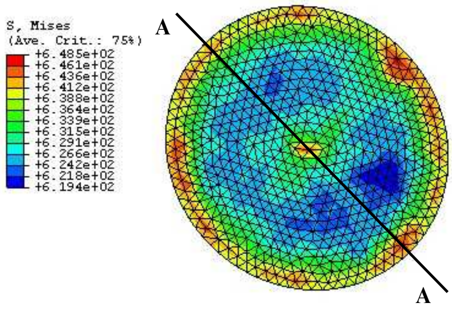 </td><td>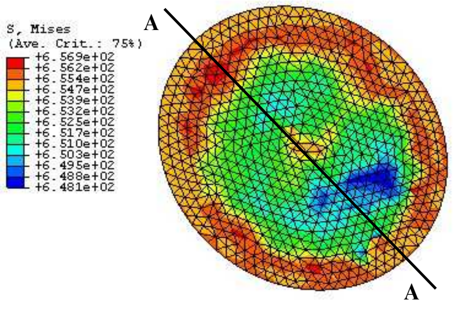 </td></tr>
<tr><td colspan="2">(b) SMG profile at cross section A-A</td></tr>
<tr><td>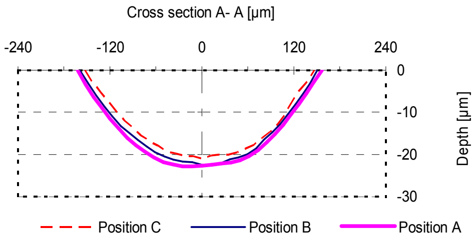 </td><td>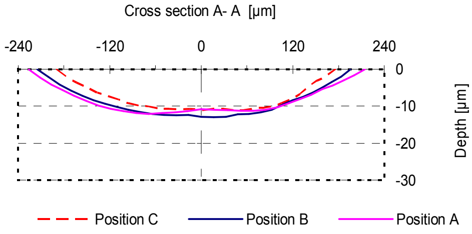 </td></tr>
</table>

Table 3.3: Shape of ESMG with initial depth of 30μm at 3 different positions (A, B and C) resulting from two levels of ring height reduction; (a) top view and (c) ESMGs profiles at cross section A-A

<table>
<tr><th>At 26% ring height reduction</th><th>At 36% ring height reduction</th></tr>
<tr><td colspan="2">(a) Top View</td></tr>
<tr><td colspan="2">at position A</td></tr>
<tr><td>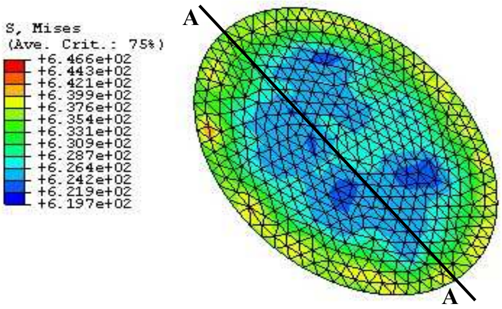
</td><td>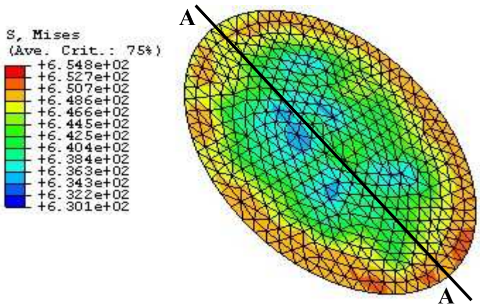
</td></tr>
<tr><td colspan="2">at position B</td></tr>
<tr><td>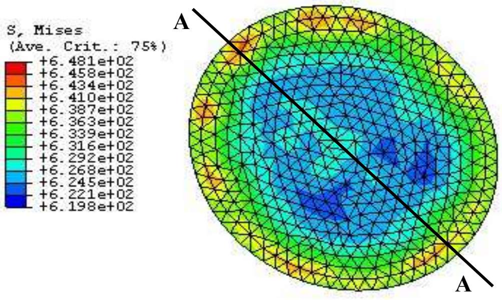
</td><td>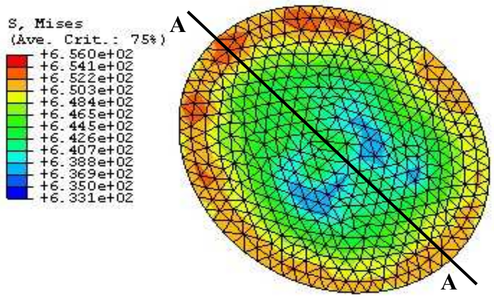
</td></tr>
<tr><td colspan="2">at position C</td></tr>
<tr><td>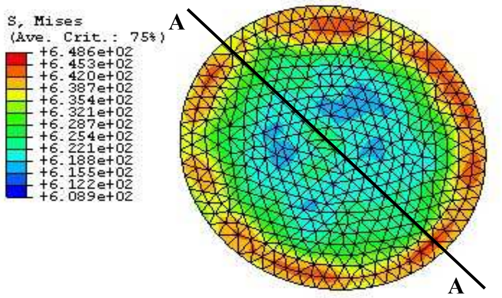
</td><td>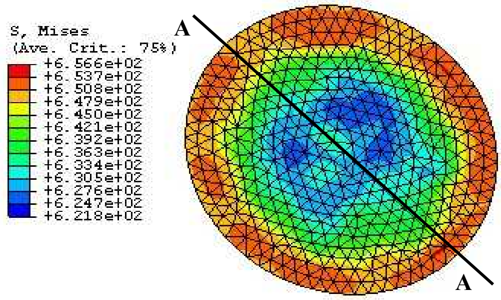
</td></tr>
<tr><td colspan="2">(b) SMG profiles at cross section A-A</td></tr>
<tr><td>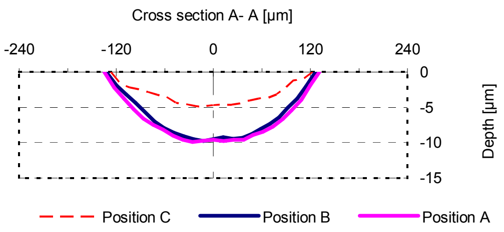
</td><td>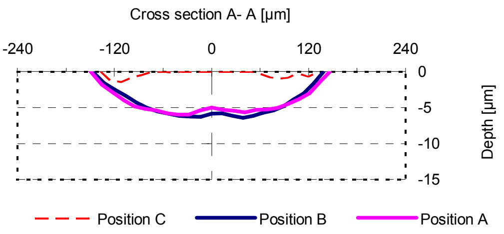
</td></tr>
</table>

Table 3.4: Shape of ESMG with initial depth of 15μm at 3 different positions (A, B and C) resulting from two levels of ring height reduction; (a) top view and (c) ESMGs profiles at cross section A-A

At 12% ring height reduction	At 22% ring height reduction
(a) Top View	
at position A	
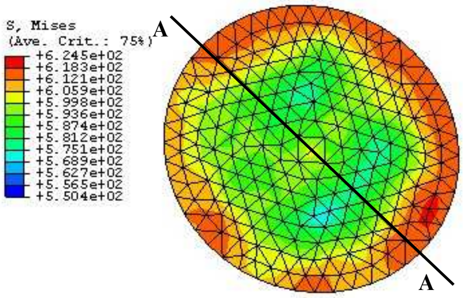	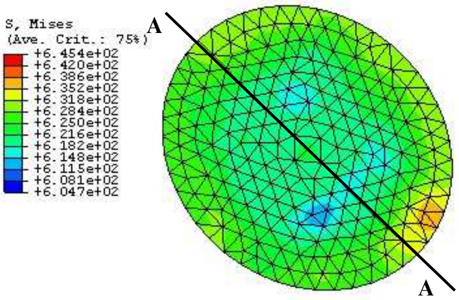
at position B	
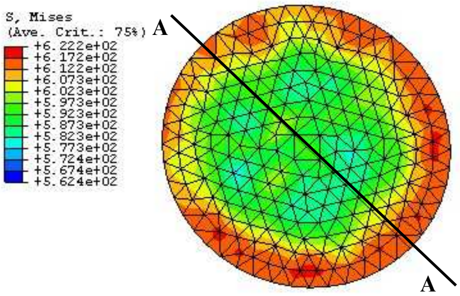	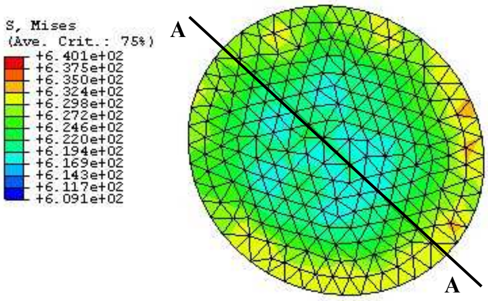
at position C	
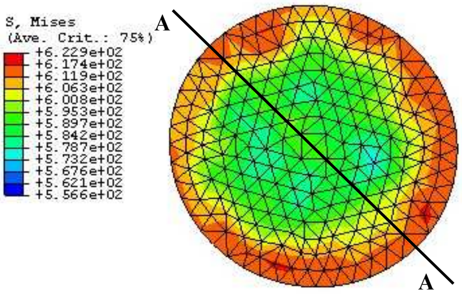	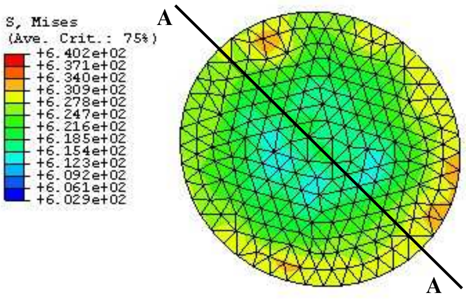
(b) SMG profiles at cross section A-A	
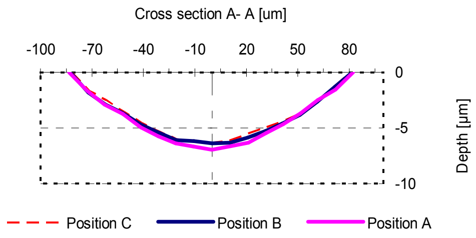	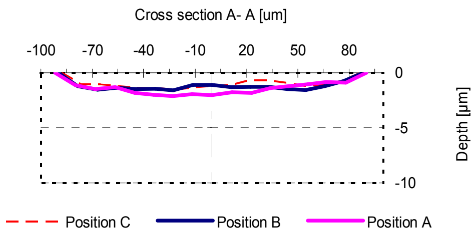

Table 3.5: Shape of ESMG with initial depth of 5µm at 3 different positions (A, B and C) resulting from two levels of ring height reduction; (a) top view and (c) ESMGs profiles at cross section A-A

<table>
<tr><th>At 4% ring height reduction</th><th>At 11% ring height reduction</th></tr>
<tr><td colspan="2">(a) Top View</td></tr>
<tr><td colspan="2">at position A</td></tr>
<tr><td>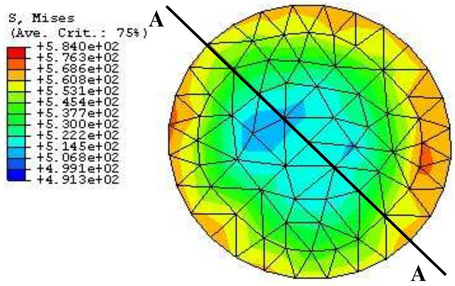
</td><td>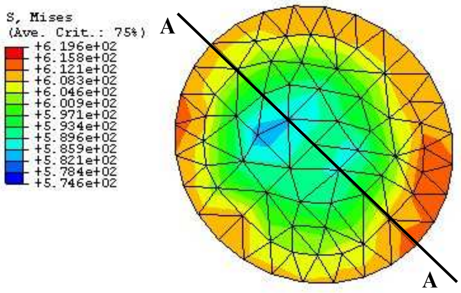
</td></tr>
<tr><td colspan="2">at position B</td></tr>
<tr><td>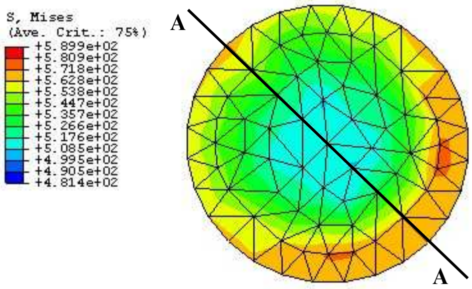
</td><td>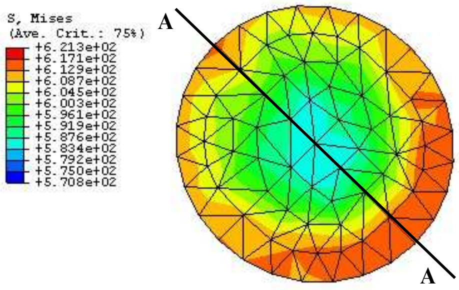
</td></tr>
<tr><td colspan="2">at position C</td></tr>
<tr><td>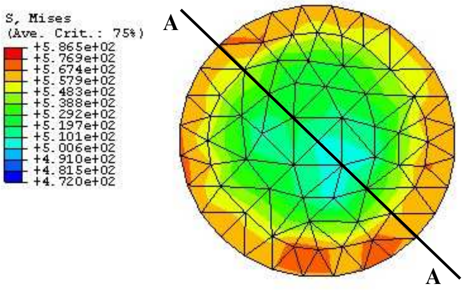
</td><td>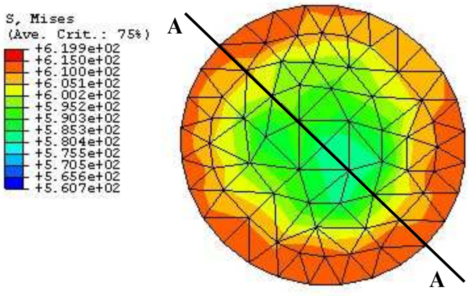
</td></tr>
<tr><td colspan="2">(b) SMG profiles at cross section A-A</td></tr>
<tr><td>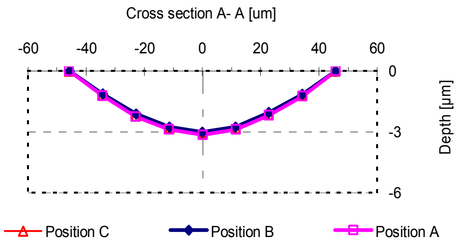
</td><td>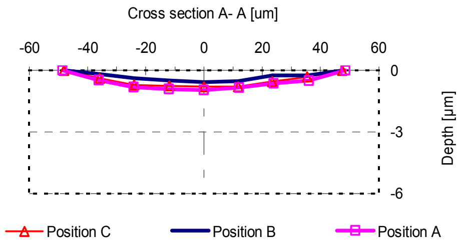
</td></tr>
</table>

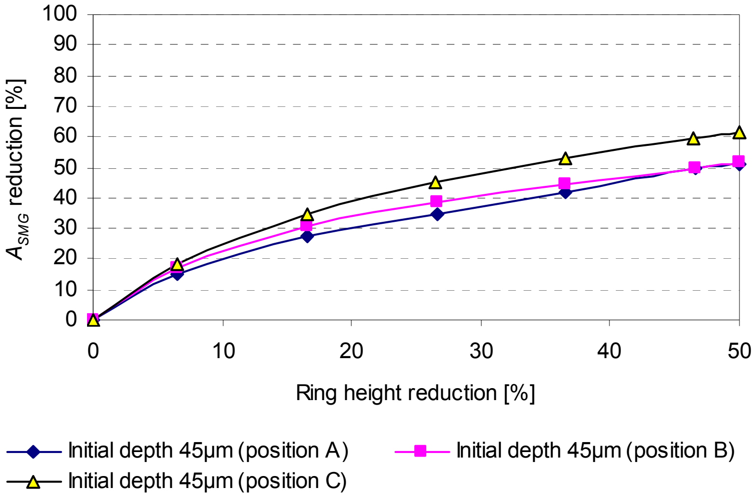

Figure 3.26: A_{ESMG} reduction at different ESMGs positions with initial depth of 45μm

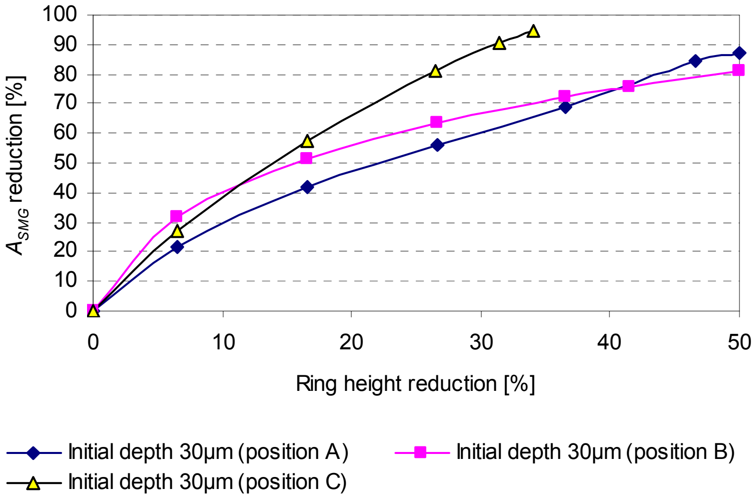

Figure 3.27: A_{ESMG} reduction at different ESMGs positions with an initial depth of 30μm

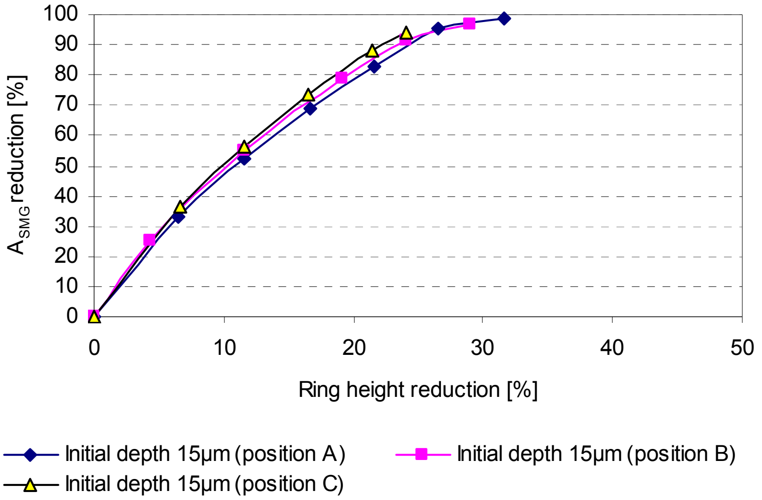

Figure 3.28: A_{ESMG} reduction at different ESMGs positions with an initial depth of 15µm

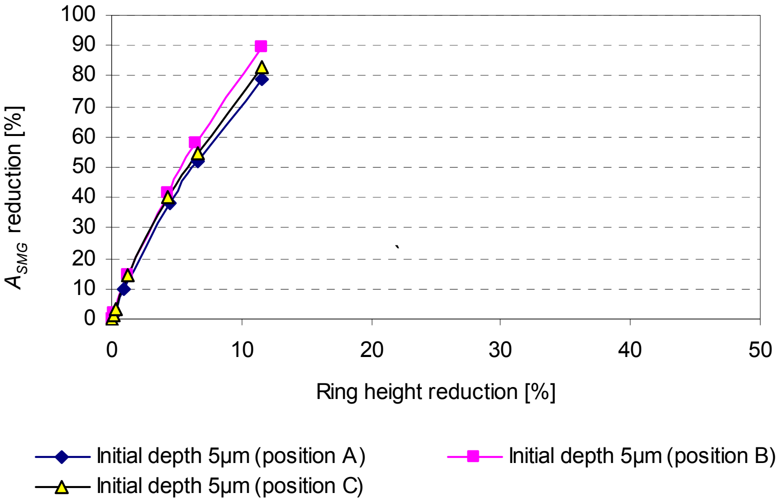

Figure 3.29: A_{ESMG} reduction at different ESMGs positions with an initial depth of 5µm

3.4 Summary

In order to understand dimensional changes of the ESMGs present on the workpiece surface subjected to compression, a 3D FE model has been developed using a special procedure involving a sub-modelling technique to obtain an accurate solution. The deformation behaviours of ESMGs with different initial geometries and dimensions have been analysed. The results obtained are summarized below:

a) The surface area closer to the edge of a conical ESMG is found to be the first surface that touches the upper die and it is then followed by the surface closer to the centre.

b) The change of the depth around the centre of the bottom surface of a cylindrical ESMG is much greater than for the surface near the edge. The cylindrical ESMG sidewall acts as a rigid surface that does not easily collapse. At the end of the deformation process, the cylindrical ESMG turns to a toroidal shape, which may result in surface defects.

c) It has been confirmed that a spherical ESMG with the depth approximately of 15μm (with opening angle $\varphi = 20°$) give uniform surface deformation throughout the material deformation, which is able to store and distribute lubricant during the compression of the ring for up to 50% reduction.

d) ESMGs close to the outer edge retain better their circular shape and also give higher A_{ESMG} reduction rates than ESMGs close to the middle and the inner edge of the ring specimen.

Chapter 4

Experimental Trials on Reducing Friction in Metal Forming Processes Using ESMGs

Glossary

σ : true stress

R_a : surface roughness

ID : ring specimen initial inner diameter

μ : coefficient of friction

h : ring specimen height

F_T : total extrusion force

r_a : reduction in cross section area

F_C : friction force at billet and chamber interface

F_d : friction force at billet and die interface

F_{dd} : deformation force of the billet in the die

τ : friction shear stress

D_o : chamber diameter

d_o : initial billet diameter

D_1 : diameter of an extruded billet

α : die opening angle

h_e : exit land aperture height

L : billet length in the chamber

S_p : area density of ESMGs

A_d : ESMG area

A_s : surface area textured with ESMGs

n_d : number of micro-ESMGs in the surface area A_s

$Depth$: ESMG depth

4.1 Introduction

This chapter presents the experimental trials of reducing friction in metal forming using ESMGs. It begins by describing the apparatus, materials and procedures of both testing methods i.e. ring test and forward extrusion test. In the next section, the evaluation trials results, with a view to defining the key characteristics of ESMGs that influence the reduction of interfacial friction, are discussed. Lastly, recommendations on the most preferred ESMG parameters are also presented.

4.2 Texturing Methods

The surface of the ring specimens, billet specimens and dies were textured using a bespoke indentation texturing system [44]. In this system, a piezoelectric actuator drives the indenter. The maximum working stroke of the indenter is 130µm that provides the maximum force of 4.3kN. The system is mounted on a 3-axis CNC machine. Present configuration, including an added rotary stage, enables structuring flat and cylindrical surfaces. The rate at which indentations may be produced is up to 50 indentations per second. The auto-compensating feature and associated control system enable the production of ESMGs with depth in a range 0.5 - 50µm. The shape of an individual ESMG depends on the shape of the indenter. For the purpose of this research a conical diamond indenter with a tip radius of 0.2mm was used; therefore ESMGs were spherical ESMGs with opening angle, φ, from 10° to 25°. **Figure 4.1** shows the geometry of the indentation tool. The use of a diamond indenter allows production of ESMGs on hard (>60HRC) surfaces. The photograph of the ESMGs structuring machine used to structure the polished ring specimens is shown in **Figure 4.2**. **Figure 4.3** shows the photograph of the system used in the structuring process of the billet specimens.

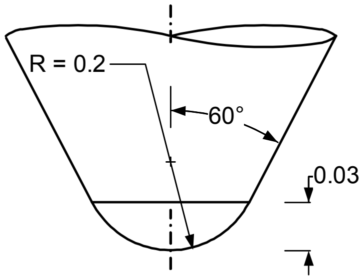

Figure 4.1: Indentation tool geometry

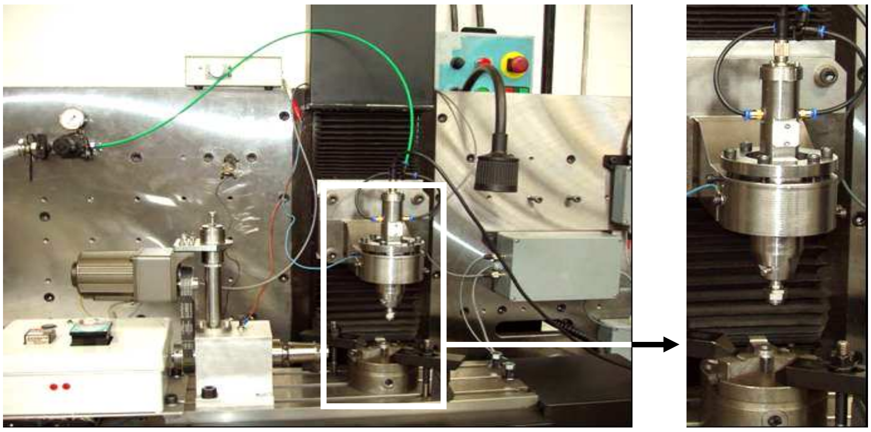

(a) **(b)**

Figure 4.2: Photograph of the ESMG structuring machine used to texture the polished ring specimens; (a) the whole machine and (b) magnification of the indentation tool and the ring specimen

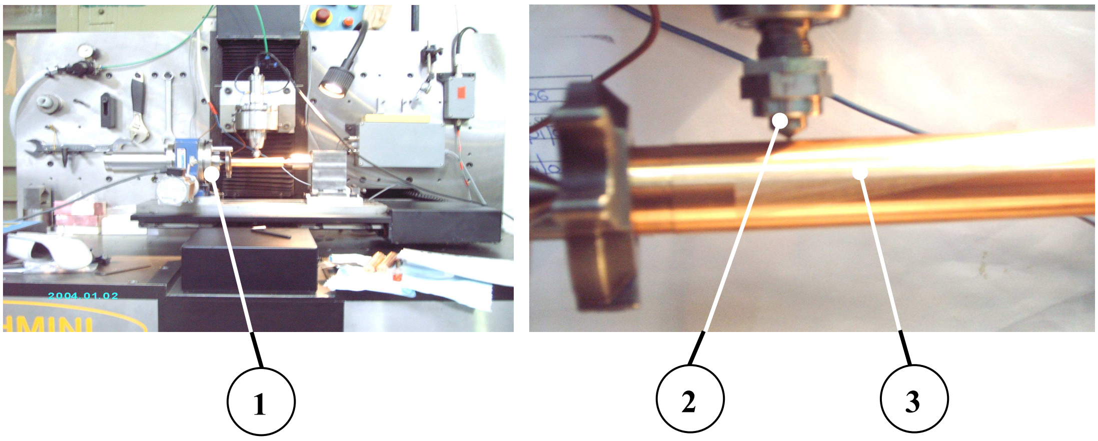

Note:

1) rotary stage
2) indentation tool (its tip is made of diamond),
3) copper billet.

Figure 4.3: Photograph of the texturing system used in the structuring process of the billet specimens; (a) the whole machine and (b) magnification of the indentation tool and the billet

After the texturing process, the specimens and die surfaces were cleaned using a white spirit solution to remove grease and dirt. Subsequently, the ESMG diameter and depth were measured using a non-contact white light interferometer, the Veeco NT 1000 system. An example of the ESMG characteristics measured using the Veeco NT 1000 system is shown in **Figure 4.4**. **Figure 4.4 (a)** shows a 3D image, **Figure 4.4 (b)** shows a 2D image, **Figure 4.4 (c)** shows the ESMG profile across A-A that gives the value of diameter d_1 = 146.4µm and *depth* = 12µm, and **Figure 4.4 (d)** shows the ESMG profile across B-B that gives the value of diameter d_2 = 180µm.

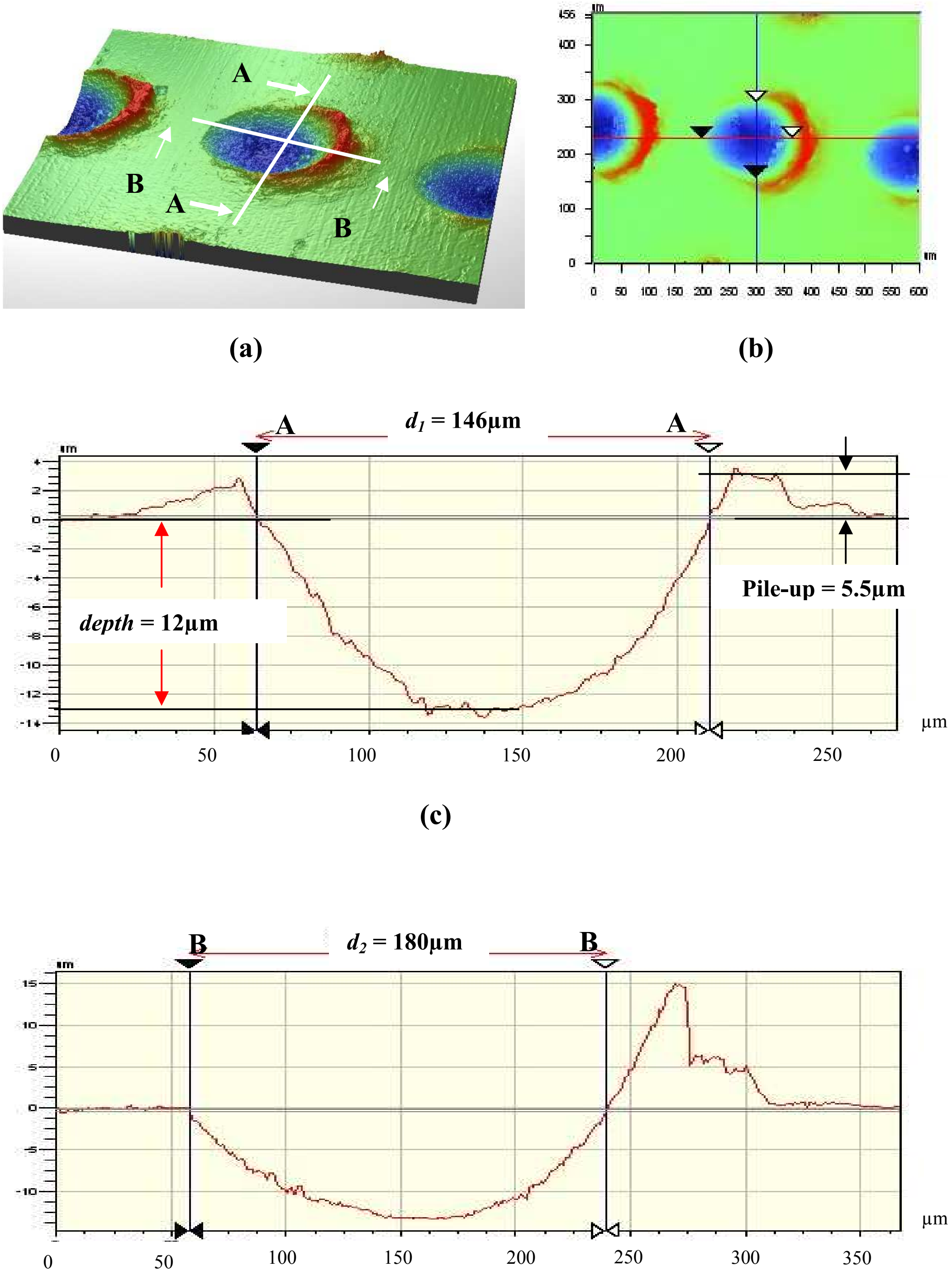
(a) (b) (c) (d)

Figure 4.4: Example of an ESMG image obtained using the Veeco NT 1000 system; (a) 3D image, (b) 2D image, (c) ESMG profile across A-A (diameter, $d_1 = 146\mu m$ and *depth* = 12µm,) and (d) ESMG profile across B-B (diameter, $d_2 = 180\mu m$)

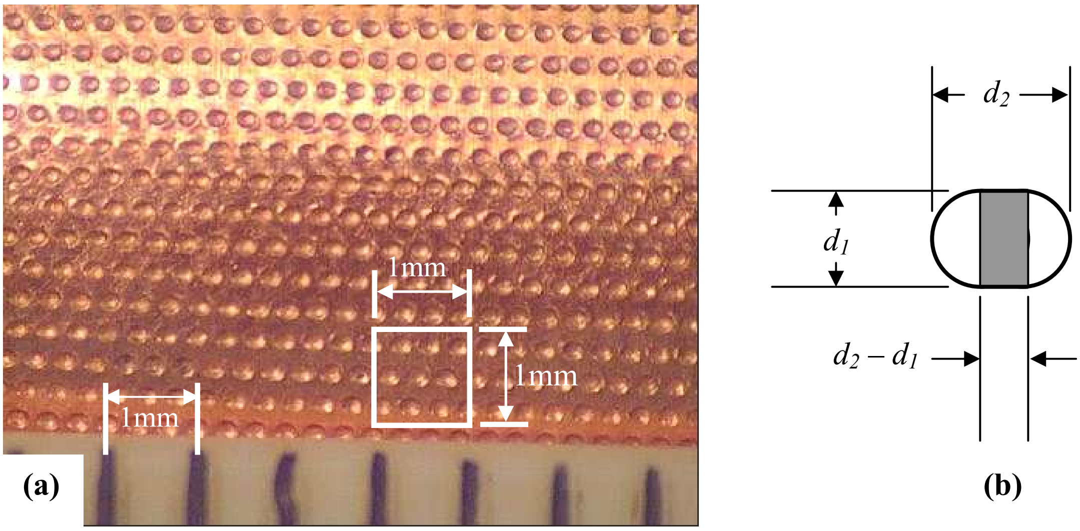

Figure 4.5: (a) Example of ESMGs textured on the billet surface - approximately 9 ESMG in the marked area of 1mm^2 and (b) ESMG shape and dimensions

The ESMG area density S_p is estimated as:

$$S_p = \left(\frac{A_d}{A_s} n_d\right) 100\% \;\ldots\ldots\ldots\ldots\ldots\ldots\ldots\ldots\ldots\ldots\ldots\ldots..(1)$$

where, S_p is ESMG area density, A_d is ESMG area, A_s is surface area textured with ESMGs, and n_d is number of ESMGs in the billet surface area A_d

The number of ESMGs in the surface area A_d was estimated from a photo obtained using a digital camera with x50 magnification. **Figure 4.5** shows an example of the photo used to estimate S_p. As shown in **Figure 4.5**, approximately 9 ESMGs were found in each area of 1mm^2. Due to the ESMGs are not being exactly round in shape (see **Figure 4.5 (b)**), the value of A_d was estimated as:

$$A_d = \left(\pi \frac{d_1^2}{4} \right) + \left(d_1\right)\left(d_2 - d_1\right) \dots\dots\dots\dots\dots\dots\dots\dots (2)$$

4.3 Apparatus, Materials and Procedures

4.3.1 Ring test

Figure 4.6 shows a drawing and a photograph of the tool set that was used to compress the ring specimens. The upper and lower compression dies are attached to rigid upper and base plates guided by the guiding columns (see **Figure 4.6**, note 1, 2 and 6). Due to this design, the platen surfaces of the dies are maintained parallel during the compression process. A 1000kN press machine manufactured by ESH Testing was used to compress the ring specimens between the upper and lower compression die by applying force on the upper plate with controlled ram speed of 0.5mm/s.

The compression dies (see **Figure 4.6** note 3 and 4), which had outer diameter of 30 mm, were made from tool steel (Vanadis 6) and hardened to 62HRC. The platens of the dies were ground and polished to R_a = 0.05µm prior to the incorporation of ESMGs. **Figure 4.7** shows a photograph of polished and textured die surfaces.

The ring specimens used in the study were made of a mild steel type CK15 with the composition of 0.12~0.18% Carbon, 0.4% Silicon, 0.6~0.9% Manganese, 0.035% Phosphorus and 0.035% Sulphur. The mechanical properties of the steel are shown in **Table E.1** in Appendix E. The work hardening properties of the specimen material used in the simulations were defined by the formula $\sigma = 870(0.004 + \varepsilon)^{0.2}$ that was derived experimentally in a compression test using Rastegaev [163, 164] type specimens as explained in Appendix E.

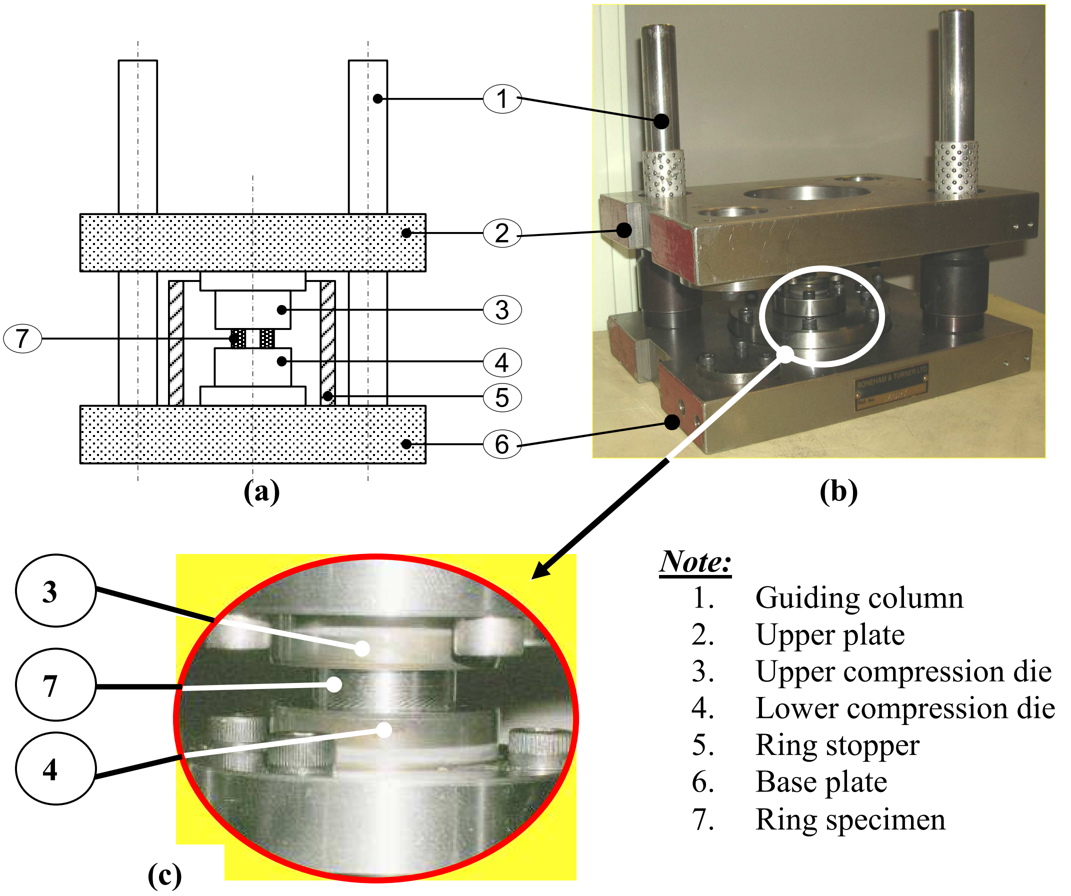

Note:
1. Guiding column
2. Upper plate
3. Upper compression die
4. Lower compression die
5. Ring stopper
6. Base plate
7. Ring specimen

Figure 4.6: Compression tool set; (a) schematic drawing, (b) photograph and (c) the ring specimen is placed between the upper and lower dies (magnification of the photograph in (b))

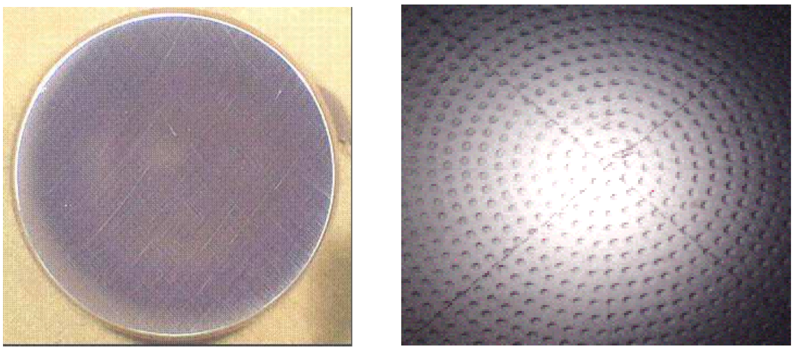
(a) (b)

Figure 4.7: Compression die surface; (a) polished and (b) textured with ESMGs

Figure 4.8: Photograph of ring specimen with textured surface

The ring specimens had the dimensional ratio of 6:3:2 (outer diameter : internal diameter : height) and the outer diameter of 18 mm. This dimensional ratio was used because it gives high sensitivity when measuring friction change and was recommended by many researchers [131, 165, 166]. In addition, as mentioned in

[131, 165, 166], this dimensional ration has become a practical standard. All specimen surfaces were ground to $R_a = 0.5$ μm prior to the incorporation of ESMGs with different depths and densities. **Figure 4.8** shows an example of a textured specimen.

To obtain an extensive and clear understanding of the influence of ESMGs on interfacial friction at the specimen-die interface during compression various ESMG parameters, as shown in **Table 4.1**, were tested. The textured compression dies were used to compress the plain ring specimens, whereas plain compression dies were used to compress the ring specimens textured with various ESMGs. The ESMGs' density was defined as a ratio of the total area of ESMGs to the total surface specimen area, expressed as a percentage (see section 4.2 for details).

As shown in **Table 4.1**, an identification code (X/Y/Z) was used to differentiate the test conditions, where:

a) X represents the texturing code i.e. S is for ESMGs textured on the specimens' surfaces and T for ESMGs textured on the compression dies' surfaces
b) Y represents the ESMGs' initial depth, and
c) Z represents the ESMGs' initial density, S_p.

Table 4.1: Parameters of ESMGs used in the ring test

Identification code (X/Y/Z) *where :* **X** : *Texturing code* **Y** : *Depth [µm]* **Z** : *Density [%]*	**Experimental Conditions**			
	Depth [µm]	**Density [%]**	**Lubrication material**	**Texturing code** ***Note:*** S : *ESMGs textured on specimens* T : *ESMGs textured on tool*
T/1.5/10	1.5	10	MoS_2	T
T/1.5/23	1.5	23		T
S/5/10	5	10		S
S/5/10	5	20		S
S/5/10	5	40		S
S/3/8	3	8	Machine oil	S
S/3/30	3	30		S
S/9/22	9	22		S
S/9/26	9	26		S
S/9/30	9	30		S
S/9/68	9	68		S
S/9/86	9	86		S
S/13/23	13	23		S
S/13/25	13	25		S
S/13/37	13	37		S
S/13/64	13	64		S
S/13/87	13	87		S
S/15/29	15	29		S
S/15/30	15	30		S
S/15/43	15	43		S
S/15/37	15	37		S
S/15/40	15	40		S

As shown in **Table 4.1**, for the first two test series, plain ring specimens lubricated with MoS_2 were compressed using two different sets of compression dies, i.e. T/1.5/10 and T/1.5/20; whereas for the following test series, the specimens textured with ESMG characteristics of S/5/10, S/5/20 and S/5/40, lubricated with MoS_2, were compressed using plain compression dies. For the rest of the test series, the specimens textured with various ESMG characteristics and lubricated with ordinary machine oil, were all compressed using plain compression dies.

For each test, the specimens were subjected to a height reduction ranging from 10% to 50%. The method proposed by Hartley at el [143] was used for measuring the inner diameter *ID* of the ring specimens (see Chapter 2, section 2.3.2). The ring height, *h,* was measured using a micrometer with an accuracy of 0.01 mm, so that the calculated *IDs* resulted in an error of 0.6%, which was considered sufficient for the purpose of the ring test.

4.3.2 Forward extrusion test

A photograph of the extrusion tool set used in the forward extrusion trials, is shown in **Figure 4.9 (a)** and its schematic illustration is shown in **Figure 4.9 (b)**. The punch and die were made from Impax Supreme steel hardened to the hardness of 60-62HRC. The die's opening angle α was 30° and the exit land aperture of the die h_e was 1mm. The extrusion process was performed using an 89,000 pounds (395.9kN) hydraulic press machine with the ram speed of 2.5 mm/s and stopped when the ram reached 75mm displacement. The force versus ram displacement data of each billet was recorded using a Lab-View data acquisition system. **Figure 4.10** shows a photo of the 89,000 pounds hydraulic press machine together with the extrusion tool set.

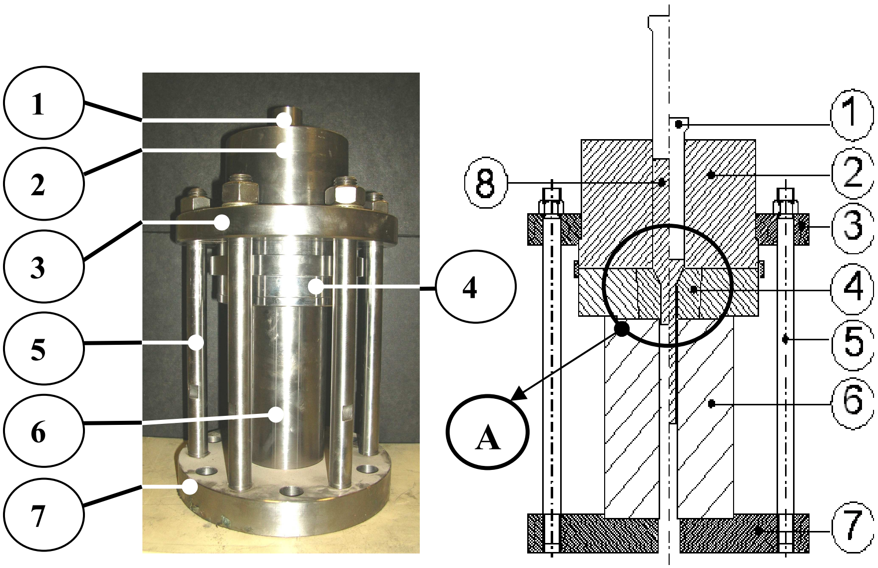

(a) **(b)**

Note:
(1) Punch, (2) chamber, (3) clamping ring, (4) die (conical shape), (5) column, (6) support, (7) base plate and (8) billet

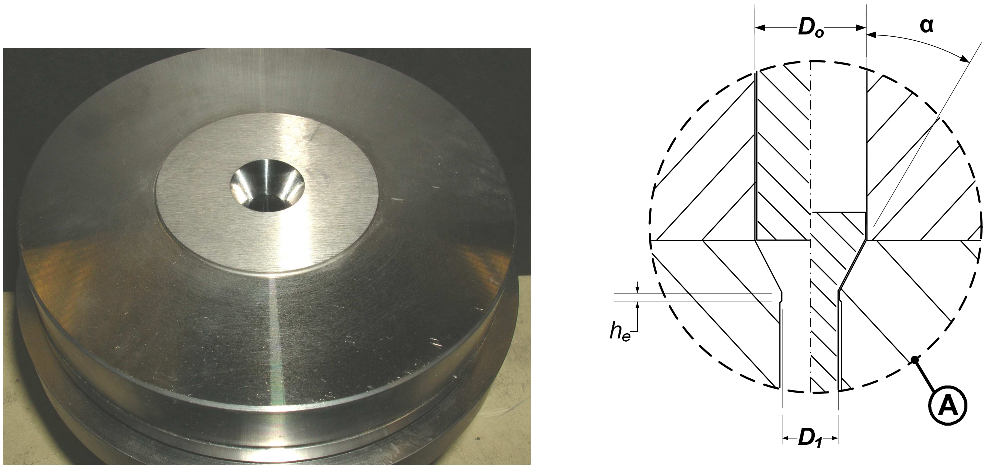

(c) **(d)**

Figure 4.9: Extrusion tool set used in the forward extrusion test; (a) photograph, (b) schematic diagram, (c) photograph of the conical shape die and (d) magnification of the area marked with **A** in (b), i.e.: $D_o = 20\text{mm}$, $\alpha = 30°$, $h_e = 1\text{mm}$

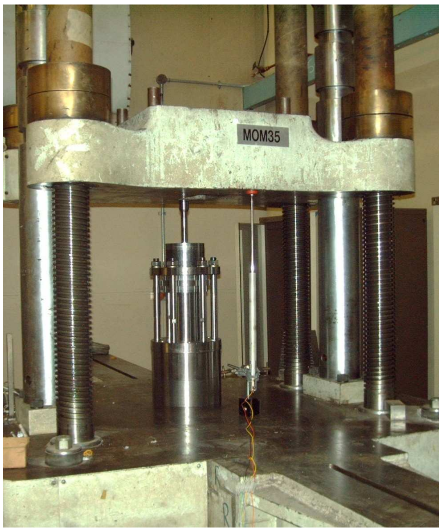

(a)

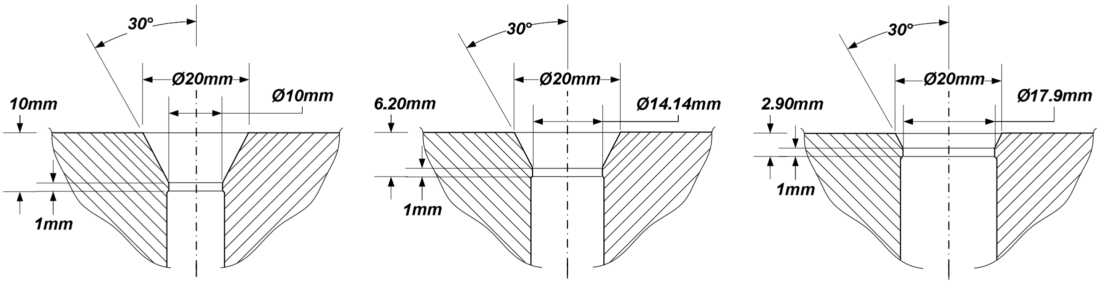

75% reduction **50% reduction** **20% reduction**

(b)

Figure 4.10: (a) Photograph of the extrusion tool set placed on the 89,000 pounds (395.9kN) hydraulic press machine and (b) drawings of the conical die with three different dimensions

The annealed copper bars were then machined into the required billet dimensions (i.e. length = 85mm and diameter = 19.95mm) as shown in **Figure 4.11**. Afterward, the surfaces of the plain billets were textured with various prescriptions of Engineered Surface Micro-Geometries (ESMGs) using a specially designed ESMG texturing system (see section 4.2). The density of ESMGs was defined as a ratio of the total area of ESMGs to the total surface specimen area, expressed as a percentage (see section 4.2 for details).

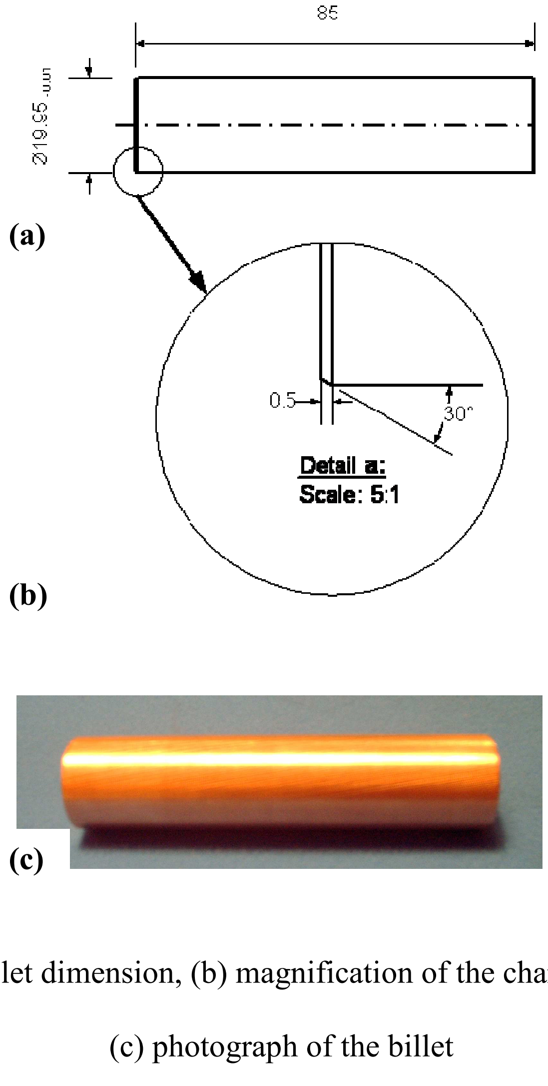

Figure 4.11: (a) Billet dimension, (b) magnification of the chamfer of the billet and (c) photograph of the billet

To obtain a clear picture of the influence of ESMGs under various extrusion pressures, three series of tests were performed; i.e.: the first was an extrusion test at a reduction of 20%, the second was at a reduction of 50% and the last was at a reduction of 75%. **Table 4.2** lists the test series with different test conditions. These three series of experiments were performed using three different dies as shown in **Figure 4.10 (b)**.

A plain billet and numerous textured billets with various prescriptions of ESMGs were extruded in every series of the experiment, as listed in **Table 4.2.** The force-displacement curve of the plain billet was considered as a reference for comparison. A reference code of (d1/d2/depth/pile-up/density) is used to represent the experimental parameters i.e. d1 corresponds to d_1, d2 to d_2, depth to ESMGs' depth, pile-up to ESMGs' pile-up height, and density to the ESMGs' area density, S_p.

In every extrusion operation, the billets, chamber wall, die and punch were cleaned using a white spirit solution to remove any grease and dirt before being lubricated with either: (1) ordinary machine oil or (2) a mixture of fatty grease (Tallow) and Zinc Stearate as stated in **Table 4.2**.

The initial results of several tests show that the assembly of the extrusion tool set was critical. Mis-positioning of the chamber and die resulted in invalid force-displacement curves. Therefore, to overcome this problem, the assembly process was carefully performed to ensure that the position of the chamber and die was along the central line.

In order to define the effect of the ESMGs on interfacial friction at the billet/chamber and billet/die interface during the extrusion process, the force-displacement curves of the textured and plain billets were compared by superimposing the curves in the same graph plot. From such graph, the effect of ESMGs on friction can be represented by different levels of the extrusion force and the slopes of the force-displacement curves at the steady state stage.

Table 4.2: Different prescriptions of ESMGs textured on the billet surface

Reference number: d_1/d_2/depth/pile-up/density (Lubricant)	**Reduction**	**Lubricant**	ESMG parameters				
			d_1 [μm]	*d_2 [μm]*	*depth [μm]*	*pile-up [μm]*	*density [%]*
plain	**20%**	Tallow + Zinc Saterate (TZ)	plain billet (without SMGs)				
187/164/12/10/9% (TZ)			187	164	12	10	9
plain (TZ)	**50%**	Tallow + Zinc Saterate (TZ)	plain billet (no micro-dimples)				
219/203/25/6/33%(TZ)			219	203	25	6	13
213/213/26/12/14%(TZ)			213	213	26	12	14
213/210/24/11/27%(TZ)			213	210	24	11	27
plain(MO)	**50%**	machine oil (MO)	plain billet (without SMGs)				
194/178/15/10/10%(MO)			194	178	15	10	10
210/205/24/0/19%(MO)			210	205	24	0 (pile-up has been ground)	9
plain(MO)	**75%**	machine oil (MO)	plain billet (without SMGs)				
130/130/11/12/9%(MO)			130	130	11	12	9
140/140/12/13/10%(MO)			140	140	12	13	10
150/150/15/13/19%(MO)			150	150	15	13	19
292/247/43/26/25%(MO)			292	247	43	26	25
298/234/38/25/26%(MO)			298	234	38	25	26
294/255/40/26/31%(MO)			294	255	40	26	31
218/206/28/22/34%(MO)			218	200	28	22	34
275/252/43/21/39%(MO)			275	252	43	21	39
303/250/44/16/42%(MO)			303	250	44	16	42
314/247/43/12/66%(MO)			314	247	43	12	66

4.4 Results and Discussions

4.4.1 Ring test

The parameters analyzed in the study were the depth and the density of ESMGs, where the influence of these two parameters on the friction coefficient, μ, was the main focus (see **Table 4.1** in section 4.3.1 for the experimental test conditions). The calibration curves that were derived using FE simulations of the ring compression test (see Chapter 3, section 3.2.1.2) were used as a base to determine the value of the coefficient of friction, μ. The reference used for the comparison of the ring test results was the friction present during the compression of the plain ring specimens with the plain dies.

4.4.1.1 The effect of ESMGs textured on the die surface

In order to investigate the influence of ESMGs textured on the die surface, two different compression cases were performed (see **Table 4.1)**, i.e.: 1) compression of plain specimens with textured dies, marked with T/1.5/10 and T/.5/20 and 2) compression of plain specimens with plain dies, marked Plain. In both cases, MoS_2 lubrication material was used. The results of these cases are shown in **Figure 4.12 (a)**. The results show that the textured dies present a higher coefficient of friction μ (approximately between 0.06 and 0.08) as compared with the plain tools (approximately 0.05). The results show that there was no significant friction difference between T/1/5/10 and T/1.5/20. Nevertheless, it is clearly shown that textured dies contributed to an increment of friction after 30% of the ring specimen reduction.

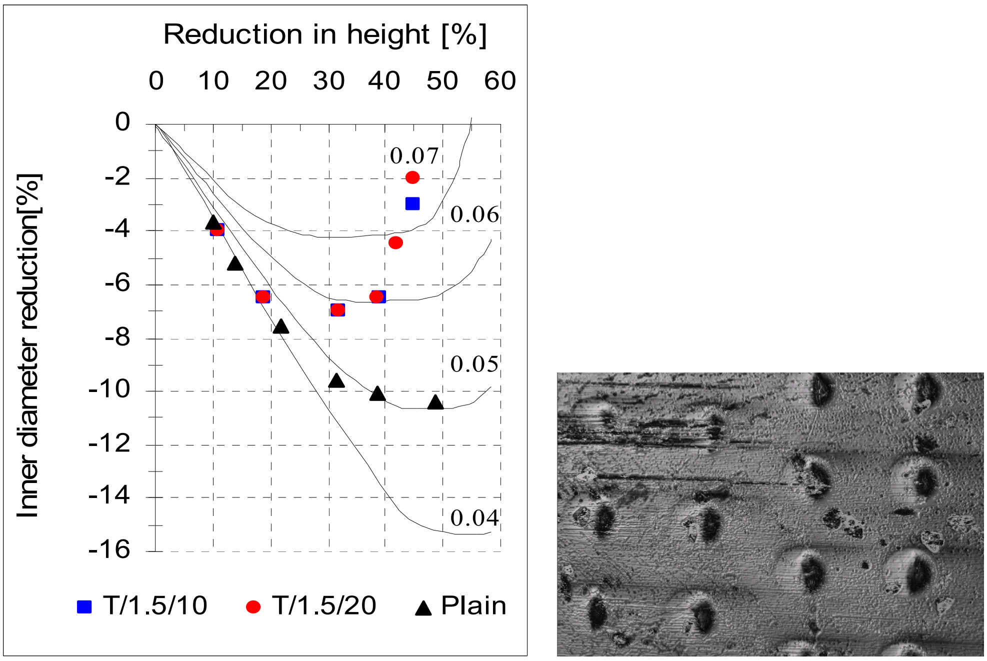

(a) **(b)**

Figure 4.12: (a) Results of the ring test conducted using the textured compression dies (T/1.5/10 and T/1.5/20) to compress the plain specimen and (b) photograph of the plain ring specimen that was compressed using the textured dies

A surface profile photograph of the plain ring specimen that was compressed using the textured dies is shown in **Figure 4.12 (b)**. The photograph is the evidence that the work material has been deformed into the ESMGs' cavities in the die which resulted in a higher resistance to the movement of the ring specimens' surface.

Therefore, it can be concluded that ESMGs textured on the die surface oppose the relative motion between the two sliding surfaces of the specimen and the die, which results in a higher friction coefficient, μ.

4.4.1.2 The effect of ESMGs textured on the ring specimen surface

This section presents the effect of ESMGs textured on the ring specimen surface on friction reduction. Numerous ring specimens textured with different ESMG parameters were compressed using plain dies (see **Table 4.1** in section 4.3.1). Before compression the specimens were lubricated with either MoS_2 or machine oil (MO).

4.4.1.2.1 The effect of ESMG density on the friction reduction

To define the effect of the ESMG density on the reduction of friction coefficient, μ, the test results were compared for ring specimens textured with ESMGs of approximately the same depth but having different density. The first comparison is among the test results of the ring specimens textured with ESMGs of 5µm depth, lubricated with MoS_2, as shown in **Figure 4.13**. This figure shows that at h reduction of 40%, the coefficient of friction μ of Plain and S/5/10 is approximately 0.05. For S/5/20 and S/5/40 it is approximately 0.045, but it increases to nearly 0.05 at h reduction of 50%. Generally, these results show that below h reduction of 40%, the plain ring specimens present higher coefficients of friction, μ, as compared with the textured ring specimens, but at 50% *h* reduction, the Plain, S/5/10 and S/5/40 specimens all present coefficients of friction μ of approximately 0.05, which are indistinguishable from each other.

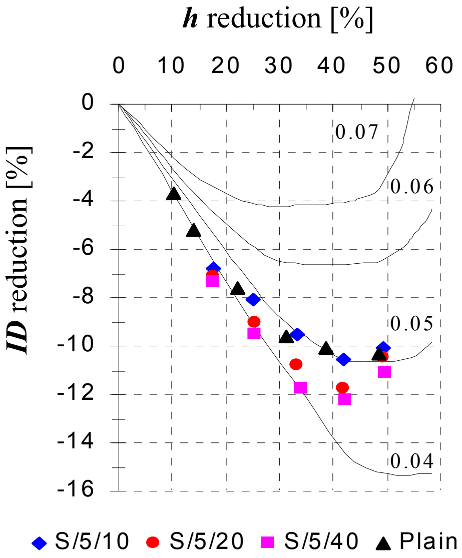

Figure 4.13: Ring test results obtained for textured test specimens with 5μm deep ESMGs, lubricated using MoS_2

Figure 4.14 shows the test results for the plain ring specimen (Plain) and textured ring specimens with ESMGs of 3μm depth and densities of 8% (S/3/8) and 30% (S/3/30) lubricated using machine oil. As shown in the figure, the plain ring and the ring textured with 8% density present the same friction coefficient, i.e. approximately 0.09. At approximately *h* reduction of 30%, the ring textured with ESMG density of 30% presents a lower coefficient of friction (approximately 0.07), but it increases to 0.09 after *h* reduction of 40%, which is approximately the same magnitude with the plain ring.

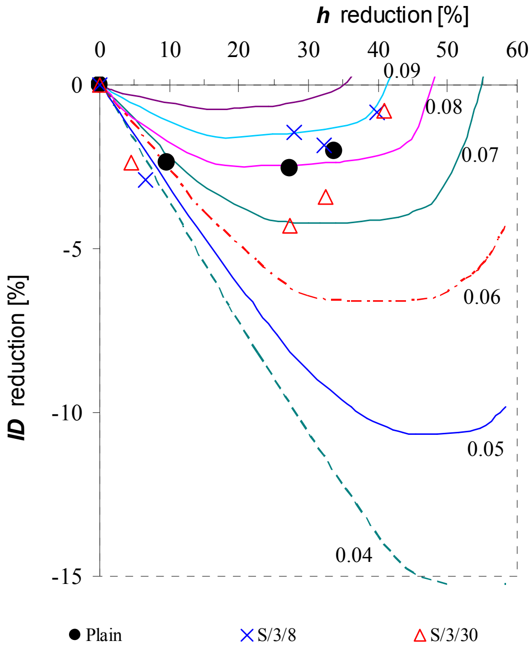

Figure 4.14: Test results for the plain ring specimen (Plain) and the textured ring specimens with ESMGs' depth of 3μm with ESMGs' densities of 8% (S/3/8) and 30% (S/3/30), lubricated with machine oil

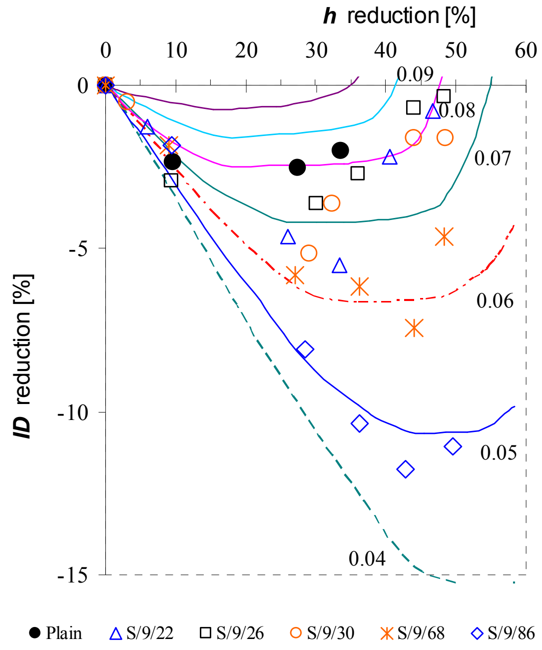

Figure 4.15: Test results for the plain specimen (Plain) and the textured specimens with ESMGs' depth of 9μm with ESMGs' densities of 22% (S/9/22), 26% (S/9/26), 30% (S/9/30), 68% (S/9/68), and 86% (S/9/86), lubricated with machine oil (MO)

The test results comparison of the plain specimen (Plain) and textured specimens with ESMGs of 9μm depth and densities of 22% (S/9/22), 26% (S/9/26), 30% (S/9/30), 68% (S/9/68) and 86% (S/9/86) lubricated with machine oil is shown in **Figure 4.15**. As shown in this figure, at *h* reduction of 30%, the specimens with the densities of 22%, 26% and 30% present a friction coefficient of approximately 0.075, but after *h* reduction of 40%, all of these specimens present an increase in the coefficient of friction μ of up to 0.08. However, the specimen with ESMGs' density of 68% presents a friction coefficient of approximately 0.06 at *h* reduction of 30%, increasing to 0.065 at *h* reduction of 50%. For the highest ESMGs' density (86%), a lower coefficient of friction was presented, maintained, approximately less than 0.05.

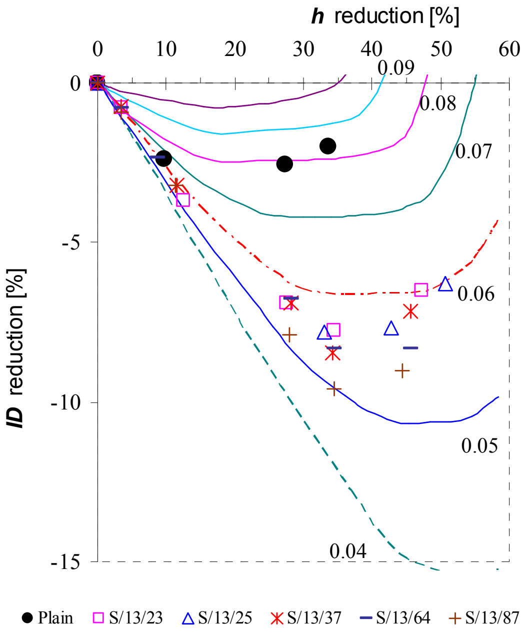

Figure 4.16: Test results for the plain specimen (Plain) and the textured specimens with ESMGs' depth of 13µm with ESMGs' densities of 23% (S/13/23), 25% (S/13/25), 37% (S/13/37), 64% (S/13/64) and 87% (S/13/87), lubricated with machine oil (MO)

The comparison of the test results of the plain specimen (Plain) and the textured specimens with ESMGs of 13µm depth and densities of 23% (S/13/23), 25% (S/13/25), 37% (S/13/37), 64% (S/13/64) and 87% (S/13/87) lubricated with machine oil is shown in **Figure 4.16**. As shown, generally, at the *h* reduction of 30%, all of the textured specimens present a friction coefficient of approximately 0.055, except for the specimen textured with ESMGs with density of 87%, which presents a lower friction coefficient (approximately 0.05). At the *h* reduction of 40%, the specimens with ESMG densities of 23% and 25% both present an increase of friction coefficient up to 0.06. However, the specimens with ESMG densities of 64% and 87% both present an increase of coefficient of friction only up to approximately 0.055.

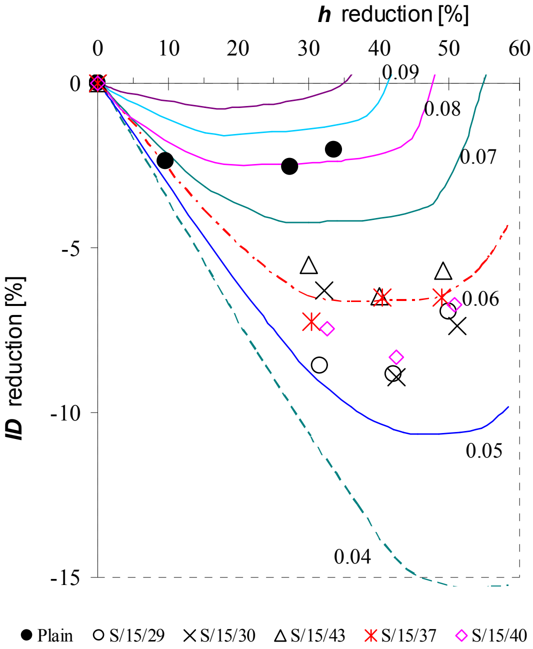

Figure 4.17: Test results for the plain specimen (Plain) and the textured specimens with ESMGs' depth of 15μm with densities of 29% (S/15/29), 30% (S/15/30), 43% (S/15/43), 37% (S/15/37) and 40% (S/15/40), lubricated with machine oil (MO)

Figure 4.17 shows the comparison of the test results of the plain specimen and the specimens textured with ESMGs of 15μm depth and densities of 29% (S/15/29), 30% (S/15/30), 43% (S/15/43), 37% (S/15/37) and 40% (S/15/40). As shown in the figure, the plain specimen presents a higher coefficient of friction μ as compared with the textured specimens. However, the results for the textured specimens are randomly distributed between 0.05 and 0.06 curves. From the test results, it has been found that ESMG density plays an important role in friction reduction, such that ESMGs with higher density present lower coefficient of friction as compared with those with lower density.

4.4.1.2.2 The effect of ESMGs' depth on the friction reduction

To define the effect of the ESMGs' depth on the reduction of the friction coefficient, μ, the test results of various ring specimens textured with ESMGs at approximately the same density, but having different depths, are compared. All of the specimens were compressed using plain compression dies lubricated with machine oil. As shown in **Figure 4.18**, for ESMGs with 30% density, the depths of 3μm and 9μm present higher coefficients of friction, μ as compared with the specimen having ESMGs with a depth of 15μm.

As shown in **Figure 4.19**, with ESMG density of around 25%, ESMGs with a depth of 9μm present a higher coefficient of friction, μ, as compared with the specimens textured with ESMGs with a depth of 13μm. **Figure 4.20** shows that both textured specimens with ESMGs of depths of 13μm and 15μm (density = 37%) present approximately the same friction coefficient.

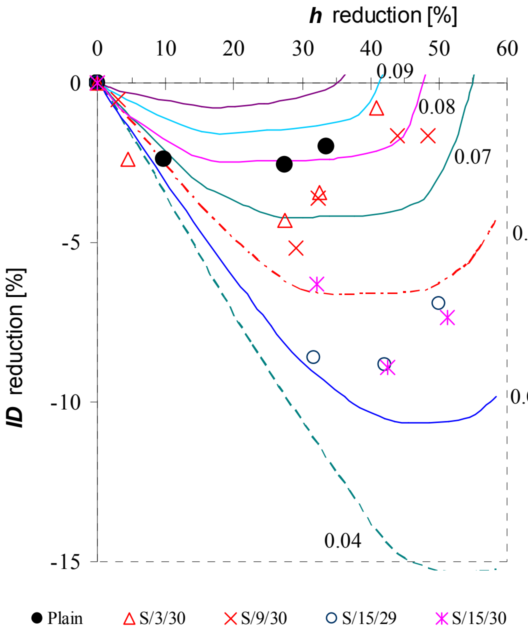

Figure 4.18: Test results of the plain specimen (Plain) and textured specimens with approximately 30% of ESMGs' density with ESMG depths of 3μm (S/3/30), 9μm (S/9/30), (S/9/29) and 15μm (S/9/29), lubricated with machine oil (MO)

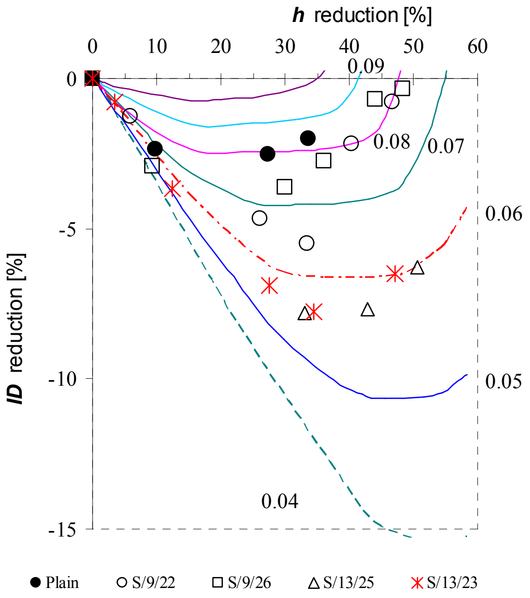

Figure 4.19: Test results of the plain specimen (Plain) and textured specimens with approximately 25% of ESMGs density with ESMG depths of 9μm (S/9/22 and S/9/26) and 13μm (S/13/25 and S/13/23), lubricated with machine oil (MO)

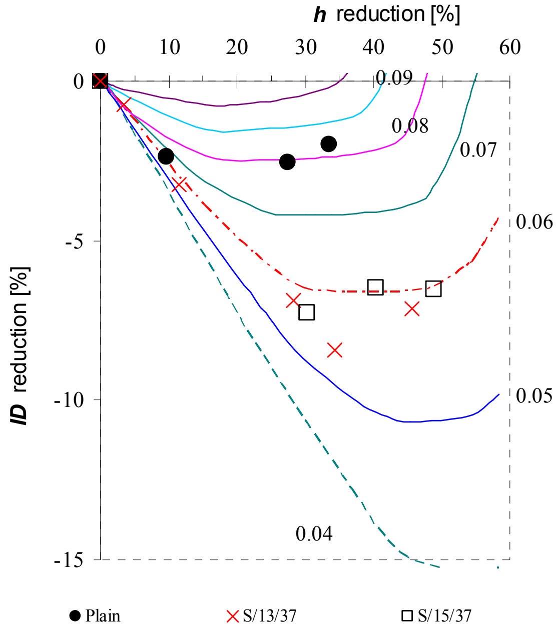

Figure 4.20: Test results of the plain specimen (Plain) and textured specimens with approximately 37% of ESMGs density with ESMG depths of 13μm (S/13/37) and 15μm (S/15/37), lubricated with machine oil (MO)

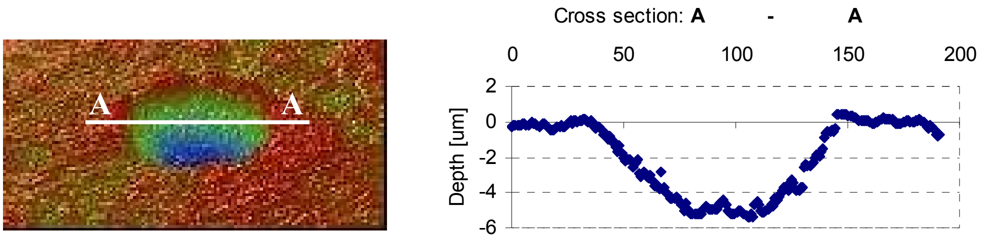

(a) at 6% of *h* reduction

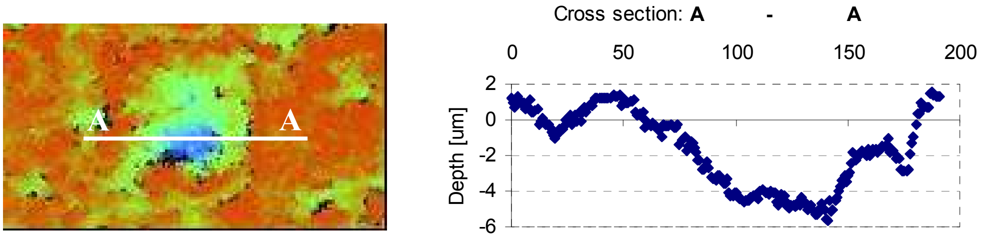

(b) at 26% of *h* reduction

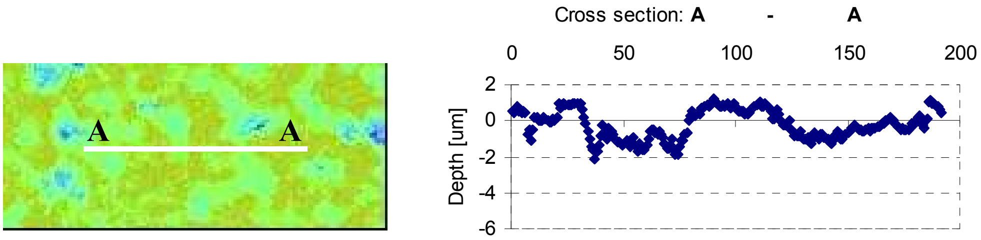

(c) at 33% of *h* reduction

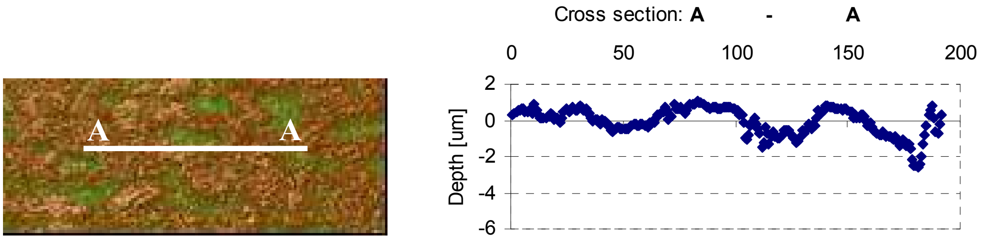

(d) at 40% of *h* reduction

Figure 4.21: 3D image and surface profile of textured specimen with ESMGs' initial depth of 9μm and density of 22% (S/9/22) obtained using Veeco NT 1000 system at various *h* reductions

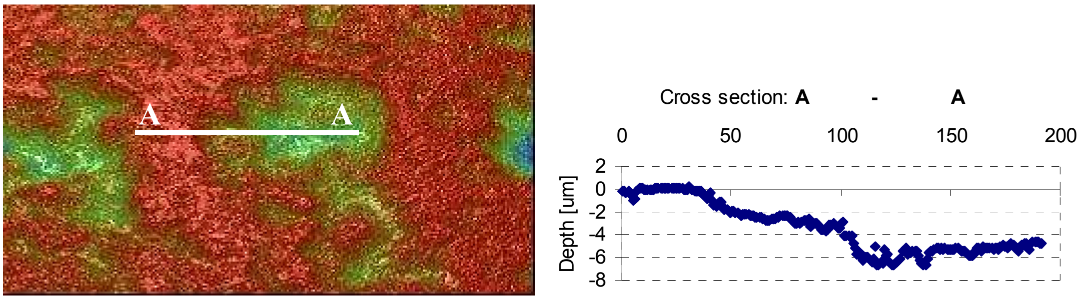

(a) at 33% of *h* reduction

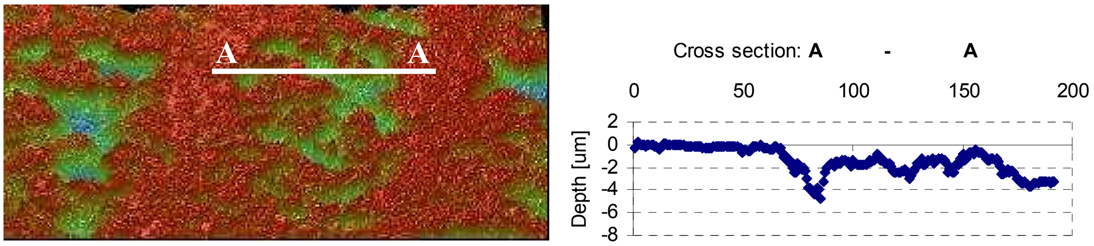

(b) at 40% of *h* reduction

Figure 4.22: 3D image and surface profile of textured specimen with ESMGs' initial depth of 15μm and density of 29% (S/15/29) obtained using Veeco NT 1000 system at various *h* reductions

The collapsing trend of ESMGs at different reduction of ring height, *h*, was observed using a non-contact white light interferometer, the Veeco NT 1000 system (see section 4.2). The 3D image and the surface profile of the textured specimens with ESMGs' initial depth of 9μm and 15μm for various *h* reductions are shown in **Figure 4.21** and **Figure 4.22**, respectively. It can be observed that at 33% of ring specimen height reduction, *h*, the ESMG with the initial depth of 9μm (see **Figure**

4.21) has been found to disappear. Whereas, the ESMG with the initial depth of 15μm is still visible with the depth of approximately 6μm and it disappeared at *h* reduction of 40%. This result shows that shallower ESMGs have been found to collapse faster as compared with the deeper ESMGs.

From these results, the evidence is that ESMGs' depth plays an important role in reducing the coefficient of friction, μ, where deeper ESMGs present lower coefficients of friction. However, considering that no further friction reduction is achieved with ESMGs' depth of more than 13μm (as shown in **Figure 4.20**), therefore it can be concluded that 13μm is the optimum ESMGs depth.

4.4.2 Forward extrusion test

This section presents the results of the extrusion tests that were performed at three different extrusion reductions, r_a, i.e. 20%, 50% and 75%, (see **Table 4.2** in section 4.3.2). The tests were performed using the specially designed test rig that was explained in section 4.3.2. It is also important to note that the diameter of the chamber bore was 20mm, the die opening angle α was 30% and the exit land aperture of the die h_e was 1mm. Billets with the diameter of 19.95mm ± 0.01 and the length of 85mm were used in the test (see **Figure 4.11**).

The results, in the form of force-displacement curves, were superimposed in several graphs to identify the differences of slope, required force and trend, as explained in the **Chapter 2**, section 2.5.3.6. The example of the interpretation method used in this test is explained in section 4.4.2.1. The experimental results, at three different level of r_a are presented in section 4.4.2.3 to section 4.4.2.5. Based on these results, the performance of ESMGs in friction reduction, specifically in forward extrusion, is discussed.

Different slopes of the force-displacement curves at the steady state, which were obtained from the extrusions of billets textured with various ESMG prescriptions and plain billets, were used as a method of identifying the friction change, whereas the slopes of the plain billet curves were used as a reference. The reduction of the slope as compared with the plain billets indicates the reduction of friction at billet/chamber interface. The slope of the curves at steady state was determined using a linear trace line function provided by MS Excel application software.

Another method used was based on the evaluation of total work. The total work was determined by estimating the total area under the force-displacement curve using a trapezoid technique. Subsequently, the total work required to extrude the textured billets was compared with the total work that was required to extrude the plain billets. The reduction of total work requirement of the textured billets, as compared with the plain billets, was used as an indication of the friction reduction that was contributed by the ESMGs. In addition, the deformation of the billet and ESMGs was also observed.

4.4.2.1 Billet and ESMG deformation behaviours

As an example, the photograph of the extruded billet is shown in **Figure 4.23 (a)**, ESMGs in the chamber bore and conical die cavity in **Figure 4.23 (b)** and after leaving the aperture die land in **Figure (c).** Based on the visual observation of the extruded billets, the ESMGs experienced three different deformation behaviours in the billet area in contact with: a) the chamber bore, b) the conical die cavity and c) the die aperture land, as shown in **Figure 4.23**.

4.4.2.1.1 Deformation in the chamber bore

The example of ESMGs in the chamber bore before and after extrusion is shown in **Figure 4.24**. 3D ESMG profiles before and after extrusion are shown in **Figure 4.24 (a)** and **Figure 4.24 (b)** respectively, and a comparison between 2D ESMG profiles before and after extrusion is shown in **Figure 4.24 (c).** As shown in **Figure 4.24 (c)**, there is no significant difference in the ESMG profile (depth, diameter and shape) before and after extrusion, however, it is shown that the ESMG pile-up height is slightly reduced.

As discussed previously, during the chamber filling phase, the billet expands in a radial direction to fill the chamber bore. As the deformation continues, the first area of the billet surface that touches the surface of the chamber bore is ESMG pile-ups. At this point, the billet and chamber bore surfaces are separated by a thin layer of lubricant. With increasing punch displacement, as copper is significantly softer than the chamber material, a normal radial pressure on the billet’s cylindrical surface and the chamber bore is developed. But, as shown in **Figure 4.24 (c)**, by line marked 2, ESMGs in the chamber bore are not significantly deformed during the extrusion process. This is due to the stress state in the chamber bore close to hydrostatic compression. In result, there is an insignificant change of the billet surface contact area and the ESMG profile in the chamber bore.

4.4.2.1.2 Deformation in the conical die cavity

When the billet starts to enter the conical die, the end of the billet deforms, which causes the ESMGs also to deform. As can be seen in **Figure 4.23(b)**, the deformation of the ESMGs becomes more severe as the billet enters the die aperture land area. It can also be observed that the shape of ESMGs was elongated along the flow of the billet material. In addition, baseed on the visual inspection, the ESMGs' depth was smaller and the pile-up flattened.

4.4.2.1.3 Deformation in the die aperture

The most severe ESMG deformation was observed in the die aperture land area, as shown in **Figure 4.25 (a)**. This figure shows the image of the ESMG on the extruded billet surface after leaving the die land area. The surface profile along A-A cross section is shown in **Figure 4.25 (b)**. As shown in this figure, the ESMGs were nearly totally flattened as a result of plastic flow of the material in the conical die cavity.

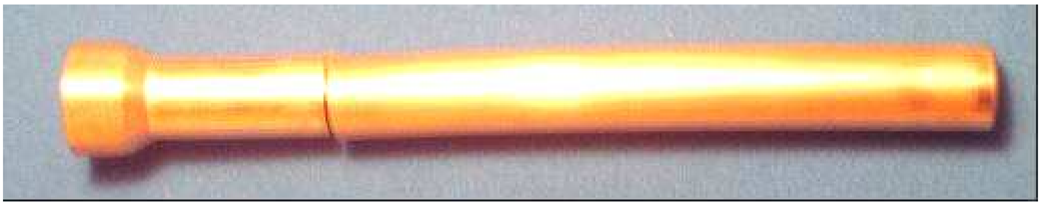

(a)

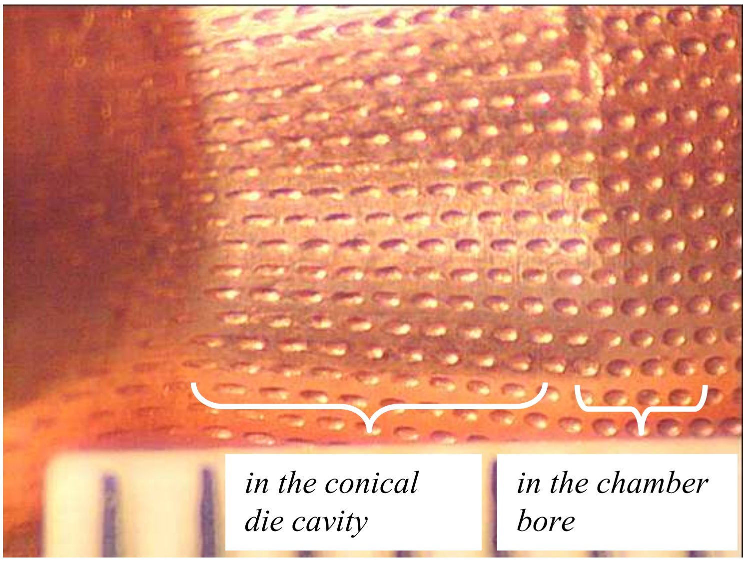

(b)

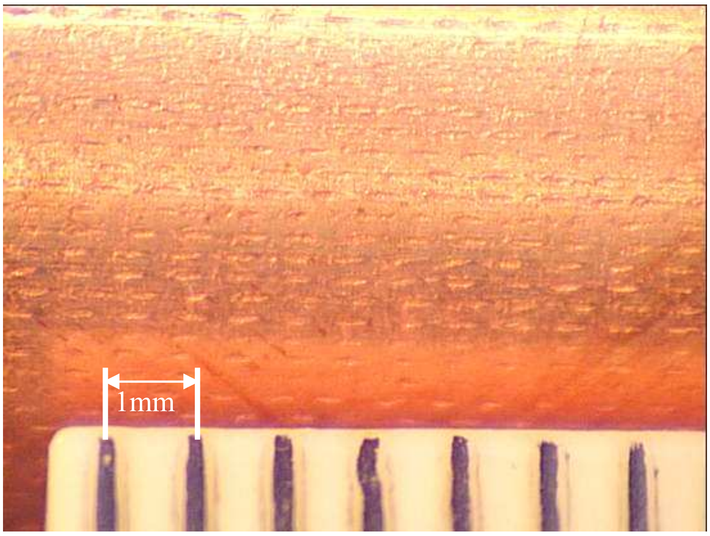

(c)

Figure 4.23: Example of the extruded billet; (a) photograph, (b) ESMGs in the chamber bore and the conical die cavity and (c) ESMGs after leaving the aperture die land

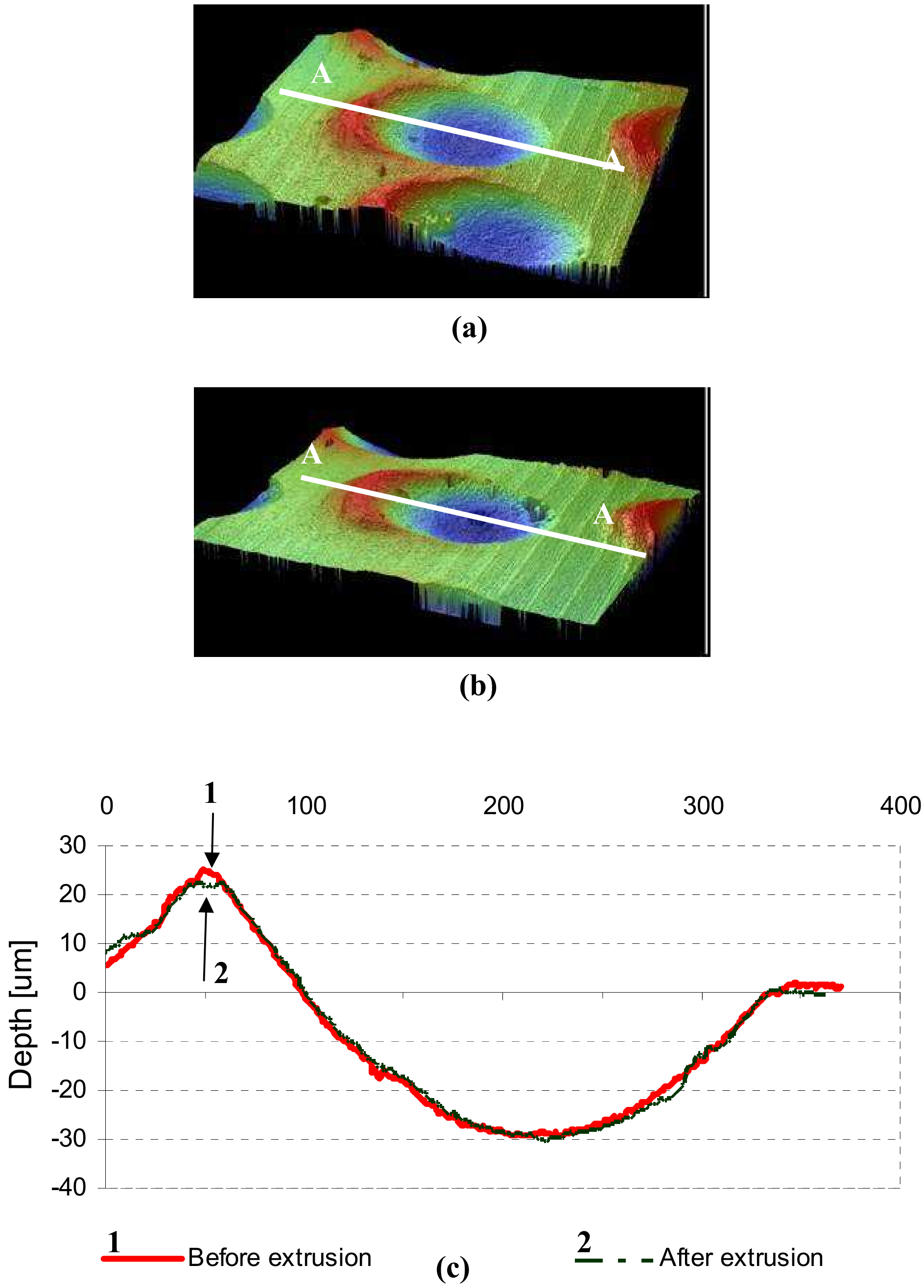

(a)

(b)

(c)

Figure 4.24: ESMG profile before and after extrusion in the chamber bore, obtained using the Veeco NT 1000 system ; (a) 3D image of ESMG before extrusion, (b) 3D image of ESMG after extrusion and (c) 2D surface profiles across A-A section, i.e.: 1) before extrusion and 2) after extrusion

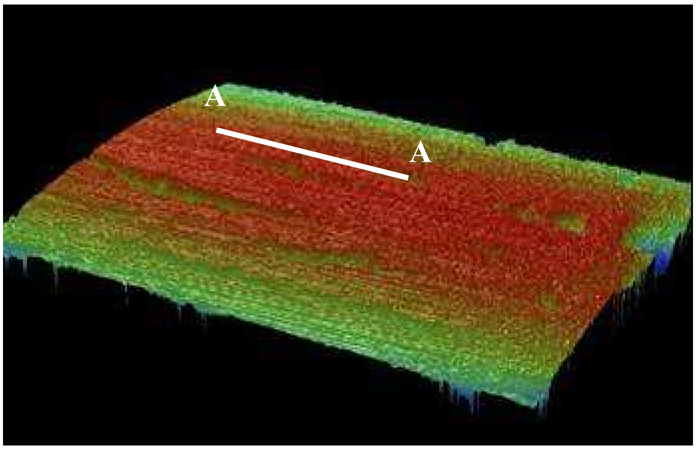

(a)

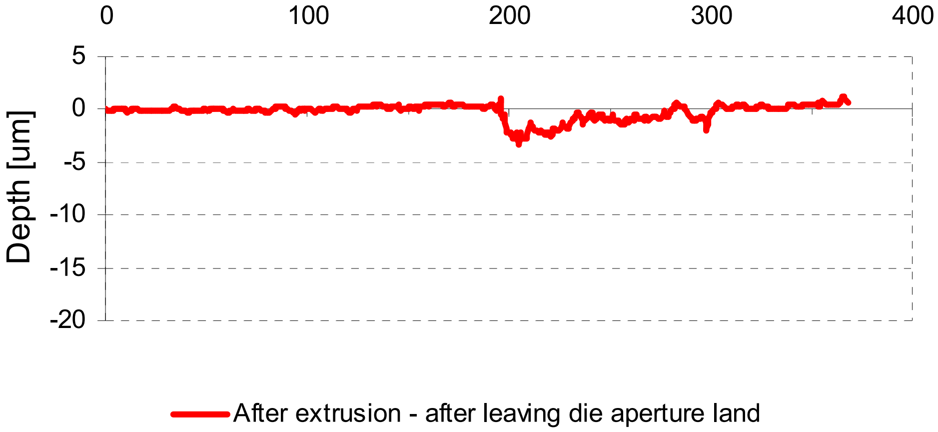

(b)

Figure 4.25: ESMG profile of the extruded billet after leaving the die aperture land, obtained using the Veeco NT 1000 system; (a) 3D image and (b) 2D surface profile across A-A section

4.4.2.2 Interpretation of force-displacement curve trends at different deformation phases

During extrusion, the billet material experienced five different deformation phases. A clear transition between those phases is shown in **Figure 4.26.** In the first phase, as the punch displacement starts to increase at the beginning of extrusion, an elastic deformation starts to develop at Point A and ends at Point B. During this phase, the billet material deforms elastically in a radial direction. With increasing punch displacement, the extrusion force increases linearly.

The second deformation phase is called chamber filling that starts at Point B. With increasing punch displacement, the billet material deforms plastically in a radial direction until it fill the chamber bore at Point C. During the first and the second phase (between Point A and Point C), it is observed that the force displacement curve is similar to that characterising an open die compression process.

The third phase starts at Point C. With increasing punch displacement, as the rigid chamber bore surface restricts the movement of the billet material in the radial direction, the material is forced to move in the axial direction to fill the conical die cavity and the die aperture land. The extrusion force reaches its maximum value at Point D when the billet material has fully filled the conical die cavity and the die aperture land.

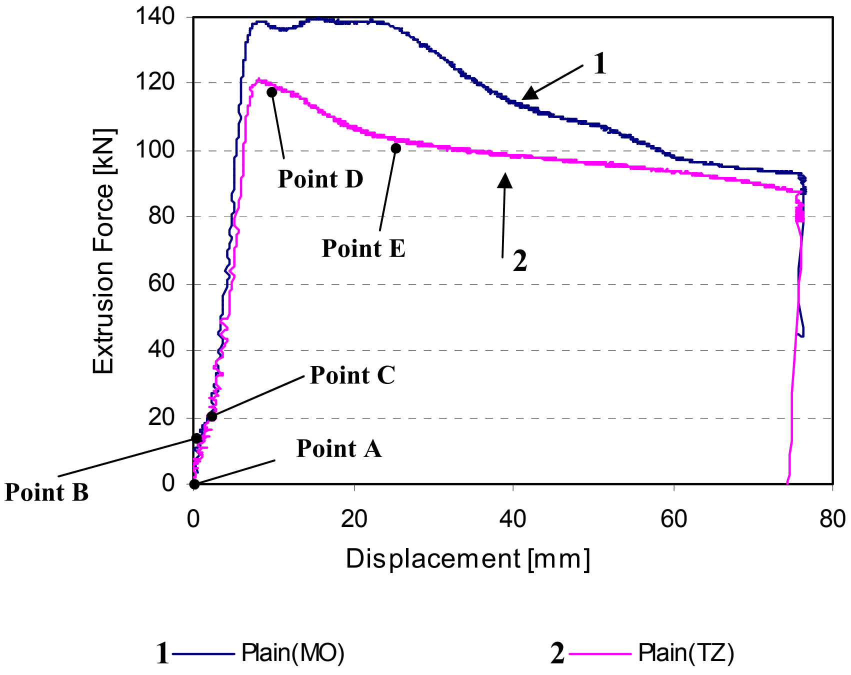

Figure 4.26: Force-displacement curve interpretation used in the extrusion test. The curves were obtained from the extrusion of plain billets down to 50% reduction in cross section area: (1) lubricated with machine oil (MO) and (2) lubricated with Tallow mixed with Zinc Stearate (TZ)

The fourth phase starts at Point D, where the billet material starts to leave the die aperture land. Therefore, it can be observed that the extrusion force decreases non-steadily. This phase ends at Point E when the billet material deformation mode reaches its steady state. But in almost all results, Point E is hard to be determined.

Lastly, the billet material experiences a steady state deformation phase, which starts at Point E. This is the phase where the billet material experiences the actual extrusion process. With increasing punch displacement, at Point E, the billet material starts to flow through the die aperture land and leaves the die with steady deformation. Consistent punch displacement and steady deformation result in constant extrusion conditions, except in the contact area between the billet and the chamber bore surface due to the reduction of L, (Chapter 2 section 2.5.3.6). Therefore, it can be observed in **Figure 4.27** to **Figure 4.36** that the extrusion force decreases with increments of the punch displacement. The results are in close agreement with that stated in equation (7) (see Chapter 2 section 2.5.3.6), where the relationship between the billet length in the chamber and the extrusion force is linear.

4.4.2.3 Extrusion tests at r_a = 20%

In this test, a plain billet (Plain (TZ)) and a billet textured with ESMGs (187/164/12/10/9%(TZ)) were lubricated with Tallow mixed with Zinc Stearate (TZ) lubricant material before being extruded at r_a = 20% (see **Table 4.2**). The force-displacement curves for these billets are shown in **Figure 4.27.** In this figure, the extrusion force required to extrude the plain billet is higher than that for the textured billet. This result was an early indication that ESMGs textured on the billet surface contributed to friction reduction at billet/chamber interface and it motivated the researcher to perform further investigation.

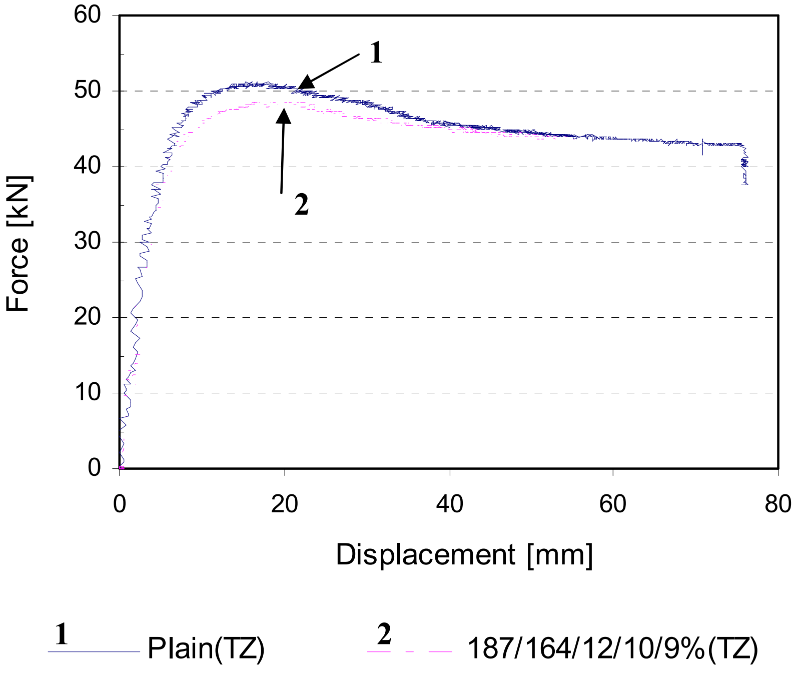

Figure 4.27: Force-displacement curves for (1) Plain (TZ) and (2) textured billets 187/164/12/10/9%(TZ). The billets were extruded with reduction in cross section area, r_a = 20% and lubricated with Tallow mixed with Zinc Stearate (TZ)

As can be seen in **Figure 4.27**, for the extrusion test with r_a = 20%, the peak of the required extrusion force, for the billet with ESMGs described by 187/164/12/10/9%(TZ), was approximately 6% lower then for the plain billet. However, at the steady state, which occurs after punch travel of approximately 40mm, the required extrusion force for the textured billet is only approximately 2% lower than for the plain billet. It has also been observed that, at the steady state, the slope difference between these two curves is insignificant. To obtain more significant results, the tests were performed at higher r_a as discussed in the following section.

4.4.2.4 Extrusion tests at r_a = 50%

As shown in **Table 4.2**, for the extrusion test at r_a = *50%*, the billets were lubricated with either Tallow mixed with Zinc Stearate (TZ) or ordinary machine oil (MO) **Figure 4.28** shows the comparison between the force-displacement curves for plain billet Plain (TZ) and textured billets 219/203/25/6/33%(TZ), 213/213/26/12/14%(TZ) and 213/210/24/11/27%(TZ). As can be observed in this figure, the textured billets, lubricated with TZ, required a lower peak extrusion force as compared with the plain billet. As can also be seen, the steady state of all the curves was reached after about 30mm of punch displacement.

The comparison between the force-displacement curves for the plain billet, Plain (MO) and textured billets, 194/178/15/10/10%(MO and 210/205/24/0/19%(MO) lubricated with MO, is shown in **Figure 4.29**. It can be observed that the plain billet required a higher peak extrusion force than the textured billets. A clear difference in reaching the steady state is also visible. The steady state for the textured billets is reached earlier than for the plain billet; for the textured billets, it is reached after about 40mm of punch displacement, whereas for the plain billet it is reached after approximately 60mm. In terms of the curve slope at the steady state, only an insignificant difference can be observed. Therefore, further tests, with increased reduction in cross section area, r_a, have been carried out as described in the next section.

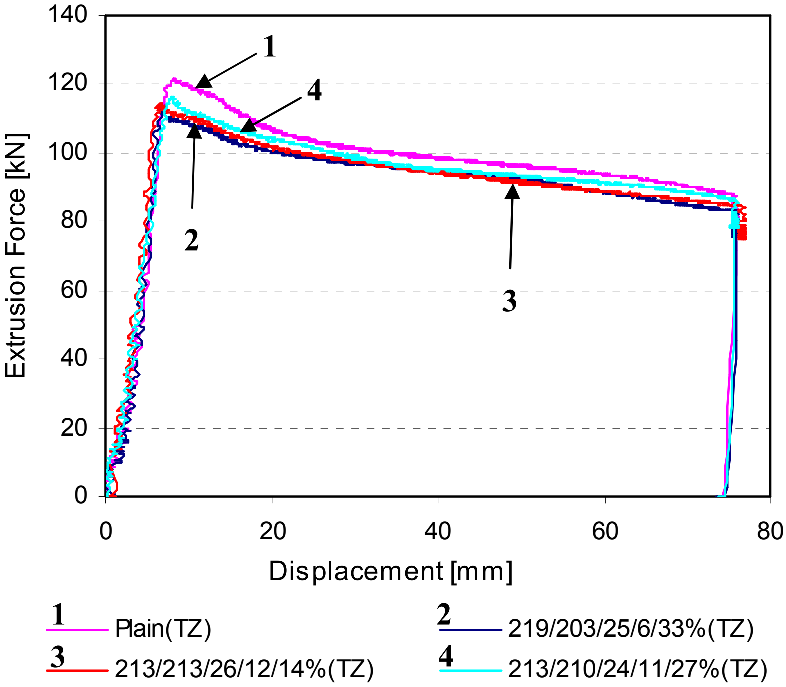

Figure 4.28: Force-displacement curves for plain billet, Plain(TZ), and textured billets with ESMG prescriptions of: (1) 219/203/25/6/33%(TZ), (2) 213/213/26/12/14%(TZ) and (3) 213/210/24/11/27%(TZ). The billets were lubricated with Tallow mixed with Zinc Stearate (TZ) and extruded with the reduction in cross section area, $r_a = 50\%$

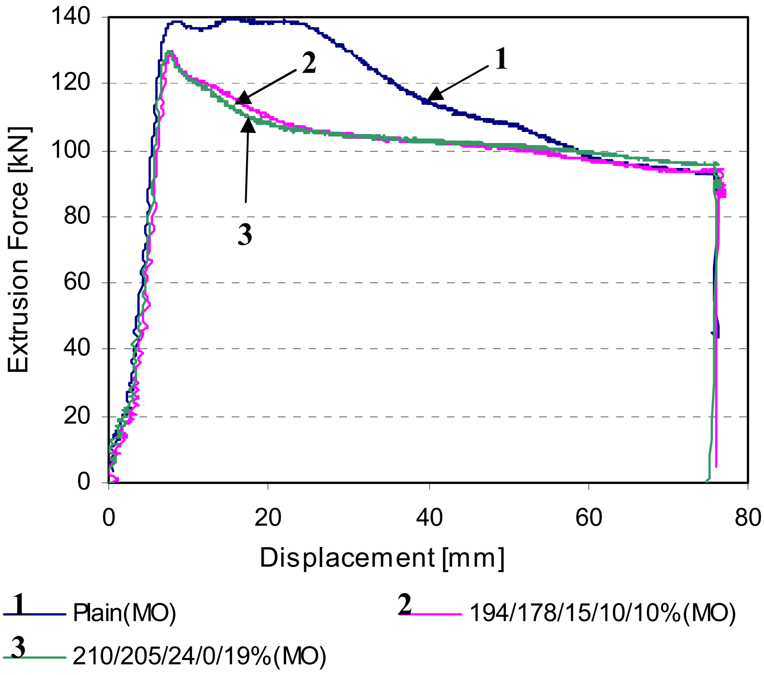

Figure 4.29: Force-displacement curves for plain billet, Plain(MO), and billets with ESMGs prescriptions of: (1) 194/178/15/10/10%(MO) and (2) 210/205/24/0/19%(MO). The billets were extruded with reduction in cross section area, r_a = 50% and lubricated with Machine Oil (MO)

4.4.2.5 Extrusion tests at r_a = 75%

For the evaluation of extrusion at r_a **= 75%**, all the billets were lubricated with MO (see **Table 4.2** in section 4.3.2). The results of the evaluation are shown in **Figure 4.30** to **Figure 4.32**. In **Figure 4.30**, the force displacement curves for three plain billets (Plain 1, Plain 2 and Plain 3) that were used as the reference curves are shown and **Figure 4.31** shows all of the force-displacement curves. The magnification of the graph plot in **Figure 4.31** is shown in **Figure 4.32**.

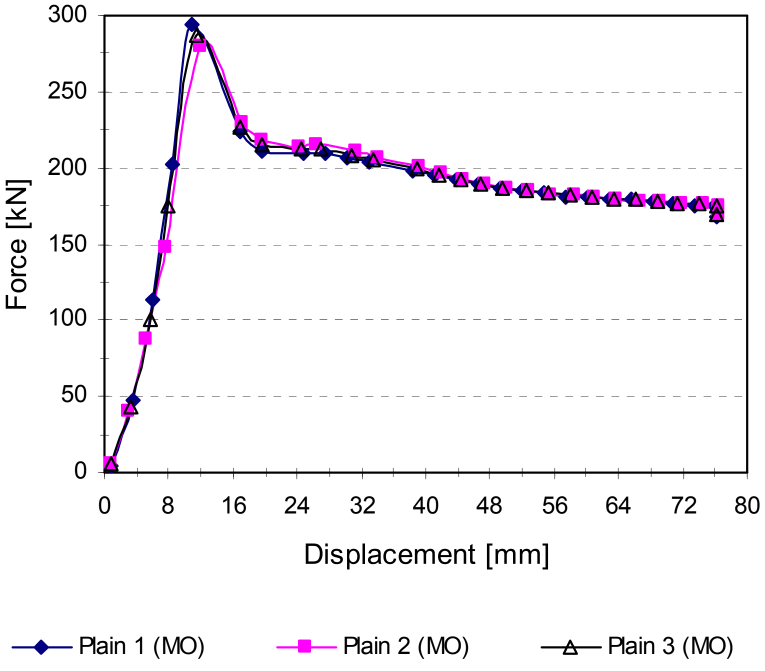

Figure 4.30: Force-displacement curves for three plain billets lubricated with machine oil (MO) and extruded with the reduction in cross section area, $r_a = 75\%$

It is can be observed from **Figure 4.31** that the steady state for the plain billets and the textured billets was achieved after approximately 20mm displacement. Even though the trend of the force-displacement curves for these billets is the same as the trend of the force-displacement curve for the plain billets, the required extrusion force, at any deformation stage, for the textured billets is lower than for the plain billets and more obvious at the peak point of the extrusion force.

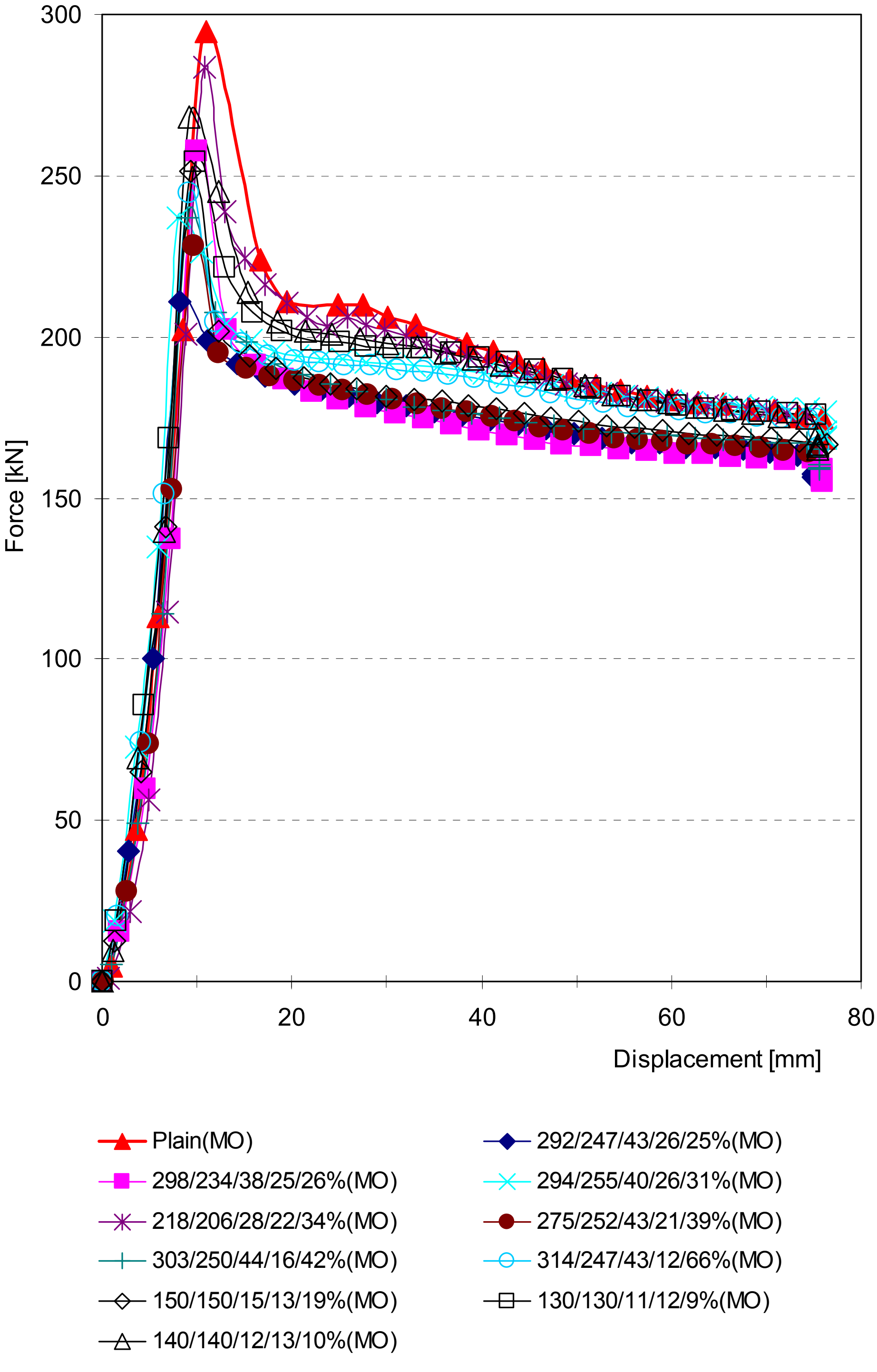

Figure 4.31: Force-displacement curves for plain billet and textured billets with various ESMG prescriptions. The billets were lubricated with machine oil (MO) and extruded with the reduction in cross section area, r_a = 75%

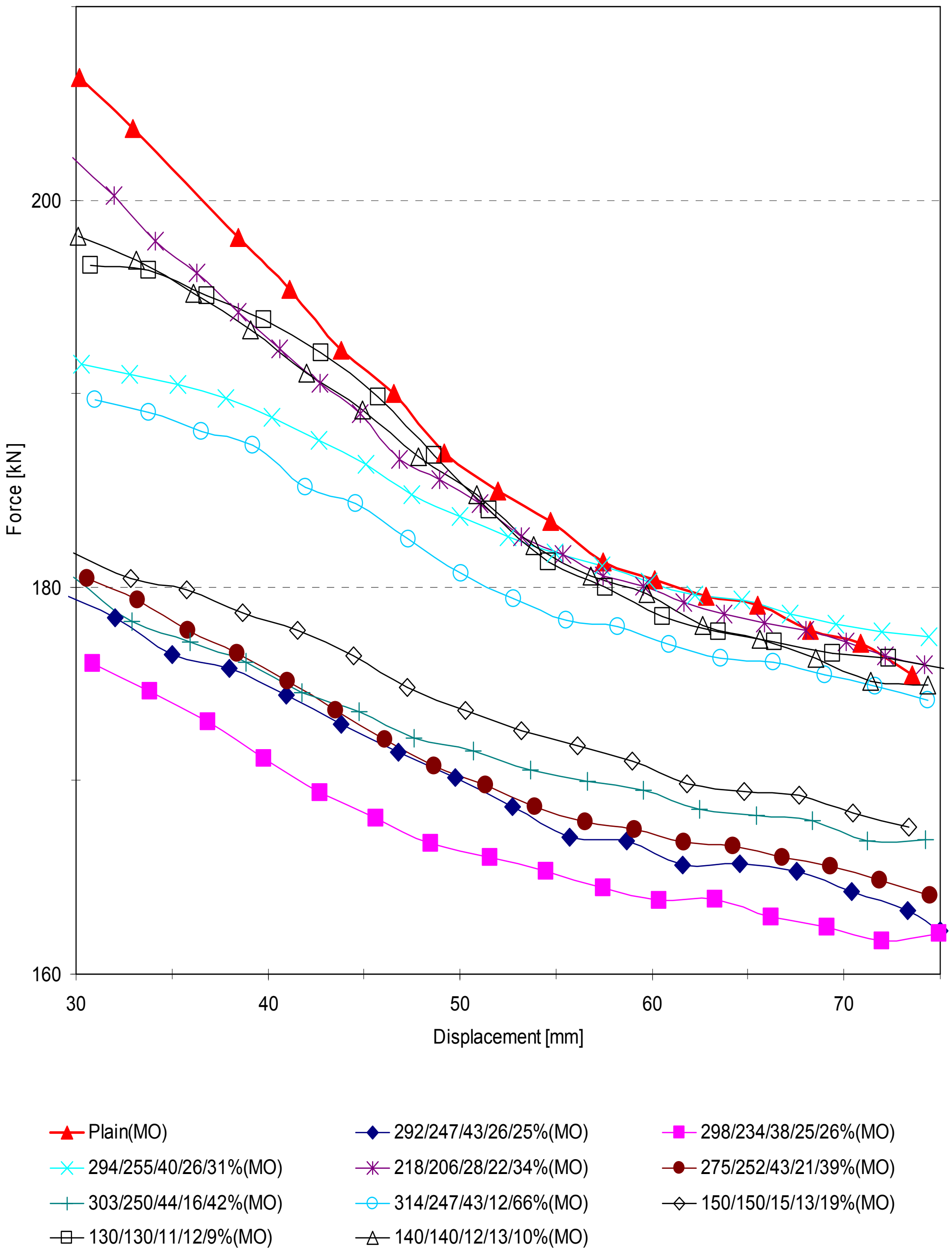

Figure 4.32: Magnification of force-displacement curves shown in **Figure 4.31**

The total area and the slope of the force-displacement curves were estimated based on the graph that shown in **Figure 4.31** and **Figure 4.32**. The bar graph in **Figure 4.33** shows the slope reduction percentage of the force-displacement curves of the textured billets as compared with the plain billet. As shown in **Figure 4.33**, the billets textured with ESMG less than 12μm deep and the density of less than 10% were contributed in the slope reduction of the less that 30% and the total work reduction of less that 2%. Another important finding is that among the textured billets, the force-displacement slope difference was insignificant.

The reduction percentage of slope and total work versus ESMG's depth and ESMG's density are shown in **Figure 4.34** and **Figure 4.35** respectively. As shown in these figures, the reductions of the total work increases as the ESMGs' density and the ESMGs' increases. However, the highest reduction of total work was only around 10%, which was contributed by the ESMGs with the depth higher that 15μm and the density higher that 20%. It can also be observed that the billets textured with the ESMGs' depth of higher than 15μm and the ESMGs' density higher than 20% contributed to a significant slope reduction, i.e. from 44% to 54%. The highest slope reduction of 54% was observed for ESMGs with depth of 44μm and density of 31%.

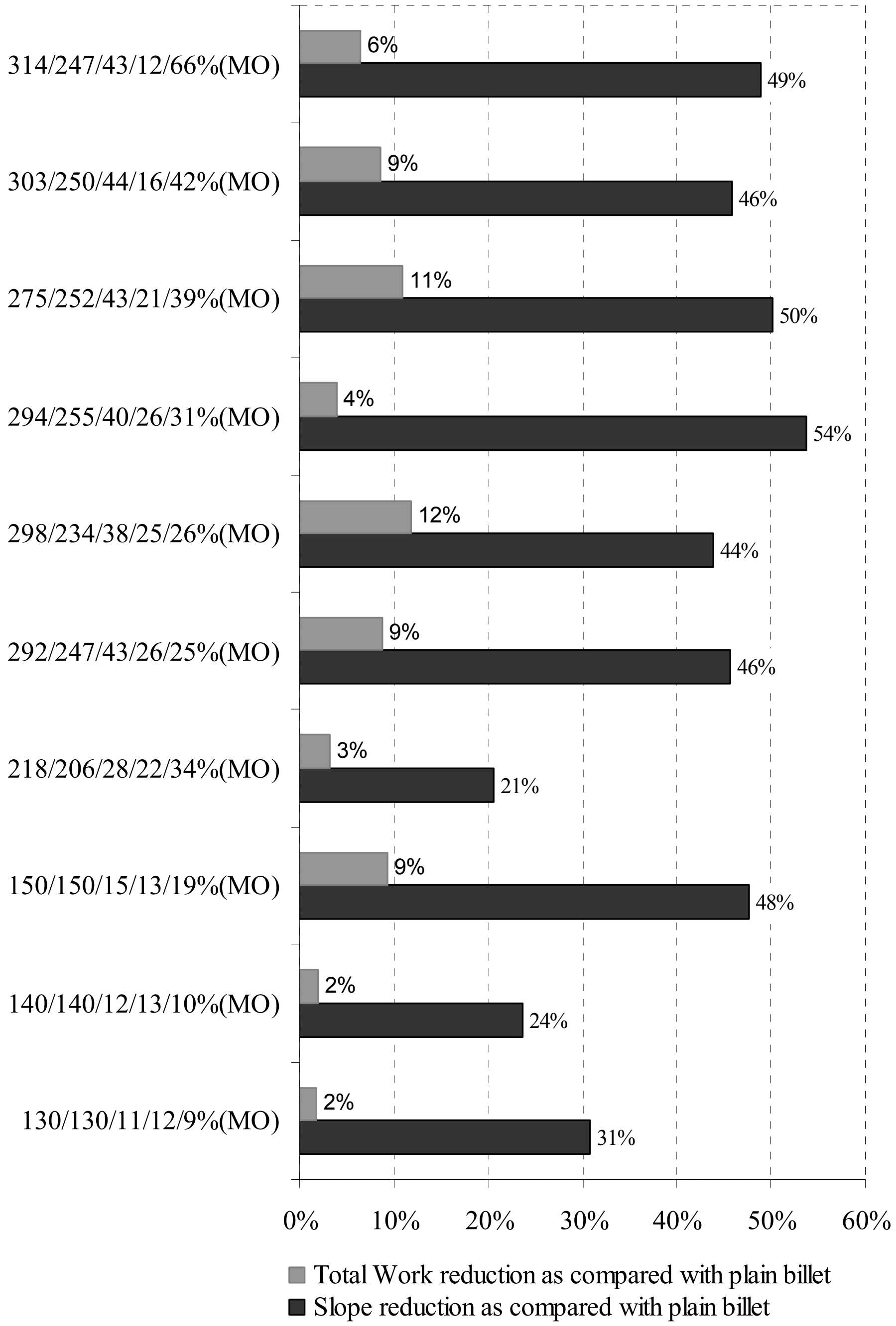

Note: The numbers at Y axis are representing the reference code of d1/d2/depth/pile-up/density

Figure 4.33: Slope and total work reduction percentage of the force-displacement curves of the textured billets (in **Figure 4.31** and **Figure 4.32)** as compared with the plain billet

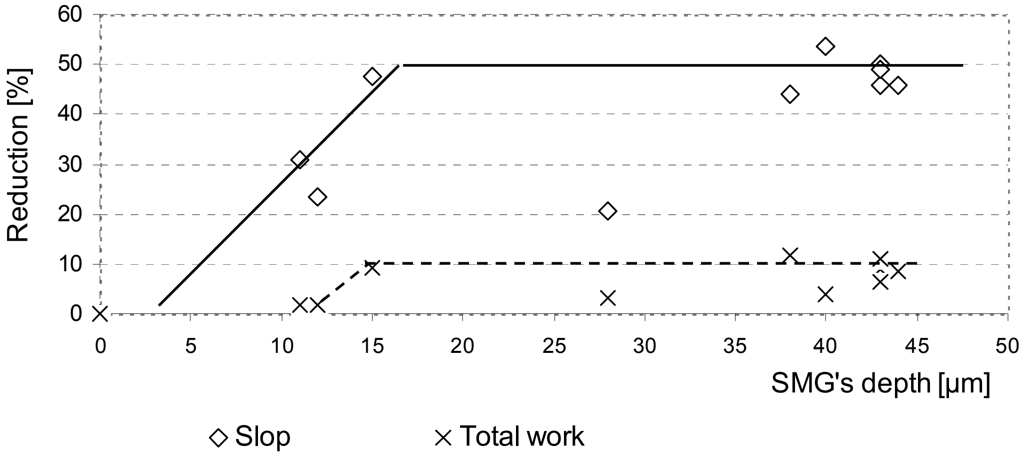

Figure 4.34: Percent reduction of slope and total work versus ESMGs' depth

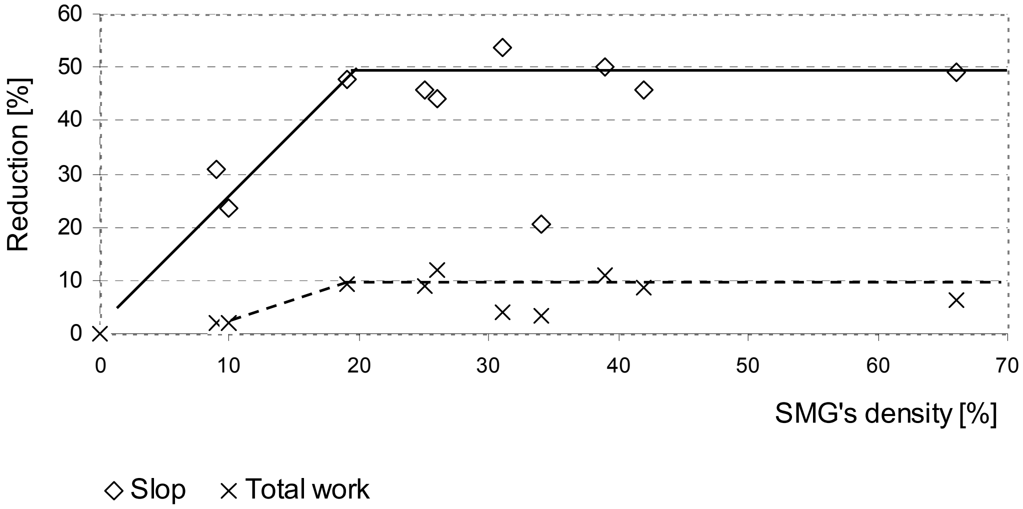

Figure 4.35: Percent reduction of slope and total work versus of ESMGs' density

4.4.2.6 Discussion of ESMG influence on friction reduction

This section discusses the influence of ESMGs on friction reduction in two different interfacial surface areas, i.e.: billet/chamber interface and billet/die interface. The analysis technique used to define the ESMGs' influence on friction reduction is to compare the force-displacement extrusion curves for the billets textured with various ESMG prescriptions with those obtained for the plain billets. The differences in terms of slope and required force are distinguished and analyzed to determine the contribution of various characteristics of ESMGs on friction reduction.

To simplify the analysis of the changes of the extrusion force, the total work required was determined by estimating the total area under the force-displacement curve using a trapezoid technique. Subsequently, the reduction of the total work of the textured billet was compared with the total work for the plain billet.

4.4.2.6.1 Friction at billet/chamber interface

As explained previously, a different friction factor, *m,* at the billet/chamber interface could be identified by the slope differences of the force-displacement curves at their steady state phase. As can be seen from the results, supplying the billets with ESMGs leads to some change in the slope of the curves at the steady state as compared with the plain billet. However, only a small difference in slope can be observed among the textured billets. These results are in agreement with the findings presented in [158] as shown in **Figure 4.36**, namely that the most significant difference in slope is for *m* between *1* and *0.8*, and not at lower friction, i.e. between *m = 0.6* and *0*.

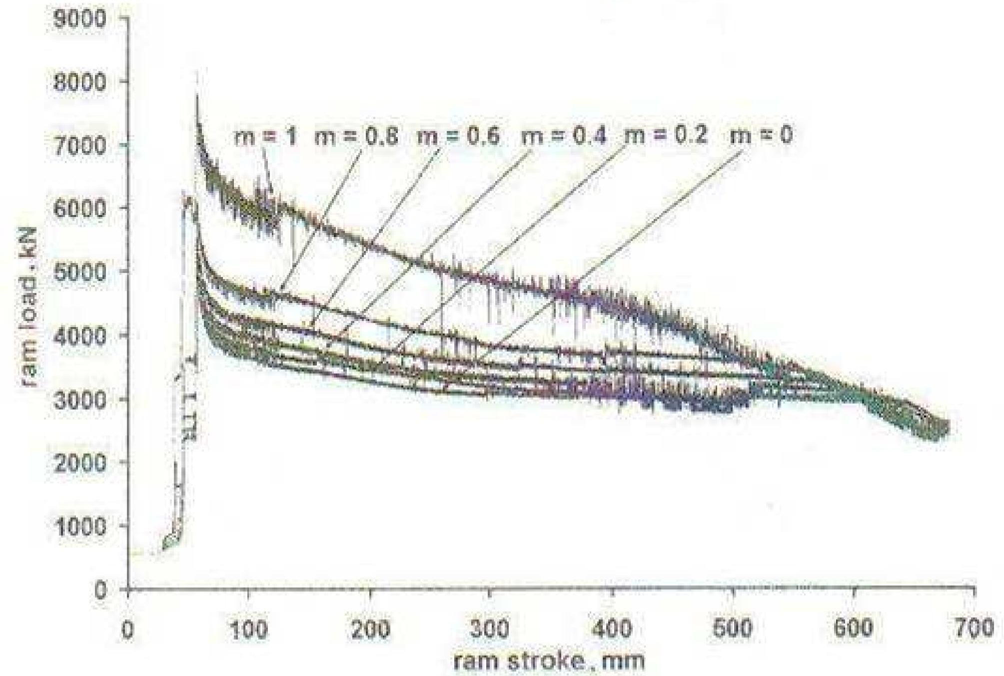

Figure 4.36: Influence of billet/chamber interfacial friction on the extrusion force (*taken from [158]).*

As discussed earlier (see section 4.4.2.1.1), the ESMG pile-up area at the billet/chamber interface is first to contact the chamber surface. With increasing punch displacement, the high pressure that develops at the ESMG pile-ups may cause the thin lubricant film layer to break down resulting in metal to metal contact. As the ESMGs at the billet/chamber interface are deformed insignificantly during the extrusion tests, the lubricant stored in the ESMGs is not squeezed out to supply more lubricant on to the billet surface to overcome the lubricant breakdown, particularly in the pile-up area. Therefore, metal to metal contact due to lubricant breakdown remains throughout the process.

4.4.2.6.2 Friction at billet/die interface

As stated in equation (3), in **Chapter 2** section 2.5.3.6, the magnitude of force F_T as a function of punch displacement (travel) depends on the values of F_c, F_d and F_{dd}, where F_c is influenced by m, and L. Due to each extrusion test being performed under the same test conditions, except for the ESMG characteristics, the decrement of L, the magnitude of $\overline{\sigma}$, d_0 and F_{dd} were always the same in each test. For this reason, the reduction of the required force, as compared with that for the plain billet, might not only be due to the reduction of F_c but might also be due to the reduction of F_d.

As can be seen in **Figure 4.33**, the total work for the extruded textured billets is lower when compared with that for the plain billet. It indicates that texturing the billets with ESMGs could decrease the required extrusion force. As shown in **Figure 4.23 (b)** and discussed in section 4.4.2.1.2, the ESMGs at the billet/die interface are significantly deformed, which results in their depth reduced significantly. Therefore, the ESMGs which act as lubricant pockets, to store microscopic quantities of lubricant, transport and expel that lubricant on to the billet/die interface. The lubricant that is expelled on to the surface forms a fresh thin lubricant film that improves the lubrication performance by repairing lubricant breakdown due to billet deformation. Meanwhile, the ESMGs might also trap particles of the billet material [36]. These phenomena contribute to the improvement of lubrication performance at the billet/die interface. As a result, F_d is reduced and consequently reduces the required total extrusion force F_T as compared with that for the plain billet.

As discussed in section 4.4.2.6, it has been found that the reduction of the total work as compared with that for the plain billet increases as the ESMG density increases. These results indicate that the amount of lubricant expelled from the ESMGs during extrusion is dependent on the density and depth of the ESMGs, which directly influences the magnitude of the billet/die interfacial friction force F_d.

As mentioned in section 4.4.2.1, at the aperture die land, the ESMGs were nearly totally flattened as a result of the plastic flow of the material in the conical die cavity. Due to this reason, it can be concluded that ESMGs have not contributed in friction reduction at billet/aperture land interface.

4.5 Summary

This chapter has presented the experimental trials of the influence of ESMGs on interfacial friction reduction during bulk metal forming processes. Two series of evaluation trials were performed using two different testing methods, i.e. ring compression test and forward extrusion test.

The ring test was used in the measurement of an average value of interfacial friction coefficient, μ, in order to evaluate the merit of ESMGs in a simple compression process application. The experimental trials of ESMGs in more complex metal forming work were performed using a forward extrusion test.

As has been found from the ring compression trials, ESMGs textured on the compression die surface increase interfacial friction at the die-work material interface. This is because ESMGs textured on the die surface oppose the relative motion between the two sliding surfaces of the specimen and the die, which results in a higher friction coefficient, μ.

Nevertheless, ESMGs textured on the work material surface improve lubrication performance. The density and the depth of ESMGs have been found to play an important role in friction reduction during deformation processes, such that an optimum depth and density should be defined to obtain a maximum reduction of friction. Shallow ESMGs (less than 9μm depth) with low density (less than 26%) have been found to contribute less to friction reduction due to ESMGs collapsing at the beginning of the deformation process. By considering that no further friction reduction is achieved with ESMGs' depth of more than 13μm, therefore it can be considered that 13μm is the optimum ESMGs depth.

In the forward extrusion trials, influence of ESMGs on friction reduction at two different interfacial surface areas, i.e.: billet/chamber interface and billet/die interface was investigated. The effect of ESMGs on billet/chamber interfacial friction was evaluated by comparing the slope of force-displacement curves at the steady state for textured billets (with various characteristics of ESMG) and plain billets. Another technique used was to compare the total work required for the plain and textured billets.

The studies have shown that ESMGs textured on the billet surface contribute to billet/chamber interfacial friction reduction. Shallow ESMGs (less than 12μm depth), with density of less than 10%, slightly contribute to friction reduction as compared with plain billets; their curve trends are nearly similar to those for plain billets. Whereas, the billets with the ESMG depth of more that 30µm and ESMG density of more than 25% cause higher friction reduction, i.e. around 45% to 55%.

However, the general finding was that the ESMGs at the billet/chamber interface were insignificantly deformed during the extrusion process; therefore the lubricant was not expelled from the ESMGs. Nevertheless the ESMGs at the billet/die interface were significantly deformed. In this interfacial area, the lubricant was expelled from the ESMGs and flowed on to the billet surface, which resulted in the billet/die friction reduction. The evidence is that the reduction of the total work and the force-displacement slope increases as the density and depth of ESMGs increases. These results indicate that the amount of lubricant expelled from the ESMGs during extrusion is dependent on the density and depth of the ESMGs, which directly influences the magnitude of the billet/die interfacial friction force, F_d.

Even though the highest achievable reduction in total work was only around 10%, it has been found that by introducing ESMGs on the billet surface, the peak extrusion load was reduced approximately up to 30%. In forward extrusion, high peak extrusion force might be occurring due to high billet/chamber interfacial friction force, F_c and billet/die interfacial friction force, F_d. Lower F_d decreases the magnitude of the peak extrusion load that occurs during the die filling phase [78], die deformation during loading and form-errors in the material contained in the die [79]. Lower F_d also results in die relaxation and prevents die defects [79]. In addition, low F_d at the billet/die interface prevents temperature rise at exit land aperture that results in maintaining material flow pattern contained in the die [80]. Therefore, it can be concluded that introducing ESMGs on the billet surface is highly beneficial for forward extrusion operations.

Chapter 5

Experimental Evaluation of Performance of Piezoelectric Actuators under Long-term Cyclic Operations

Glossary

$\left(\varepsilon_{33}^{T}/\varepsilon_{0}\right)$: Relative dielectric constant

E_c : Coercive field

K_p : Electromechanical coupling factor

Q_m : Mechanical quality factor

d_{33} : Piezoelectric coefficient

$\left(\varepsilon_{33}^{T}/\varepsilon_{0}\right)$: Relative dielectric constant

5.0 Introduction

As discussed in **Chapter 4**, the results of the experimental trials have indicated that ESMGs textured on a workpiece surface reduce friction. In the experiment trials, the surface of the ring specimens and billet specimens were textured using a bespoke indentation texturing system. However, this system was only capable to render ESMGs up to 50 indentations per second. In real production, texturing workpieces with ESMGs will be an additional process increasing production cost and time. Therefore, for in mass production operations, a durable and high performance texturing system is required. This can be achieved by increasing the speed of the texturing process.

As discussed in **Chapter 2**, section 2.4, a multi-layer stack ceramic actuator (MSCA) is used to drive the displacement of the diamond indenter during the ESMG texturing operations. It should be noted that the geometry of the diamond indenter tip determines the geometry of the ESMGs, whereas the dimensions of the ESMGs are determined by the MSCA actuator displacement. Therefore, to obtain uniform dimensions of ESMGs throughout a long term texturing operation, the actuator displacement must be consistent. However, as noted in section 2.5, the actuator displacement may degrade, which may result in ESMG characteristics change, such as depth and diameter, changing.

In order to increase the productivity of the indentation texturing system, one of the possible methods is to increase the operating frequency of the actuator. However, since the piezoelectric stack used in the actuator was a newly developed product, by Noliac A/S Denmark, the information on its long-term performance was not available. Therefore, it was decided that the performance of the actuator under long-term cyclic operation would be evaluated with a view to assessing its degradation and, if necessary, introducing a possible compensating method for the decay of the actuator characteristics.

The aim of this chapter is to evaluate experimentally the multi-layer stack ceramic actuator (MSCA) performance under long term operation. In order to evaluate the reliability of various types of MSCAs, specially designed testing equipment was used. The details of the testing procedure and the evaluation results are discussed in this chapter.

5.1 Materials, Equipment and Experimental Procedures

5.1.1 Materials

Four different multi-layer stack ceramic actuators (MSCAs) manufactured by Noliac A/S Denmark were evaluated. Photographs of the MSCAs are shown in **Figure 5.1**. The actuators were constructed from several Ceramic Multi-layer Actuator (CMA) chips, glued together [103]. The chips were made from medium soft-doped PZT material layers (called S1) with a thickness of 50μm. Such actuators are recommended for application at an operational temperature of up to 200°C and nominal field strength of 2-3kV/mm [103].

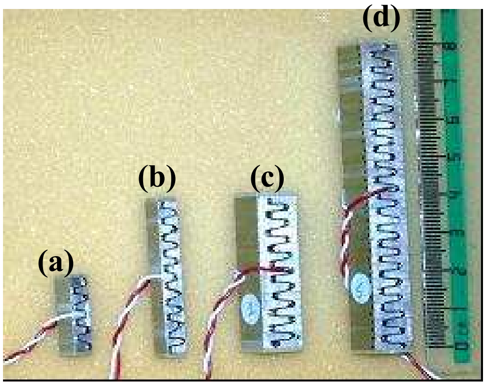

Figure 5.1: Photograph of four different MSCA actuators; (a) 5 x 5 x 20mm^3, (b) 5 x 5 x 40 mm^3, (c) 10 x 10 x 40 mm^3 and (d) 10 x 10 x 80 mm^3

5.1.2 Equipment

As well as standard commercial measurement devices such a digital oscilloscope, multimeter and capacitance meter, two specially designed pieces of equipment were used in the test, i.e.: an actuator-tester and a power pulse generator. All these devices were arranged into two different equipment setups: the first setup was used at the actuator characteristic measurement test stage, while the second one was used at the long-term cyclic operation test stage. The following sections explain the details of the actuator-tester, power pulse generator and the equipment setups.

5.1.2.1 Actuator-tester

A specially designed actuator-tester was developed to evaluate the performance of MSCA actuators with four different dimensions, as shown in **Figure 5.1**. The assembly drawing and photograph of the actuator-tester are shown in **Figure 5.2**. **Table A.1** in Appendix A shows the part list of the actuator-tester.

The function of the rigid lower plate, 1, intermediate plate, 2, and upper plate, 3, which are aligned by the two pillars, 4, is to constrain the force generated by the actuator and the load-spring during testing. The upper die, 6, can be adjusted up and down by turning the screw, 8, using the arm, 10. Almost all of the parts of the actuator-tester were made from steel (Impax Supreme), except for the upper die, which was made from brass and the arm, which was made from mild steel.

Two different tests were performed using the actuator-tester, i.e.: actuator characteristics test and long-term cyclic test. To perform the tests on four different actuators, with different dimensions, the actuator-tester was assembled with other parts according to the assembly drawing shown in **Figure A.1** to **Figure A.8**, in Appendix A. In the long-term cyclic test, the actuator was applied with preloading and loading forces using two different types of tailor made load-springs. The load-springs characteristic measurements were performed using the actuator-tester that was assembled according to the assembly drawing shown in **Figure A.1**. The assembly drawing of actuator-tester used in the actuator characteristic test is shown in **Figure A.2** to **Figure A.4** and for the long-term cyclic test in **Figure A.5** to **Figure A.8**.

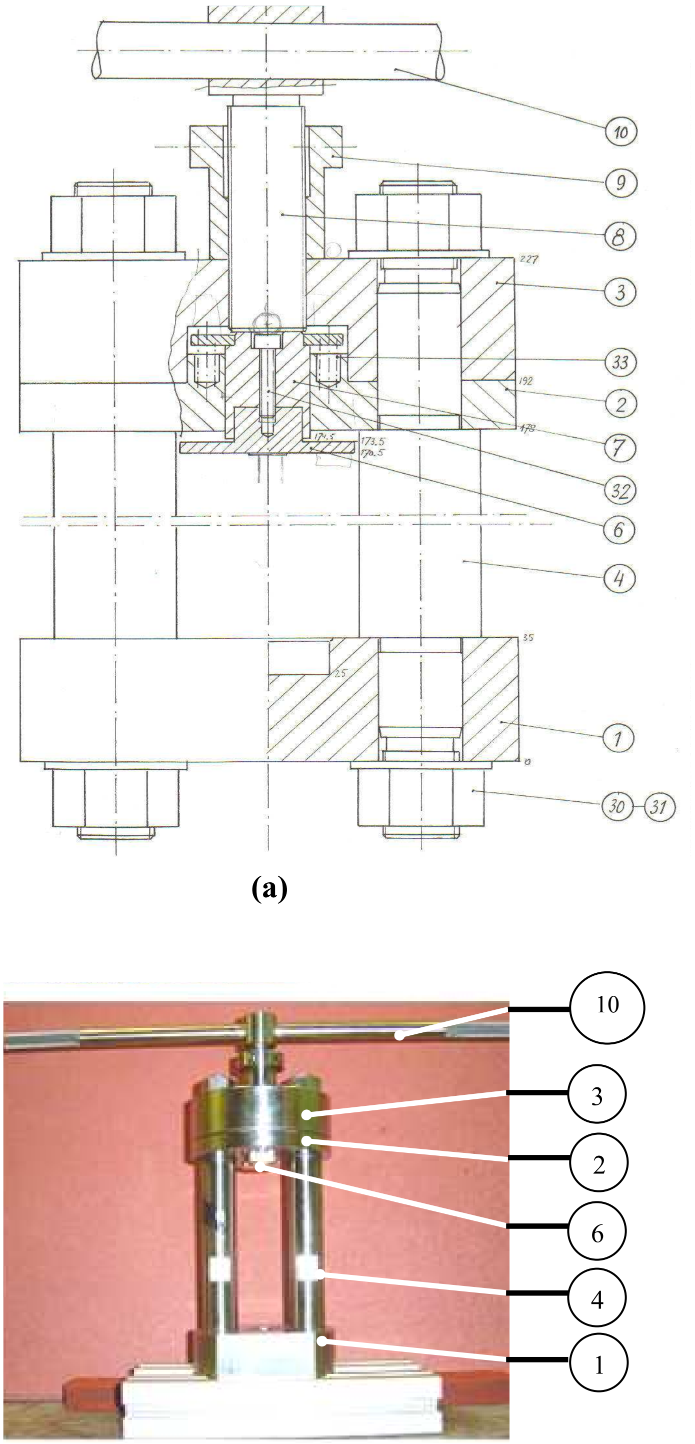

(a)

(b)

Figure 5.2: Full assembly of the actuator-tester; (a) schematic drawing and (b) photograph (see part list in **Table A.1** in Appendix A)

5.1.2.2 Power pulse generator

As the expansion and contraction of MSCA actuator result from the charging and discharging operations, the power pulse generator (PPG) was specially designed and developed to operate under either: a) a manual charging/discharging mode or b) a continuous charging/discharging mode. The photograph of this generator is shown in **Figure 5.3** and its schematic diagram is shown in **Figure 5.4**. The operation procedure for setting the PPG to these modes is explained below.

5.1.2.2.1 Manual charging/discharging mode

To set this mode, switch S_4 (refer to **Figure 5.3**) must be turned off (open) to ensure that the MOSFETs, S_1 and S_2, operate in a 'block' (off) state. Under this condition, the voltage source U_o = 200V could be connected to the MSCA actuator via switch S_3.

When S_3 is turned to Position 1, the voltage U_o will be connected to the actuator through the resistor R_1. The equivalent circuit diagram is shown in **Figure 5.5 (a)**. The voltage U_o provides energy to allow the charge to be stored in the actuator. As the charge accumulates in the actuator, the voltage across the actuator, u_c, increases as a function of time, as shown in **Figure 5.5 (b)**. Thus, the instantaneous value of u_c can be determined as:

$$u_c\left(t\right) = \mathrm{U}_0\left(1 - e^{\frac{-t}{RC}}\right) \ldots\ldots\ldots\ldots\ldots\ldots\ldots\ldots\ldots\ldots\ldots\ldots\ldots \quad (1)$$

Where: $R = R_1 + R_L$ and C is the actuator capacitance

Note:

① Cycle total counter (H7EC)

② Solid state timer (H3CA-A)

③ Digital voltmeter (DMM939)

④ Digital voltmeter (DMM939) control switch [current measurement or voltage measurement selection]

⑤ 3 poles selection switch: **left**-to discharge the actuator manually, **centre** – to set to the cyclic output voltage, **right** – to charge the actuator manually

⑥ 3 poles selection switch for mode selection: **left** – continuous cyclic mode, **centre** – charging/discharging mode, **right** – not used

⑦ ⑧ Duty cycle adjustment: lower edge, high edge

⑨ ⑩ Output voltage adjustment (10V – 200V)

⑪ **Out 1**: Output voltage

⑫ Out 2: not used

⑬ Black push button: Press the button to switch OFF the Cyclic voltage output

⑭ Red push button: Press the button to switch ON the Cyclic voltage output

Figure 5.3: Photograph of the power pulse generator (PPG)

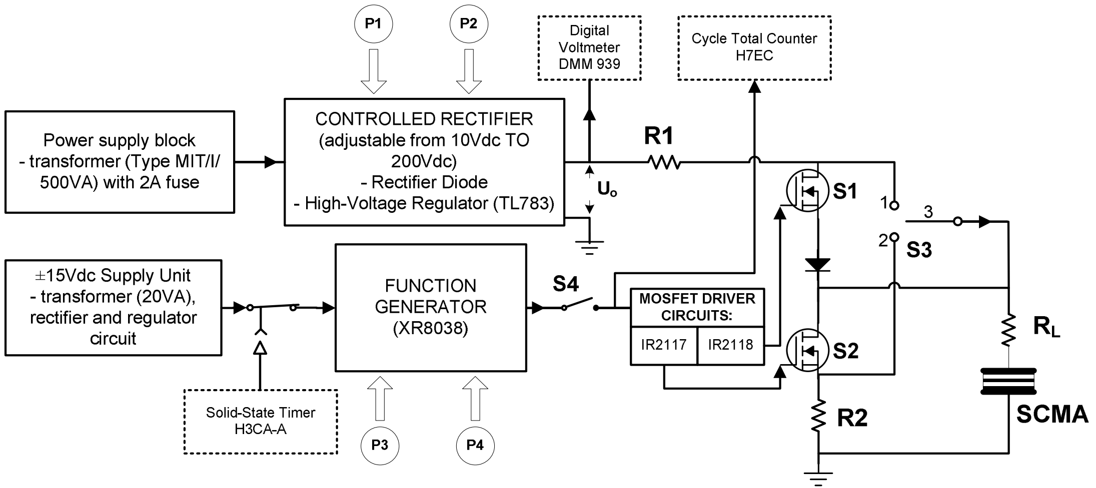

P1 & P2
10 turns potentiometers for voltage adjustment

P3 & P4
10 turns potentiometer
P3 : charging duration
P4 : discharging duration

S3 (used only when S4 opened)
at position 1 : charging state
at position 2 : discharging state
At centre : cyclic voltage

S4
Closed : cyclic operation on
Opened : cyclic operation off

Figure 5.4: Schematic diagram of the power pulse generator circuit

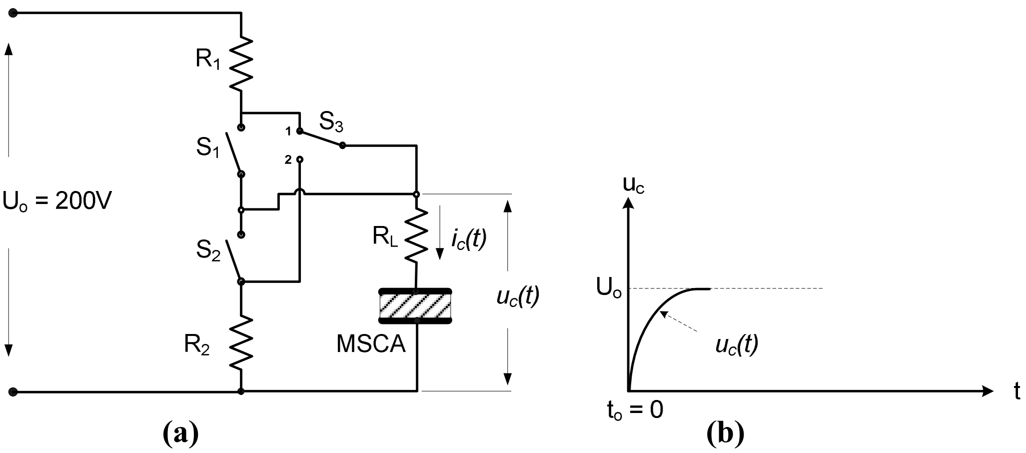

(a) **(b)**

Figure 5.5: (a) Equivalent circuit diagram under charging state and (b) voltage across the MSCA actuator under the charging state

However, when S_3 is turned to Position 2, the generator would operate under the discharging mode. The equivalent circuit diagram for this mode is shown in **Figure 5.6 (a)**. The energy stored in the actuator will be discharged through the resistors R_2 and R_L and, as the charge disperses, the voltage u_d across the actuator decreases. as shown in **Figure 5.6 (b)**.

The instantaneous value of u_d can be determined as:

$$u_d(t) = \begin{cases} U_o & \text{for } 0 < t <= t_1 \ \ldots\ldots\ldots\ldots\ldots\ldots \quad (2) \\ U_o\left(e^{-(t-t_1)/R'C}\right) & \text{for } t > t_1 \ \ldots\ldots\ldots\ldots\ldots\ldots\ldots\ldots \quad (3) \end{cases}$$

where:

$R' = R_2 + R_L$

It should be noted that the slope of the charging and discharging curves varies depending on the value of the resistors R_1 and R_2.

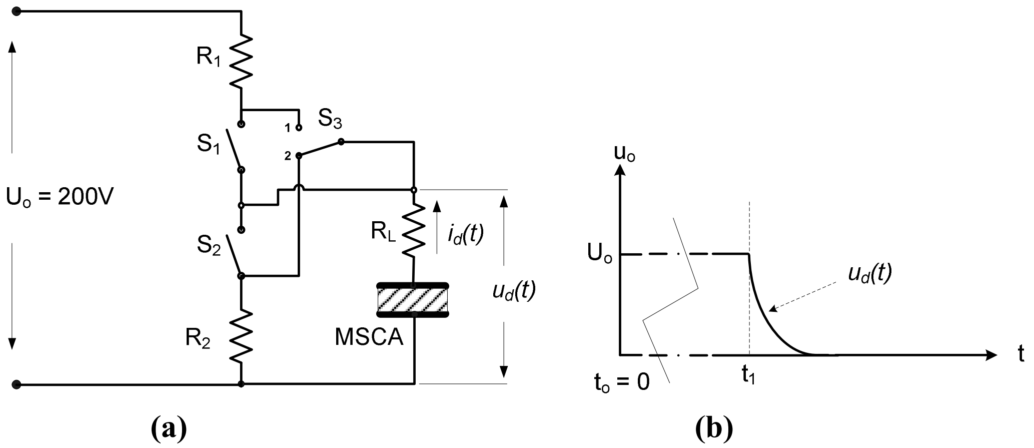

Figure 5.6: (a) Equivalent circuit diagram under discharging state and (b) voltage across the MSCA actuator under the discharging state

5.1.2.2.2 Continuous charging/discharging mode

To set this mode, switch S_4 (see **Figure 5.4**) must be turned to ON (closed), and S_3 must be turned to the centre position. Under this operational mode, the charging or discharging operations are determined by the switching positions of S_1 and S_2, which are continuously controlled by the MOSFET DRIVER CIRCUIT. When S_1 is turned ON and S_2 is turned OFF simultaneously, the generator operates under the charging mode, whereas when S_1 is turned OFF and S_2 is turned ON simultaneously, the generator operates under the discharging mode. The equivalent circuit diagrams for this mode are shown in **Figure 5.7 (a)** and **(b)**.

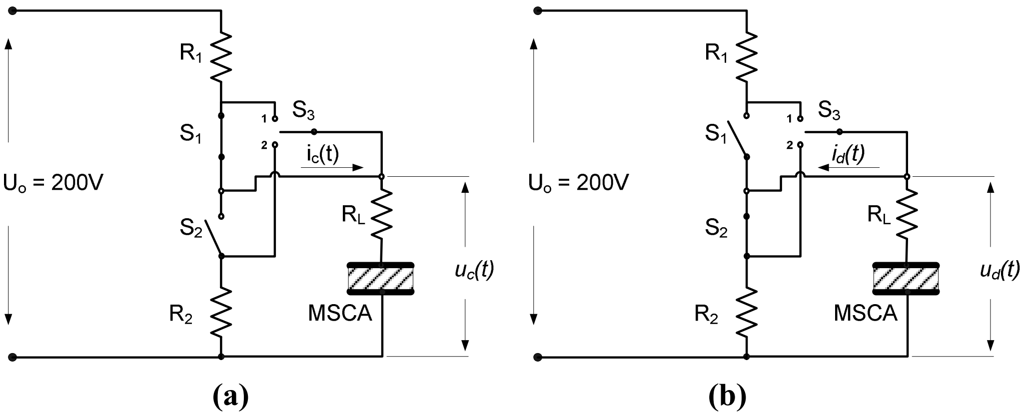

Figure 5.7: Equivalence circuit diagrams for the continuous charging and discharging mode; (a) charging state and (b) discharging state

The frequency of the cyclic voltage can be controlled using potentiometers P_3 and P_4 (P_3 is used for changing the charging duration and P_4 is used for changing the discharging duration). For example, if the charging duration (t_1- t_o) is set to 2.5ms and the discharging duration ($t_2 - t_1$) is set to 2.5ms as well, the frequency of the voltage will be equal to 200Hz.

The waveform of one cycle of the cyclic voltages, $u_{MSCA}(t)$, across the actuator is shown in **Figure 5.8**.

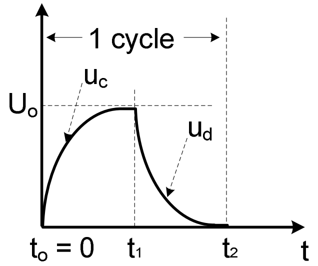

Figure 5.8: One cycle voltage signal, $u_{MSCA}(t)$, across the MSCA obtained in the continuous charging/discharging mode

5.1.2.3 Equipment setup for force-displacement characteristic test

The devices and equipment setup, which were used to obtain the force-displacement characteristic curves of MSCA actuators under a DC voltage field, are shown in **Figure 5.9**, where **Figure 5.9 (a)** shows the schematic diagram, **Figure 5.9 (b)** shows the photograph and **Figure 5.9 (c)** shows the magnification of the MSCA actuator placed in the actuator-tester.

As explained in section 5.2.2.1, the actuator-tester, which was used for different actuator dimensions, was assembled according to the assembly drawing shown in **Figure A.2**, **Figure A.3** and **Figure A.4** of Appendix A. As shown in **Figure 5.9 (a)**, the measurement system that consists of a 9021A Load Washer and a TYPE 5011 charge amplifier from Kistler was used to measure the force generated by the actuator and the output of the measurements was displayed using an MX1 analogue multimeter. Copies of the calibration documents for the system and the force-voltage characteristic are shown in **Figure C.1** and **Figure C.2** in Appendix C.

The KD-2300 non-contacting displacement measuring system, operates based on eddy current principle, was used to measure displacements of the MSCA actuators. The displacement sensor measured the gap between itself and the upper-die. The output voltage of the sensor was converted into a DC voltage, which was displayed using the DM-8300 digital multimeter. Technical data regarding the displacement sensor used in the KD-2300 measurement system is shown in **Table 5.1**, and the displacement versus output voltage characteristic of the system is shown in **Figure C.3** in Appendix C.

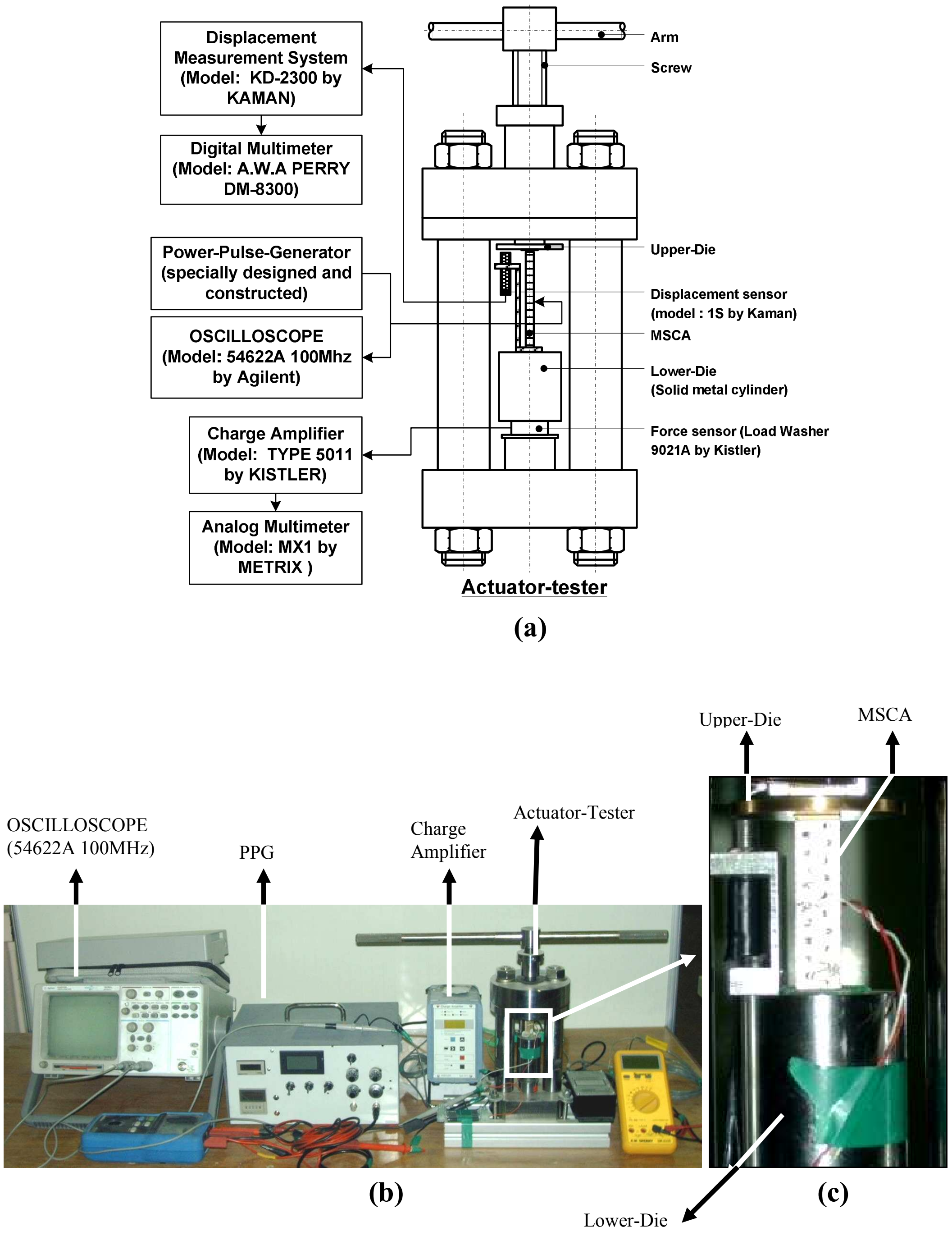

Figure 5.9: Equipment setup used throughout the actuator characteristics measurement; (a) schematic diagram, (b) photograph and (c) magnification of the MSCA actuator placed in the actuator-tester

Another device used was a capacitance meter B131 Dual Display L/C/R Meter made by Megger, with the test frequency set to 1 kHz for measuring the capacitance values of the actuators. The accuracy of the meter depends on the measurement range as shown in Appendix D.

The power pulse generator that set to the manual charge/discharge mode was used to supply the DC voltage to the actuator. The voltage across the actuator was displayed using the oscilloscope (model: Agilent 54622A 100MHz).

Table 5.1: Specification of the displacement sensor used by the KD-2300 Non-contacting Displacement Measuring System

Descriptions	**Parameters**
Measurement range	500µm
Target material	Non-magnetic
Resolution	0.1µm
Frequency response	50kHz

5.1.2.4 Equipment setup for long-term cyclic test

The schematic diagram and a photograph of the device setup used in the long-term cyclic test is shown in **Figure 5.10.** As explained in section 5.2.2.1, the actuator-tester, which was used for different actuator dimensions, was assembled according to the assembly drawing shown in **Figure A.5**, **Figure A.6**, **Figure A.7** and **Figure A.8** of Appendix A.

As shown in **Figure 5.10 (a)**, the actuator is placed between the load-spring and the upper-die. The load-spring was used for applying the preloading force, $F_{preloading}$, and the loading force, $F_{loading}$. Two types of load-spring with different dimension were used in the test, and a photograph of these is shown in **Figure 5.11**. The load-displacement characteristics of these two load-springs, obtained using the actuator-tester that assembled as in **Figure A.1** in Appendix A, are shown in **Figure 5.12**.

The power pulse generator, set to the continuous charging/discharging mode, was used to supply the cyclic voltage to the actuator. The voltage across the actuator was displayed using an oscilloscope (model: Agilent 54622A 100MHz) for the purpose of monitoring.

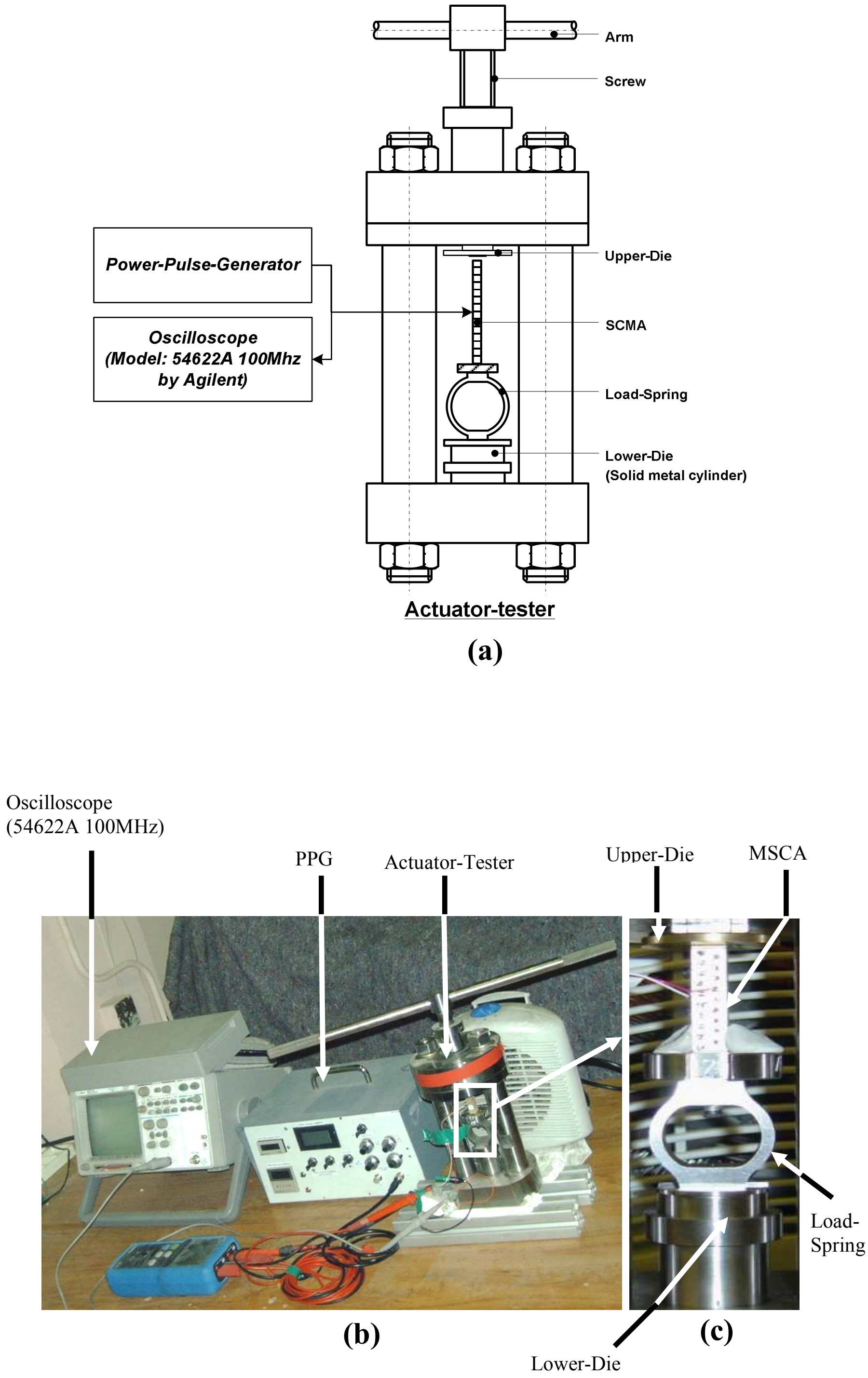

Figure 5.10: Equipment setup used throughout the long-term cyclic test; (a) schematic diagram, (b) photographs and (c) magnification of the actuator placed between the load-spring and upper-die

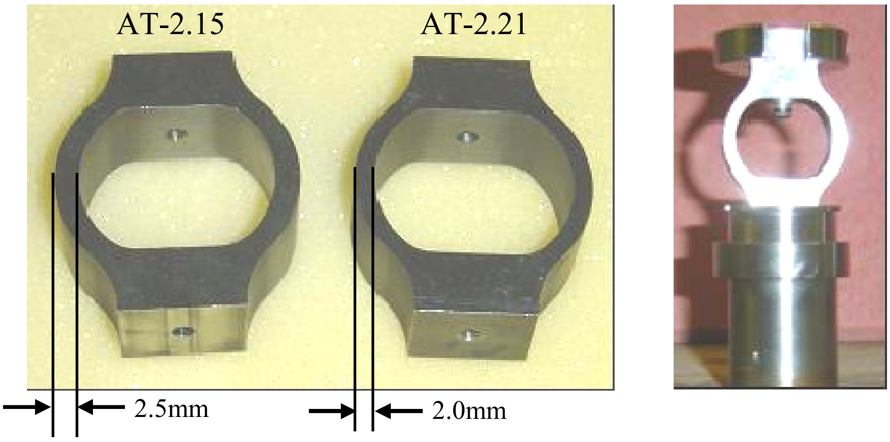

(a) **(b)**

Figure 5.11: Photograph of the load-spring; (a) two different types of load-spring (AT-2.15 and AT-2.21) and (b) a load-spring mounted on the load-spring holder

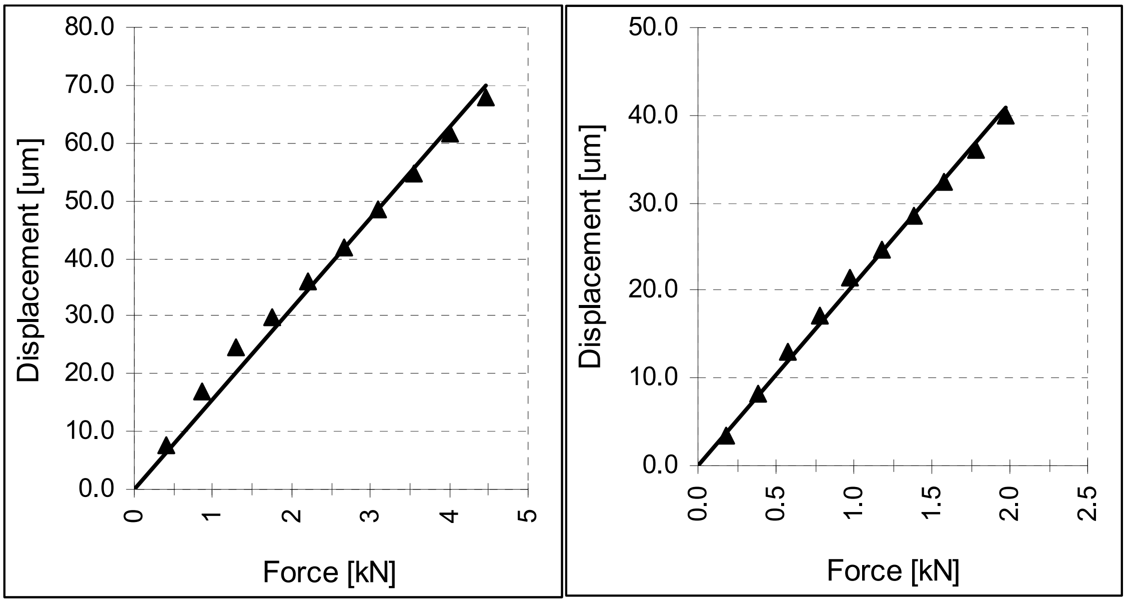

(a) **(b)**

Figure 5.12: Characteristics of the load-spring: (a) AT-2.15 – stiffness $k = 70$kN/mm and (b) AT-2.21 – stiffness $k = 50$kN/mm

5.1.3 Experimental procedures

The summary of the test procedure used is shown in **Figure 5.13**. In Step 1, the characteristics of the actuators, as received from Noliac A/S, are firstly determined, and considered as a reference. In the following steps, the test is divided into two stages: the first is the long-term cyclic operation stage (up to the number of cycles as stated in **Figure 5.13**), and the second is the actuator characteristics measurement stage.

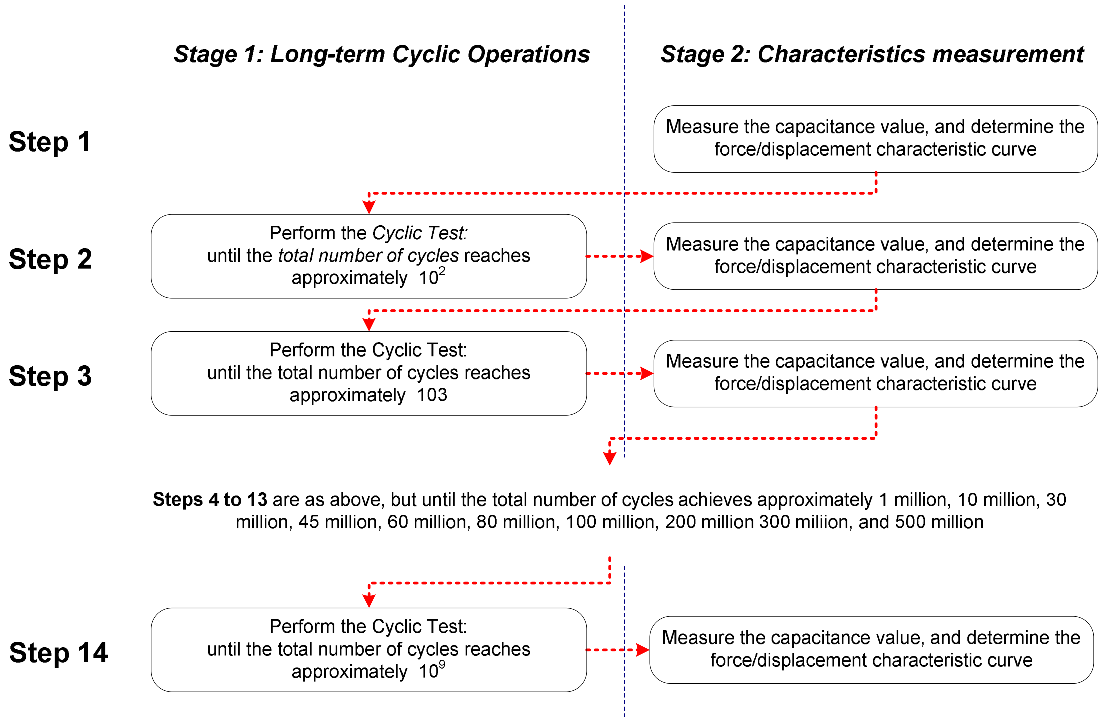

Figure 5.13: Step-by-step sequence used throughout the experimental evaluation of MSCA actuator performance

5.1.3.1 Actuator characteristics measurement procedure

It is important to note that the equipment setup, as explained in section 5.2.2.3, was used in the force-displacement characteristic measurement. Power pulse generator was set to the manual charging/discharging mode (as explained in section 5.2.2.2.1) to supply a voltage U_o= 200V to the actuator. The level of the voltage, U_o, was monitored by observing the waveform using an oscilloscope (model: Agilent 54622A 100MHz).

The parameters determined in the characteristics measurement were capacitance, C_a, blocking force, F_{max}, and actuator stroke at zero force (free stroke), ΔL_o. It is important to note that the value of C_a was measured using the capacitance meter, whereas the value of F_{max} and ΔL_o were determined from the force-displacement characteristic curves.

The step-by-step procedure for measurement of the force-displacement characteristics is illustrated in **Figure 5.14 (a)** and **Figure 5.14 (b)**. The measurement results were recorded in a characteristics measurements table, example of which is shown as **Table 5.2**.

In Step 1, to obtain an accurate measurement, both end surfaces of the actuator were cleaned using white spirit to remove micro-particles before placing the actuator-tester in position as shown in **Figure 5.14 (a)**. At this position, the upper end surface of the actuator corresponds to Point A in **Figure 5.14 (b)**. Next, in Step 2, the upper-die was moved downwards until the force measurement system showed the value of the force F = 24N (based on several trials, force F = 24N was the best force sufficient to ensure that the upper-die touched the MSCA upper surface firmly). Under this condition, the MSCA was compressed to Point A', which was represented by the output voltage V_1, (refer to **Table 5.2**) of the displacement measurement system. Point A' represents the origin of the virtual axes as shown by the dotted line in the graph of **Figure 5.14 (b).**

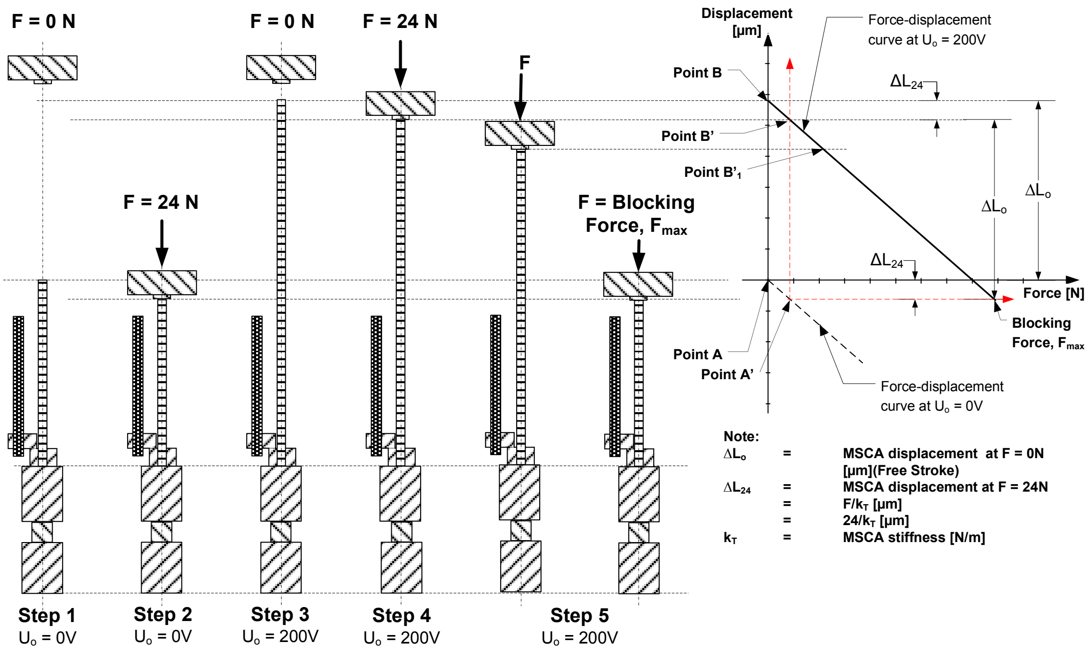

(a) **(b)**

Figure 5.14: Step-by-step procedure used during the force-displacement characteristics measurement; (a) step-by-step measurement procedure and (b) force-displacement characteristic curves corresponding to the step-by-step procedure

In Step 3, the upper-die was firstly moved upwards, and subsequently the DC voltage U_o = 200V was supplied to the actuator. This voltage caused the actuator to be elongated to Point B shown in **Figure 5.14 (b).** The voltage U_o = 200V is equivalent to the electrical field strength of 4kV/mm of the actuator.

In Step 4, the upper-die was again moved downwards until the force measurement system showed the value of the force as F = 24N, which caused the actuator to be compressed to Point B' as shown in **Figure 5.14 (b).** Subsequently, the output voltage, V2, of the displacement measurement system was recorded in **Table 5.2**.

In Step 5, the upper-die was gradually moved further downwards to get several measurement results of force, F, and output voltage, V_2, of the displacement measurement system. Due to the movement of the upper-die, the upper surface of the actuator was displaced to Point B'_1, and finally to Point F_{max} (as shown in **Figure 5.14 (b)** and **Table 5.2**). Different values of V_2 for different forces F were recorded in **Table 5.2**. The values of actuator stroke, ΔL, for each different force were determined as:

$$\text{Stroke} = (V_2 - V_1)ə$$

where ə is the displacement sensor system coefficient, which is 500μm/V.

Finally, the voltage U_o was switched off before removing the actuator from the actuator-tester.

Table 5.2: Example of the characteristic measurement table

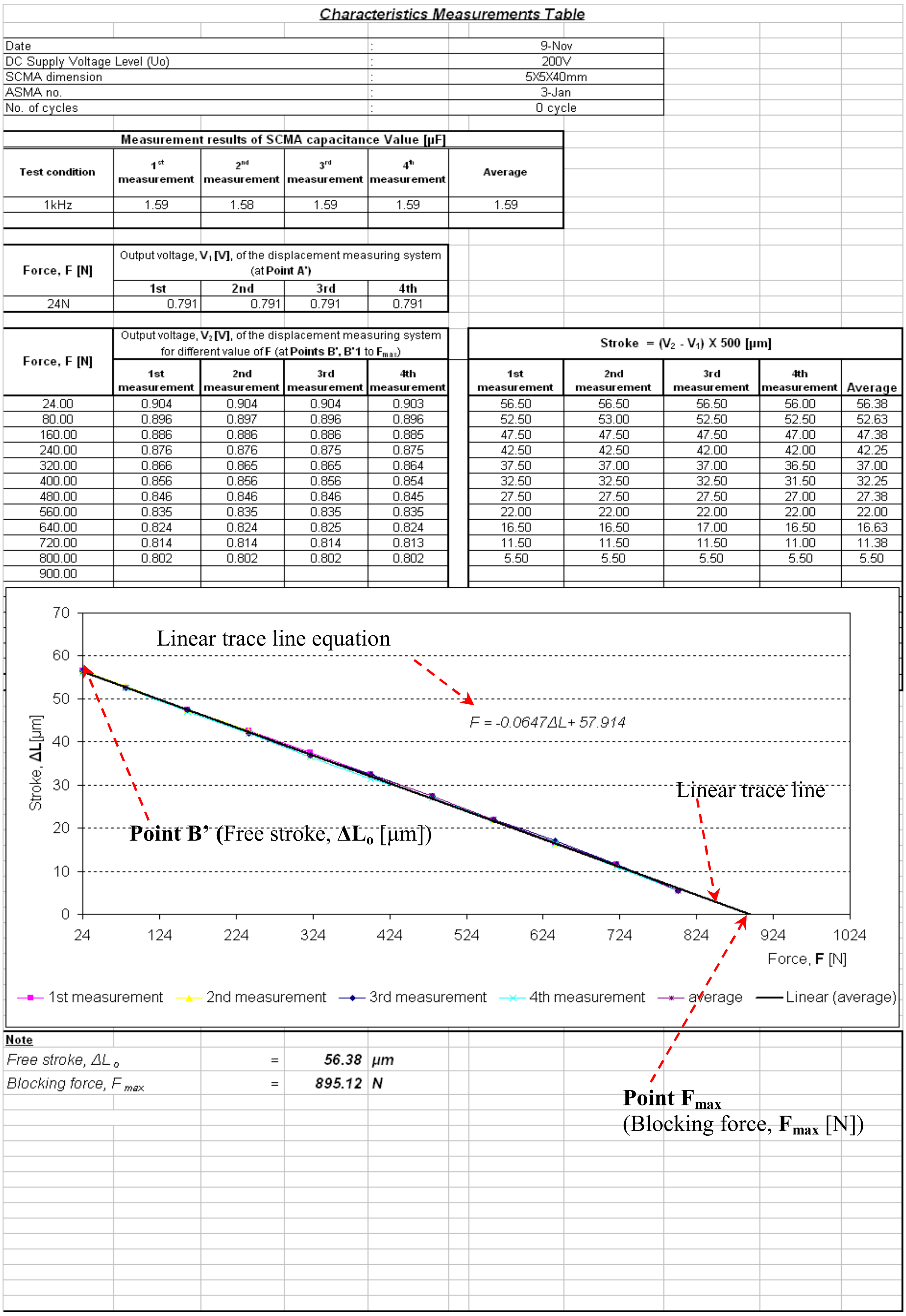

Characteristics Measurements Table

Date	:	9-Nov
DC Supply Voltage Level (Uo)	:	200V
SCMA dimension	:	5X5X40mm
ASMA no.	:	3-Jan
No. of cycles	:	0 cycle

Measurement results of SCMA capacitance Value [µF]

Test condition	**1st measurement**	**2nd measurement**	**3rd measurement**	**4th measurement**	**Average**
1kHz	1.59	1.58	1.59	1.59	1.59

Force, F [N]	Output voltage, V_1 **[V]**, of the displacement measuring system (at **Point A'**)			
	1st	**2nd**	**3rd**	**4th**
24N	0.791	0.791	0.791	0.791

Force, F [N]	Output voltage, V_2 **[V]**, of the displacement measuring system for different value of **F** (at **Points B', B'1** to F_{max})				**Stroke = (V_2 - V_1) X 500 [µm]**				
	1st measurement	**2nd measurement**	**3rd measurement**	**4th measurement**	**1st measurement**	**2nd measurement**	**3rd measurement**	**4th measurement**	**Average**
24.00	0.904	0.904	0.904	0.903	56.50	56.50	56.50	56.00	56.38
80.00	0.896	0.897	0.896	0.896	52.50	53.00	52.50	52.50	52.63
160.00	0.886	0.886	0.886	0.885	47.50	47.50	47.50	47.00	47.38
240.00	0.876	0.876	0.875	0.875	42.50	42.50	42.00	42.00	42.25
320.00	0.866	0.865	0.865	0.864	37.50	37.00	37.00	36.50	37.00
400.00	0.856	0.856	0.856	0.854	32.50	32.50	32.50	31.50	32.25
480.00	0.846	0.846	0.846	0.845	27.50	27.50	27.50	27.00	27.38
560.00	0.835	0.835	0.835	0.835	22.00	22.00	22.00	22.00	22.00
640.00	0.824	0.824	0.825	0.824	16.50	16.50	17.00	16.50	16.63
720.00	0.814	0.814	0.814	0.813	11.50	11.50	11.50	11.00	11.38
800.00	0.802	0.802	0.802	0.802	5.50	5.50	5.50	5.50	5.50
900.00									

Note

Free stroke, ΔL_o = ***56.38*** ***µm***

Blocking force, F_{max} = ***895.12*** ***N***

Steps 1 to 5 were repeated to obtain four different sets of measurements (as shown in **Table 5.2**) and the force-displacement characteristic curves were determined from the average value of the measurements results. The interceptions of the linear trace line on the force-axis and the stroke-axis represent the blocking force F_{max} and the free stroke ΔL_o respectively.

It is important to note that during the force-displacement characteristic measurement, a great deal of care is needed to make sure that the position of the actuator is correct. The actuator must be placed along the centre axis line as shown in **Figure 5.15 (a)**. Mis-positioning as shown in **Figure 5.15 (b)** to **Figure (e)** led to inaccurate displacement measurements due to the bending or tilting of the upper-die. To ensure that the actuator was positioned along the centre axis line, guides as shown in **Figure 5.16** were used.

Due to the fact that actuators were driven using an open loop power pulse generator (PPG), another aspect which needed to be kept in mind was the effect of creep and hysteresis on piezoelectric materials. Generally, creep and hysteresis effects are due to a delay response in the domain switching [167]. Therefore, in order to obtain an accurate measurement, 5 minutes waiting time was introduced at every step of the measurement process as illustrated in **Figure 5.14**.

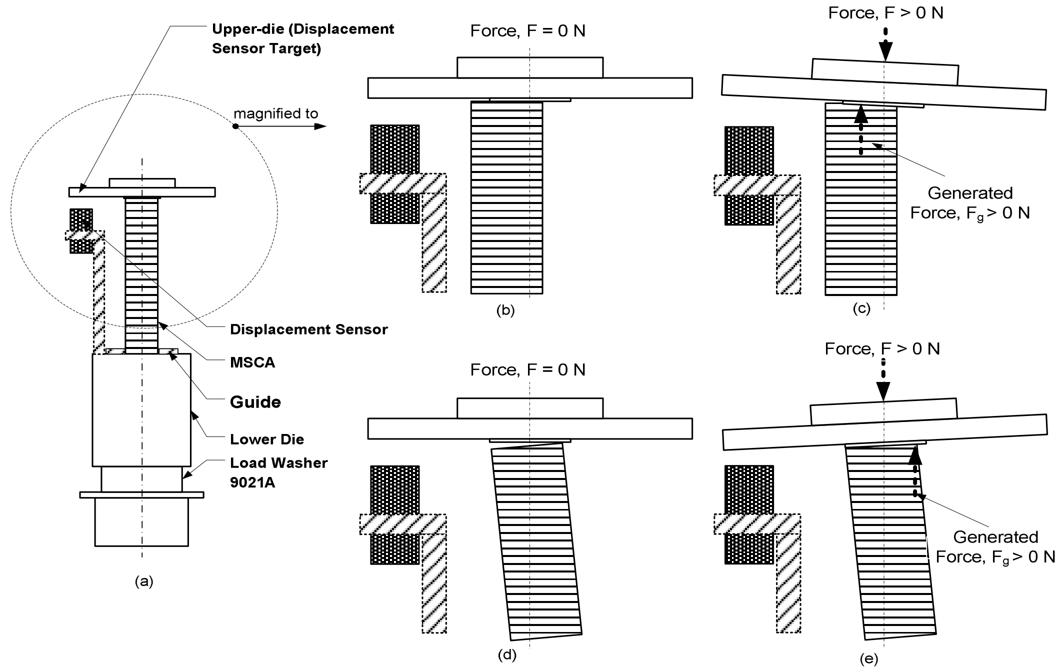

Figure 5.15: Example of correct positioning (a) and mis-positioning (b, c, d and e) of the actuator during the force-characteristic measurement

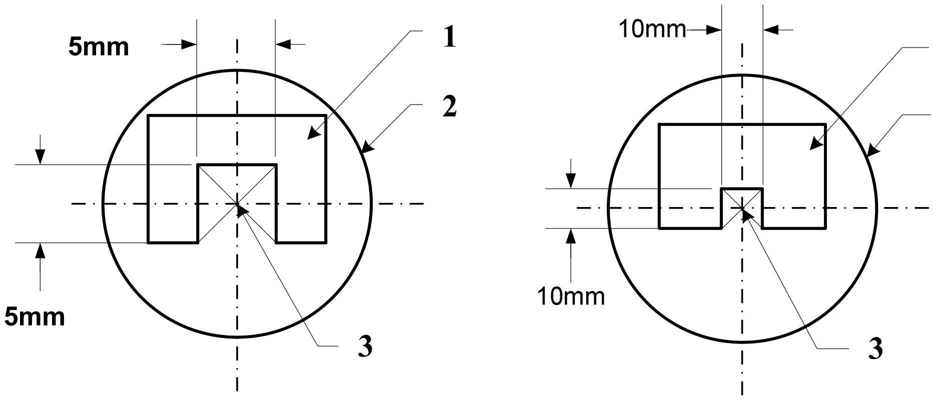

(a) (b)

Figure 5.16: Guide, 1, attached to the lower-die, 2, to position the MSCA actuator along the centre axis line, 3; (a) used for the MSCA actuators with the dimensions of 10x10x40 mm^3 and 10x10x80 mm^3 and (b) used for the MSCA actuators with the dimensions of 5x5x20 and 5x5x40 mm^3

5.1.3.2 Long-term cyclic operation procedure

In this operation, the actuators were subjected to cyclic forces and voltages for a specific number of cycles as shown in **Figure 5.13**. After running to the proper number of cycles, the machine was stopped, and the characteristics measurements (capacitance and force-displacement characteristics as explained in section 5.2.3.2), are then performed. The long-term cyclic operations were performed using the equipment setup as shown in **Figure 5.10**.

The step-by-step procedure of applying forces and cyclic voltages to the actuator is illustrated in **Figure 5.17**. At Step 1, the actuator was first placed between the load-spring and the upper-die. Afterwards, at Step 2, as the upper-die was moved downwards by Δl_t, the actuator was subjected to the preloading force $F_{preload}$ that corresponds to Point 0* (as shown in **Figure 5.18**). Rotating the actuator-tester arm could alter the magnitude of $\Delta l_{t,}$, where one full turn (360°) of the arm gives 500μm movement of the upper-die.

Subsequently, at Step 3, the electrical load in the form of cyclic pulse voltage was then supplied to the actuator from the power pulse generator. The generator was set to the continuous charging/discharging mode (refer to section 5.2.2.2.2). . An example of the cyclic voltage being applied across the actuator is shown in **Figure 5.19**. As the voltage across the actuator increased, the actuator elongated and the load-spring was gradually compressed. As the voltage across the actuator increased up to 200V, the actuator elongated to as much as ΔL, as shown in **Figure 5.17**. Under this condition, the actuator was subjected to the loading force F_{load} that corresponded to Point A, as shown in **Figure 5.18**. The diagrams used to estimate the magnitude of Δl_t, $F_{preload}$, and F_{load} for different dimensions of MSCA actuators are shown in Appendix B.

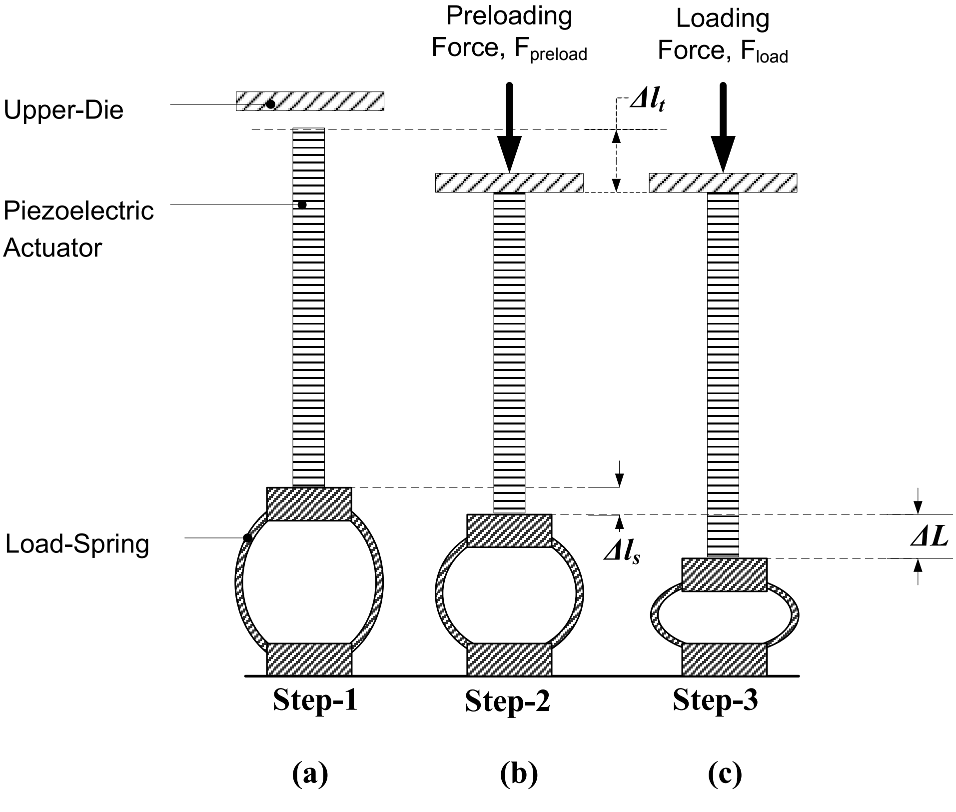

Figure 5.17: Long-term cyclic test procedure; (a) load-spring and MSCA actuator arrangement, (b) the preloading force is applied by the load-spring as the upper-die moves downwards by Δl_t and (c) the loading force is applied to the MSCA actuator as the voltage across the actuator reaches 200V

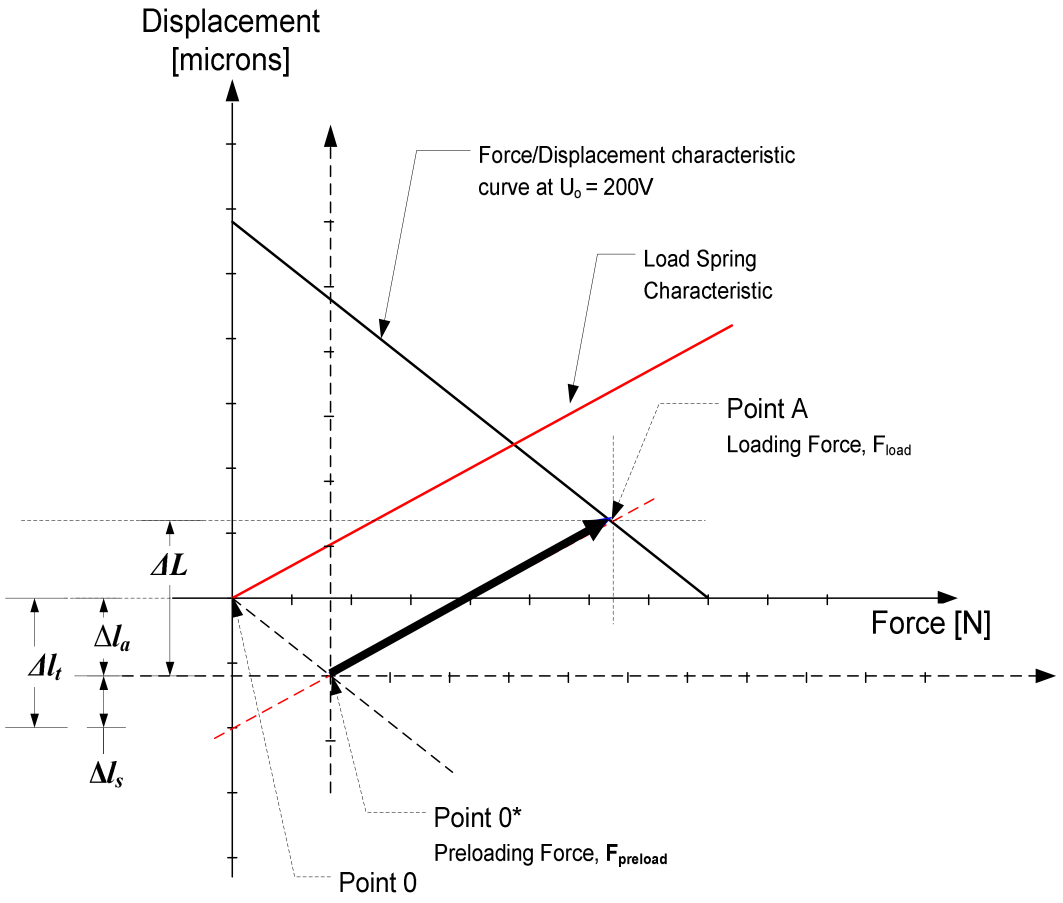

Note:

Δl_s = Compression of the load-spring due to preloading force, $F_{preloading}$

Δl_a = Compression of MSCA actuator due to preloading force, $F_{preloading}$

Δl_t = Total displacement of the upper-die to apply preloading force, $F_{preload}$, to the MSCA actuator

= $\Delta l_a + \Delta l_s$

ΔL = MSCA actuator stroke under the conditions of preloading force, $F_{preloading}$, loading force, $F_{loading}$ and $U_o = 200V$

Figure 5.18: Conceptual graph used for determining the preloading and loading forces

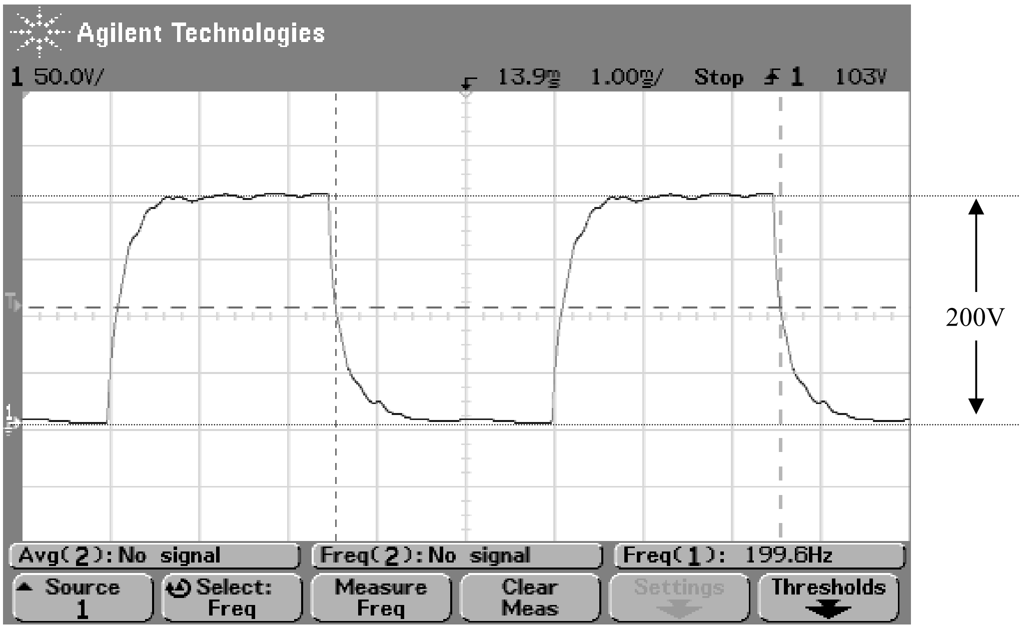

Figure 5.19: Example of cyclic voltage, $u_{MSCA}(t)$, (with peak voltage = 200V and frequency = 199.6Hz) across the actuator (5 x 5 x 20 mm^3) during the long-term cyclic test. This waveform was captured in Step 3, as stated in **Figure. 5.17**, using the oscilloscope (model: Agilent 54622A 100MHz)

5.2 Results and Discussions

In total, 15 actuator units were tested under the experimental test conditions as stated in **Table 5.3**. As shown in this table, in the first round of tests (as stated in the rows filled with grey colour), 10 actuators were tested under preloading forces, $F_{preload}$, of approximately 15% of their blocking forces, F_{max}, and cyclic voltage of up to 10^8 numbers of cycles.

Figure 5.20 to **Figure 5.29** show the force-displacement characteristic curves of the actuators obtained after various total number of cycles. Whereas, the characteristics of blocking force, free stroke and capacitance as a function of total number of cycles are shown in **Figure 5.30** to **Figure 5.33** for the blocking force, F_{max}, **Figure 5.34** to **Figure 5.37** for the stroke at zero force (free stroke), ΔL_o and **Figure 5.38** to **Figure 5.41** for the capacitance. As shown in these figures, no significant changes in the force-displacement curves blocking force, free stroke and capacitance were found during the tests. This indicated that, under the experimental test conditions, the actuators were able to provide excellent reliability performance.

In order to observe the performance degradation trends of the actuators, further evaluation, in the second round of tests, was performed. In these tests, five 10x10x40mm^3 actuator units were tested under a higher magnitude of preloading forces $F_{preload}$, as shown in the rows without grey colour, in **Table 5.3**.

It is important to note that the actuator with the reference number of 13/10x10x40/3600/5510/150/200 was tested up to 10^9 total numbers of cycles, whereas the other two were tested up to 10^8 total numbers of cycles. But the last two actuators have been found damaged at the beginning of the cyclic test, i.e.: the actuator with the reference number of 14/10x10x40/3950/5920/150/200 was damaged after 588 kilocycles and for 15/10x10x40/4749/6720/150/200 just after 10 cycles.

Table 5.3: Test conditions for long-term cyclic tests

Actuator reference number: [actuator no./actuator diamension/preloading force/loading force/frequency/peak voltage]	**Test conditions**					
	Forces			**Cyclic voltage**		
	Preloading force (**$F_{preload}$**)		Loading force (**F_{load}**)	Frequency (***f***)	Peak Voltage (**V_p**)	Number of cycles
	Value	descriptions				
1/5X5X20/160/670/200/200	160N	approximetely 15% of F_{max}	670N	200Hz	200V	up to 10^8 milion cycles
2/5X5X20/160/670/200/200	160N		670N	200Hz	200V	
3/5X5X20/160/670/200/200	160N		670N	200Hz	200V	
4/5X5X40/170/865/200/200	170N		865N	200Hz	200V	
5/5X5X40/170/865/200/200	170N		865N	200Hz	200V	
6/5X5X40/170/865/200/200	170N		865N	200Hz	200V	
7/10X10X40/620/2680/150/200	620N		2680N	150Hz	200V	
8/10X10X40/620/2680/150/200	620N		2680N	150Hz	200V	
9/10X10X80/750/3750/125/200	750N		3750N	125Hz	200V	
10/10X10X80/750/3750/125/200	750N		3750N	125Hz	200V	
11/10X10X40/1580/3500/150/200	1580N	approximetely 35% of F_{max}	3500N	150Hz	200V	up to 10^8 milion cycles
12/10X10X40/3150/5100/150/200	3150N	approximetely 70% of F_{max}	5100N	150Hz	200V	up to 10_8 milion cycles
13/10X10X40/3600/5510/150/200	3600N	approximetely 80% of F_{max}	5510N	150Hz	200V	up to 10^9 milion cycles
14/10X10X40/3950/5920/150/200	3950N	approximetely 90% of F_{max}	5920N	150Hz	200V	up to 588 kcycles
15/10X10X40/4740/6720/150/200	4740N	5% higher than the F_{max}	6720N	150Hz	200V	up to 10 cycles

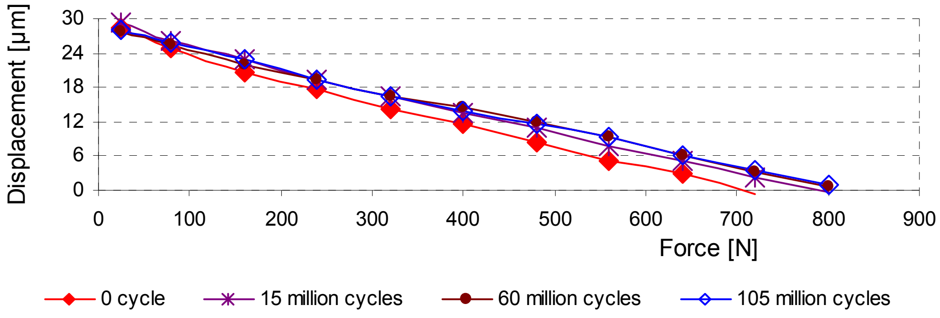

Figure 5.20: Force-displacement characteristic curves for the actuator with the reference number of 1/5x5x20/160/670/200/200 after subjected to different numbers of cycles

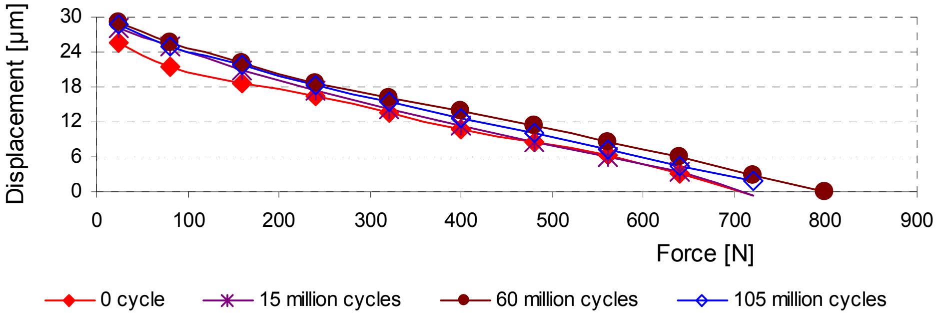

Figure 5.21: Force-displacement characteristic curves for the actuator with the reference number of 2/5x5x20/160/670/200/200 after subjected to different numbers of cycles

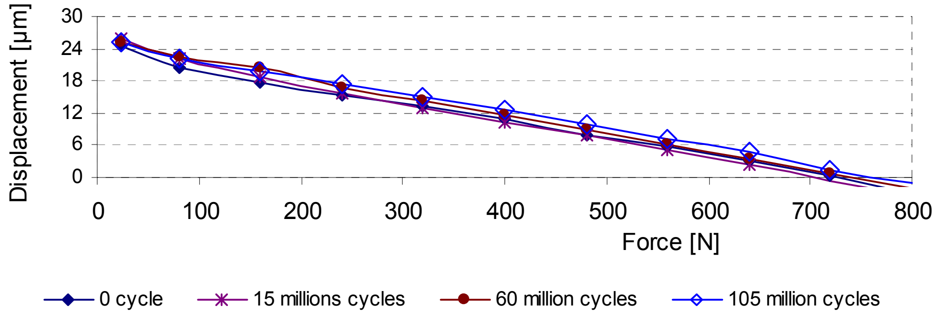

Figure 5.22: Force-displacement characteristic curves for the actuator with the reference number of 3/5x5x20/160/670/200/200 after subjected to different numbers of cycles

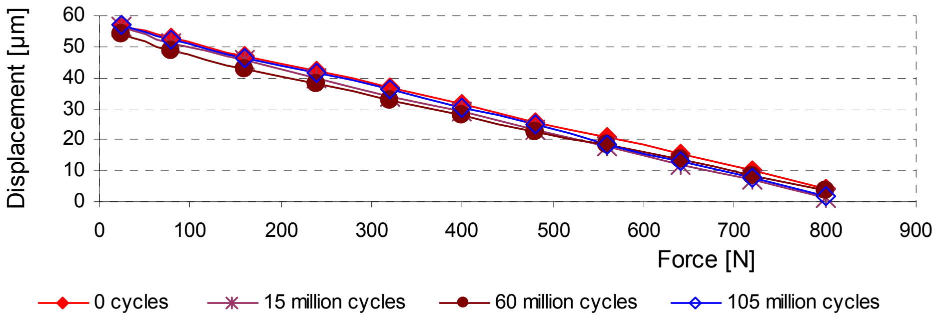

Figure 5.23: Force-displacement characteristic curves for the actuator with the reference number of 4/5x5x40/170/865/200/200 after subjected to different numbers of cycles

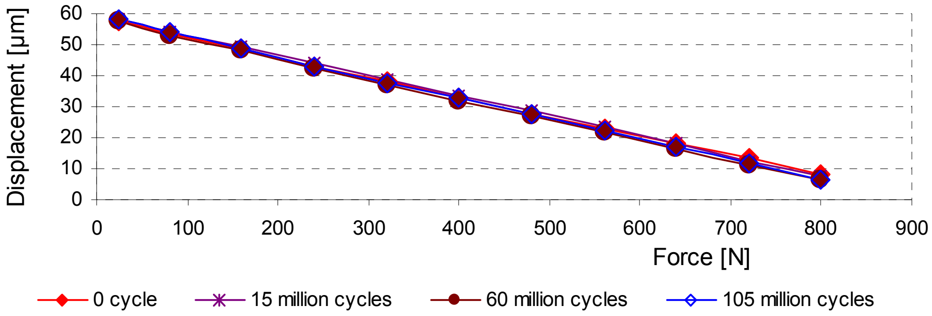

Figure 5.24: Force-displacement characteristic curves for the actuator with the reference number of 5/5x5x40/170/865/200/200 after subjected to different numbers of cycles

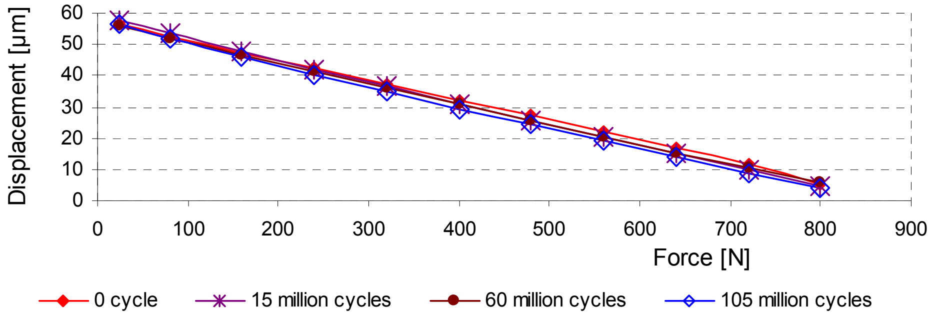

Figure 5.25: Force-displacement characteristic curves for the actuator with the reference number of 6/5x5x40/170/865/200/200 after subjected to different numbers of cycles

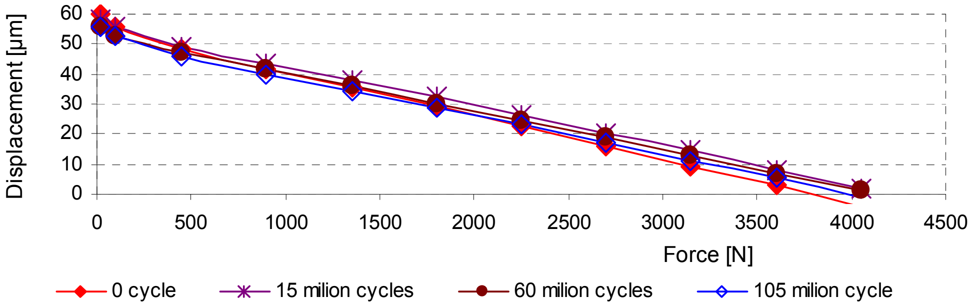

Figure 5.26: Force-displacement characteristic curves for the actuator with the reference number of 7/10x10x40/620/2680/150/200 after subjected to different numbers of cycles

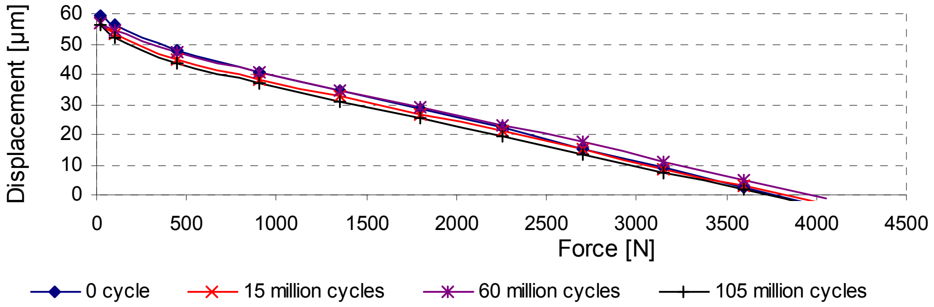

Figure 5.27: Force-displacement characteristic curves for the actuator with the reference number of 8/10x10x40/620/2680/150/200 after subjected to different numbers of cycles

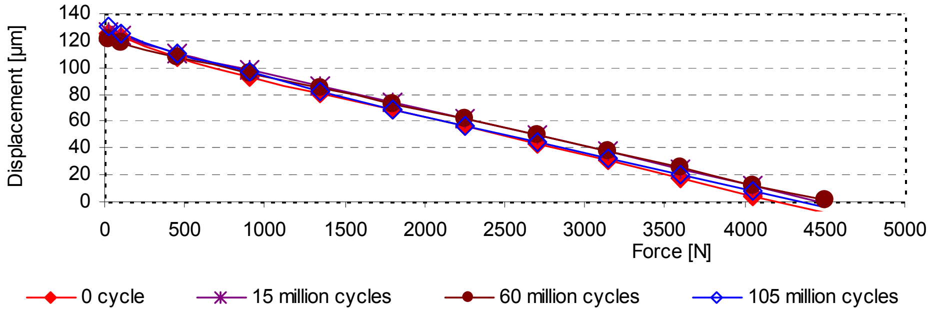

Figure 5.28: Force-displacement characteristic curves for the actuator with the reference number of 9/10x10x80/750/3750/125/200 after subjected to different numbers of cycles

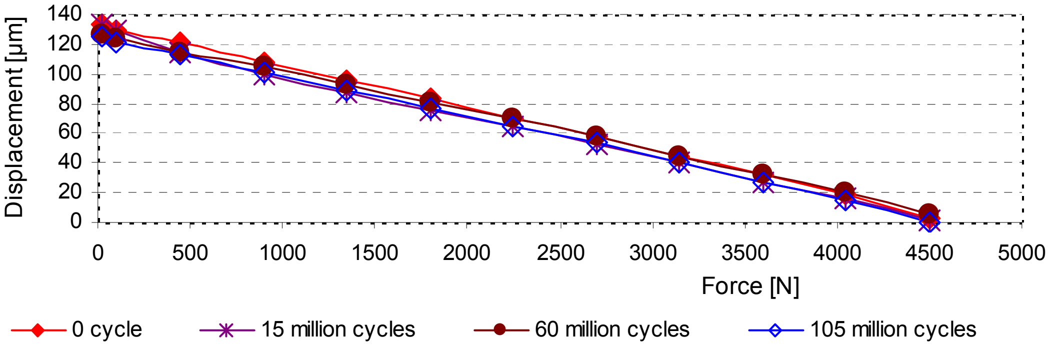

Figure 5.29: Force-displacement characteristic curves for the actuator with the reference number of 10/10x10x80/750/3750/125/200 after subjected to different numbers of cycles

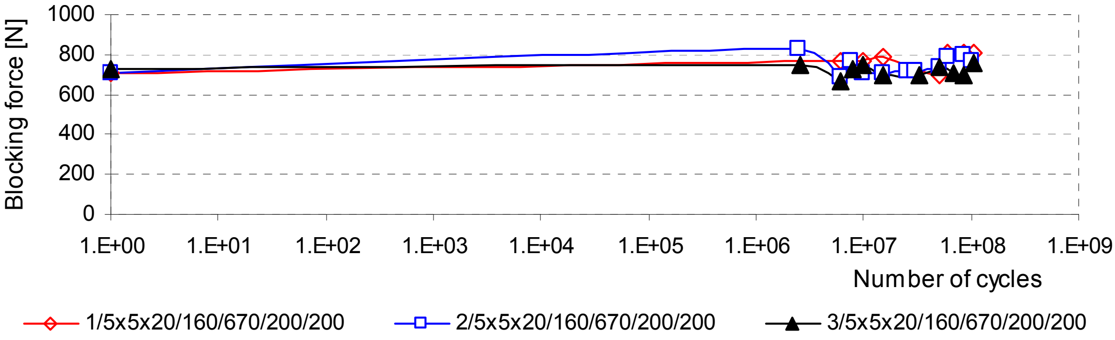

Figure 5.30: Blocking force, F_{max}, as a function of number of cycles for the actuators 1/5x5x20/160/670/200/200, 2/5x5x20/160/670/200/200 and 3/5x5x20/160/670/200

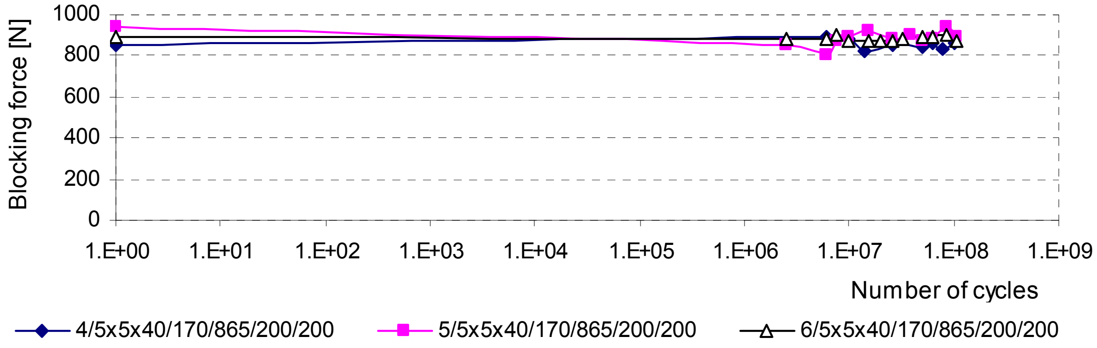

Figure 5.31: Blocking force, F_{max}, as a function of number of cycles for the actuators 4/5x5x40/170/865/200/200, 5/5x5x40/170/865/200/200 and 6/5x5x40/170/865/200/200

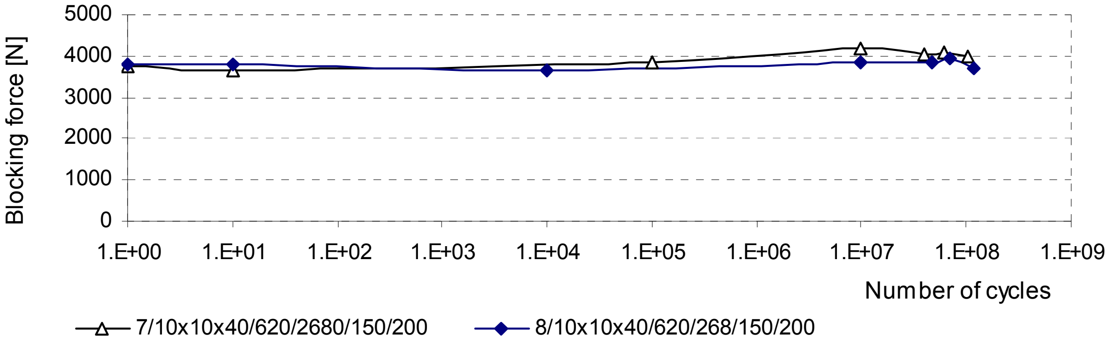

Figure 5.32: Blocking force, F_{max}, as a function of number of cycles for the actuators 7/10x10x40/620/2680/150/200 and 8/10x10x40/620/2680/150/200

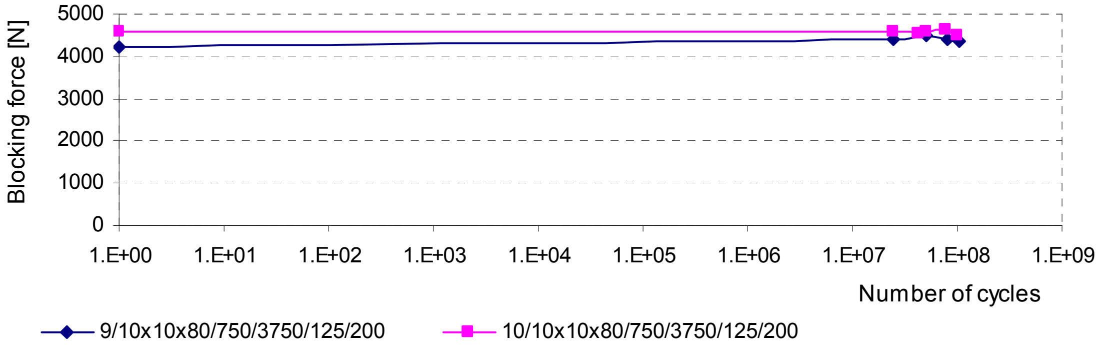

Figure 5.33: Blocking force, F_{max}, as a function of number of cycles for the actuators 9/10x10x80/750/3750/125/200 and 10/10x10x80/750/3750/125/200

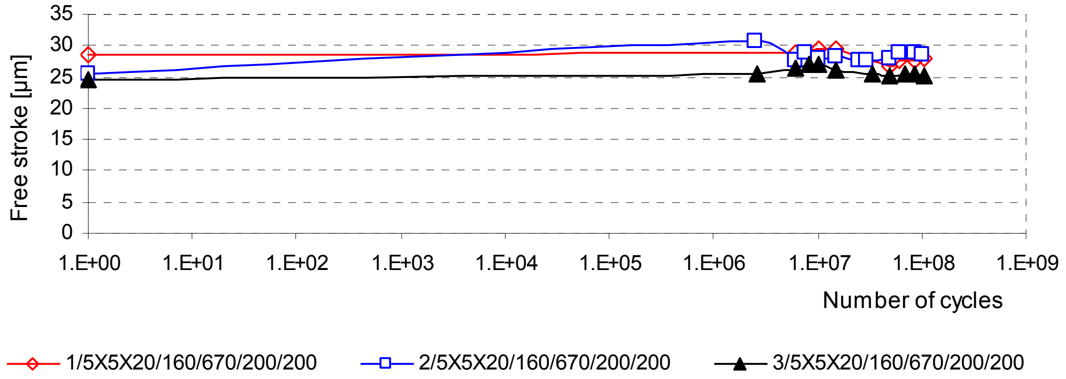

Figure 5.34: Free stroke, ΔL_o, as a function of number of cycles for the actuators 1/5x5x20/160/670/200/200, 2/5x5x20/160/670/200/200 and 3/5x5x20/160/670/200

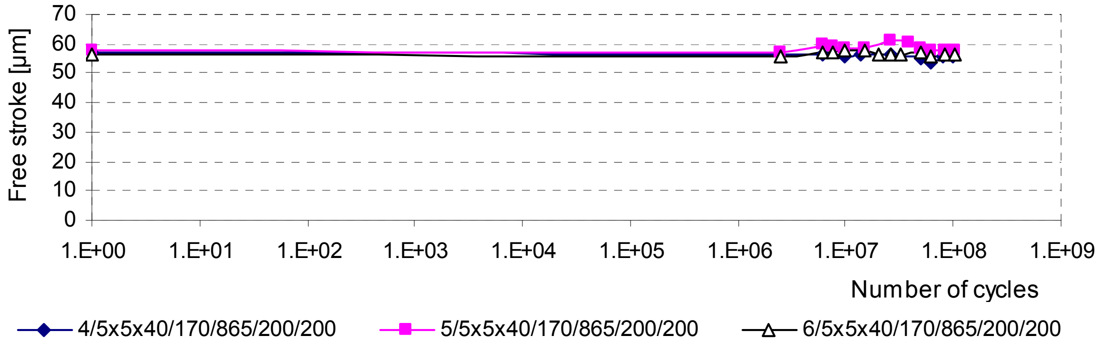

Figure 5.35: Free stroke, ΔL_o, as a function of number of cycles for the actuators 4/5x5x40/170/865/200/200, 5/5x5x40/170/865/200/200 and 6/5x5x40/170/865/200/200

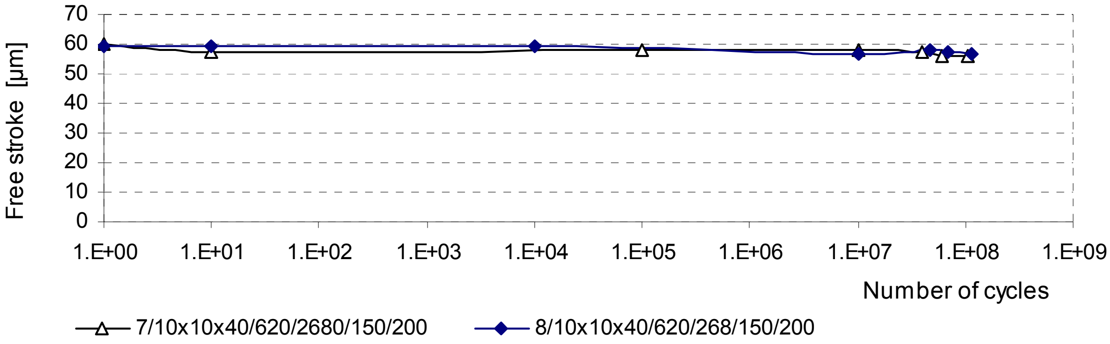

Figure 5.36: Free stroke, ΔL_o, as a function of number of cycles for the actuators 7/10x10x40/620/2680/150/200 and 8/10x10x40/620/2680/150/200

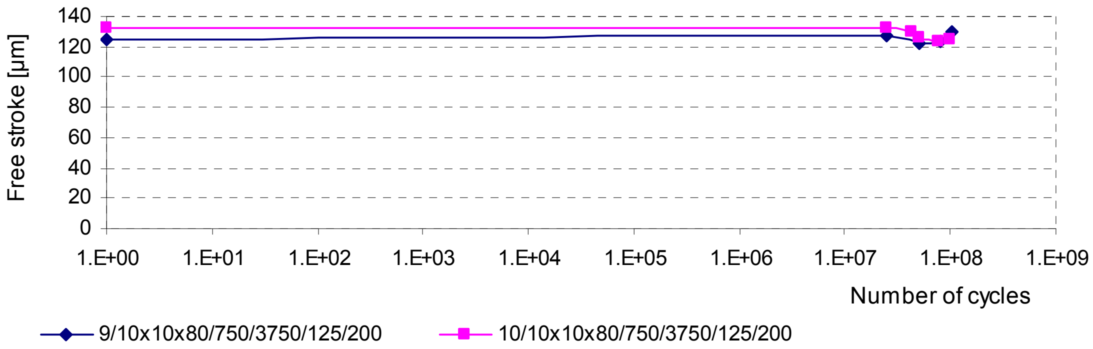

Figure 5.37: Free stroke, ΔL_o, as a function of number of cycles for the actuators 9/10x10x80/750/3750/125/200 and 10/10x10x80/750/3750/125/200

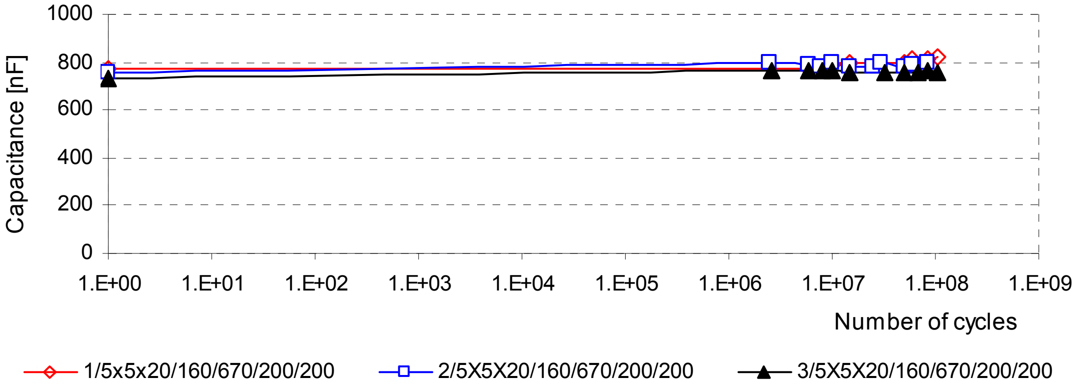

Figure 5.38: Capacitance as a function of number of cycles for the actuators 1/5x5x20/160/670/200/200, 2/5x5x20/160/670/200/200 and 3/5x5x20/160/670/200/200

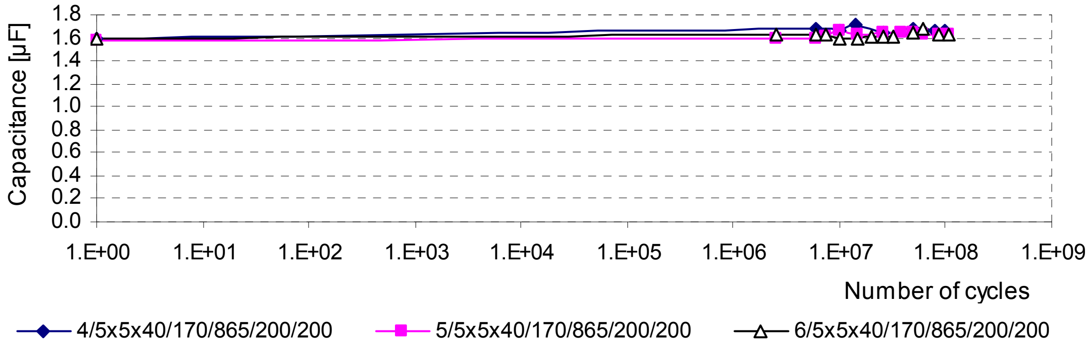

Figure 5.39: Capacitance as a function of number of cycles for the actuators 4/5x5x40/170/865/200/200, 5/5x5x40/170/865/200/200 and 6/5x5x40/170/865/200/200

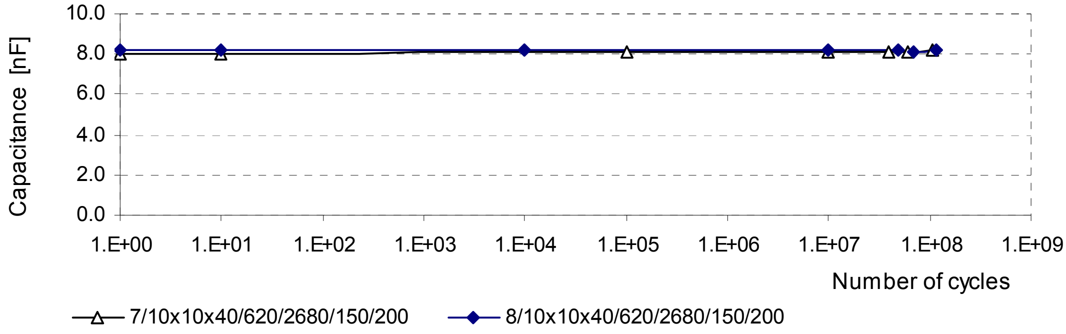

Figure 5.40: Capacitance as a function of number of cycles for the actuators 7/10x10x40/620/2680/150/200 and 8/10x10x40/620/2680/150/200

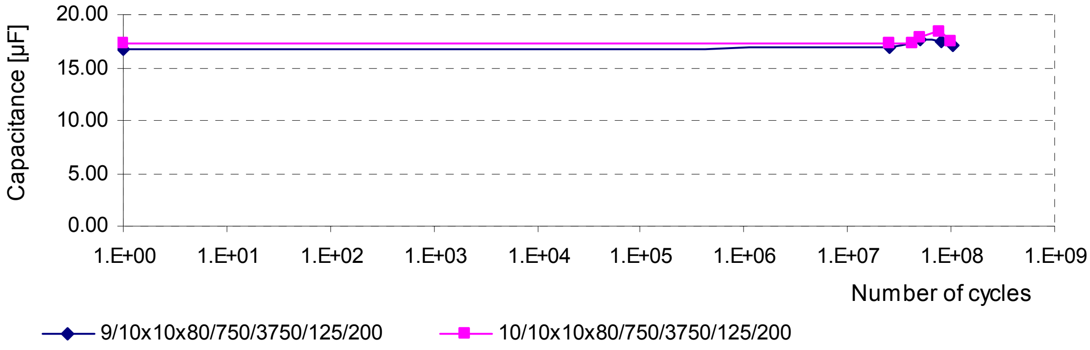

Figure 5.41: Capacitance as a function of number of cycles for the actuators 9/10x10x80/750/3750/125/200 and 10/10x10x80/750/3750/125/200

Force-displacement characteristic curves of the actuators with the reference number 11/10x10x40/1580/3500/150/200 and 12/10x10x40/3150/5100/150/200 that were tested up to 10^8 numbers of cycles are shown in **Figure 5.42** and **Figure 5.43**, respectively. The force-displacement characteristic curves of the actuator with the reference number 13/10x10x40/3600/5510/150/200, that was tested up to 10^9

numbers of cycles is shown in **Figure 5.44**. As shown in these figures, no significant change in the force-displacement curves characteristics has been found.

After running the long-term cyclic operation for a number of cycles the actuators with the reference numbers 14/10x10x40/3950/5920/150/200 and 15/10x10x40/4749/6720/150/200 were found to be electrically broken down after a spark was observed to appear at the middle of the actuator:

(a) 14/10x10x40/3950/5920/150/200 – after approximately 588,000 cycles (1 minute after application of cyclic voltage)

(b) 15/10x10x40/4740/6720/150/200 – after approximately 10 cycles.

The actuators failed probably due to short circuit that occurred between the internal electrodes. The capacitance values of the damaged actuators have been measured and the results are as below:

(a) 14/10x10x40/3950/5920/150/200 – before damage was 7.95µF and after damaged was 8.4µF

(b) 15/10x10x40/4749/6720/150/200 – before damage was 7.923µF and after damage was 8.946µF,

Based on these capacitance values, it was found that the capacitance of the fractured actuators was slightly higher than the capacitance of good actuators.

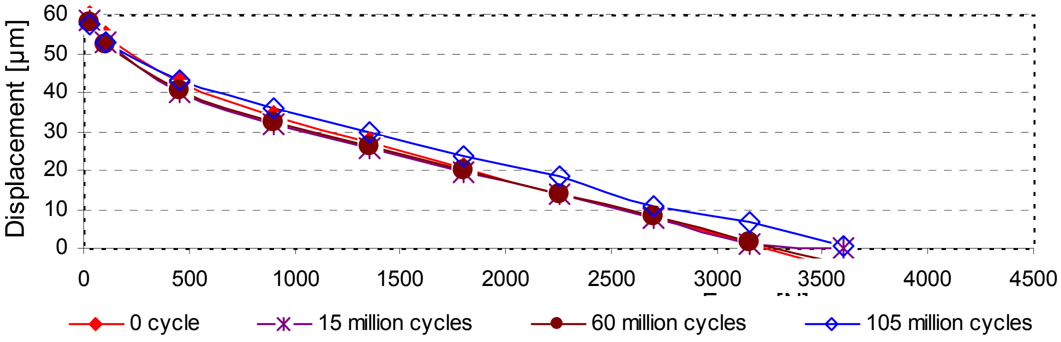

Figure 5.42: Force-displacement characteristic curves of the actuator 11/10x10x40/1580/3500/150/200 after subjected to different numbers of cycles

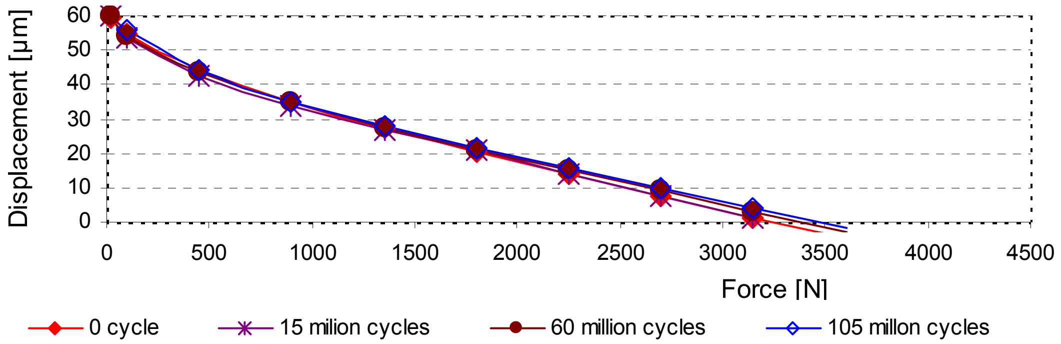

Figure 5.43: Force-displacement characteristic curves of the actuator 12/10x10x40/3150/5100/150/200 after subjected to different numbers of cycles

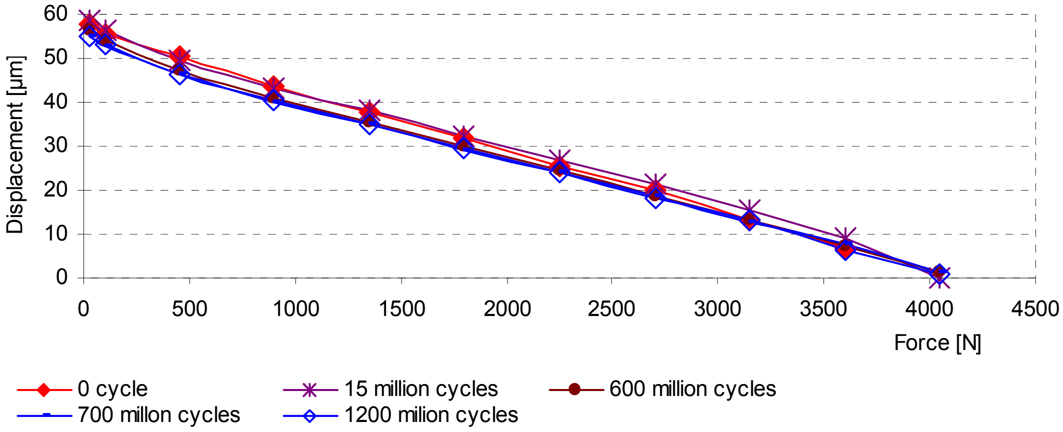

Figure 5.44: Force-displacement characteristic curves of the actuator with the reference number of 13/10x10x40/3600/5510/150/200 after subjected to different numbers of cycles

Figure 5.45 shows the blocking force characteristic, **Figure 5.46** shows the free stroke characteristic and **Figure 5.47** shows the capacitance characteristic of the actuators with the reference numbers of 11/10x10x40/1580/3500/150/200, 12/10x10x40/3150/5100/150/200 and 13/10x10x40/3600/5510/150/200. It can be observed that there are no substantial changes in the blocking force and free stroke. **Figure 5.47** shows a slight increase of capacitance after being tested up to 1 million cycles, but not significant.

Based on these results, it can be concluded that the actuators are able to provide good performance and exhibit consistent characteristics with no degradation during the long-term cyclic operation up to 10^9 cycles, even if they have been subjected to a preloading force of 3600N (80% of blocking force) and loading force of 5510N (approximately 40% higher than the blocking force).

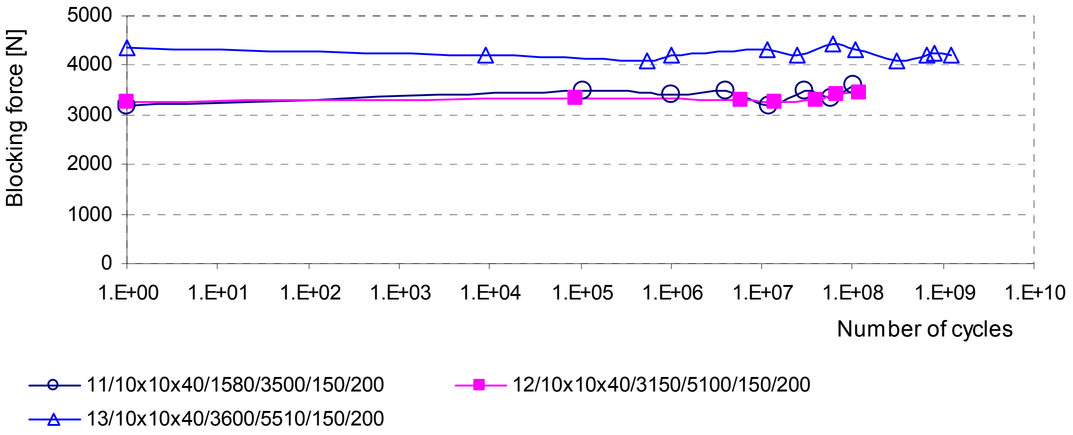

Figure 5.45: Blocking force, F_{max}, as a function of number of cycles for the actuators 11/10x10x10x40/1580/3500/150/200, 12/10x10x40/3150/5100/150/200 and 13/10x10x40/3600/5510/150/200

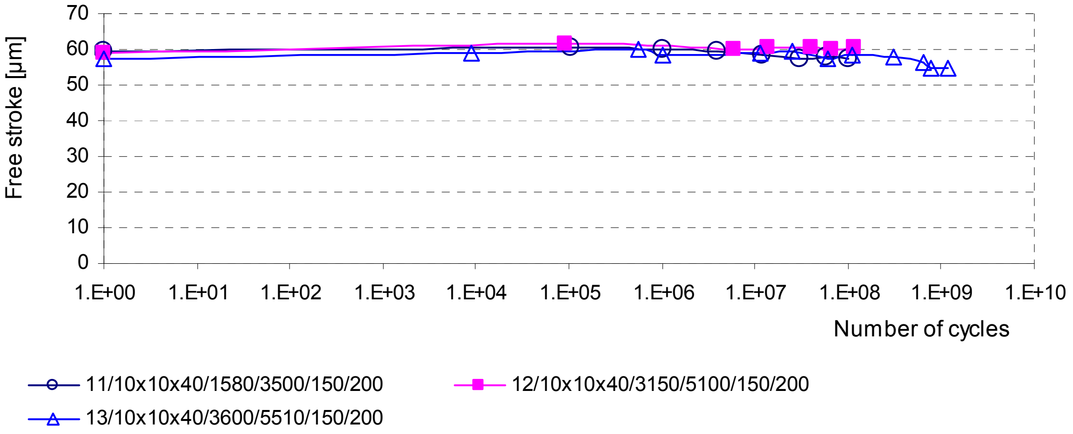

Figure 5.46: Free stroke, ΔL_o, as a function of number of cycles for the actuators 11/10x10x40/1580/3500/150/200, 12/10x10x40/3150/5100/150/200 and 13/10x10x40/3600/5510/150/200

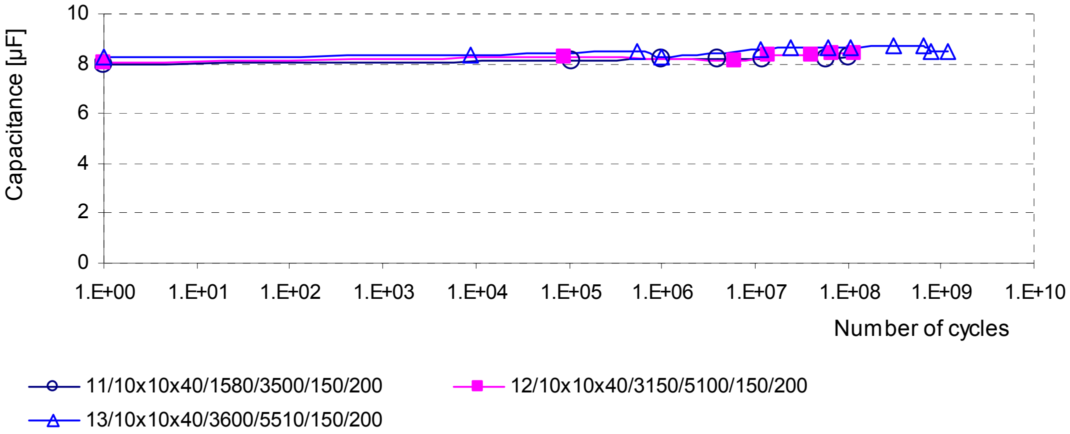

Figure 5.47: Capacitance as a function of number of cycles for the actuators 11/10x10x40/1580/3500/150/200, 12/10x10x40/3150/5100/150/200 and 13/10x10x40/3600/5510/150/200

5.3 Summary

Long-term cyclic tests have been performed for four different dimensions of stack ceramic multilayer actuators (MSCAs) for up to 10^9 cycles under various mechanical loading conditions. Based on the test results, the conclusions of the tests are summarized as follows:

1. A simple method of conducting long-term cyclic performance tests of multi-layer stack ceramic actuator (MSCAs), under various mechanical conditions, has been developed

2. Under the conditions of a loading force of less than F_{max}, field voltage of up to 200V (corresponding to an electrical field strength of 4kV/mm) and cyclic

operations at frequency of up to 200Hz, the tested actuators were able to provide excellent performance with no degradation of blocking force, free stroke and capacitance for up to 10^9 cycles

3. No performance degradation as a function of number of cycles was observed, however the actuators were found to suffer fatal failure (burn and crack) when they were operated under the loading force of 5510N (approximately 40% higher than the blocking force)

4. By using the MSCA actuator, it might be possible to increase the speed of the texturing ESMGs up to 200 indentations per second to improve the productivity of the texturing system.

Chapter 6

Discussion

6.0 Introduction

This chapter presents an overview and brief discussion of the research work that has been presented in the thesis. The discussion is firstly about the conditions surrounding the collapse of ESMGs during workpiece deformation processes. Secondly, experimental evaluations of the performance of ESMGs in friction reduction are discussed. Lastly, the discussion is focused on the performance of piezoelectric actuators that may influence the dimensions of ESMGs during long-term indentation processes. In addition, the factors that determine the optimum prescription of ESMGs to achieve maximum friction reduction are also discussed in this chapter.

6.1 Collapsing of ESMG Due to Material Deformation

In some metal forming processes, certain amount of friction is beneficial, but normally friction is undesirable because it results in tool damage and low quality products. For example, in forward extrusion process, high peak extrusion force might be occurring due to high friction at billet/chamber and billet/die interface. In addition, lower friction decreases die deformation that results in reducing form-errors in the material contained in the die. Therefore, understanding frictional conditions, when considering ways of controlling friction, is essential, in order to obtain components with a desired shape and accurate dimensions. Alongside many other methods of reducing friction, texturing ESMGs on the work material surface, in order to change interfacial friction conditions at the work material/tools interface, has been found promising.

Deformation behaviours of the workpiece and the ESMGs, which act as lubricant pockets, are interrelated and rather complex. The changes of the ESMGs' (pockets) characteristics, such as geometry and dimensions, during deformation of the workpiece, determine the lubricant volume that is squeezed out from the pocket on to the contact surface. Since experimental investigation of the deformation behaviour of ESMGs with different shapes and dimensions would be very expensive and is time-consuming, a 3D FE model was used to simulate the deformation of ESMGs during ring compression.

The model was developed using a sub-modelling technique. In this technique, a cube, with the dimensions of approximately 0.5 x 0.5 x 0.5 mm and a micro-sized indentation (ESMG) on its surface, acted as a sub-model. The sub-model was meshed using finite elements with the edges not exceeding 5μm to obtain accurate representation. The boundary of the sub-model was assumed to represent the deformation of the ring specimen that acted as the global-model.

In this study, only one indentation was simulated to simplify the calculation performed by the FE program. Therefore, interaction between indentations that may occur during the deformation was not considered. Another factor that was not considered in this simulation was the lubrication itself. However, the agreement between the simulated (calculated) and the experimental results (as shown in **Figure 3.8**, in section 3.2.1.3) are the evidence of model ability to give an acceptable representation of the real situation. Therefore, the FE model was considered capable of showing the dimensional changes in ESMGs during workpiece deformation.

Three different shapes of ESMGs, i.e. conical, cylindrical and spherical, with various dimensions, were simulated using this model. Based on the simulation results, it was predicted that a spherical ESMG with a depth of approximately 15μm, a diameter of 152μm and opening angle, φ, of 20° would be able to provide the maximum amount of lubricant throughout the deformation process up to 50% ring height reduction and leave minimal surface defects.

6.2 Influence of ESMGs on Interfacial Friction

Various depths and densities of spherical ESMGs with an opening angle φ from approximately 10° to 25° were evaluated experimentally using two different test methods, i.e. ring test and forward extrusion test. Due to the ring test representing only simple deformation behaviour, a forward extrusion test was also performed in order to evaluate ESMGs under more complex deformation conditions.

6.2.1 Ring test

The aim of this test was to evaluate the influence of various prescriptions of ESMGs, which were textured either on the die surface or the workpiece. In the ring test, the measurements of the internal diameter and the height of the ring are crucial. Thus, these two parameters were measured very carefully and measurements repeated several times to obtain correct results, even though this was a tedious and time-consuming procedure. The results of the tests were superimposed on the calibration curves that were generated by 2D FE simulation of the ring test to obtain the average value of friction coefficient, μ.

The test results confirmed that ESMGs textured on the compression die surface increase interfacial friction at the die/workpiece interface. During the deformation operation, the workpiece material has been found to flow in and out of the ESMGs' cavities. It appears that ESMGs textured on the die surface oppose the relative motion of the two sliding surfaces of the specimen and the die, which results in a higher friction coefficient, μ. It is important to note that the results of this test are in agreement with the results of the FE simulation that was performed by H. Saiki and Y. Maruno [87], but contradict with the results of the experimental tests made by Geiger, M et al [37] and Wagner, K et al. [38]. The contradiction of these results may be due to different type of lubrication and different texturing technique used in their experimental trials.

However, ESMGs textured on the work material surface have been found to improve lubrication performance, which results in a lower friction coefficient, μ. It has been confirmed that ESMGs' density and depth play an important role in friction reduction. In addition, by comparing the experimental ring test results with those generated by the FE simulation (Chapter 3), the ESMGs' collapsing behaviour has been confirmed as an important factor influencing the reduction of interfacial friction. Shallow ESMGs (less than 9μm depth) with low density (less than 20%) have been found to contribute less to friction reduction due to ESMGs collapsing at the beginning of the deformation process.

By considering that for a given ESMG density, no further friction reduction is achieved with the depth of ESMGs being greater than 13μm, and this depth giving minimum surface defects. Therefore, it can be considered that 13μm is the optimum ESMG depth. Another interesting finding is that, for ESMGs with depths of 13μm, higher ESMG density results in lower interfacial friction. However, it has been found that after the deformation of approximately 45%, increasing ESMG density does not change the interfacial friction due to ESMGs collapsing before achieving 45% ring height reduction (see **Figure 3.9** in section 3.3.1).

6.2.2 Extrusion test

To evaluate frictional conditions in a more complex process, the forward extrusion test was used. Since the process is very well known, the results of the test were easy to interpret and analyse. Based on the test results, the influence of various ESMG prescriptions on friction in two different interfacial areas, i.e. 1) the billet/chamber interface and 2) the billet/die interface, has been defined. Different friction conditions at the billet/chamber interface were recognised by comparing the slope of force-displacement curves at the steady state stage. Whereas, the different friction conditions at the billet/die interface were recognised by comparing the total work.

Generally, texturing ESMGs on the billet surface has been confirmed to reduce friction at both the billet/chamber interface and the billet/die interface. However, the ESMGs at the billet/chamber interface were not significantly deformed during the extrusion process. For this reason, the lubricant at the billet/chamber interface was not expelled from the ESMGs. As a result, the slope difference between force-displacement curves was rather small. This indicates that ESMGs do not contribute significantly to friction reduction at the billet/chamber interface. On the contrary, the ESMGs at the billet/die interface, especially near the exit land aperture interface, were significantly deformed, which caused the lubricant being expelled from the ESMGs and flowing on to the billet surface. However, the test results show that shallow ESMGs (less than 12µm depth), with a density of less than 10%, contribute less to friction reduction at the billet/die interface as compared with deeper ESMGs (greater than 15µm).

6.3 Optimal ESMGs Prescription in Metal Forming Operations

The optimal ESMGs prescription was determined by considering the ability of ESMGs to provide a maximum reduction of interfacial friction throughout the deformation operation and give a minimum surface defects at the end of the operation.

Two steps of determining the optimal ESMG prescriptions were used. Firstly, the finite element simulation method was used to evaluate the collapsing trend for different geometries and dimensions of ESMGs (see Chapter 3). Based on the results of FE simulation, it has been confirmed that a spherical ESMG gives uniform surface deformation throughout the material deformation. The spherical ESMG with 15μm depth, diameter of 152μm and opening angle, φ, of 20° was assumed to be an optimal ESMG geometry, which is able to store and distribute lubricant during the compression of the ring for up to 50% reduction. Secondly, the merit of different depths and densities of the spherical ESMG on friction reduction was evaluated experimentally using ring test and forward extrusion test.

The results of the simulations and experimental tests have shown that the deformation behaviour of ESMGs was influenced by many factors such as the position of the ESMGs on the workpiece surface and the position of this surface with influence to the die. These factors have been found to influence the ability of ESMGs to store and distribute lubricant during the deformation of the material and finally result in different interfacial conditions. In reality, metal forming operations are burdened with numerous considerations such as end product shape, dimensions and function, tool design, production process, workpiece material and type of lubricant. Due to these reasons, in order to control friction using ESMGs in metal forming, the determination of the optimal prescriptions of ESMGs for a specific product and a specific metal forming process needs to be done. The determination procedure should include the whole process of product development, i.e. starting from product design and end at product manufacture, as shown in **Figure 6.1**.

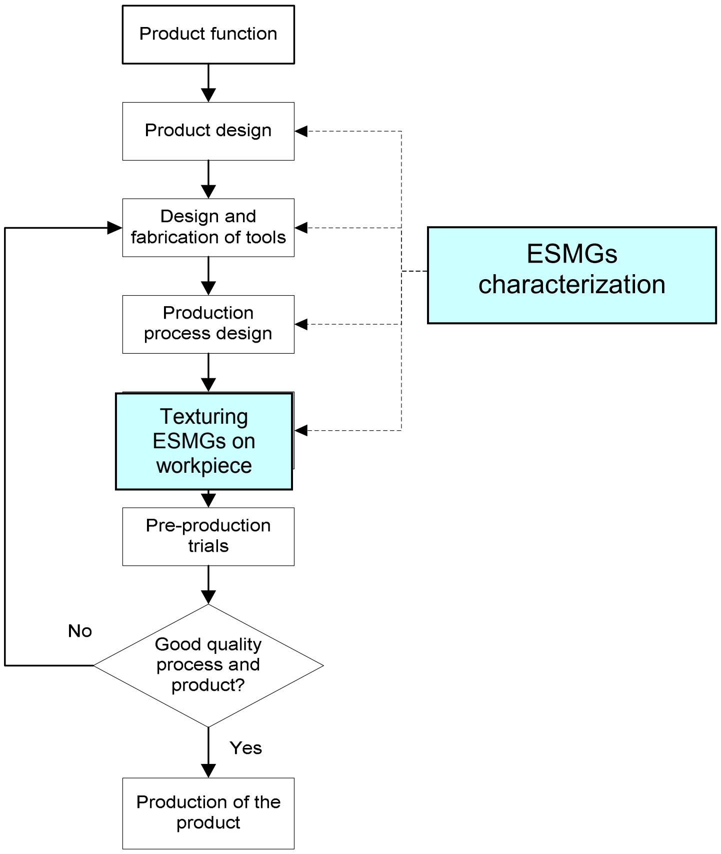

Figure 6.1: Proposed procedure for determining the optimal prescription of ESMGs in a metal forming process of a new product

6.4 Performance of MSCA Actuators Under Long-term Cyclic Operation

In order to increase the productivity of the indentation texturing system, the operating frequency of the MSCA actuator, which is used to actuate the indentation tool, should be increased. However, as reported in literature, the MSCA actuator characteristics may degrade under long term operation, which may result in the change of the ESMG depth and diameter. Unfortunately, the actuator used in this research was a newly developed product, so information related to its long-term performance was not available. For this reason, it was decided that the long-term performance of the new actuator would be evaluated with a view to assessing its degradation and, if necessary, introducing a possible compensating method for the decay of the actuator characteristics.

The force and stroke produced by the actuator are the parameters that apply during texturing operations. Therefore, evaluation of these parameters is essential. In addition to force and displacement, the actuator’s electrical properties, such as capacitance, can also be measured and evaluated. In order to shorten the test duration, the actuators were tested under cyclic frequency of 125Hz, 150Hz or 200Hz, depending on the actuator dimensions. Under these cyclic frequencies, the total test duration was shortened by up to 75% compared to the time taken under the actual texturing operation frequency of 50Hz. Incidentally, the highest cyclic frequency of 200Hz was also successfully tried on the texturing system but this was done outside the scope of the research reported in this thesis.

The results of the tests provided a clear picture of the actuator's performance under long-term cyclic operation. The results confirmed that the piezoelectric actuators, made of medium soft-doped PZT material layers with a thickness of 50μm, as used in the ESMGs texturing system, were able to deliver an acceptable performance, with no substantial changes in force, stroke and capacitance during the long-term cyclic operation for up to 10^9 cycles. Therefore, assuming that the ESMGs texturing system is operated for 8hrs/day and 7 days/week, it can be confirmed that the system using the tested type of actuator is able to produce consistent ESMG characteristics for at least 99 weeks or 2 years of continuous operation. Thus, based on the evaluation results, the ESMGs texturing system has proven to be fast, reliable and consistent.

Chapter 7

Summary of Conclusions, Main Original Contributions of the Thesis and Recommendations for Future Work

7.1 Summary of Conclusions

This study has investigated the potential for using ESMGs to reduce interfacial friction in metal forming operations. It encompassed three research themes: 1) FE simulation of the collapsing behaviour of various shapes of ESMGs during workpiece deformation, 2) experimental evaluation of the performance of ESMGs in reducing interfacial friction in metal forming operations and 3) experimental evaluation of the reliability of the existing ESMG texturing system. This research has demonstrated a successful method for reducing friction using ESMGs. The results and the findings obtained indicate that the objectives outlined in section 1.2 have all been met.

A 3D FE model has been used as a basis for predicting ESMG collapsing behaviour during workpiece deformation for various initial shapes and dimensions of ESMGs. Based on the results of FE simulations, it has been confirmed that a spherical ESMG with the depth of approximately 15µm, the diameter of 152µm and opening angle, φ, of 20° is able to store and distribute lubricant during the compression of the ring for up to 50% of the ring height reduction. Therefore, it was assumed to be an optimal ESMG geometry.

A series of experimental trials on the performance of various ESMGs' prescriptions in reducing friction have been performed using a ring test and a forward extrusion test. The experimental results of the ring test have shown that ESMGs textured on the metal forming tool increase friction. It has been found that the workpiece material was deformed and flowed in to the ESMGs' cavities. Due to this phenomenon, ESMGs textured on the die surface oppose the relative motion of the two sliding surfaces of the work material and the die, which results in a higher friction coefficient, μ.

ESMGs textured on the work material surface reduce friction. The ESMGs' characteristics, i.e. density and depth, have been found to play important roles in friction reduction during deformation processes. However, the ESMGs' optimal characteristics for the upsetting process and the forward extrusion process have been found to be different, i.e. the optimal ESMG for upsetting has depth of 13µm and the density of 30%, whereas for forward extrusion it has depth of 30µm and the density of approximately 25%.

The results of the extrusion tests show that the ESMGs at the billet/chamber interface are insignificantly deformed. While, the ESMGs at the billet/die interface are significantly deformed during the extrusion process. Due to this reason, the amount of lubricant expelled from the ESMGs and flowing on to the billet/chamber and billet/die interfaces is different, which results in a different magnitude of the interfacial friction reduction. In short, the deformation behaviour of ESMGs depends on the plastic strain distribution at the workpiece/tool interface, which is different for different metal forming processes and components.

The texturing system has been proven to enable the creation of of 0.5 - 50μm deep ESMGs at a rate of up to 200Hz on undulating surfaces. It has been confirmed that the peizoactuator actuator used is able to deliver good performance, with no substantial changes in force and stroke during long-term cyclic operations of up to 10^9 cycles, which enables achieving consistent ESMG characteristics such as depth and diameter for up to 2 years texturing operation.

As a whole, this research has shown the potential for reducing and controlling friction in metal forming operations by using ESMGs.

7.2 Main Original Contributions of the Thesis

This research work resulted in several original contributions that filled the knowledge gaps in the functional surface engineering and its application in metal forming operations in the form of ESMGs. The original contributions of this research include:

1. A 3D FE model, using a special procedure involving sub-modelling, has been developed to simulate collapsing of an indented ESMG during workpiece deformation. It enables the collapsing phenomenon of

ESMGs, with various initial characteristics such as shape and dimensions, to be analysed without performing a physical experiment that would be costly and time consuming.

2. A method of evaluating the performance of ESMGs in friction reduction using ring test has been proposed. The developed procedures enabled the determination of the optimum ESMGs' characteristics for friction reduction in the upsetting type of metal forming operations.

3. A method of evaluating the performance of ESMGs in reduction of interfacial friction during forward extrusion has been proposed. The developed procedures enabled the evaluation of friction reduction at billet/chamber and billet/die interfaces. The evaluation results have confirmed that ESMGs contributed to friction reduction at both interfacial areas i.e. billet/chamber and billet/die. ESMGs at the billet/die interface have been found much more deformed compared with ESMGs at the billet/chamber interface. Thus, they provide more significant friction reduction then ESMGs at the billet/chamber interface.

4. As part of ESMGs texturing system development, the piezoelectric actuator (multi-layer stack ceramic actuator (MSCA)) used to actuate the diamond indenter has been proven reliable and able to deliver consistent stroke and force for up to 10^9 cycles of operations. This has demonstrated high performance and effectiveness of the ESMG

texturing system, and, therefore, its suitability for industrial applications.

5. And lastly, since the magnitude of friction reduction has been found influenced by several factors such as position of ESMG, depth of ESMG, workpiece deformation conditions, ESMG collapsing behaviour and lubricant performance, a model of ESMG application in the new process development has been proposed.

7.3 Recommendations for Future Work

The possibility of using ESMGs to control and reduce friction in metal forming operations has been defined in this thesis. As discussed earlier, the proposed method is not without its limitations and, therefore, further improvements are needed in order to enhance its chances of practical applications. The improvements identified include:

1. 3D FE model: Although the model is able to demonstrate the deformation behaviour of ESMGs, it can still be improved by considering the initial material pile-up caused by indentation, the lubrication interaction between the die and the specimen surface, as well as interaction between ESMGs. However, this requires a high capability computer system to shorten the time of simulation.

2. ESMG texturing system: It cannot be denied that productivity and quality are important aspects in all manufacturing operations. To improve the productivity of the proposed texturing system, one possible way is by installing multi-indentation tools on one system that can operate in parallel. Another way is by increasing the indentation operating frequency to a value that will not cause the actuator to suffer damage. Extending system ability to cover 3D irregular surfaces is also desired.

3. Actuator failure monitoring system: Based on the evaluation results, when the actuator is subjected to a force higher than its maximum blocking force, it may suffer damage (electrical breakdown) before achieving 10^8 cycles. The proposed evaluation method was not able to show any indication, in terms of force, stroke or capacitance, of imminent failure. To avoid unexpected cessation of the texturing operation, further research can be performed to understand the failure phenomenon.

4. Economical factors: Although the research has led to promising findings, the operation of texturing ESMGs is an additional element in the production process that must surely incur an additional cost. In reality, metal forming operations are burdened with numerous considerations such as end product shape, dimensions and function, tool design, production process, workpiece material and type of lubricant. Therefore, further research to define the cost effectiveness of

implementing the proposed method for a specific product and metal forming operation needs to be done. The research should include the whole process of product development, i.e. starting from product design and ending at product manufacture.

References

1. Giardini, C., E. Ceretti, and G. Maccarini, *Formability in extrusion forging: The influence of die geometry and friction conditions.* Journal of Materials Processing Technology, 1995. **54**(1-4): p. 302-308.
2. Hallstrom, J., *Influence of friction on die filling in counterblow hammer forging.* Journal of Materials Processing Technology, 2000. **108**(1): p. 21-25.
3. Yuli, L., et al., *A study of the influence of the friction conditions on the forging process of a blade with a tenon.* Journal of Materials Processing Technology, 2002. **123**(1): p. 42-46.
4. Kato, K., *Wear in relation to friction -- a review.* Wear, 2000. **241**(2): p. 151-157.
5. Dubar, M., et al., *Wear criteria of cold forging tools.* Surface Engineering, 2001. **17**(2): p. 119-122.
6. Barrau, O., et al., *Analysis of the friction and wear behaviour of hot work tool steel for forging.* Wear -14th International Conference on Wear of Materials, 2003. **255**(7-12): p. 1444-1454.
7. Dubar, M., A. Dubois, and L. Dubar, *Wear analysis of tools in cold forging: PVD versus CVD TiN coatings.* Wear - 15th International Conference on Wear of Materials, 2005. **259**(7-12): p. 1109-1116.
8. Kataoka, S., et al., *Tribology of dry deep-drawing of various metal sheets with use of ceramics tools.* Surface and Coatings Technology - Proceedings of the 30th International Conference on Metallurgical Coatings and Thin Films, 2004. **177-178**: p. 582-590.
9. Blaha, F. and B. Langenecker, Naturwissenschaften, 1955. **42**: p. 556.
10. Langenecker, B., *Effects of ultrasound on deformation characteristics of metals.* IEEE Transactions on Sonics and Ultrasonics, 1966. **13**: p. 1-8.
11. Pohlman, R. and E. Lehfeldt, *Influence of ultrasonic vibration on metallic friction.* Ultrasonics, 1966. **4**: p. 178-185.
12. Lehfeldt, F., *Influence of surface friction by ultra-sonic vibration and examples of technical application.* Wear, 1969. **13**(4-5): p. 372.
13. Mikhenl'man, A.I. and A.N. Mashchinov, *Effect of ultrasonic vibrations on friction between solids.* Wear, 1970. **16**(5): p. 382.
14. Andreev, G., L. Kobtseva, and T.E. Mirotvorskii, *Internal friction and heat release in structural and tool steels subjected to intense ultrasonic vibrations.* Ultrasonics, 1973. **11**(3): p. 143.
15. Atanasiu, N., *The wire drawing process with axial ultrasonic vibration of the die.* Ultrasonics, 1976. **14**(2): p. 69-72.

16. Goto, H., M. Ashida, and Y. Terauchi, *Effects of ultrasonic vibration on the wear characteristics of a carbon steel: Analysis of the wear mechanism.* Wear, 1984. **94**(1): p. 13-27.
17. Pasierb, A. and A. Wojnar, *An experimental investigation of deep drawing and drawing processes of thin - walled products with utilization of ultrasonic vibrations.* Journal of Materials Processing Technology, 1992. **34**(1-4): p. 489-494.
18. Lucas, M., *Vibration sensitivity in the design of ultrasonic forming dies.* Ultrasonics, 1996. **34**(1): p. 35-41.
19. Kumar, V.C. and I.M. Hutchings, *Reduction of the sliding friction of metals by the application of longitudinal or transverse ultrasonic vibration.* Tribology International, 2004. **37**(10): p. 833-840.
20. Daud, Y., M. Lucas, and Z. Huang, *Modelling the effects of superimposed ultrasonic vibrations on tension and compression tests of aluminium.* Journal of Materials Processing Technology, 2007. **186**(1-3): p. 179-190.
21. Hung, J.-C., Y.-C. Tsai, and C. Hung, *Frictional effect of ultrasonic-vibration on upsetting.* Ultrasonics, 2007.
22. Mousavi, S.A.A.A., H. Feizi, and R. Madoliat, *Investigations on the effects of ultrasonic vibrations in the extrusion process.* Journal of Materials Processing Technology - 3rd International Conference on Advanced Forming and Die Manufacturing Technology, 2007. **187-188**: p. 657-661.
23. Ashida, Y. and H. Aoyama, *Press forming using ultrasonic vibration.* Journal of Materials Processing Technology - 3rd International Conference on Advanced Forming and Die Manufacturing Technology, 2007. **187-188**: p. 118-122.
24. Lakshmipathy, R. and R. Sagar, *Effect of die surface topography on die-work interfacial friction in open die forging.* Int.J.Mach.Tools Manufact., 1992. **32**(5): p. 685-693.
25. Azushima, A. and T. Tanaka, *Lubricant behavior trapped within pockets on workpiece surface in lubricated upsetting by means of direct flourescence observation technique.* Annals of the CRIP, 2000. **49**(1): p. 165-168.
26. Wihlborg, A. and R. Crafoord, *Steel sheet surface topography and its influence on friction in a bending under tension test.* International Journal of Machine Tools & Manufacture, 2001. **41**: p. 1953-1959.
27. Azushima, A., *Direct observation of interface for tribology in metal forming.* Metal Forming Science and Practice, 2002: p. 61-85.
28. Bay, N., I.B. Jakob, and J.L. Andreasen, *Studies on micro plasto hydrodynamic lubrication in metal forming.* Metal Forming Science and Practice, 2002: p. 115-134.
29. Pfestorf, M., U. Engel, and M. Geiger, *3D surface parameters and their application on deterministic textured metal sheets.* International Journal of Machine Tools and Manufacturing, 1998. **38**(5-6): p. 607-614.
30. Evans, C.J. and J.B. Bryan, *"Structured", "Textured" or "Engineered" Surfaces.* Annals of the CIRP, 1999. **48**(2): p. 541-556.
31. Costa, H.L. and I.M. Hutchings, *Effects of die surface patterning on lubrication in strip drawing.* Journal of Materials Processing Technology, 2008.

32. Rasp, W. and C.M. Wichern, *Effects of idealized surface geometry on lubricant entrapment during plane-strain upsetting - an FEM study.* Steel Grips : Suppl.Metal Forming, 2004. **2**: p. 355-359.
33. Kudo, H., *A Note on the Role of Microscopically Trapped Lubricant at the Tool-Works Interface.* International Journal of Mechanical Sciences, 1965. **7**: p. 383-388.
34. Azushima, A., et al., *Direct observation of microcontact behavior at the interface between tool and workpiece in lubricated upsetting.* Annals of the CIRP, 1996. **45**(1): p. 205-210.
35. Bech, J., N. Bay, and M. Eriksen, *A study of mechanisms of liquid lubrication in metal forming.* Annals of the CIRP, 1998. **47**(1): p. 221-226.
36. Varenberg, M., G. Halperin, and I. Etsion, *Different aspects of the role of wear debris in fretting wear.* Wear, 2002. **252**: p. 902-910.
37. Geiger, M., U. Popp, and U. Engel, *Excimer laser micro texturing of cold forging tool surfaces-influence on tools life.* Annals of the CIRP, 2002. **51**(1): p. 231-234.
38. Wagner, K., A. Putz, and U. Engel, *Improvement of tool life in cold forging by locally optimized surfaces.* Journal of Materials Processing Technology - Proceedings of the 11th International Conference on Metal Forming 2006, 2006. **177**(1-3): p. 206-209.
39. Shimizu, I., *Influence of workpiece surface topography on the mechanisms of liquid lubrication in strip drawing.* Transactions of the ASME, 2001. **123**: p. 290-294.
40. Rasp, W. and C.M. Wichern, *Effect of surface-topography directionality and lubrication condition on friction behaviour during plastic deformation.* Journal of Materials Processing Technology, 2002. **125-126**: p. 379-386.
41. Pettersson, U. and S. Jacobson, *Influence of surface texture on boundary lubricated sliding contacts.* Tribology International, 2003. **36**(11): p. 857-864.
42. Pettersson, U. and S. Jacobson, *Friction and wear properties of micro textured DCL coated surfaces in boundary lubricated sliding.* Tribology letters, 2004. **17**(3): p. 553-559.
43. Schreck, S. and K.H. Zum Gahr, *Laser-assisted structuring of ceramic and steel surfaces for improving tribological properties.* Applied Surface Science, 2005. **247**(1~5): p. 616-622.
44. Rosochowska, M., et al., *Flexible tool system for creation of Engineered Surface Micro-Geometries.* First International Conference on Multi-Material Micro Manufacture Proceedings, 2005: p. 189-192.
45. Wang, D., Y. Fotinich, and G.P. Carman, *Influence of temperature on the electromechanical and fatigue behavior of piezoelectric ceramics.* Journal of Applied Physics, 1998. **83**(10): p. 5342-5350.
46. Hooker, S., et al., *Fatigue resistant miniature piezoceramic actuators.* Journal of Intelligent Material Systems and Structures, 2007. **18**: p. 153-157.
47. Cain, M.G., *Experiment measurement methods for the evaluation of degradation in piezoelectric ceramic.* NPL UK Report CMMT(A), 1998. **116**.
48. Koh, J.-H. and T.-g. Kim, *Reliability of* $Pb(Mg,Nb)O_3$-$Pb(Zr, Ti)O_3$ *multilayer ceramic actuators by Weibull method.* Microelectronics and Reliability, 2006. **46**(1): p. 183-188.

49. Wang, X., et al., *Optimizations of the surface texture for silicon carbide sliding in water.* Applied Surface Science, 2006. **253**: p. 1282-1286.
50. Banks, B.A., S. K.Rutledge, and S.A. Snyder. *Electric arc and electrochemical surface texturing technologies*. in *11th International Conference on Surface Modification Technologies*. 1997. Paris, France: National Aeronautics and Space Administration.
51. Costa, H.L. and I.M. Hutchings, *Hydrodynamic lubrication of textured steel surfaces under reciprocating sliding conditions.* Tribology International, 2007. **40**: p. 1227-1238.
52. Arbuckle, H.J., *Advanced laser texturing tames tough tasks*, in *Metal Forming Magazine Online*. 1996.
53. Pantelis, D.I., G. Pantazopoulos, and S.S. Antoniou, *Wear behaviour of anti-galling surface textured gray cast iron using pulsed-CO_2 laser treatment.* Wear, 1997. **205**: p. 178-185.
54. Geiger, M., S. Roth, and W. Becker, *Influence of laser-produced microstructures on the tribological behaviour of ceramics.* Surface and Coating Technology, 1998. **100-101**: p. 17-22.
55. Haefke, H., et al. *Microtexturing of functional structure surface for improving their tribological performance*. in *Proceeding of the International Tribology Conference*. 2000. Nagasaki.
56. Ryk, G., Y. Kligerman, and I. Etsion, *Experimental investigation of laser surface texturing for reciprocation automotive components.* Tribology Transactions, 2002. **45**(4): p. 444-449.
57. Brizmer, V., Y. Kligerman, and I. Etsion, *A laser surface textured parallel thrust bearing.* Tribology Transactions, 2003. **46**(3): p. 397-403.
58. Kovalchenko, A., et al., *The effect of laser surface texturing on transitions in lubrication regimes during unidirectional sliding contact.* Tribology International, 2005. **38**(3): p. 219-225.
59. Ranjan, R., et al., *Laser texturing for low-flying-height media.* Journal of Applied Physics, 1991. **69**(8): p. 5745-5747.
60. Erdemir, A., *Review of engineered tribological interfaces for improved boundary lubrication.* Tribology International, 2005. **38**(3): p. 249-256.
61. Ryk, G., et al., *Experimental investigation of partial laser surface texturing for piston-ring friction reduction.* Tribology Transactions, 2005. **48**: p. 583-588.
62. Du, D., et al., *Laser texturing of rollers by pulsed Nd:YAG laser.* Journal of Materials Processing Technology, 2005. **161**: p. 456-461.
63. Ryk, G. and I. Etsion, *Testing piston rings with partial laser surface texturing for friction reduction.* Wear, 2006. **261**(7-8): p. 792-796.
64. Neves, D., A.E. Diniz, and M.S.F. de Lima, *Efficiency of the laser texturing on the adhesion of the coated twist drills.* Journal of Materials Processing Technology -Proceedings of the 11th International Conference on Metal Forming 2006 3rd Brazilian Congress on Manufacturing Engineering, 2006. **179**(1-3): p. 139-145.
65. Etsion, I., G. Halperin, and E. Becker, *The effect of various surface treatments on piston pin scuffing resistance.* Wear, 2006. **261**(7-8): p. 785-791.

66. Mourier, L., et al., *Transient increase of film thickness in micro-textured EHL contacts.* Tribology International, 2006. **39**(12): p. 1745-1756.
67. Voevodin, A.A. and J.S. Zabinski, *Laser surface texturing for adaptive solid lubrication.* Wear, 2006. **261**(11-12): p. 1285-1292.
68. Andersson, P., et al., *Microlubrication effect by laser-textured steel surfaces.* Wear, 2007. **262**(3-4): p. 369-379.
69. Mills, D., et al., *Surface texturing of Si, porous Si and TiO2 by laser ablation.* Applied Surface Science, 2007. **253**: p. 6575-6579.
70. Rapoport, L., et al., *Friction and wear of MoS_2 films on laser textured steel surfaces.* Surface and Coating Technology, 2007. **202**(14): p. 3332-3340.
71. Etsion, I. and E. Sher, *Improving fuel efficiency with laser surface textured piston rings.* Tribology International, 2009. **42**: p. 542-547.
72. Kim, D.E., K.H. Cha, and I.H. Sung, *Design of surface micro-structures for friction control in micro-system applications.* Annals of the CIRP, 2002. **51**(1): p. 495-498.
73. Jonasson, M., et al., *Comparative study of shotblasted and electrical-discharge-textured rolls with regard to frictional behaviour of the rolled sheet surfaces.* Wear, 1997. **207**: p. 34-40.
74. Wakuda, M., et al., *Effect of surface texturing on friction reduction between ceramic and steel materials under lubricated sliding contact.* Wear, 2003. **254**(3-4): p. 356-363.
75. Pettersson, U. and S. Jacobson, *Tribological texturing of steel surface with a novel diamond embossing tool technique.* Tribology International, 2006. **39**: p. 659-700.
76. Lange, K., *Hand book of Metal Forming*. 1985: Mc Graw-Hill.
77. Matthews, A., et al., *Design aspects for advanced tribological surface coatings.* Surface and Coatings Technology, 1998. **100-101**: p. 1-6.
78. Tan, X., N. Bay, and W. Zhang, *Friction measurement and modelling in forward rod extrusion tests.* Journal of Engineering Tribology, 2003. **217**: p. 71-82.
79. Qin, Y. and R. Balendra, *FE simulation of the influence of die-elasticity on component dimension in forward extrusion.* Int.J.Mach.Tools Manufact., 1997. **37**(2): p. 183-192.
80. Ajiboye, J.S. and M.B. Adeyemi, *Temperature changes with die profile in axisymmetric forward extrusion process.* Advanced Materials Research, 2010. **83-86**: p. 165-173.
81. Kalpakjian, S. and S. Schmid, *Manufacturing engineering and technology*. 5 ed. 2006: PEARSON Prentice Hall.
82. Hwang, D.H., D.E. Kim, and S.J. Lee, *Influence of wear particle interaction in the sliding interface on friction of metals.* Wear, 1999. **225-229**: p. 427-439.
83. Jianxin, D., Y. Xuefeng, and W. Jinghai, *Wear mechanism of Al2O3/TiC/Mo/Ni ceramic wire-drawing dies.* Materials Science and Engineering A, 2006. **424**: p. 347-354.
84. Kudo, H., et al., *An investigation into Plasto-Hydrodynamic Lubrication with a cold sheet drawing test.* Annals of the CIRP, 1982. **31**(1): p. 175-180.

85. Popp, U. and U. Engel. *Micro texturing of cold forging tools - influence on tool life.* in *Proceeding of the 2nd. International conference on Tribology in Manufacturing Process,*. 2004. Nyborg, Denmark.
86. Mizuno, T. and M. Okamoto, *Effects of lubricant viscosity at pressure and sliding velocity on lubricating conditions in the compression-friction test on sheet metals.* Transactions of the ASME: Journal of Lubricant Technology, 1982. **104**: p. 53-59.
87. Saiki, H. and Y. Marumo, *Influence of the roughness geometry of tool surface and flow stress of coated solid lubricants on tribo-conditions in cold forging.* Journal of Materials Processing Technology, 2003. **140**: p. 25-29.
88. http://gltrs.grc.nasa.gov/reports/1997/TM-107508.pdf.
89. http://archive.metalformingmagazine.com/1996/01/laser.htm.
90. Park, D.-S., et al., *Micro-grooving of glass using micro-abrasive jet machining.* Journal of Materials Processing Technology, 2004. **146**: p. 234-240.
91. Uehara, Y., et al., *Tribological properties of dimpled silicon nitride under oil lubrication.* Journal of the European Ceramic Society, 2004. **24**: p. 369-373.
92. Sakai, T., M. Ishikiriyama, and R. Shimazaki, *Durability of piezoelectric ceramics for an actuator.* Japanese Journal of Applied Physics, 1992. **31**: p. 3051-3054.
93. Sakai, T. and H. Kawamoto, *Durability properties of piezoelectric stack actuator.* Japanese Journal of Applied Physics, 1998. **37**: p. 5338-5341.
94. Chaplya, P.M., et al., *Durability properties of piezoelectric stack actuators under combined electromechanical loading.* Journal of Applied Physics, 2006. **100**(12): p. 124111-13.
95. Koh, J.-H., et al., *Degradation and cracking behaviour of* $0.2(PbMg_{1/3}Nb_{2/3}O_3)$*-*$0.8(PbZr_{0.475}\,Ti_{0.525}O_3)$ *multilayer ceramic actuators.* Sensor and Actuators A, 2004. **112**: p. 232-236.
96. Dausch, D.E., *Ferroelectric polarization fatigue in PZT-based RINBOWs and bulk ceramics.* J. Am. Ceram. Soc., 1997. **80**(9): p. 2355-2360.
97. Thongrueng, J., T. Tsuchiya, and K. Nagata, *Lifetime and degradation mechanism of multilayer ceramic actuator.* Japanese Journal of Applied Phycsic, 1998. **37**: p. 5306-5310.
98. Andresen, B., F. Jensen, and S. Ouchouse, *Reliability of piezoelectric actuators at extreme operating conditions*, Noliac A/S, Kvistgaard, Denmark.
99. Yamamoto, T. and F. Mizuno, *Degradation of piezoelectric properties at resonant operational mode by a large input power.* Japanese Journal of Applied Physics, 1995. **34**: p. 2627-2631.
100. Nagata, K. and S. Kinosnita, *Relationship between lifetime of multilayer ceramic actuator and temperature.* Japanese Journal of Applied Physics, 1995. **34**: p. 5266-5269.
101. Uchino, K., *Materials issues in design and performance of piezoelectric actuators: an overview.* Acta Materialia, 1998. **46**(11): p. 3745-3753.
102. Sakai, T. and H. Kawamoto, *Improvement in time-dependent degradation of piezoelectric ceramics by manganese/indium addition.* J. Am. Ceram. Soc., 2000. **83**(6): p. 1423-1427.
103. http://www.noliac.com.

104. Alguero', M., et al., *Degradation of the d_{33} piezoelectric coefficient for PZT ceramics under static and cyclic compressive loading.* Journal of the European Ceramic Society, 2001. **21**: p. 1437-1440.
105. Jiang, Q.Y. and L.E. Cross, *Effects of porosity on electric fatigue behaviour in PLZT and PZT ferroelectric ceramics.* Journal of Materials Science, 1993. **28**: p. 4536-4543.
106. Qiu, W., et al., *Study for multilayer piezoelectric composite structure as displacement actuator by Moire' interferometry and infrared thermography experiments.* Materials Science & Engineering A, 2007. **452-453**(228-234).
107. Cain, M.G., M. Stewart, and M. Gee, *Degradation of piezoelectric materials.* NPL UK Report CMMT(A) 148, 1999.
108. Kaftanoglu, B., *Determination of coefficient of friction under conditions of deep-drawing and stretch forming.* Wear, 1973. **25**: p. 177-188.
109. Le, H.R. and M.P.F. Sutcliffe, *Measurement of friction in strip drawing under thin film lubrication.* Tribology International, 2002. **35**: p. 123-128.
110. Lancaster, P.R. and G.W. Rowe, *A compression of boundary lubricants under light and heavy loads.* Wear, 1958. **2**: p. 428-437.
111. Han, S.S., *The influence of tool geometry on friction behaviour in sheet metal forming.* Journal of Materials Processing Technology, 1997. **63**: p. 129-133.
112. Vollertsen, F. and M. Plancak, *On possibilities for the determination of the coefficient of friction in hydroforming of tubes.* Journal of Materials Processing Technology, 2002. **125-126**: p. 412-420.
113. Fratini, L., S.L. Casto, and E.L. Valvo, *A technical note on an experimental device to measure friction coefficient in sheet metal forming.* Journal of Materials Processing Technology, 2006. **172**: p. 16-21.
114. Rigaut, J.M., et al., *A new friction test procedure for the improvement of drawing and similar process.* Journal of Materials Processing Technology, 1990. **3**: p. 3-28.
115. Pawelski, O., W. Rasp, and C. Wolff, *Analysis of the asymmetric upsetting test with extremely high strain rate as tool for friction measurement.* Journal of Materials Processing Technology, 1998. **80-81**: p. 287-291.
116. Montmitonnet, P., F. Delamare, and B. Rizoulieres, *Transfer layer and friction in cold metal strip rolling process.* Wear, 2000. **245**: p. 125-135.
117. Wakuda, M., Y. Yamauchi, and S. Kanzaki, *Material response to particle impact during abrasive jet machining of alumina ceramics.* Journal of Materials Processing Technology, 2003. **132**(1-3): p. 177-183.
118. Ledocq, J.H.M., *The transition from hydrodynamic to boundary regime of tilting thrust pads.* Tribology, 1974. **7**(1): p. 7-13.
119. Felder, E. and V. Samper, *Experimental study and theoretical interpretation of the frictional mechanisms in steel sheet forming.* Wear, 1994. **178**(1-2): p. 85-94.
120. Czichos, H., *Failure criteria in thin film lubrication: Investigation of the different stages of film failure.* Wear, 1976. **36**(1): p. 13-17.
121. Kajdas, C., J. Nita, and K. Krawczyk, *A new method for the rapid estimation of the antifriction performance of lubricants.* Wear, 1981. **70**(2): p. 187-195.
122. Kobs, K., et al., *Enhanced endurance life of sputtered MoSx films on steel by ion beam mixing.* Materials Science and Engineering, 1987. **90**: p. 281-286.

123. Sebastian, K.S. and V.R. Bhaskar, *A new design for the pin and V-blocks tribometer.* Tribology International, 1995. **28**(4): p. 219-223.

124. Masjuki, H.H. and M.A. Maleque, *Investigation of the anti-wear characteristics of palm oil methyl ester using a four-ball tribometer test.* Wear, 1997. **206**(1-2): p. 179-186.

125. Godfrey, D., *Friction oscillations with a pin-on-disc tribometer.* Tribology International, 1995. **28**(2): p. 119-126.

126. Wakuda, M., Y. Pongsuwanna, and K. Taniguchi, *Complete nucleotide sequences of two RNA segments of human picobirnavirus.* Journal of Virological Methods, 2005. **126**(1-2): p. 165-169.

127. Nakamura, T., N. Bay, and Z.L. Zhang, *FEM simulation of a friction testing method based on combined forward conical can-backward straight can extrusion.* Journal of Tribology, 1998. **120**: p. 716-723.

128. Kunogi, M., *A new method of cold extusion.* J Sci Res Inst (Tokyo), 1956. **50**: p. 215-246.

129. Male, A.T. and M.G. Cockcroft, *A method for the determination of the coefficient of friction of metals under condition of bulk plastic deformation.* J Inst Metals, 1964-1965. **93**: p. 38-46.

130. Petersen, S.B., P.A.F. Martins, and N. Bay, *Friction in bulk metal forming: a general friction model vs. the law of constant friction.* Journal of Materials Processing Technology, 1997. **66**(1-3): p. 186-194.

131. Rao, K.P. and K.A. Sivaram, *A review of ring-compression testing and applicability of the calibration curves.* Journal of Materials Processing Technology, 1993. **37**: p. 295-318.

132. Oh, H.K. and J.H. Mun, *An analysis of the ring upsetting of sintered material.* Journal of Mechanical Working Technology, 1984. **9**: p. 279-290.

133. Sofuoglu, H. and J. Rasty, *On the measurement of friction coefficient utilizing the ring compression test.* Tribology International, 1999. **32**(6): p. 327-335.

134. Dutton, R.E., et al., *Effect of flow softening on ring test calibration curves.* Materials Science and Engineering A, 1999. **270**(2): p. 249-253.

135. Bhattacharyya, D. and G. Moltschaniwskyj, *Measurement of anisotropy by the ring compression test.* Journal of Mechanical Working Technology, 1986. **13**: p. 325-330.

136. Sahi, M., et al., *The influence of viscoplasticity in the interpretation of the ring test.* Journal of Materials Processing Technology, 1996. **58**(2-3): p. 286-292.

137. Andersson, K., S. Kivivuori, and A.S. Korhonen, *Effect of the heat-transfer coefficient in ring-compression tests.* Journal of Materials Processing Technology, 1996. **62**(1-3): p. 10-13.

138. Sofuoglu, H., H. Gedikli, and J. Rasty, *Determination of friction coefficient by employing the ring compression test.* Transactions of the ASME, 2001. **123**.

139. Petersen, S.B., P.A.F. Martins, and N. Bay, *An alternative ring-test geometry for the evaluation of friction under low normal pressure.* Journal of Materials Processing Technology, 1998. **79**(1-3): p. 14-24.

140. Robinson, T., H. Ou, and C.G. Armstrong, *Study on ring compression test using physical modelling and FE simulation.* Journal of Materials Processing Technology, 2004. **153-154**: p. 54-59.

141. Wang, F. and J.G. Lenard, *Experimental study of interfacial friction-hot ring compression.* Journal of Engineering Materials and Technology, Transactions of the ASME, 1992. **114**(1): p. 13-18.
142. Li, L.X., et al., *An experimental study of the lubrication behavior of A5 glass lubricant by means of the ring compression test.* Journal of Materials Processing Technology, 2000. **102**(1-3): p. 138-142.
143. Hartley, R.S., T.J. Cloete, and G.N. Nurick, *An experimental assessment of friction effects in the split Hopkinson pressure bar using the ring compression test.* International Journal of Impact Engineering, 2007. **34**(10): p. 1705-1728.
144. Bakhshi-Jooybari, M., *A theoretical and experimental study of friction in metal forming by the use of the forward extrusion process.* Journal of Materials Processing Technology, 2002. **125-126**: p. 369-374.
145. Shen, G., et al., *A method for evaluating friction using a backward extrusion-type forging.* Journal of Material Processing Technology, 1992. **33**: p. 109-123.
146. Nakamura, T., N. Bay, and Z.L. Zhang, *FEM simulation of friction testing method based on combined forward rod-backward can extrusion.* Journal of Tribology, 1997. **119**(3): p. 501-506.
147. Sofuoglu, H. and H. Gedikli, *Determination of friction coefficient encountered in large deformation process.* Tribology International, 2002. **35**(1): p. 27-34.
148. Bay, N., O. Wibom, and J.A. Nielsen, *A new friction and lubrication test for cold forging.* Annals of the CRIP, 1995. **44**(1): p. 217-221.
149. Wagener, H.W. and J. Wolf, *Coefficient of friction in cold extrusion.* Journal of Material Processing Technology, 1994. **44**: p. 283-291.
150. Buschhausen, A., et al., *Evaluation of lubrication and friction in cold forging using a double backward-extrusion process.* Journal of Materials Processing Technology, 1992. **33**(1-2): p. 95-108.
151. Forcellese, A., et al., *Evaluation of friction in cold metal forming.* Journal of Engineering Tribology, 1994. **45**: p. 619-624.
152. Ghobrial, M.I., et al., *Factors affecting the double cup extrusion test for evaluating of friction in cold and warm forging.* CIRP Annals, 1993. **42**(1): p. 347-351.
153. Tan, X., N. Bay, and W. Zhang, *On parameters affecting metal flow and friction inthe double cup extrusion test.* Scandinavian Journal of Metallurgy, 1998. **27**(6): p. 246-252.
154. Schrader, T., M. Shirgaokar, and T. Altan, *A critical evaluation of the double cup extrusion test for selection of cold forging lubricants.* Journal of Material Processing Technology, 2007. **189**: p. 36-44.
155. Nakamura, T., N. Bay, and Z.L. Zhang, *FEM simulation of friction testing method based on combined forward rod-backward can extrusion.* American Society of Mechanical Engineers (Paper) : Proceeding of the 1996 ASME/STLE Joint Tribology Conference, 1996.
156. Depierre, V., *Experimental measurement of force during extrusion and correlation with theory.* Journal of Lubricant Technology: Transactions of the ASME, 1970: p. 398-405.

157. Brethenoux, G., et al., *Cold forming process: some examples of predictions and design optimization using numerical simulations.* Journal of Materials Processiong Technology, 1996. **60**: p. 555-562.
158. Hatzenbichler, T., B. Buchmayr, and A. Umgeher, *Influence of container friction on the main process parameters in direction extrusion.* Steel Grips, 2005. **3**(2): p. 126-129.
159. Kuzman, K., et al., *Control of material flow in a combined backward can - forward rod extrusion.* Journal of Materials Processing Technology: Proceedings of the 6th International Conference on Metal Forming, 1996. **60**(1-4): p. 141-147.
160. Epler, M.E. and W.Z. Misiolek, *Experimental evaluation method for determining of friction characteristics and performance of cold headings coatings.* Wear, 2005. **260**: p. 909-914.
161. Gelin, J.C., J. Oudin, and Y. Ravalard, *An improved finite element method for the analysis of damage and ductile fracture in cold forming processes.* Annals of the CIRP, 1985. **34**(1): p. 209-213.
162. Gelin, J.C., *Finite element analysis of ductile fracture and defects forming in cold and hot forging.* Annals of the CIRP, 1990. **39**(1): p. 215-218.
163. Jaspers, S.P.F.C. and J.H. Dautzenberg, *Material behaviour in conditions similar to metal cutting: flow stress in the primary shear zone.* Journal of Material processing Technology, 2002. **122**: p. 322-330.
164. Kuczyn'ski, K. and S. Erbel, *Obrobka plastycna*. 1984: Wydawnictwa Politechniki Warszawskiej Warszawa.
165. Male, A.T. and V. DePierre, *The Validity of mathematical solutions for determining friction from the ring compression test.* Journal of Lubrication Technology, 1970. **39**: p. 389-397.
166. Hwu, Y.-J., C.-T. Hsu, and F. Wang, *Measurement of friction and the flow stress of steels at room and elevated temperatures by ring-compression tests.* Journal of Materials Processing Technology, 1993. **37**: p. 319-335.
167. Chen, P.J., *Macroscopic theory for the existence of the hysterisis and butterfly loops in ferroelectricity.* Ferroelectrics, 1980. **23**: p. 199-208.
168. http://www.engineersedge.com/sutface_finish.html

Appendix A

(Actuator-tester)

Table A.1: Parts list of the actuator-tester

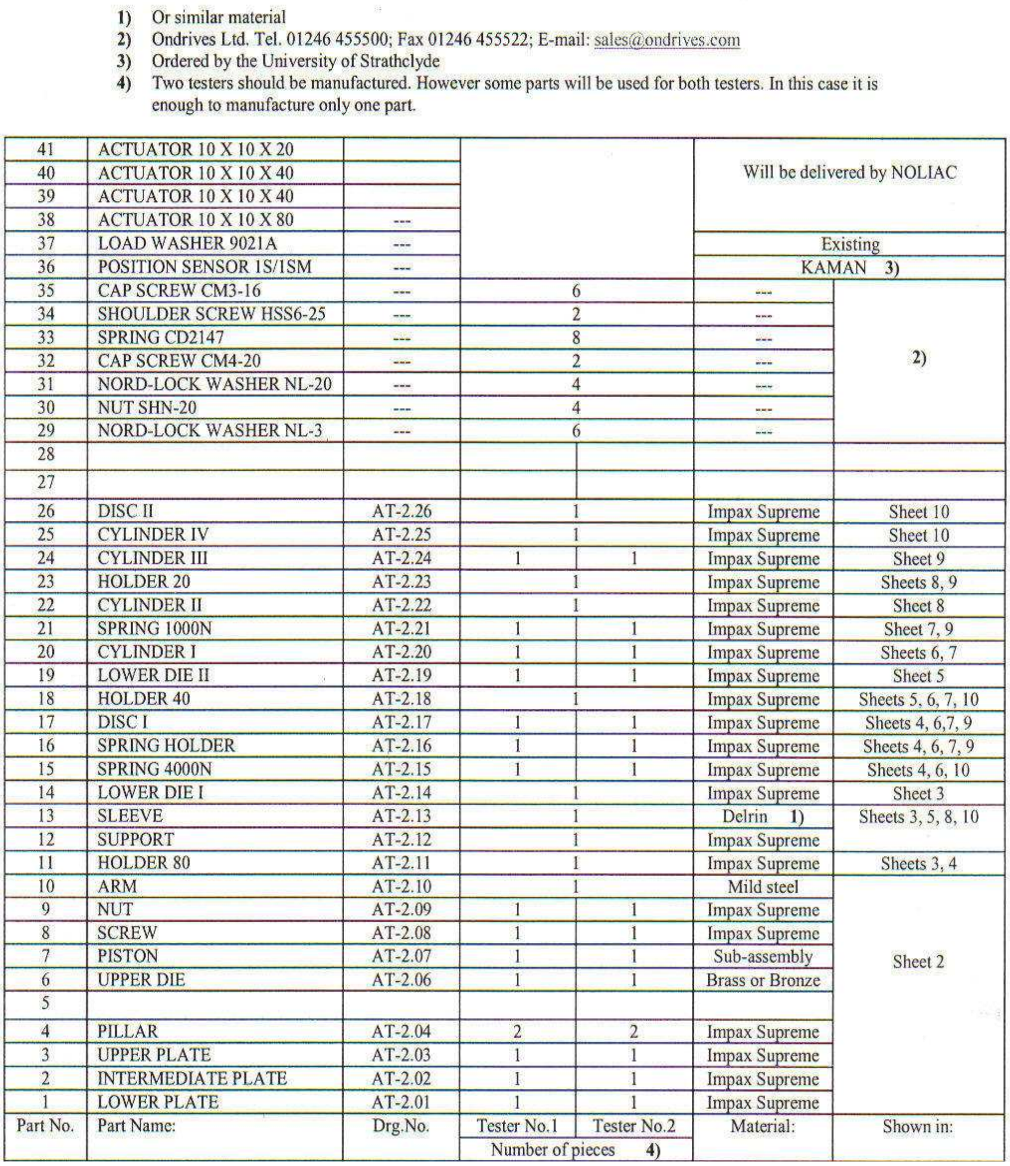

1) Or similar material
2) Ondrives Ltd. Tel. 01246 455500; Fax 01246 455522; E-mail: sales@ondrives.com
3) Ordered by the University of Strathclyde
4) Two testers should be manufactured. However some parts will be used for both testers. In this case it is enough to manufacture only one part.

41	ACTUATOR 10 X 10 X 20				Will be delivered by NOLIAC	
40	ACTUATOR 10 X 10 X 40					
39	ACTUATOR 10 X 10 X 40					
38	ACTUATOR 10 X 10 X 80	---				
37	LOAD WASHER 9021A	---			Existing	
36	POSITION SENSOR 1S/1SM	---			KAMAN 3)	
35	CAP SCREW CM3-16	---	6		---	2)
34	SHOULDER SCREW HSS6-25	---	2		---	
33	SPRING CD2147	---	8		---	
32	CAP SCREW CM4-20	---	2		---	
31	NORD-LOCK WASHER NL-20	---	4		---	
30	NUT SHN-20	---	4		---	
29	NORD-LOCK WASHER NL-3	---	6		---	
28						
27						
26	DISC II	AT-2.26	1		Impax Supreme	Sheet 10
25	CYLINDER IV	AT-2.25	1		Impax Supreme	Sheet 10
24	CYLINDER III	AT-2.24	1	1	Impax Supreme	Sheet 9
23	HOLDER 20	AT-2.23	1		Impax Supreme	Sheets 8, 9
22	CYLINDER II	AT-2.22	1		Impax Supreme	Sheet 8
21	SPRING 1000N	AT-2.21	1	1	Impax Supreme	Sheet 7, 9
20	CYLINDER I	AT-2.20	1	1	Impax Supreme	Sheets 6, 7
19	LOWER DIE II	AT-2.19	1	1	Impax Supreme	Sheet 5
18	HOLDER 40	AT-2.18	1		Impax Supreme	Sheets 5, 6, 7, 10
17	DISC I	AT-2.17	1	1	Impax Supreme	Sheets 4, 6,7, 9
16	SPRING HOLDER	AT-2.16	1	1	Impax Supreme	Sheets 4, 6, 7, 9
15	SPRING 4000N	AT-2.15	1	1	Impax Supreme	Sheets 4, 6, 10
14	LOWER DIE I	AT-2.14	1		Impax Supreme	Sheet 3
13	SLEEVE	AT-2.13	1		Delrin 1)	Sheets 3, 5, 8, 10
12	SUPPORT	AT-2.12	1		Impax Supreme	
11	HOLDER 80	AT-2.11	1		Impax Supreme	Sheets 3, 4
10	ARM	AT-2.10	1		Mild steel	Sheet 2
9	NUT	AT-2.09	1	1	Impax Supreme	
8	SCREW	AT-2.08	1	1	Impax Supreme	
7	PISTON	AT-2.07	1	1	Sub-assembly	
6	UPPER DIE	AT-2.06	1	1	Brass or Bronze	
5						
4	PILLAR	AT-2.04	2	2	Impax Supreme	
3	UPPER PLATE	AT-2.03	1	1	Impax Supreme	
2	INTERMEDIATE PLATE	AT-2.02	1	1	Impax Supreme	
1	LOWER PLATE	AT-2.01	1	1	Impax Supreme	
Part No.	Part Name:	Drg.No.	Tester No.1	Tester No.2	Material:	Shown in:
			Number of pieces 4)			

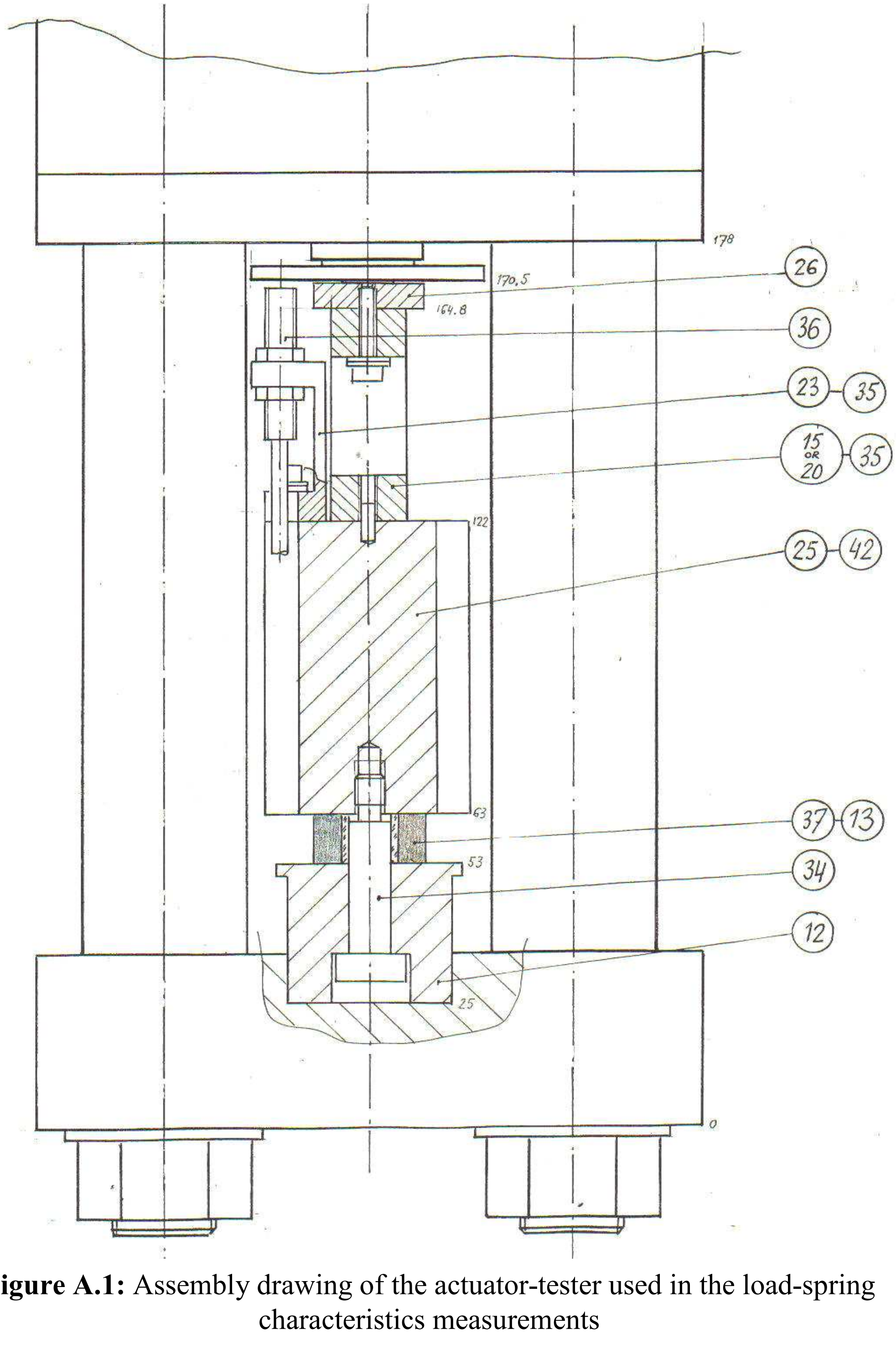

Figure A.1: Assembly drawing of the actuator-tester used in the load-spring characteristics measurements

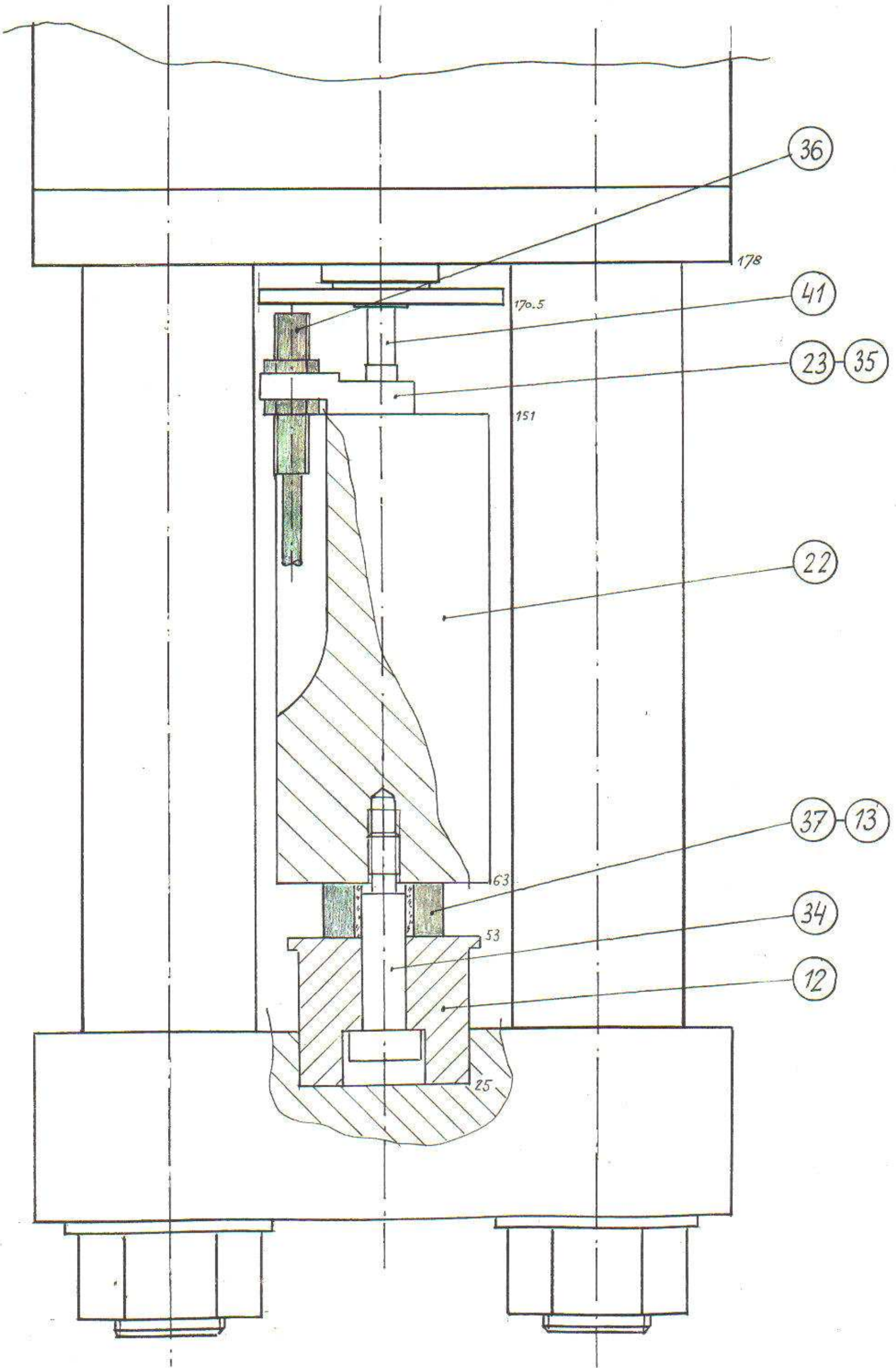

Figure A.2: Assembly drawing used for the characteristics test of the actuator with the dimensions of 5 x 5 x 20 mm^3

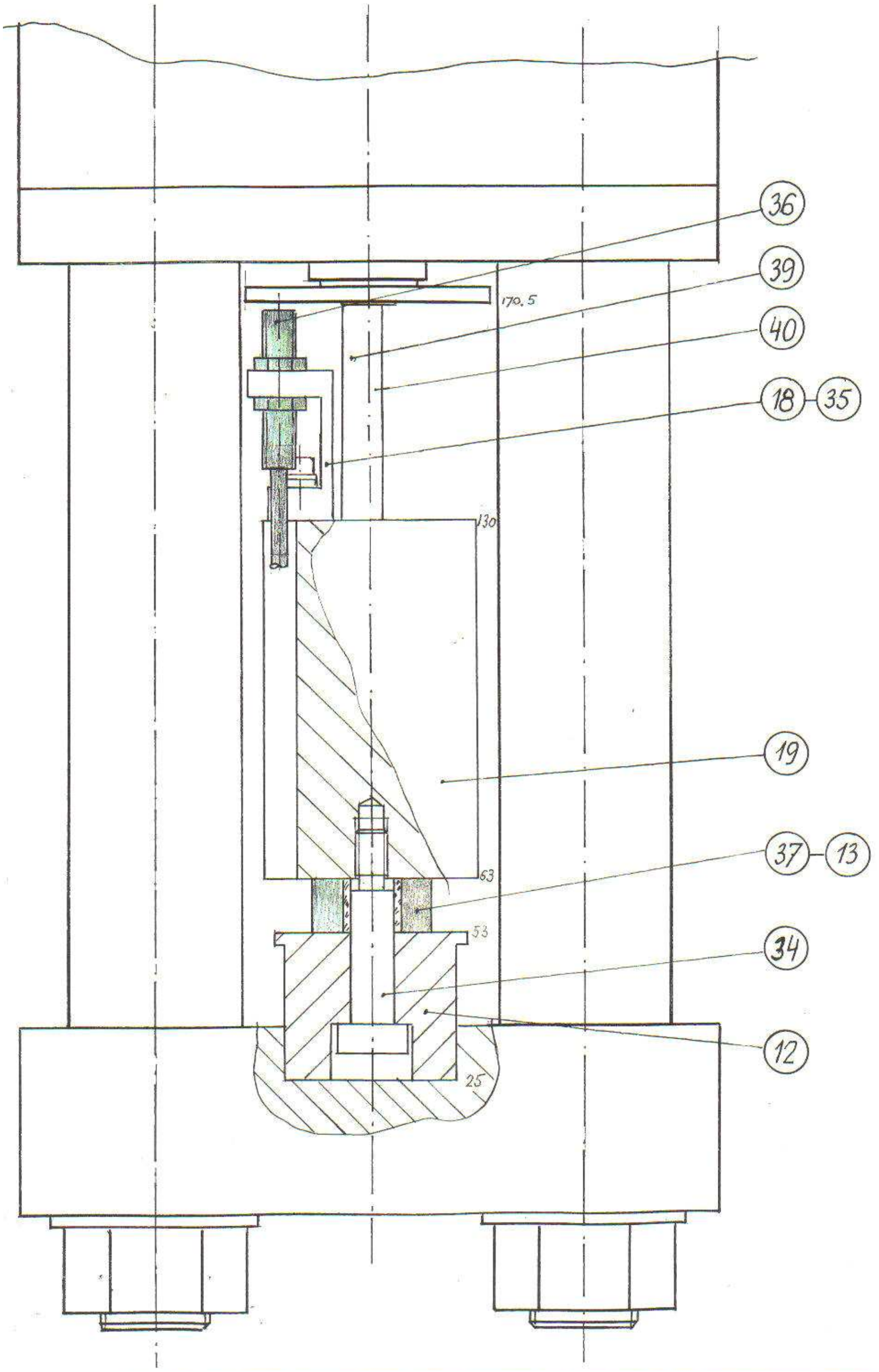

Figure A.3: Assembly drawing used for the characteristics test of the actuator with the dimensions of 10 x 10 x 40 mm^3

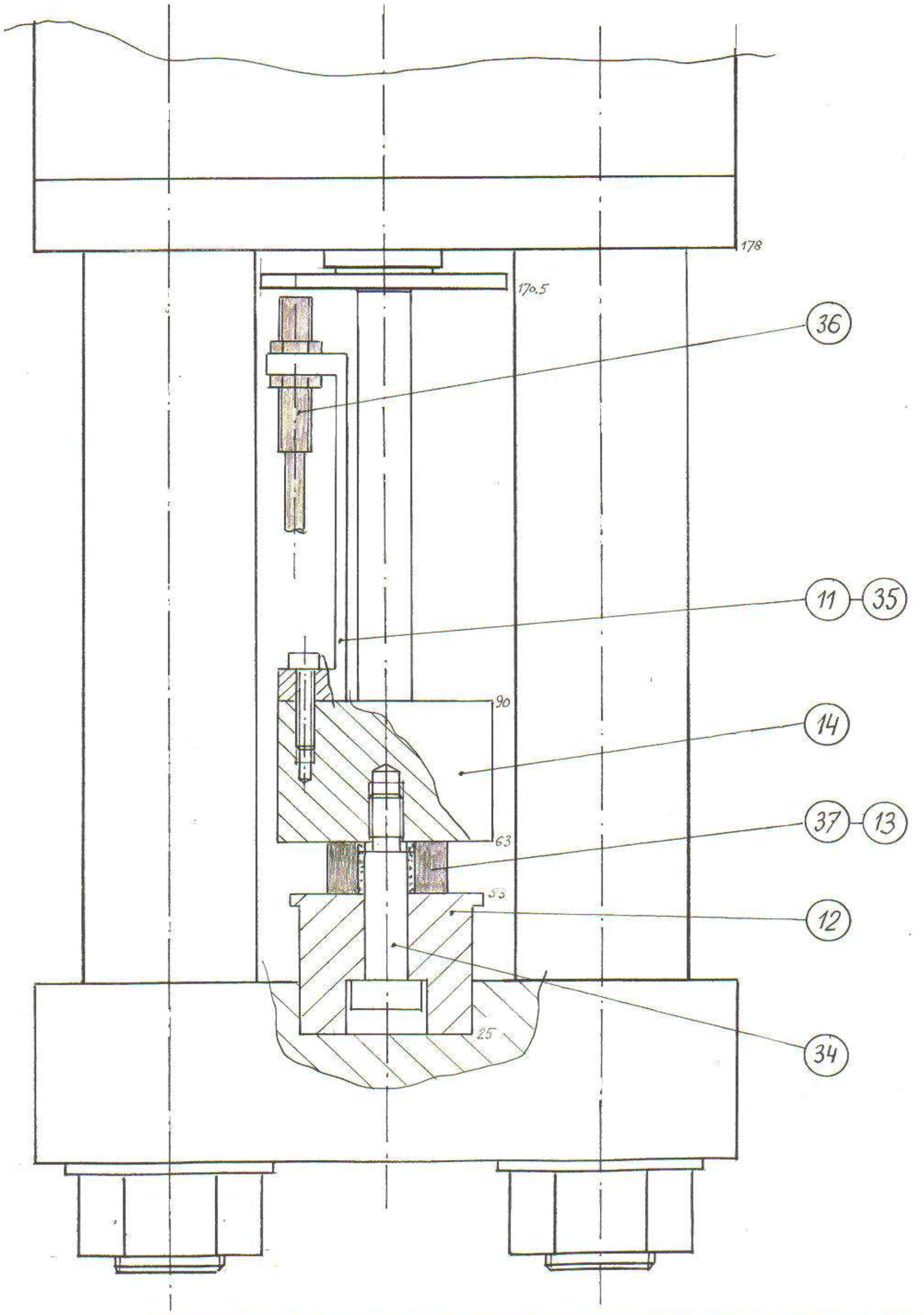

Figure A.4: Assembly drawing used for the characteristics test of the actuator with the dimensions of 10 x 10 x 80mm^3

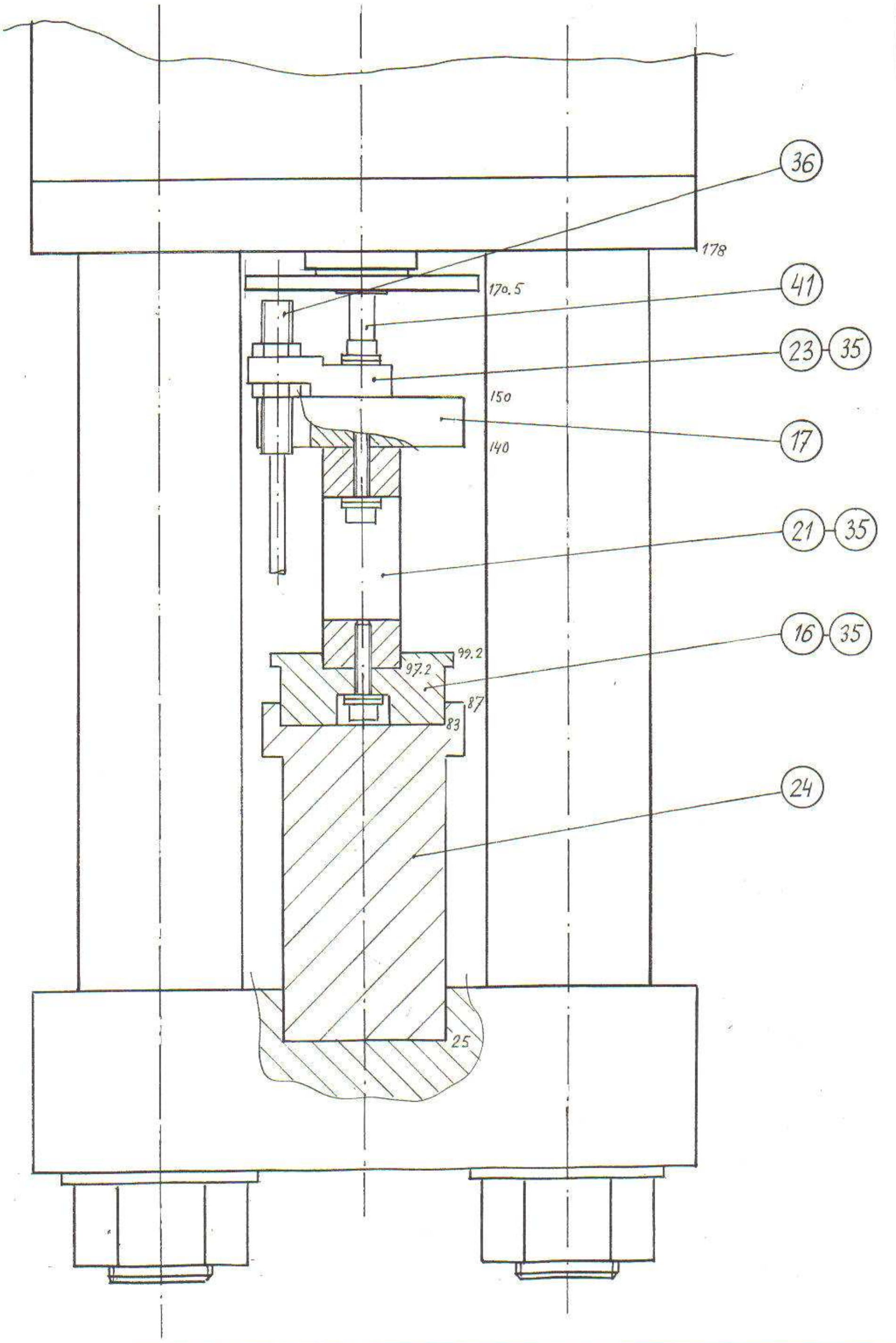

Figure A.5: Assembly drawing used for the long-term cyclic test of the actuator with the dimensions of 5 x 5 x 20 mm^3

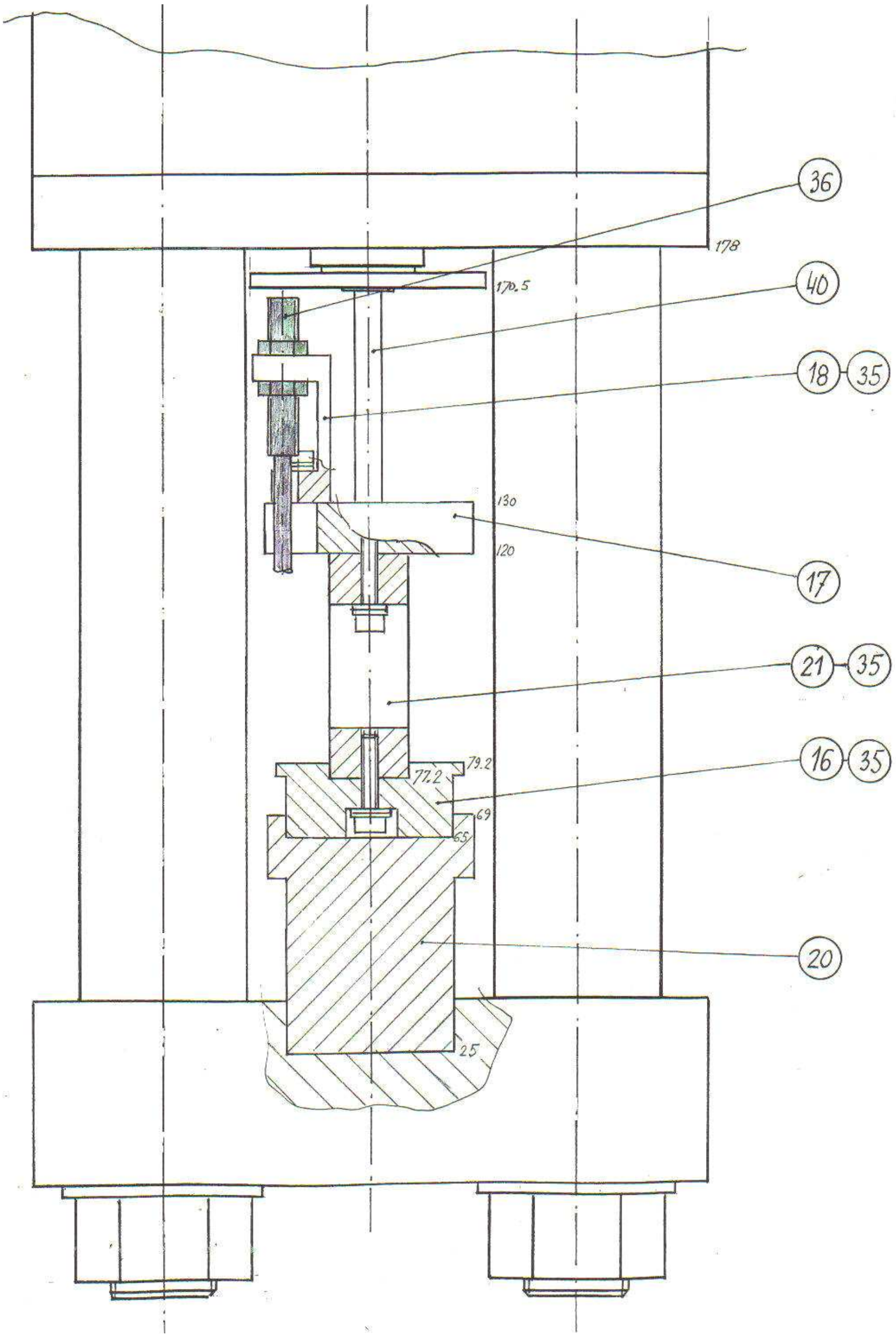

Figure A.6: Assembly drawing used for the long-term cyclic test of the actuator with the dimensions of 5 x 5 x 40 mm^3

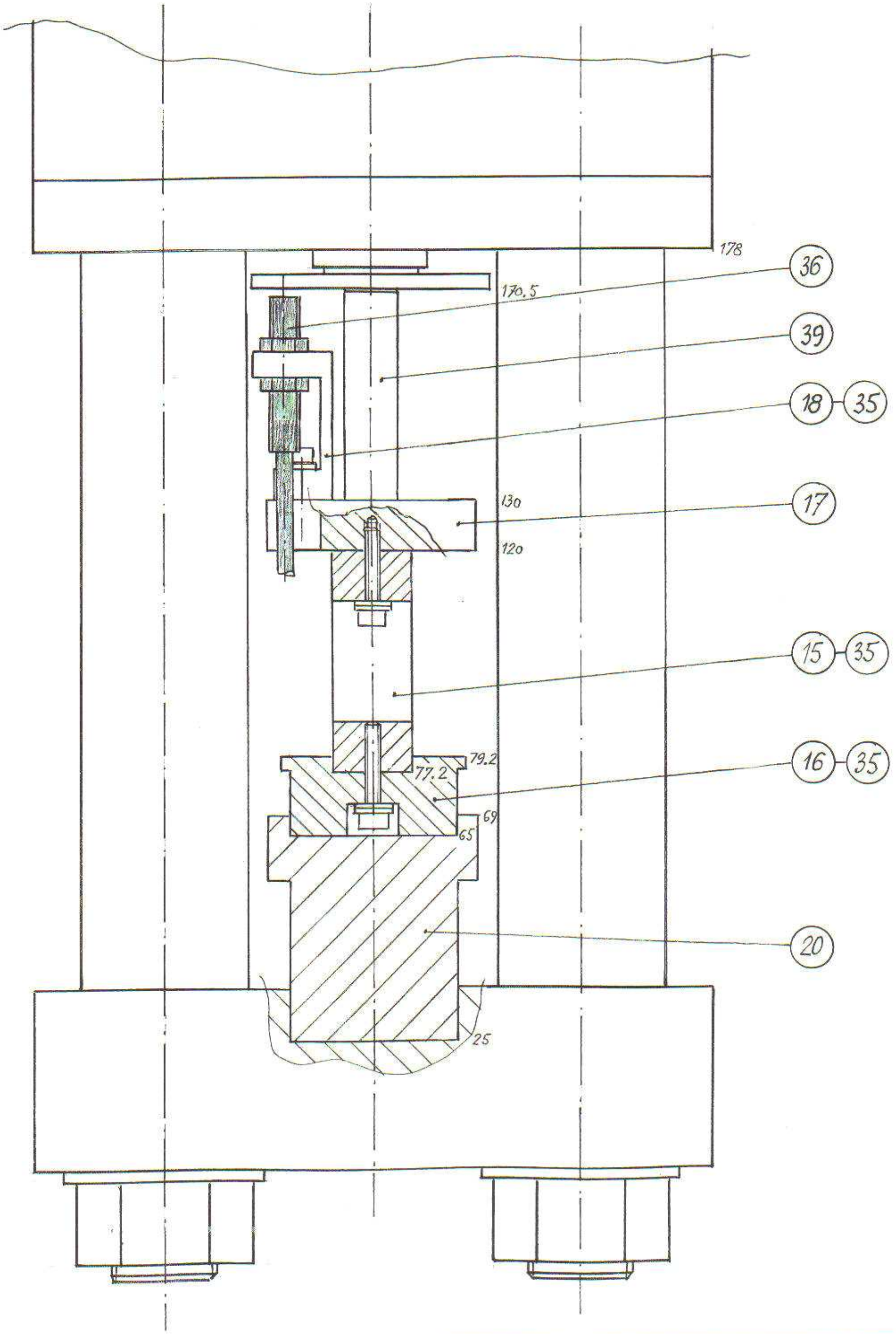

Figure A.7: Assembly drawing used for the long-term cyclic test of the actuator with the dimensions of 10 x 10 x 40 mm^3

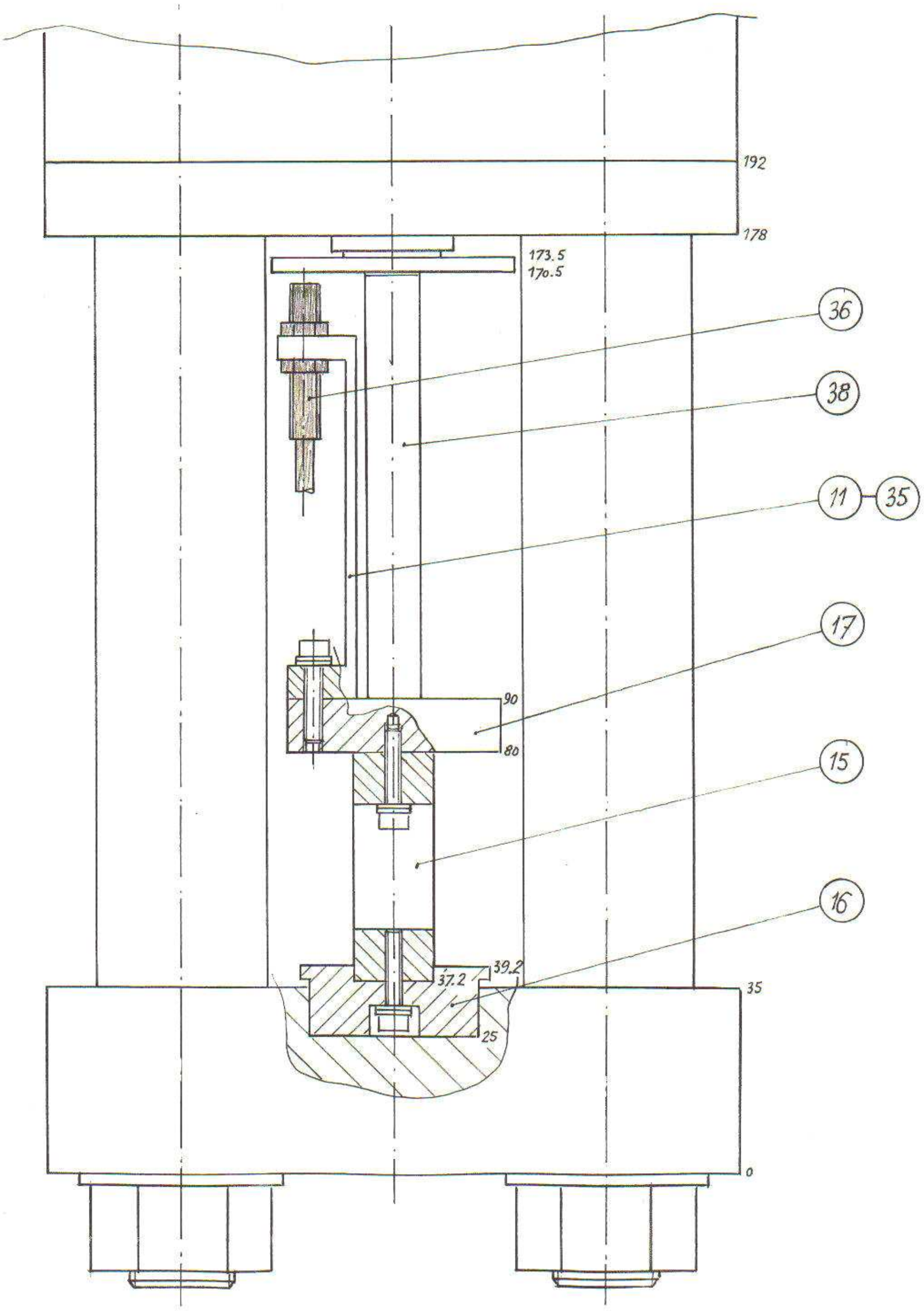

Figure A.8: Assembly drawing used for the long-term cyclic test of the actuator with the dimensions of 10 x 10 x 80mm^3

Appendix B

Preloading and Loading Force Conditions

Note:

Actuator stiffness = 30 N/µm
Load-spring stiffness, k_s = 50 N/µm
Δl_t = 9 µm

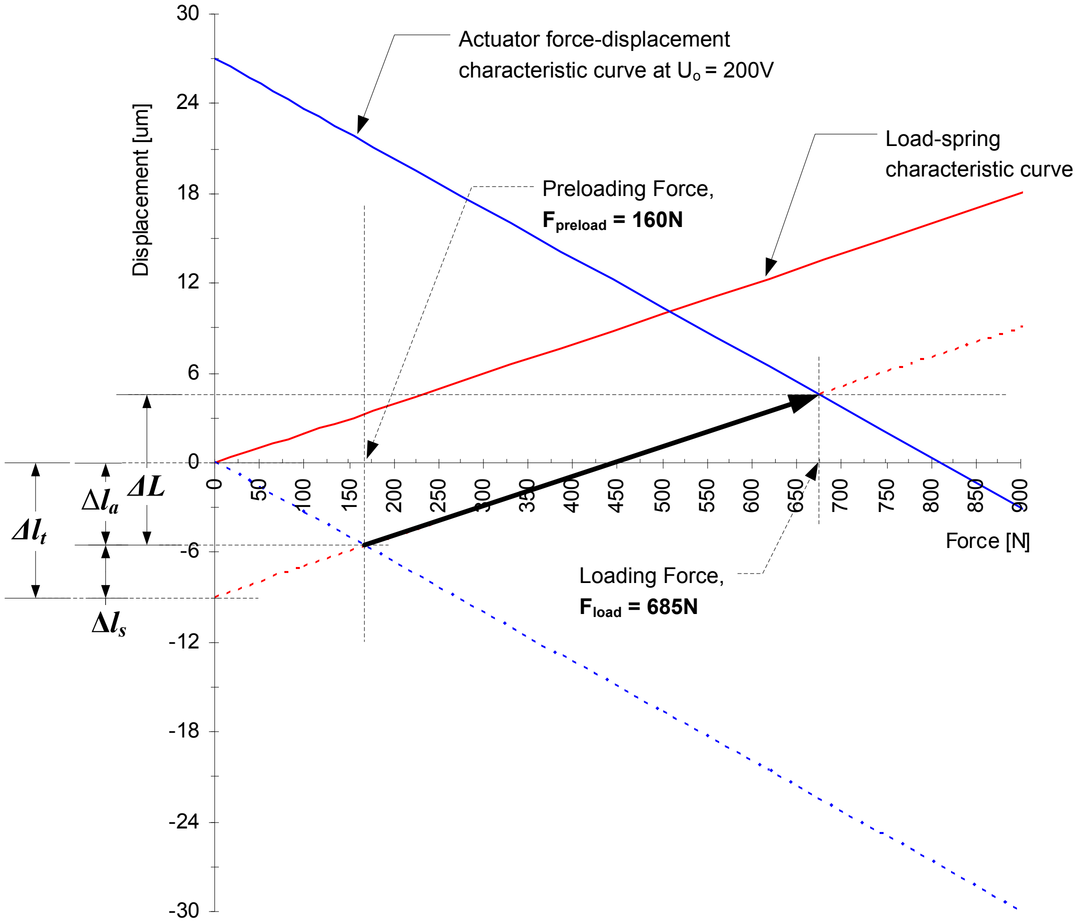

Figure B.1: The preloading and loading conditions of the actuators with the reference numbers 1/5x5x20/160/685/200/200, 2/5x5x20/160/685/200/200 and 3/5x5x20/160/685/200/200

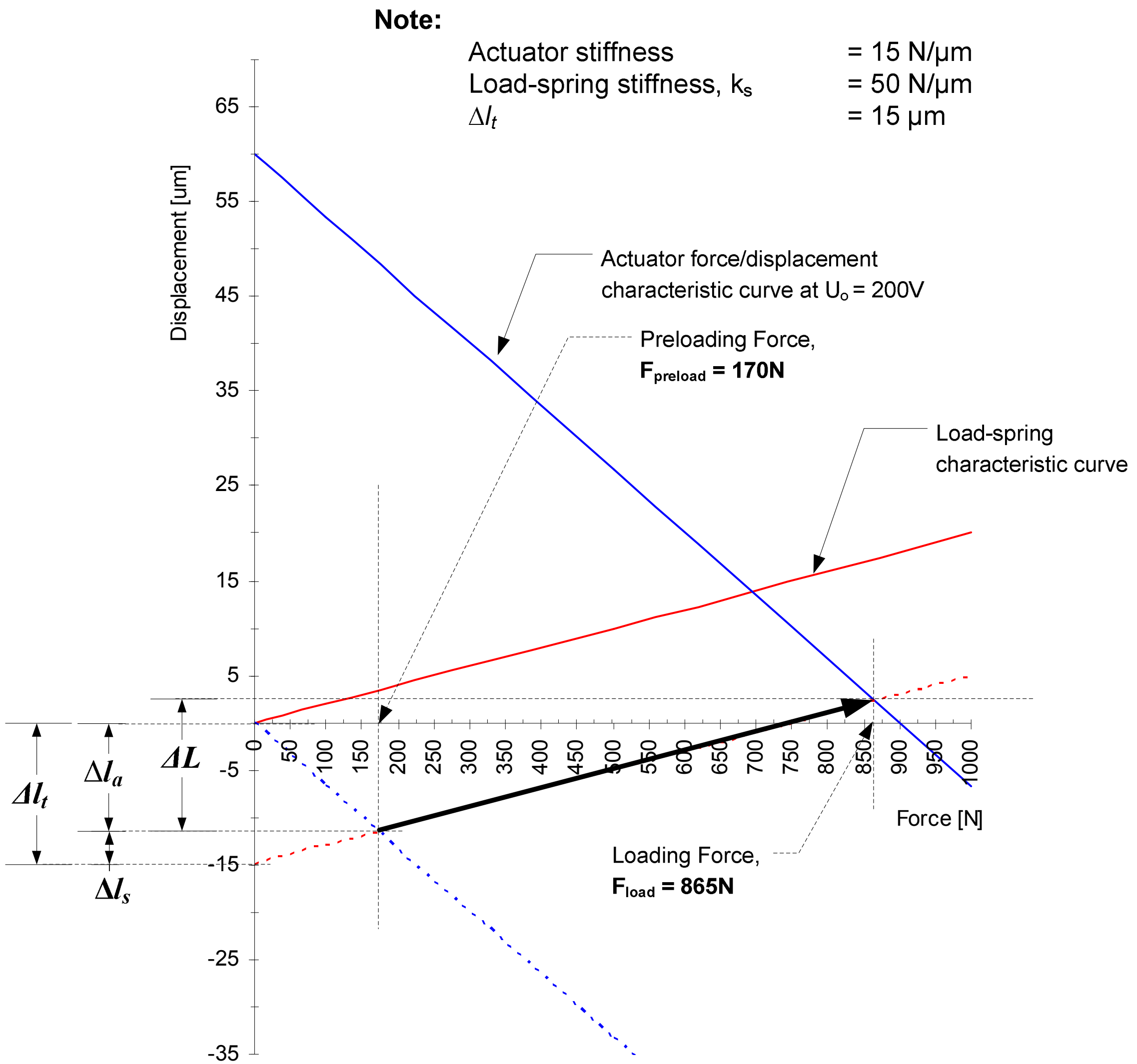

Figure B.2: The preloading and loading conditions of the actuators with the reference numbers 4/5x5x40/170/865/200/200, 5/5x5x40/170/865/200/200 and 6/5x5x40/170/865/200/200

Note:

Actuator stiffness = 61 N/µm
Load-spring stiffness, k_s = 70 N/µm
Δl_t = 21 µm

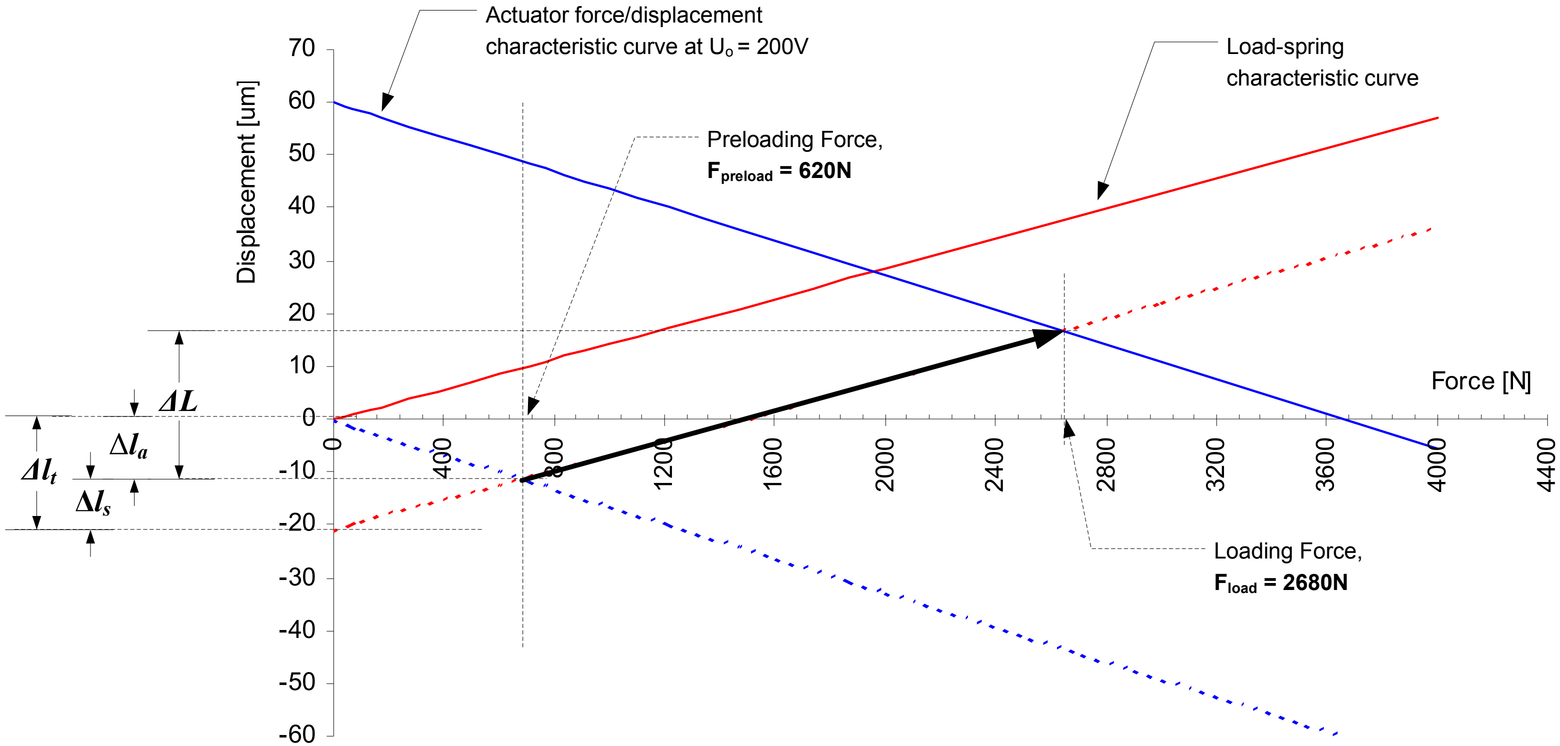

Figure B.3: The preloading and loading conditions of the actuators with the reference numbers 7/10x10x40/620/2680/150/200 and 8/10x10x40/620/2680/150/200

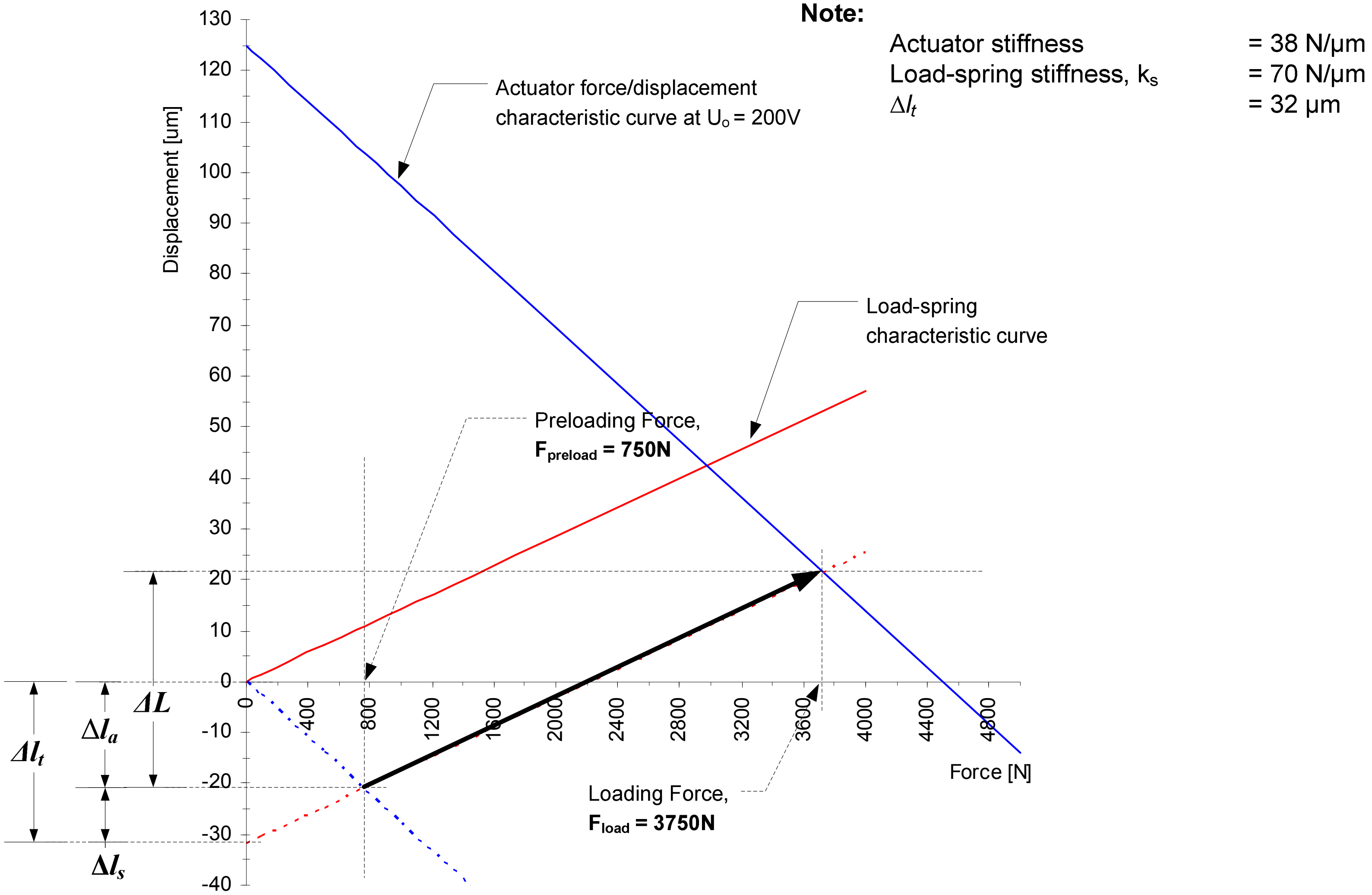

Note:

Actuator stiffness = 38 N/µm
Load-spring stiffness, k_s = 70 N/µm
Δl_t = 32 µm

Actuator force/displacement characteristic curve at U_o = 200V

Load-spring characteristic curve

Preloading Force, **$F_{preload}$ = 750N**

Loading Force, **F_{load} = 3750N**

Figure B.4: The preloading and loading conditions of the actuators with the reference numbers 9/10x10x80/750/3750/125/200 and 10/10x10x80/750/3750/125/200

Note:

Actuator stiffness = 61 N/µm
Spring stiffness = 70 N/µm
Δl_t = 48 µm

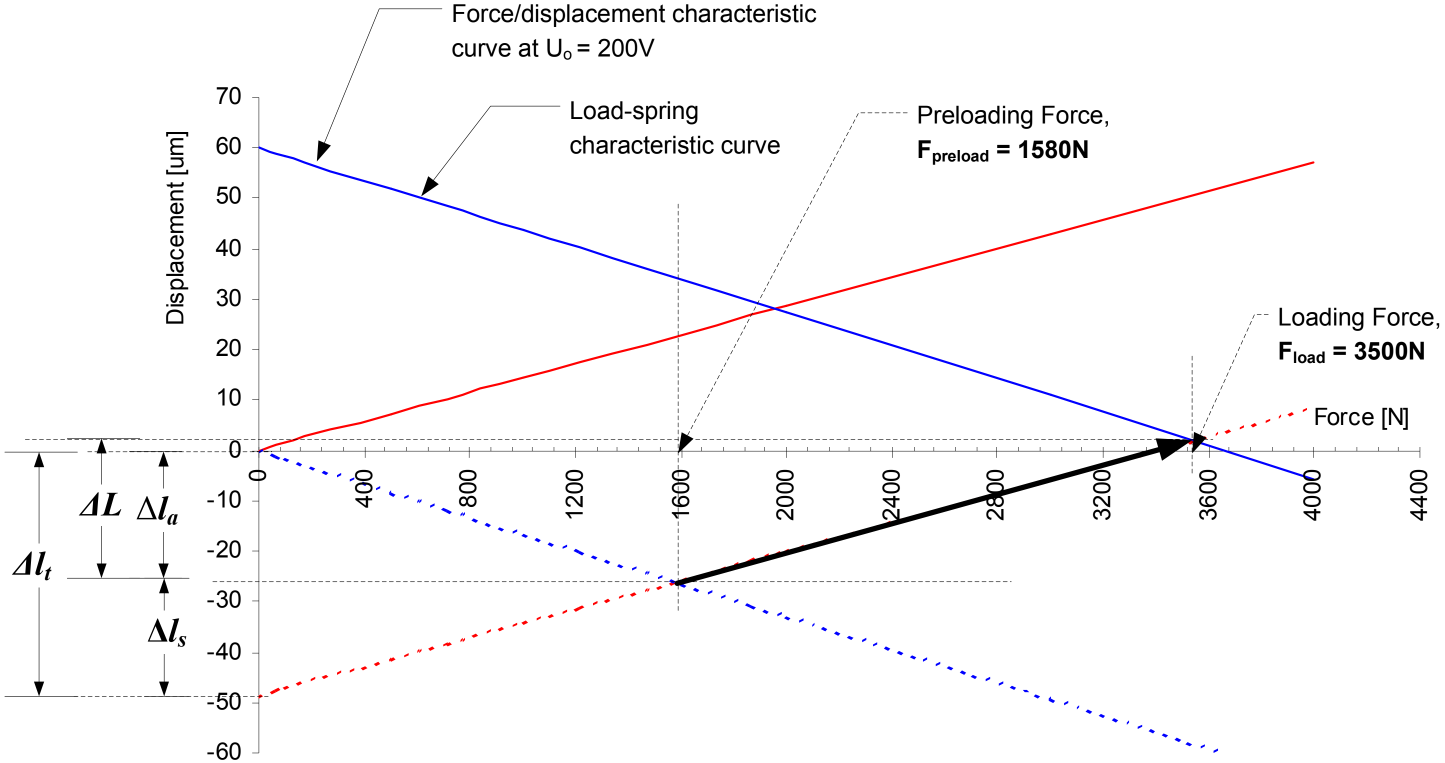

Figure B.5: The preloading and loading conditions of the actuator with the reference number 11/10x10x40/1580/3500/150/200

Note:

Actuator stiffness = 61 N/μm
Load-spring stiffness, k_s = 70 N/μm
Δl_t = 97 μm

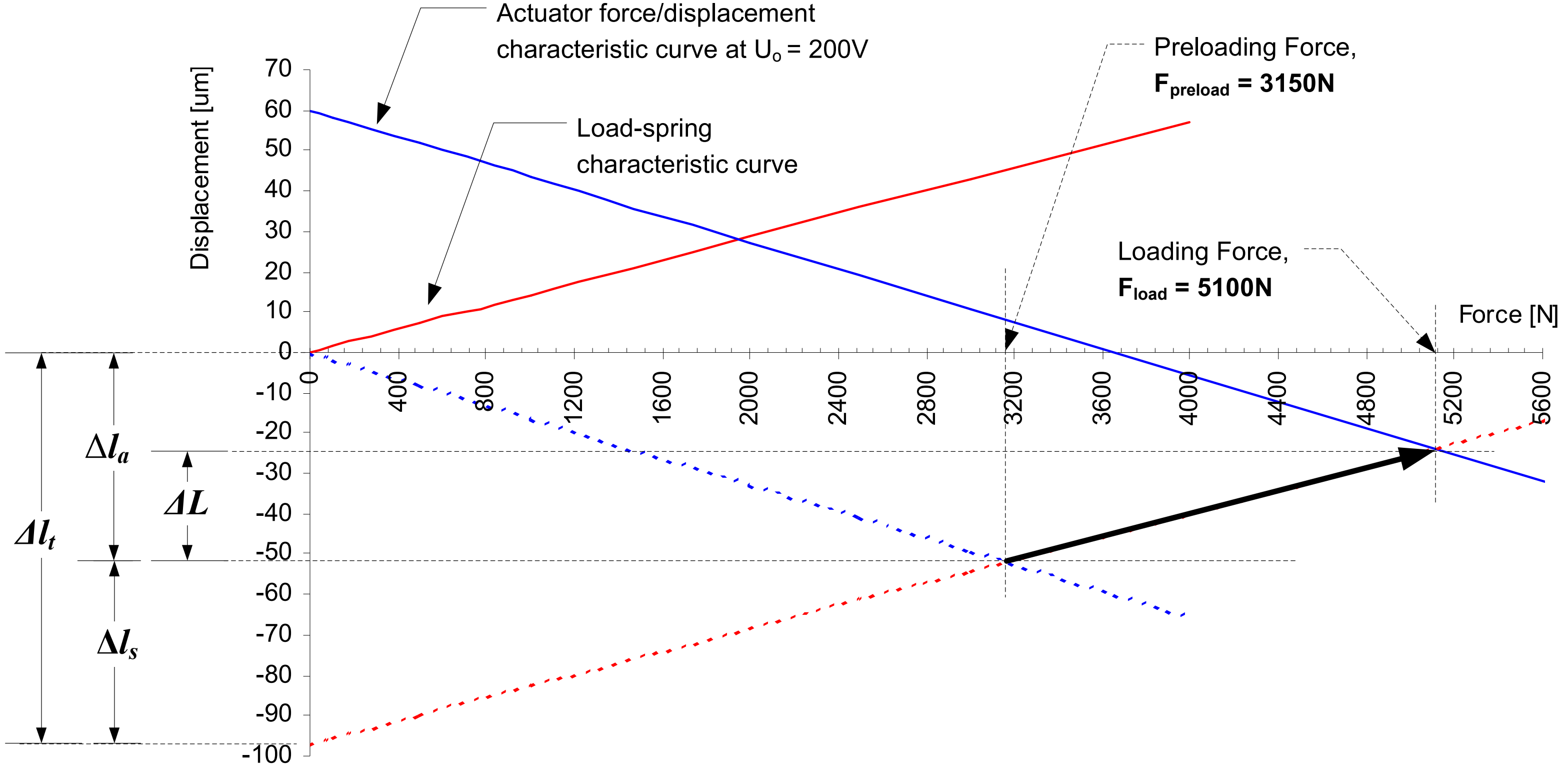

Figure B.6: The preloading and loading conditions of the actuator with the reference number 12/10x10x40/3150/5100/150/200

Note:

Actuator stiffness = 61 N/µm
Load-spring stiffness, k_s = 70 N/µm
Δl_t = 110 µm

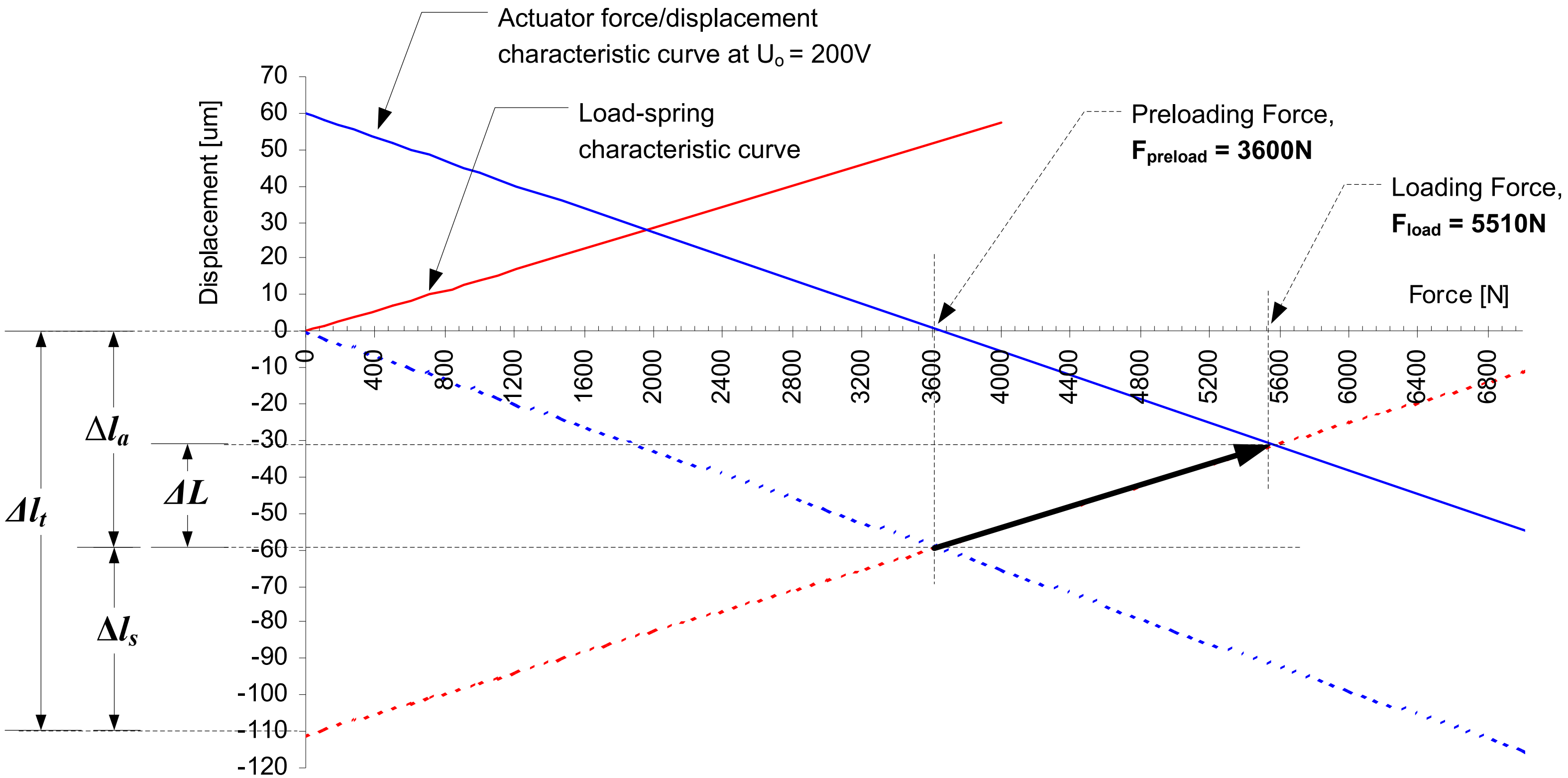

Figure B.7: The preloading and loading conditions of the actuator with the reference number 13/10x10x40/3600/5510/150/200

Note:

Actuator stiffness = 61 N/µm

Load-spring stiffness, k_s = 70 N/µm

Δl_t = 120 µm

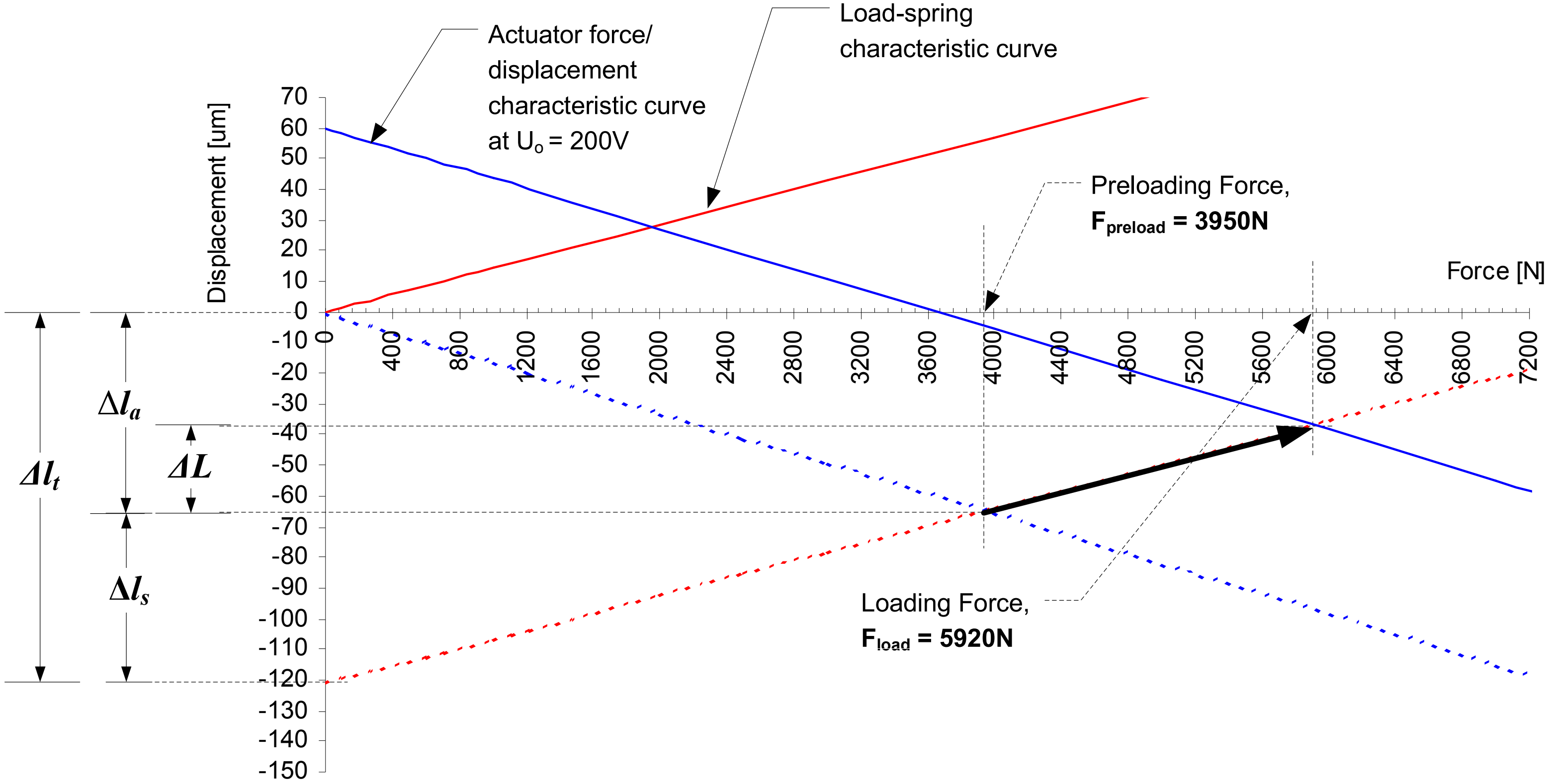

Figure B.8: The preloading and loading conditions of the actuator with the reference number 14/10x10x40/3950/5920/150/200

Note:

Actuator stiffness = 61 N/μm
Load-spring stiffness, k_s = 70 N/μm
Δl_t = 145 μm

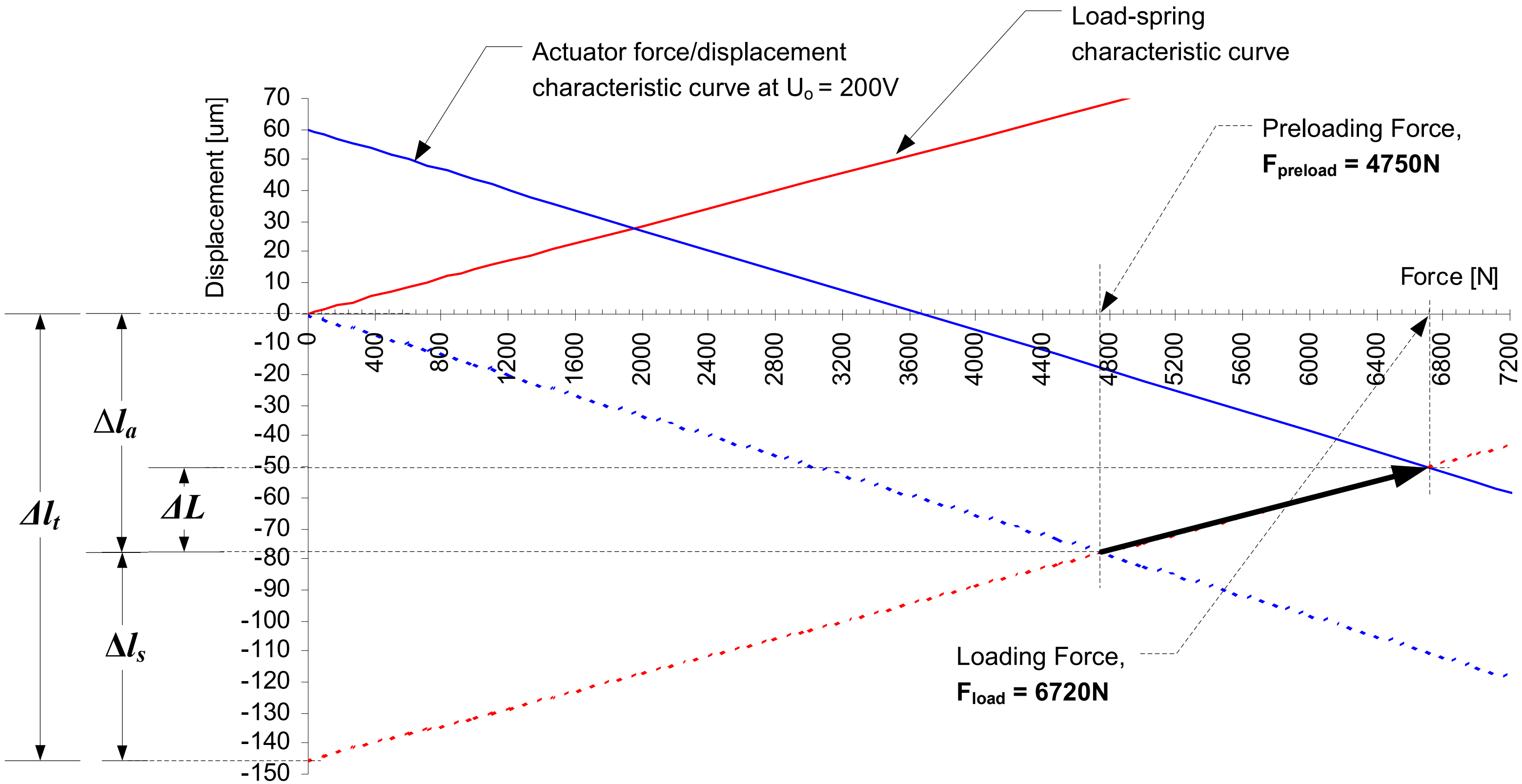

Figure B.9: The preloading and loading conditions of the actuator with the reference number 15/10x10x40/4750/6720/150/200

Appendix C

Calibrations of Force and Displacement Measurement System)

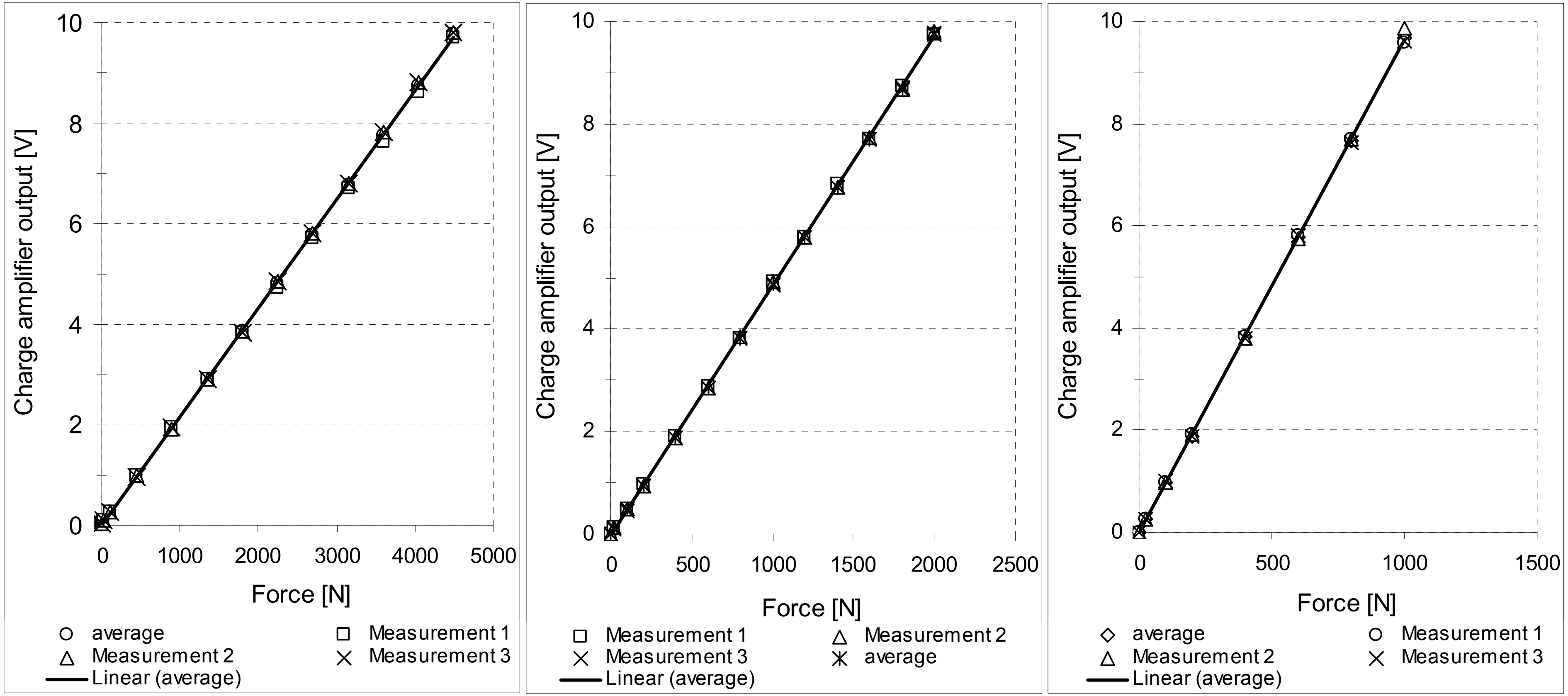

(a) (b) (c)

Figure C.1: Force-voltage characteristics of the force measurement system; (a) measurement setting range = 450N/V, (b) measurement setting range = 200N/V and (c) measurement setting range = 100N/V

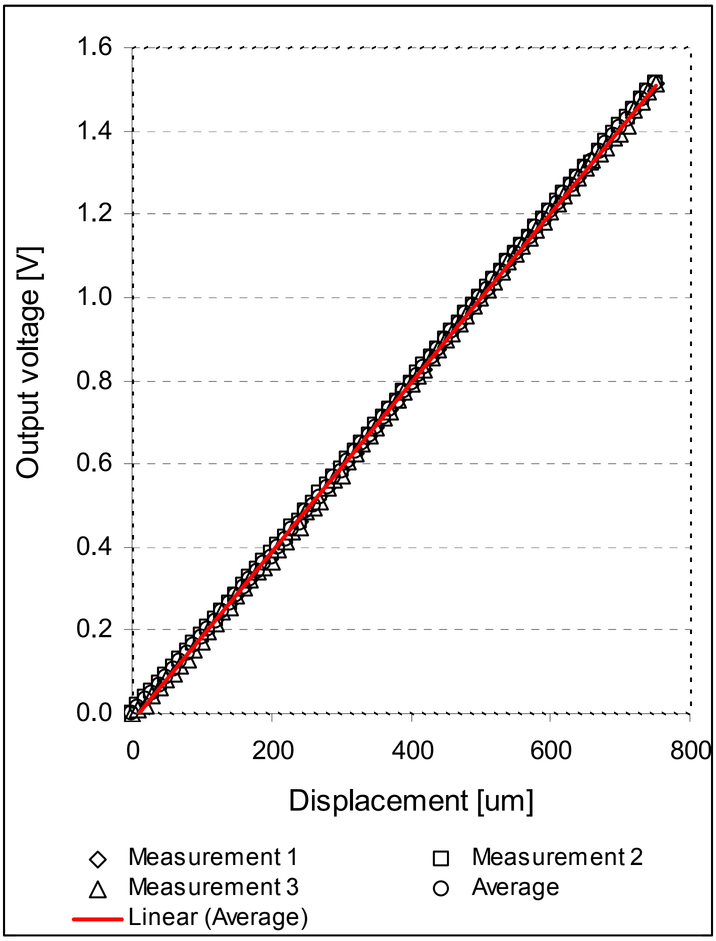

Figure C.2: Displacement-voltage of the displacement measurement system

Appendix D

Accuracy of the B131 Dual Display L/C/R Meter

Table D.1: Accuracy of the B131 Dual Display L/C/R Meter (adopted from the B131 Dual Display L/C/R Meter User Guide booklet).

Range	**Max Display**	**Accuracy**		**Specified Note**
		Cx	**DF**	
1000uF	0.999mF	±(5%+ 5 counts) (DF <0.1)	±(10%+ 100/Cx + 5 counts) (DF <0.1)	After short cal.
100uF	99.99uF	±(1%+ 5 counts) (DF <0.1)	±(2%+ 100/Cx + 5 counts) (DF <0.1)	After short cal.
10uF	9.999uF	±(0.7%+ 3 counts) (DF <0.5)	±(0.7%+ 100/Cx + 5 counts) (DF <0.5)	-
1000nF	999.9nF	±(0.7%+ 3 counts) (DF <0.5)	±(0.7%+ 100/Cx + 5 counts) (DF <0.5)	-
100nF	99.99nF	±(0.7%+ 3 counts) (DF <0.5)	±(0.7%+ 100/Cx + 5 counts) (DF <0.5)	-
10nF	9.999nF	±(0.7%+ 5 counts) (DF <0.5)	±(0.7%+ 100/Cx + 5 counts) (DF <0.5)	After short cal.
1000pF	999.9pF	±(1%+ 5 counts) (DF <0.1)	±(2%+ 100/Cx + 5 counts) (DF <0.1)	After short cal.

Appendix E
Material properties of the ring specimens

Mechanical Properties

The ring specimens used in the study are made from a mild steel type CK15 with the composition of 0.12~0.18% Carbon, 0.4% Silicon, 0.6~0.9% Manganese, 0.035% Phosphorus and 0.035% Sulphur. The mechanical properties of the steel are shown in **Table E.1**.

Table E.1: The mechanical properties of the mild steel type CK15 [1].

Mechanical Properties	**Values**
Modulus of elasticity	205GPa
Yield	340MPa
Ultimate Strength	405Mpa
Density	7870kg/m^3
Poisson's Ratio	0.29

Plastic Strain Behaviour

Details of the material plastic strain behaviour of the steel specimens was obtained by compressing the cylindrical specimens with end recesses between the upper and lower platens as recommended by Rastegaev [2, 3]. An illustration of the compression test is shown in **Figure E.1**. As suggested by Rastegaev, to obtain an accurate result, the ratio between original length l_o and diameter D_o must be equal to

6:5 [2], and the interfacial friction must be as low as possible to avoid barrelling. Therefore, cylindrical specimens with very shallow cavities at the end face, filled with wax as a lubricant, were used in the test. It has been found that this method is the most effective way of reducing friction in the compressing of cylindrical specimens. The detailed dimensions of the specimen used in the test are shown in **Figure E.2**. After compression of the specimen to the length l with minimum interfacial friction, the original diameter D_o was increased to the new diameter D, and therefore the specimen was changed to the new dimensions (after compression) as shown in **Figure E.1**.

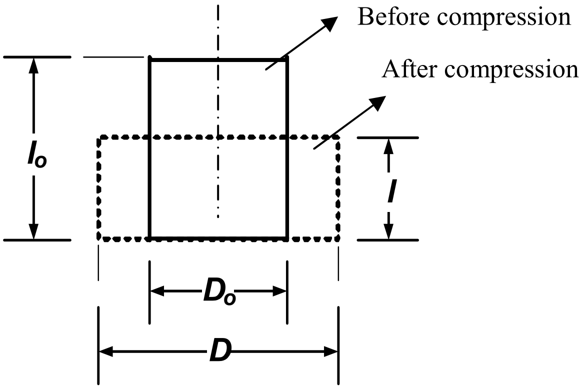

Figure E.1: Rastegaev compression test, before and after compression

Photos of the original cylindrical steel and copper specimens are shown in **Figure E.3.** As shown in **Figure E.3 (b)** and **Figure E.3 (d)**, the cylindrical end recesses of the specimens were filled with wax. Photos of the tool set with the upper and lower platens are shown in **Figure E.4**.

Compressions were performed by using a 1000kN type press machine from ESH Testing, reducing the original length l_o of the specimens by approximately 50% at a constant speed of 0.1mm/s. During the compression, the compression force and displacement measurement data were obtained using the LabView data acquisition system, and the compression force/displacement curve was plotted as shown in **Figure E.5**.

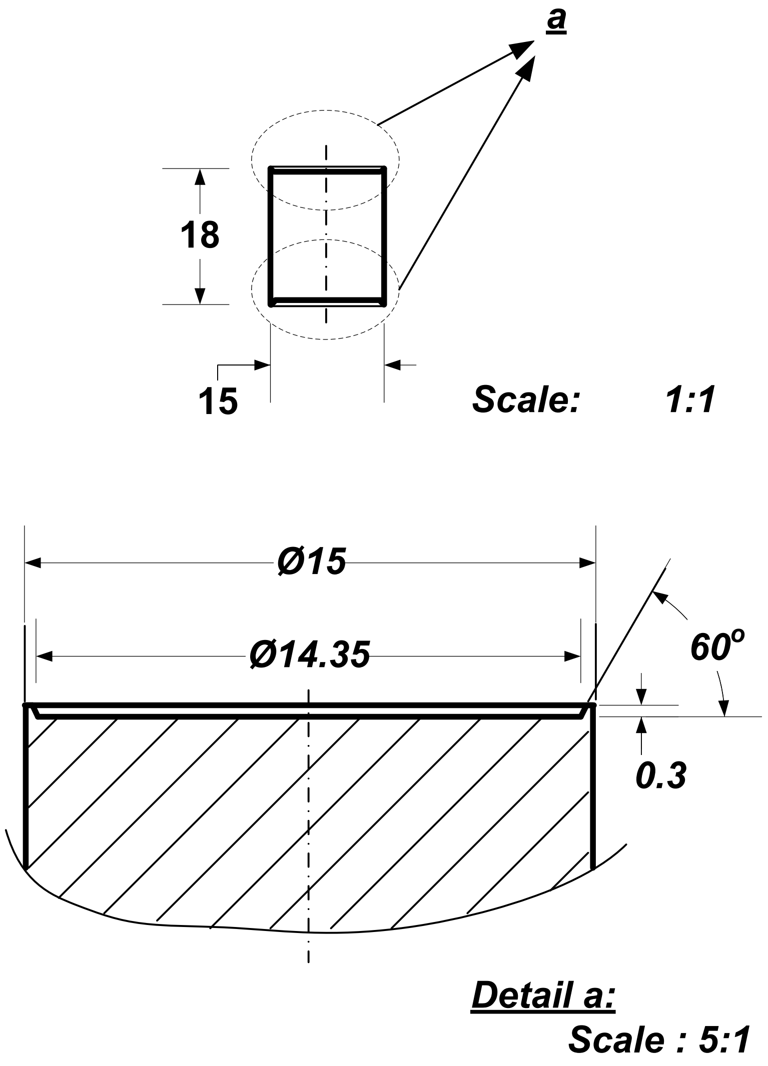

Figure E.2: Detailed drawing of the cylindrical specimen with end recesses

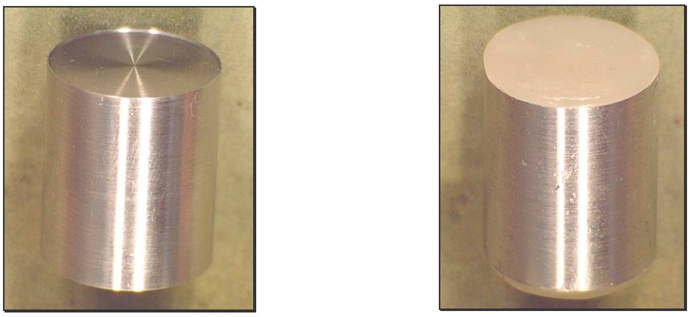

(a) **(b)**

Figure E.3: Examples of cylindrical specimens with end recesses; (a) steel cylinder and (b) steel cylinder with wax

Figure E.4: Compression tool set with platens

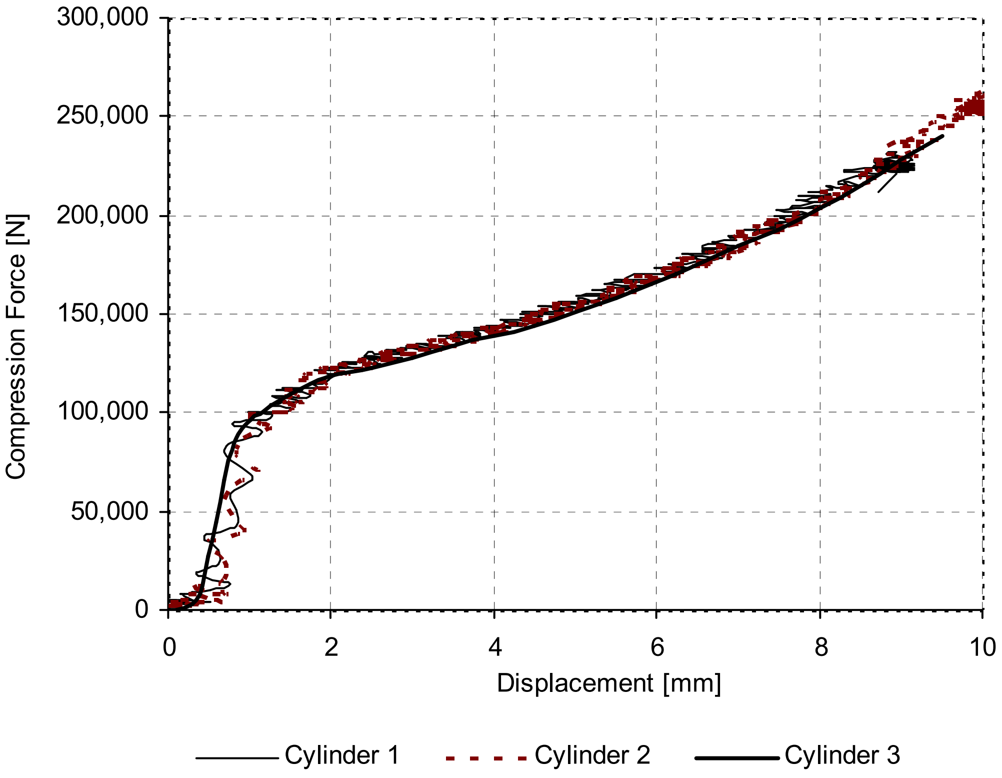

Figure E.5: Force-displacement curves of the cylindrical steel specimens

Subsequently, the true strain and stress values were determined from the force-displacement measurement data is calculated as below:

a. True stress

The true stress data was calculated as:

$$\sigma = \frac{F}{A} \qquad \text{..} \qquad (1)$$

where:

σ : true stress,

F : compression force,

A : instantaneous area

During the compression, the volume of the specimen is always constant, which can be written as:

$$V_o = V \quad \text{……………………………………} \quad (2)$$

where $V_o = l_o A_o$ …………………………………… (3)

and $V = lA$ …………………………………… (4)

$\therefore$ $l_o A_o = lA$ …………………………………… (5)

Or, it can be written as $\frac{l_o}{l} = \frac{A}{A_o}$ ……………….. (6)

Thus, the instantaneous area A *is* determined as:

$$A = \left(\frac{l_o}{l}\right) A_o \quad \text{……………………………………} \quad (7)$$

where:

l : instantaneous length,

l_o : original length,

A_o : original area = $\pi \left(\frac{D_o}{2}\right)^2$ ……….….. (8)

D_o : original specimen diameter

b. True strain

The true strain values were calculated as below:

$$\varepsilon = \ln\left[\frac{l}{l_o}\right] \quad \dots\dots\dots\dots\dots\dots\dots\dots\dots\dots \quad (9)$$

substituting equation (6) into equation (9), the true strain equation can be written as below:

$$\varepsilon = \ln\left(\frac{l}{l_o}\right) = \ln\left(\frac{A_o}{A}\right) \quad \dots\dots\dots\dots\dots\dots\dots\dots \quad (10)$$

Table E.2 shows the calculated true stress and true strain data of the steel specimens, which is used to plot the true stress-strain curve as shown in **Figure E.6**. Because the metal plasticity model in ABAQUS defines the post-yield behaviour for most metals [4], it is necessary to determine the post-yield plasticity behaviour of the specimen material that is required by ABAQUS. The strain data values obtained in the test are not the real values of plastic strain in the specimen's material. They are composed of the total of elastic and plastic strain. Therefore, decomposition of these total strain values into the elastic and plastic strain components is really important. As shown in **Figure E.6**, the real values of plastic strain of the specimens are obtained after Point A on Line A. The region before line A is considered to be the elastic strain of the total component of the specimens and the compression tool set. Lastly, the data for the post-yield plasticity behaviour of the specimens that was obtained from **Figure E.6** is shown in **Table E.3**. The post-yield plastic strain curve of the steel specimens that obtained from **Table E.3** is shown in **Figure E.7.**

Table E.2: True stress-strain data of the steel specimens

Average True Stress/Strain	
True Strain	**True Stress [MPa]**
0.000	0.0
0.011	11.0
0.016	15.0
0.022	24.8
0.030	54.2
0.036	161.5
0.039	253.0
0.044	367.6
0.050	435.5
0.055	470.5
0.060	492.8
0.072	522.2
0.087	547.4
0.102	570.7
0.117	581.6
0.149	601.1
0.181	610.8
0.215	619.2
0.250	620.8
0.286	625.8
0.323	628.4
0.362	632.8
0.403	638.3
0.445	644.6
0.489	648.1
0.535	648.8
0.583	652.3
0.634	655.1
0.688	656.9
0.744	654.8

Table E.3: Post-yield plasticity stress-strain data of the steel

Plastic Strain	*True Stress [MPa]*
0.000	367.6
0.006	435.5
0.011	470.5
0.016	492.8
0.028	522.2
0.043	547.4
0.058	570.7
0.073	581.6
0.105	601.1
0.137	610.8
0.171	619.2
0.206	620.8
0.242	625.8
0.279	628.4
0.318	632.8
0.359	638.3
0.401	644.6
0.445	648.1
0.491	648.8
0.539	652.3
0.590	655.1
0.644	656.9
0.700	654.8

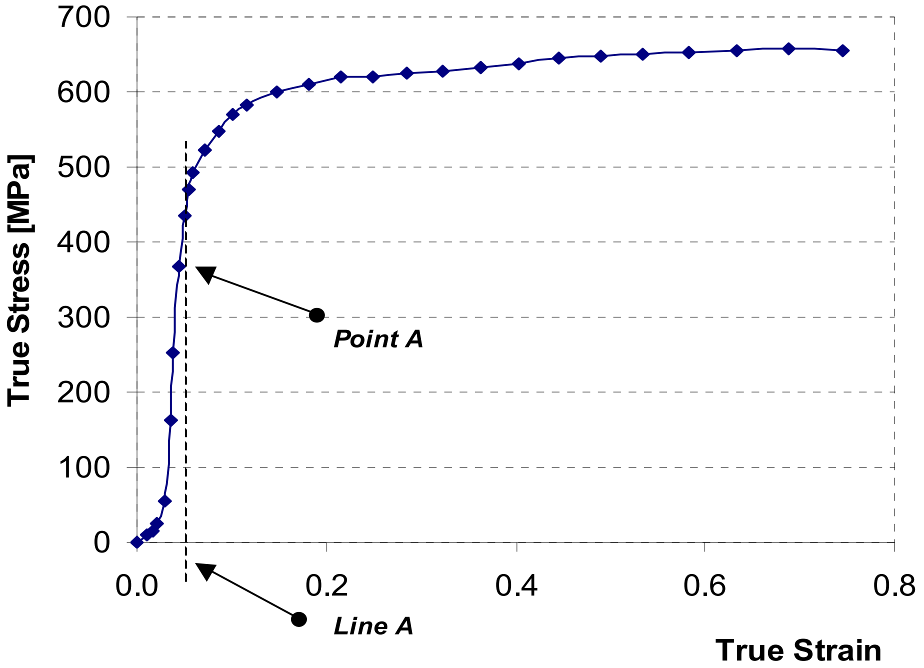

Figure E.6: True stress-strain curve of the steel specimens

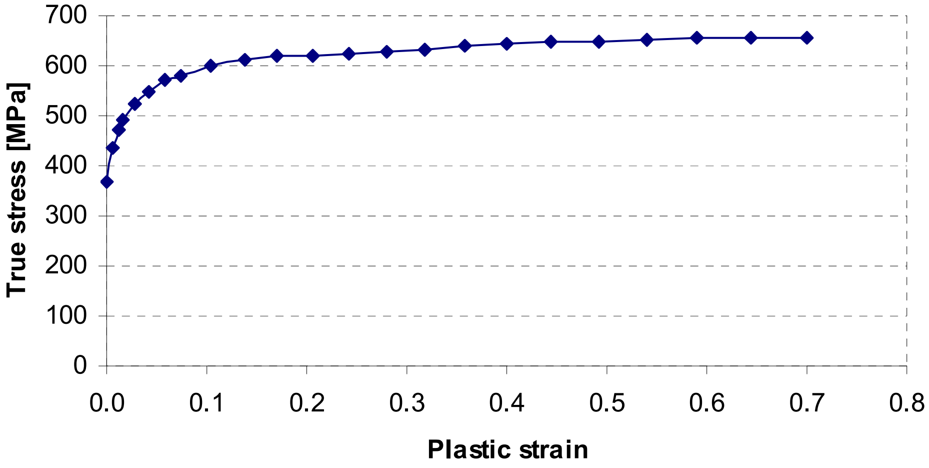

Figure E.7: Post-yield plastic strain curve of the steel specimens

References

1. http://www.matweb.com/search/SpecificMaterial.asp?bassnum=M1017A.
2. Kuczyn'ski, K. and S. Erbel, *Obrobka plastycna*. 1984: Wydawnictwa Politechniki Warszawskiej Warszawa.
3. S.PFC.Jaspers, J.H.D., *Material behavipur in conditions similar to metal cutting:flow stress in the primary shear zone.* Journal of Material processing Technology, 2002. **122**: p. 322-330.
4. Hibbitt, K.S.I., ed. *ABAQUS User Manual*. 1995.